



HAL
open science

Nanoémulsions auto-assemblées par des méthodes physico-chimiques

Kevin Roger

► **To cite this version:**

Kevin Roger. Nanoémulsions auto-assemblées par des méthodes physico-chimiques. Chimie-Physique [physics.chem-ph]. Université Pierre et Marie Curie - Paris VI, 2013. Français. NNT: . pastel-00921639

HAL Id: pastel-00921639

<https://pastel.hal.science/pastel-00921639v1>

Submitted on 20 Dec 2013

HAL is a multi-disciplinary open access archive for the deposit and dissemination of scientific research documents, whether they are published or not. The documents may come from teaching and research institutions in France or abroad, or from public or private research centers.

L'archive ouverte pluridisciplinaire **HAL**, est destinée au dépôt et à la diffusion de documents scientifiques de niveau recherche, publiés ou non, émanant des établissements d'enseignement et de recherche français ou étrangers, des laboratoires publics ou privés.

THESE DE DOCTORAT

Spécialité : Chimie Physique

Présentée par

Kevin Roger

pour obtenir le grade de

DOCTEUR DE L'UNIVERSITE PIERRE ET MARIE CURIE

Nanoémulsions auto-assemblées

par des méthodes physico-chimiques

Soutenue le 8 novembre 2013 devant le jury composé de :

| | | |
|-----|----------------------------|-----------------------|
| Mme | Véronique Schmitt | Rapporteur |
| M. | Håkan Wennerström | Rapporteur |
| M. | Bernard Cabane | Directeur de thèse |
| M. | David Quéré | Co-directeur de thèse |
| Mme | Martine Meireles-Masbernat | Examinatrice |
| M. | Jean-François Joanny | Examineur |
| M. | Jérôme Bibette | Examineur |
| M. | Jean-François Berret | Examineur |

Contents

| | |
|---|-----------|
| Forewords | 1 |
| 1 Equilibrium Self-Assembly | 7 |
| 1.1 Mixing <i>vs.</i> Separation : Energy/Entropy competition | 7 |
| 1.2 Phase separation implies interfaces | 14 |
| 1.3 Reducing the interfacial cost with amphiphiles | 15 |
| 1.4 Preferred curvature | 16 |
| 1.5 Macroemulsions <i>vs.</i> microemulsions | 19 |
| 1.6 Many self-assembly structures at low preferred curvatures | 21 |
| 1.7 From droplets to bicontinuous networks | 24 |
| 2 Non-equilibrium pathways and barriers | 27 |
| 2.1 Coalescence | 28 |
| 2.1.1 Approach of charged droplets | 28 |
| 2.1.2 Hole opening between droplets | 32 |
| 2.1.3 Hole growth between droplets | 34 |
| 2.1.4 Relaxation | 36 |
| 2.2 Ostwald Ripening | 37 |
| 2.2.1 Laplace pressure | 37 |
| 2.2.2 Pathway : solubilization | 39 |
| 2.2.3 Flux | 40 |
| 2.2.4 Inhibiting Ostwald Ripening | 44 |
| 3 Experimental designs | 45 |
| 3.1 Scattering | 45 |
| 3.1.1 Scattering and eye sight | 45 |
| 3.1.2 Scattering equations | 47 |
| 3.1.3 Small-Angle and static scattering | 49 |
| 3.1.4 Dynamic light scattering | 50 |
| 3.2 Phase Diagrams | 53 |
| 3.2.1 The equilibrium is our reference | 53 |

| | | |
|----------|---|------------|
| 3.2.2 | Griding the sample : a bad idea | 53 |
| 3.2.3 | Choosing the starting point | 54 |
| 3.2.4 | Identify metastability barriers | 55 |
| 3.2.5 | Observation | 55 |
| 4 | Summary | 57 |
| 4.1 | Physicochemical methods | 58 |
| 4.2 | Main Findings | 60 |
| 4.3 | Non-equilibrium self-assembly through surfactant fast hydration | 62 |
| 4.3.1 | Rapid quench from access states rather than phase inversion | 62 |
| 4.3.2 | Hydration through interaction changes | 63 |
| 4.3.3 | Hydration through addition of water | 65 |
| 4.3.4 | Systems investigated | 66 |
| 4.4 | Non-equilibrium self-assembly through Solvent-Shifting | 67 |
| 4.5 | Destabilization pathways and barriers | 68 |
| 4.5.1 | Contact Ripening | 68 |
| 4.5.2 | Repulsion controlled coalescence | 69 |
| 4.5.3 | Origin of repulsions in "surfactant-free" conditions | 71 |
| 5 | Articles | 73 |
| | Paper 1: Formation of 10-100 nm Size-Controlled Emulsions through a Sub-PIT Cycle | 73 |
| | Paper 2: Emulsification through surfactant hydration : The PIC process revisited | 82 |
| | Paper 3: Superswollen microemulsions stabilized by shear and trapped by a tem- perature quench | 90 |
| | Paper 4: Why are hydrophobic/water interfaces negatively charged? | 98 |
| | Paper 5: Uncontaminated interfaces are uncharged : a reply | 102 |
| | Paper 6: Coalescence of repelling colloidal droplets : a route to monodisperse populations | 105 |
| | Paper 7: Surface charge of polymer particles in water : The role of ionic end-groups | 117 |
| | Paper 8: Destabilization of emulsions through molecular permeation : Contact Ripening | 124 |
| | Paper 9: The link between preferred curvature and nanoemulsion formation | 133 |
| | Paper 10: Solvent-Shifting : hydrodynamics vs. precipitation | 140 |
| | Bibliography | 145 |
| 6 | Résumé | 149 |
| 6.1 | Introduction | 149 |
| 6.2 | Méthodes d'auto-assemblage | 154 |

| | | |
|-------|---|-----|
| 6.3 | Découvertes principales | 155 |
| 6.4 | Auto-assemblage hors-équilibre : | |
| | Hydratation du tensioactif | 157 |
| 6.4.1 | Trempe d'états d'accès plutôt qu'inversion de phase | 157 |
| 6.4.2 | Hydratation par modification des interactions | 158 |
| 6.4.3 | Hydratation par ajout d'eau | 160 |
| 6.4.4 | Systèmes étudiés | 161 |
| 6.5 | Auto-assemblage hors-équilibre : basculement de solvant | 162 |
| 6.6 | Chemins hors-équilibre | 163 |
| 6.6.1 | Mûrissement de contact | 163 |
| 6.6.2 | Coalescence contrôlée par les répulsions | 165 |
| 6.6.3 | Origine des répulsions dans des conditions sans tensioactif | 166 |

Remerciements**169**

Forewords

We perceive the world by dividing it into systems, such as different objects, people and surroundings. A system may adopt different states, with each state corresponding to a set of macroscopic properties, each of which being the average of microscopic properties. Amongst all the possible states, some are relatively favorable and can be pictured as valleys in the landscape of the possible states, whereas some are relatively unfavorable and can be pictured as mountains. There exists a most favorable state of the system, which is the equilibrium state. If the system can explore all its possible states, or said otherwise is ergodic, it will reach its equilibrium state, given enough time.

Once a system has found its equilibrium state, all the other possible states become irrelevant. The system is then constrained to a single location of the landscape, the deepest valley. However we might desire other properties than those of the equilibrium state to satisfy our purpose. Typical examples are systems whose equilibrium states are a phase separation, macroscopic and/or microscopic, of at least two phases that do not mix. By phase we mean a homogeneous region of space with continuous properties and structure.

This investigation focuses on two such examples: oil/water systems and polymer/bad-solvent systems, which lead to macroscopic phase separation for most conditions. If an additional species is added, such as amphiphiles molecules that populate the interface, the phase separation can be restrained to the microscopic scale. This corresponds to equilibrium self-assembly states, with a variety of structures obtained only in narrow intervals of conditions.

Strong motivations to avoid these equilibrium states are the inconvenience of macroscopic phase separations and the difficulty to maintain the conditions that yield a given microscopic phase separation structure. Instead we may desire to obtain a type of structures for a wide range of conditions and this work focuses on the production of nanometric droplets of controlled sizes.

However, as we move away from the equilibrium state we decrease the number of constraints on the system. Since constraints are necessary for well-controlled structures, it may thus seem paradoxical to aim for size-controlled droplets out of equilibrium. This paradox can be solved by noticing that not all constraints are important to obtain a given structures. Thus the selection of constraints, more than their number, determines the efficiency of the structural control.

The dominant set of emulsification methods requires a high mechanical energy input to cross the barriers that oppose fragmentation of a big oil domain into two smaller ones. Many types of instruments exist, from the cooking whip to the high pressure homogenizer, and each type is associated with a number of constraints that determine the size range and uniformity of the collection of droplets. Such mechanical methods are easily extendable to many types of oil/surfactant/water systems but the production of monodisperse droplets of controlled sizes requires high operating cost in conditions that may also damage some compounds. The system is taken out of equilibrium at high energy cost.

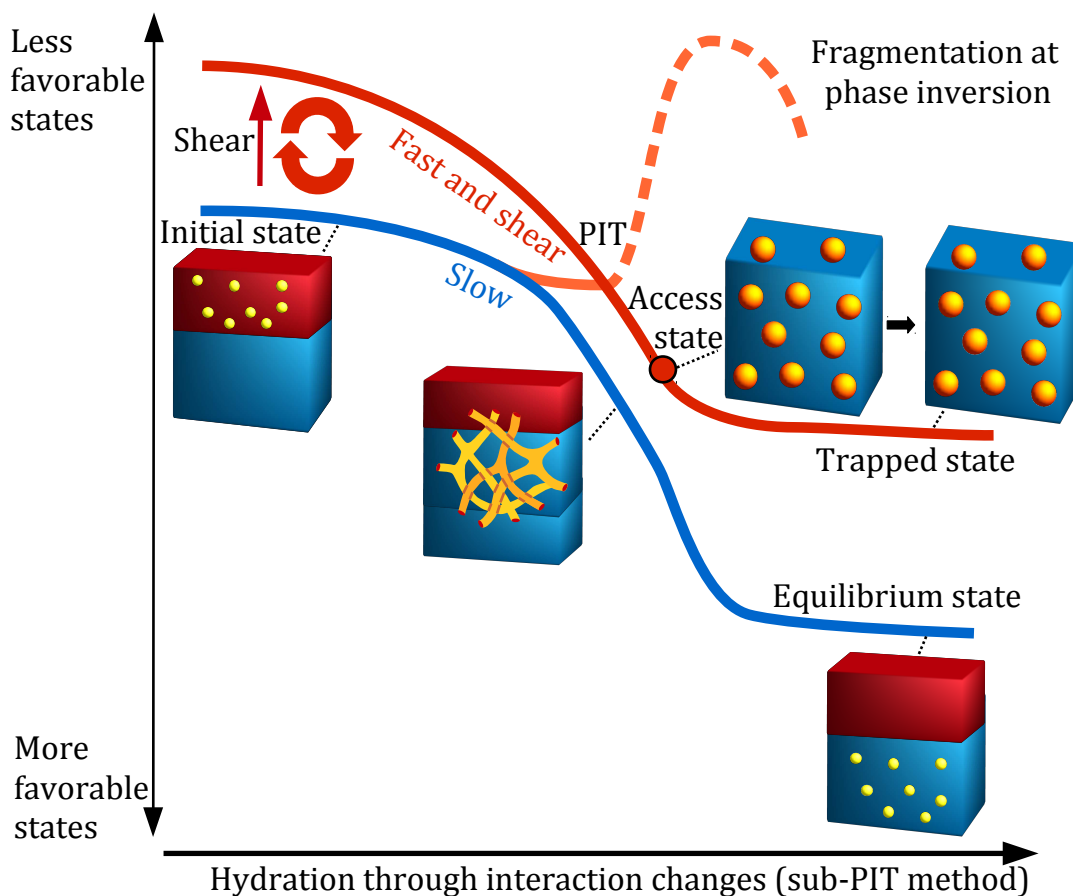


Figure 1: A fine nanoemulsion can be obtained by a hydration increase of a water/oil/surfactant system through a change of interactions, such as with the temperature for C_iEO_j surfactants. A fast temperature quench under shear lead the system along a pathway that crosses an access state, which controls the final emulsion properties and structure.

The physical chemistry approach was historically introduced as a way to optimize mechanical methods. Indeed a reduction of the interfacial cost can be operated by a fine control of the interfacial interactions, and leads to a decrease in the fragmentation cost. The cost is minimized when the surfactant layer is closely balanced between the oil and the water phases. This corresponds to the vicinity of phase inversion, which is the transition from a oil in water state to a water in oil state. The properties of the surfactant layer can be tuned by the hydration of the hydrophilic head. Historically these methods

were designed with oxyethylenated surfactants (C_iEO_j) and the hydration can be tuned by the temperature, and there exists a Phase Inversion Temperature (PIT), or through water addition and there is a Phase Inversion Composition (PIC).

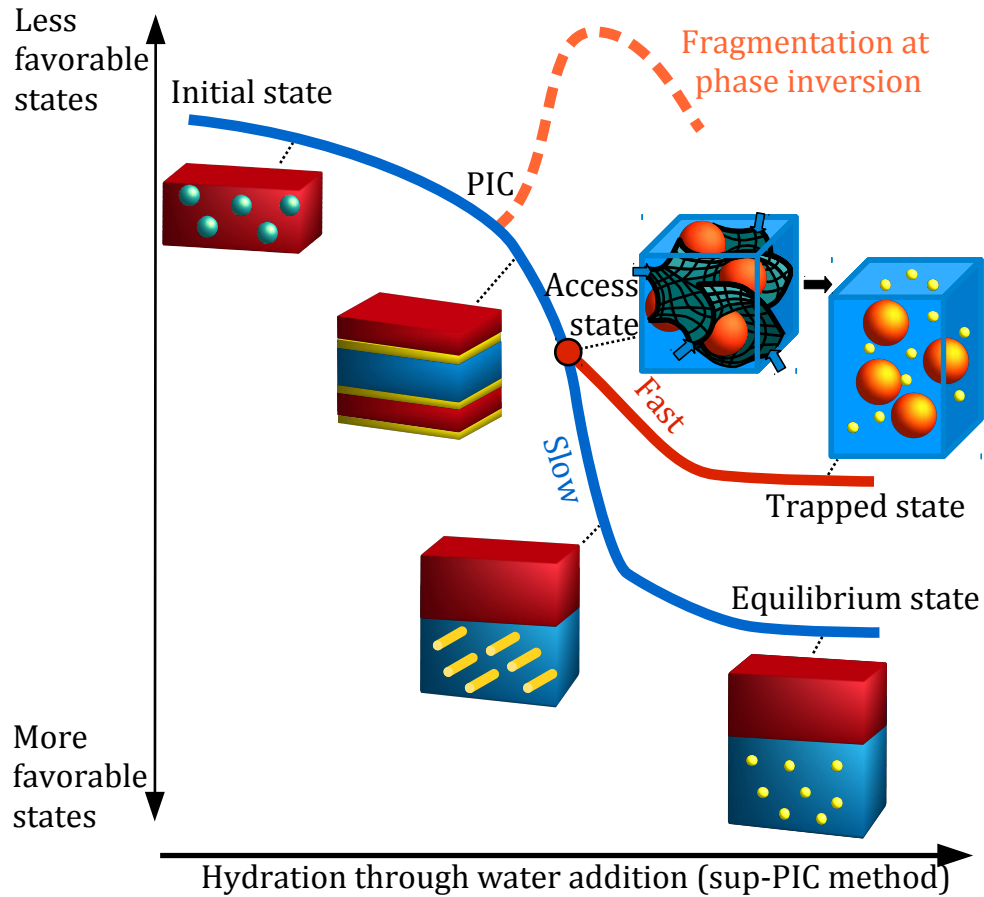


Figure 2: A nanoemulsion can be obtained by a hydration increase of a water/oil/surfactant system through a rapid water addition. At low water content the sequence is similar to the equilibrium one but further addition lead to a bifurcation, which is correspond to an access state that controls the final emulsion properties and structure.

Although this reasoning is correct, this thesis will demonstrate that the fragmentation at phase inversion is actually irrelevant to describe the emulsification mechanism. For both hydration triggers, the barrier to fragmentation is tunneled by another pathway. The mechanism consists in the crossing of an access state that determines the final structure and properties of the nanoemulsion. The methods are in fact truly physicochemical as the constraints are of intermolecular origin, in this case linked to the interface structure and composition, rather than linked to the geometry of the setup as in mechanical emulsification.

If the hydration is regulated by the interaction changes, such as temperature changes, the access state is obtained through a shear perturbation of the system that modify the relative cost of the bicontinuous structures compared to spherical ones. The sequence of states under shear moves slightly away from its equilibrium counterpart. As the access state

is crossed, the system does not change its structure and this trapped state then becomes far away from equilibrium. This sequence is schemed in Figure 1. The structure of the access state is well-controlled by the local constraints of the surfactant layer interactions. Starting directly from this access state, located at temperatures lower than the Phase Inversion Temperature, we can thus design a sub-PIT emulsification method, of physicochemical nature.

If the hydration is increased by the rapid addition of water, the sequence of states is at first similar to the equilibrium one. However, at water content slightly higher than the Phase Inversion Composition there is a bifurcation. This corresponds to the hydration of a sponge phase that templates the oil phase separation rather than convert to the next equilibrium structure. This sponge phase is another access state, also strongly constrained by the surfactant layer interactions, and determines the final properties of the emulsion. This physicochemical method is a sup-PIC method and the sequence is schemed in Figure 2.

These two variants correspond to a common main scenario in which the system is brought to a well defined state, from which it can not escape, as the rest of the landscape continues to evolve around it.

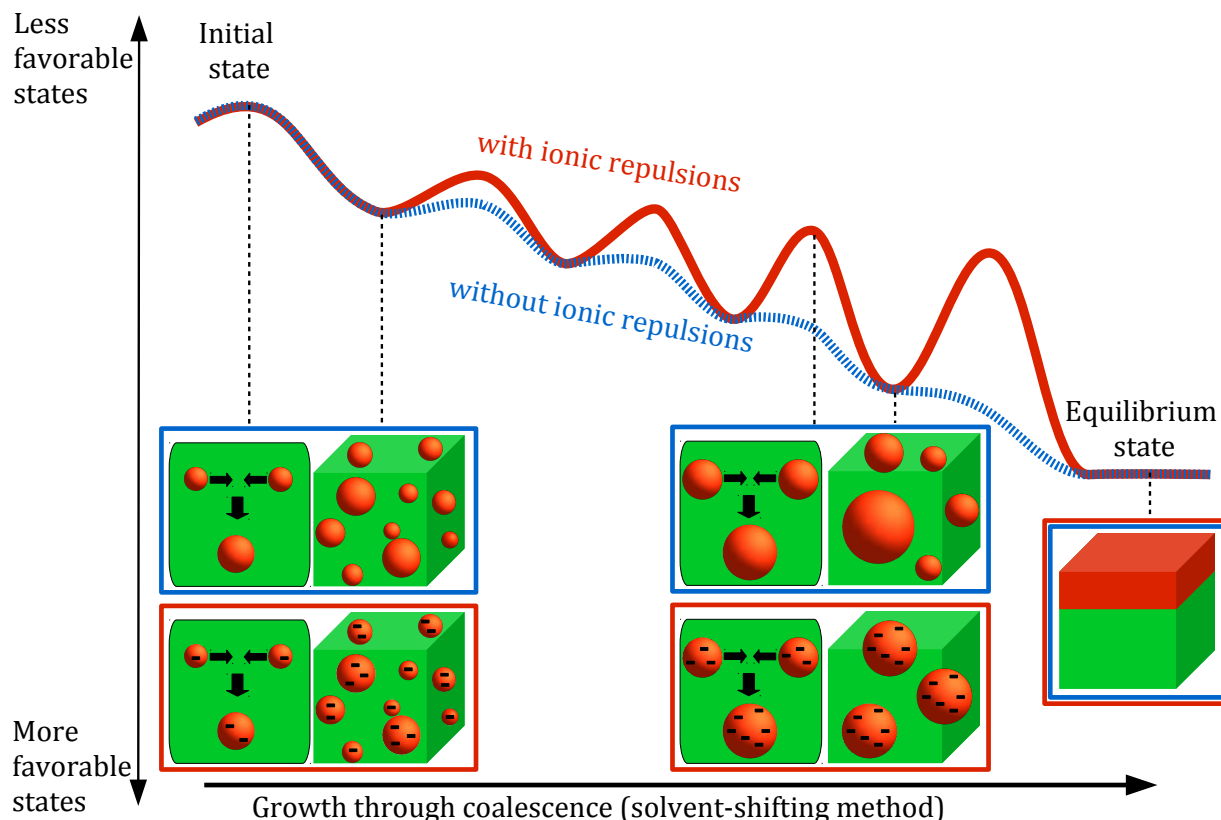


Figure 3: A rapid decrease of the solvent quality leads to precipitation of the solute as droplets. Without any repulsions between the droplets, coalescence takes place more and more easily as the size increases, the barriers decrease in height. To the contrary, if the droplets repel, coalescence is more and more difficult as the size increases, the barriers increase in height. This last sequence constrain the population of droplets to a narrow size-distribution.

An alternative scenario is to push the system towards its equilibrium state but play on the succession of barriers to slow down its progression and control its structure in the process. An illustration is provided by solvent-shifting, which is a nano-precipitation method. The transformation occurs through addition of a bad-solvent to a solution of a solute in a good solvent, which triggers precipitation of the solute. If we don't control the pathway, the solute will form droplets, which will merge and form bigger one until macroscopic phase separation is reached. This corresponds to a climb down with smaller and smaller barriers as the size of the droplets increase. However if we add repulsions between droplets, the barriers will instead increase as the size of the droplets increase. This succession of increasing height barriers leads to a fine control of the collection of droplets, which is illustrated in Figure 3.

Designing methods following one of these three schemes requires a well-furnished arsenal. First a good understanding of the possible equilibrium states is essential, although we aim to avoid reaching them. Indeed either the non-equilibrium states encountered will share with them similar constraints, as the interfacial interactions in the sub-PIT and sup-PIC methods, or the system will evolve towards its equilibrium state, as in the solvent-shifting method. Equilibrium states structures and ranges of existence, especially the case of macroscopic phase separation and its microscopic counterpart, self-assembly, are discussed in Chapter 1.

Since the system evolves from one state to another along pathways, they should be described in details. Furthermore, controlling the pathways is key to access the flexibility of non-equilibrium states. Indeed, in many practical purposes it is more interesting to store the system in one state and then use it in a different state, which is compromised if the system remains locked in a single state such as equilibrium. These pathways may consist of a succession of barriers and the evolution is far from equilibrium, as for coalescence in which two droplets merge to form a bigger one, or relate directly to a relaxation process towards the equilibrium state, as in Ostwald ripening where big droplets solubilize smaller droplets through monomer diffusion in the continuous phase. Understanding these pathways allows to hinder or favor them and they are described in details in Chapter 2.

Experimental methods to probe the equilibrium states and the pathways are then described in Chapter 3. The emphasis is put on a careful observation of the system to determine its state. Basics of scattering theory are then presented, scattering methods being powerful characterization tools in the nanodomain, as well as a methodology to simplify the experimental determination of phase diagrams, which map the equilibrium states.

Chapter 4 presents the main results of this thesis, which revolve around the scenarios presented in these forewords. The aim is to give a practical summary of the different facets of this thesis work, so that the reader can bring them to different horizons. Finally, Chapter 5 contains the sequence of the research articles on which this work is based. These articles contain the detailed evidences, reasoning and conclusions that are used to build this thesis.

Chapter 1

Equilibrium Self-Assembly

Contents

| | | |
|------------|--|-----------|
| 1.1 | Mixing <i>vs.</i> Separation : Energy/Entropy competition | 7 |
| 1.2 | Phase separation implies interfaces | 14 |
| 1.3 | Reducing the interfacial cost with amphiphiles | 15 |
| 1.4 | Preferred curvature | 16 |
| 1.5 | Macroemulsions <i>vs.</i> microemulsions | 19 |
| 1.6 | Many self-assembly structures at low preferred curvatures . . | 21 |
| 1.7 | From droplets to bicontinuous networks | 24 |

Independently of the pathway taken, all systems eventually reach their equilibrium state, providing they are ergodic and can thus explore all possible states. We always define the non-equilibrium states by comparison to the equilibrium states, which are then reference states. Furthermore we can identify the drive for evolution, from a given initial state to the equilibrium state, through an understanding of what determines the equilibrium structure of a given system. The aim of this chapter is to study oil/water mixtures and the equilibrium self-assembly structures obtained upon addition of amphiphilic molecules. The approach is to derive the thermodynamic theory on a simple but explicit example and then build mesoscopic quantities from this microscopic theory.

1.1 Mixing *vs.* Separation : Energy/Entropy competition

Some liquids mix and form a single phase, while some others separate into different phases. Typically oil separates from water (immiscibility) but ethanol mixes with water in all proportions (miscibility). The type of behavior is determined by the structures of the molecules, which determine the interactions, and the external parameters, such as the

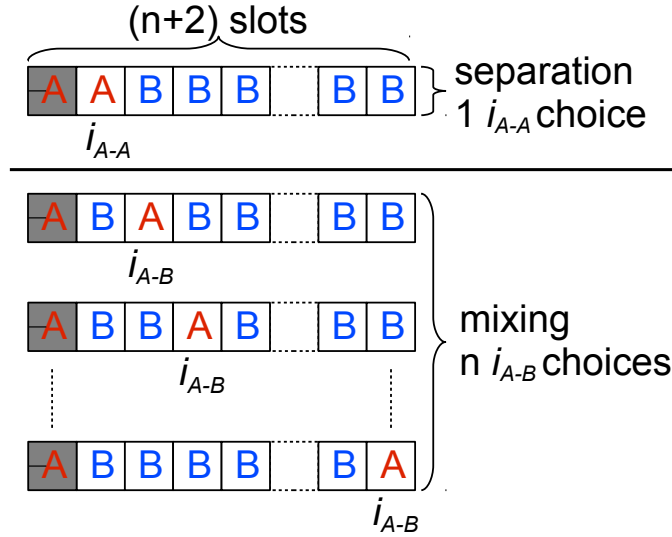


Figure 1.1: One-dimension grid composed of $(n + 2)$ slots. The interactions are different if the free A is close or far from the bound A. We can then easily calculate the probabilities for one slot to be occupied by the free A.

temperature. Describing the equilibrium state requires a theoretical frame, thermodynamics. The thermodynamic frame is also useful for more complex systems that have been investigated in this thesis. However the application of thermodynamics requires a clear view of the links between the thermodynamic functions and the microscopic details. I have thus chosen to present first a simple situation in a one dimension system, which allows straightforward calculations of the key functions. However, being one-dimensionnal, it can not fully describe the important notions of phases and phase transitions[20]. I will thus follow the presentation by an extension of this simple model.

We consider two types of molecules A and B and grid the space into the same number of slots as of molecules A and B. Rather than look at all the molecules A and all the molecules B, we first focus on one molecule A and try to predict whether it is preferentially located next to another A or surrounded by B's. For simplification, we consider a one-dimension grid as displayed in Figure 1.1. The grid is composed of $(n + 2)$ slots. The left slot is occupied by a A specie somehow bound to it. One slot is occupied by another specie A and the n other slots are occupied by species B. If the interactions between one A and one B are the same as between one A and another A, the free A has the same probability to occupy any slot and this probability is $p = 1/(n + 1)$. However if the interactions are different, the probability for A to occupy the slot next to the bound A, which corresponds to separation, is different from the probability for A to occupy any other slot, which corresponds to mixing. We can affect an interaction coefficient for each slot, i_{A-A} for the slot next to the bound A and i_{A-B} for the n other slots. These coefficients are used to ponder the probabilities and since the free A is either in a mixing or separation state, $p_{separation} + p_{mixing} = 1$. We can then define the coefficients from the probabilities of the two states :

$$p_{separation} = \frac{i_{A-A}}{i_{A-A} + n \cdot i_{A-B}} \quad (1.1)$$

$$p_{mixing} = \frac{n \cdot i_{A-B}}{i_{A-A} + n \cdot i_{A-B}} \quad (1.2)$$

The variations of $p_{separation}(n)$ and $p_{mixing}(n)$ for a given set of interaction coefficients are displayed in Figure 1.2, taking $i_{A-A} > i_{A-B}$. Mixing is more probable than separation when $p_{mixing} > p_{separation}$, which corresponds to $n \cdot i_{A-B} > i_{A-A}$. For a given set of interaction coefficients, there always exist a range of values $n > i_{A-A}/i_{A-B}$ for which the mixing is more probable than the separation. We can reformulate this by saying that a specie A can always be solubilized by another specie B, if diluted enough. We can define a solubility i_{A-B}/i_{A-A} that increases as the interaction A-B matches the interaction A-A. We can conclude that the competition between mixing and separation is determined by the competition between the interactions, i_{A-A}/i_{A-B} , that favor the separation and the number of choices, n , that favor the mixing.

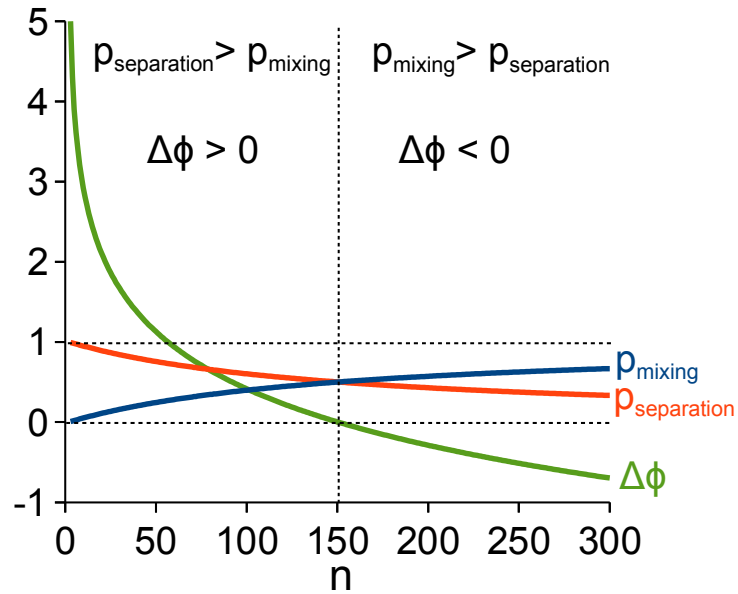


Figure 1.2: Evolution of the mixing and separation probabilities and the potential difference with the number of slots.

We want a tool to predict whether mixing or separation is more favorable in more complicated situations, such as a collection of A and B in a three-dimensional grid, which is closer to real systems. Since we have explicitly the probabilities in our simple geometry, we can look for a function $\Delta\phi = \phi_{mixing} - \phi_{separation}$ that is negative when $p_{mixing} > p_{separation}$, positive when $p_{mixing} < p_{separation}$ and zero when $p_{mixing} = p_{separation}$, i.e. $n = i_{A-A}/i_{A-B}$. To account for the competition, we can write it as the difference between an interaction term $\Delta e = e_{mixing} - e_{separation}$ and a number of choices term $\Delta s = s_{mixing} - s_{separation}$, that we now need to link to the interaction parameters and the number of slots.

Δe corresponds to the difference in interactions between the mixing state and the separation state. For the mixing state, A not next to another A, we count 3 interactions A-B and $(n - 2)$ interactions B-B, whereas for the separation state, A next to another A, we count 1 interaction A-B, 1 interaction A-A and $(n - 1)$ interactions B-B. The difference in interactions between mixing and separation states is thus $(2e_{A-B} - e_{A-A} - e_{B-B})$. This difference increases with the difference in interactions between the different molecules, which is unfavorable to mixing according to experiments. Applying a scale factor f to the interaction coefficients leaves the probabilities p_{mixing} and $p_{separation}$ unchanged, we thus want to constrain the function e to be also unchanged upon application of a scale factor. This corresponds to the condition :

$$\Delta e(f.i_{A-B}, f.i_{A-A}) = e(f.i_{A-B}) - e(f.i_{A-A}) = e(i_{A-B}) - e(i_{A-A}) + e(f) - e(f) = \Delta e(i_{A-B}, i_{A-A}).$$

If the interactions are all the same, such as with a single type of molecule, $\Delta e(i_{A-A}, i_{A-A}) = 0$.

Δs corresponds to the difference in number of choices between the mixing and the separation. In our example the number of choices is the number of possible slots for a given state. Since there are more possible slots (n) in the mixing state than in the separation state (1), we look for a function s that follows $\Delta s > 0$. This term favors the mixing state, opposing the interaction term Δe . Furthermore if we consider two independent grids, with respectively n_1 and n_2 slots, we want to express the total entropy $s(n_1, n_2)$ from the separate entropy of each independent grid, $s(n_1)$ and $s(n_2)$. To constrain the function s to be extensive requires that : $s(n_1, n_2) = s(n_1.n_2) = s(n_1) + s(n_2)$. This relation is thus not true for coupled grids but will however hold approximately if the grids are large enough (this is corresponds to the thermodynamic limit). We can also constrain s to be zero when there is only one possible choice for a given state so that $s(1) = 0$.

To sum up we are looking in both cases for a function g so that $g(x.y) = g(x) + g(y)$ and this leads naturally to using the logarithm function. We then define Δe and Δs so that :

$$\Delta e = e_{mixing} - e_{separation} = -\ln(i_{A-B}) + \ln(i_{A-A}) = \ln(i_{A-A}/i_{A-B}) \quad (1.3)$$

$$\Delta s = s_{mixing} - s_{separation} = \ln(\text{choices}_{mixing}) - \ln(\text{choices}_{separation}) = \ln(n) \quad (1.4)$$

Which leads to :

$$\Delta \phi = \phi_{mixing} - \phi_{separation} = \ln\left(\frac{i_{A-A}}{n.i_{A-B}}\right) \quad (1.5)$$

The variation of $\Delta \phi(n)$ for a given set of interaction parameters is compared to the variations of $p_{separation}(n)$ and $p_{mixing}(n)$ in Figure 1.2. At the solubility, $p_{mixing} = p_{separation}$ and indeed $\Delta \phi = 0$. $\Delta \phi > 0$ when the mixing is less probable (unfavorable) and $\Delta \phi < 0$ when it is more probable (favorable). This is conceptually equivalent to a (non-dimensional) potential difference between a potential of mixing, ϕ_{mixing} , and of separation, $\phi_{separation}$. The most probable state is the one of lowest probability potential ϕ . The ratio of the

separation and mixing partition functions, $(i_{A-A}/n.i_{A-B})$, is logarithmically linked to the potential difference.

At this point we have build non-dimensional quantities that describe efficiently the probability distribution. We must now relate these to physical quantities. Thermodynamic was build historically to describe work and heat exchange, which have the dimension of an energy. The reference energy is the thermal energy, which is written as $k_B T$, where k_B is the Boltzmann constant and T the temperature. To match the microscopic description to the classical description we must define the energy as $E = e.k_B.T$ and the entropy as $S = k_B.s$.

The interactions should be expressed in energy units and thus ϕ , e and s have to be converted. We choose to define the interaction energy as $E = e.k_B.T$ and the entropy as $S = k_B.s$. The thermodynamic potential is then $\Phi = \phi.k_B.T$ and takes the following form :

$$\Phi = E - T.S \quad (1.6)$$

The thermodynamic potential is a tool to compare two states as the most probable state is that of lowest thermodynamic potential. We can thus identify the most probable state, the equilibrium state, by minimizing the thermodynamic potential. This tool becomes interesting when the systems get more complicated than the simple example used to construct it. Typically if we consider the full mixing of many A's and many B's, the calculation of all the probabilities of each state becomes quickly difficult since we have to represent all the configurations. To the contrary the calculation of the thermodynamic potential is achievable through two main options. The first is to use a mean field approach, which is to consider an average environment of each A and B. The second is to perform simulations that calculate the thermodynamic potential for each state and relates the probability of each state to this potential, this is typically the basis of Monte Carlo simulations. Hence the thermodynamic frame is useful to understand which macroscopic state (separation or mixing) is chosen through knowledge of microscopic parameters (interactions, size of the system, composition), without knowing all the microscopic details (the different positions of each A and each B).

To describe the phase separation phenomenon, which is the most common equilibrium state we will try to avoid in this work, we must now extend the dimension of the system. I will present below the classical derivation of the Bragg-Williams model, which is fully detailed in the books of Evans and Wennerström[9] and of Cabane and Hénon[5]. We consider a two dimensions grid with N slots all occupied by N_A A molecules and N_B B molecules. To predict whether the equilibrium state is a phase separation between a phase of pure A and a phase of pure B or a solution of mixed A and B, we must compare the thermodynamic potential of these two states. From equation (1.6) this requires calculating the variation of entropy and of energy from the phase separation state to the mixing state.

We can first calculate the entropy variation. Since the phase separation state corresponds to a single configuration, its entropy is zero. The entropy variation is thus equal to the entropy of the mixing state and is given by the number of mixing choices Ω :

$$\Omega = \frac{N!}{N_A!N_B!} \quad (1.7)$$

$$\Delta S = S_{mixing} - S_{separation} = k_B \cdot \ln \Omega = k_B (\ln(N!) - \ln(N_A!) - \ln(N_B!)) \quad (1.8)$$

Since the number of molecules is large, we can use the Stirling approximation :

$$\ln(N!) \approx N \cdot (\ln N - 1) \quad (1.9)$$

Which leads to :

$$\Delta S \approx -k_B [N_A \ln(\frac{N_A}{N}) + N_B \ln(\frac{N_B}{N})] \quad (1.10)$$

The entropy of mixing is maximal when $N_A = N_B = N/2$, which corresponds to the largest number of choices.

To calculate the energy we must count the interactions of each molecule with its neighbors. Constraining the molecules to a grid already provide some simplifications compared to the real problems, since we don't consider density fluctuations, but the energy calculation still requires another approximation. Indeed each molecule interacts with many neighbors, A or B, and this many-body problem is difficult. Instead we assume that all the interactions can be counted by pairs. For example in the phase of pure A we can then assume that the interaction of one A surrounded by z other A is the same as z interactions between one A and another A. Being careful not to count twice the same interaction, the total interaction energy of the pure A phase is then :

$$E_{pureA} = \frac{1}{2} N_A \cdot z \cdot \epsilon_{A-A} = n_{A-A}^{sep} \cdot \epsilon_{A-A} \quad (1.11)$$

with ϵ_{A-A} the energy of a A-A pair interaction and n_{A-A}^{sep} the number of A-A pairs in the pure phase of A. The energy of the phase separation state is then :

$$E_{separation} = n_{A-A}^{sep} \cdot \epsilon_{A-A} + n_{B-B}^{sep} \cdot \epsilon_{B-B} \quad (1.12)$$

With the same reasoning we can calculate the energy of the mixing state :

$$E_{mixing} = n_{A-A}^{mix} \cdot \epsilon_{A-A} + n_{B-B}^{mix} \cdot \epsilon_{B-B} + n_{A-B}^{mix} \cdot \epsilon_{A-B} \quad (1.13)$$

We can count the number of pairs in the mixing state and thus relate them to the number

of molecules A and B through the relations :

$$2n_{A-A} + n_{A-B} = z.N_A \quad (1.14)$$

$$2n_{B-B} + n_{A-B} = z.N_B \quad (1.15)$$

This leads to the energy variation :

$$\Delta E = E_{mixing} - E_{separation} = n_{A-B}^{mix} \left(\epsilon_{A-B} - \frac{1}{2}\epsilon_{A-A} - \frac{1}{2}\epsilon_{B-B} \right) \quad (1.16)$$

We can define an effective interaction parameter :

$$\epsilon = z \cdot \left(\epsilon_{A-B} - \frac{1}{2}\epsilon_{A-A} - \frac{1}{2}\epsilon_{B-B} \right) \quad (1.17)$$

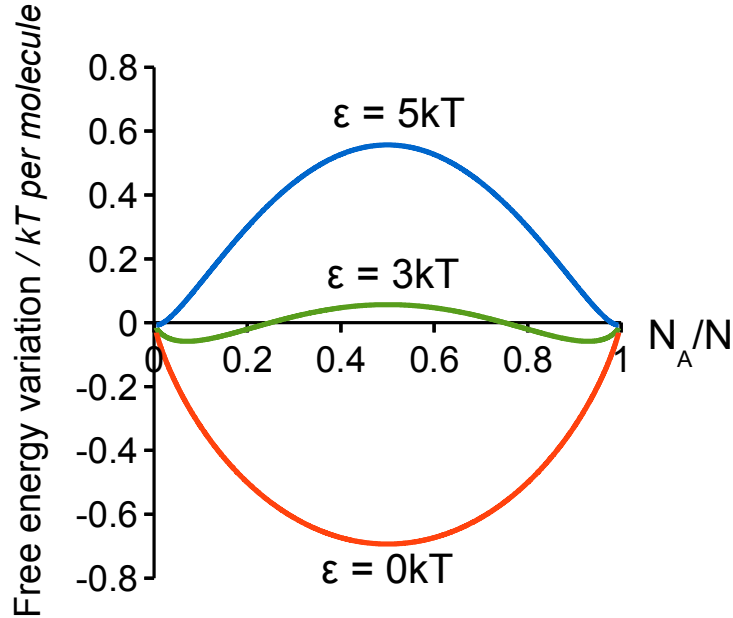


Figure 1.3: Free energy difference between phase separation and mixing as a function of the fraction of A molecules, for three values of the effective interaction parameter ϵ . The energy term favors phase separation and thus competes with the entropy term, which favors mixing.

Finally we assume that the molecules mix in a random way to estimate the number of pairs, which is then :

$$n_{A-B}^{mix} = z.N_A \frac{N - N_A}{N} \quad (1.18)$$

We have then achieved the final goal, which is to express the variation of the thermodynamic potential (or free energy F) :

$$\Delta F = F_{mixing} - F_{separation} \quad (1.19)$$

$$\Delta F = N \left[\frac{N_A}{N} \frac{N_B}{N} \epsilon + k_B T \left(\frac{N_A}{N} \ln \left(\frac{N_A}{N} \right) + \frac{N_B}{N} \ln \left(\frac{N_B}{N} \right) \right) \right] \quad (1.20)$$

We can plot ΔF for different values of the effective interaction parameter ϵ , as displayed in Figure 1.3. I have plotted the free energy variation, in units $k_B T$ per molecule, as a function of the fraction N_A/N , for the two limiting cases. The first corresponds to similar interactions A-B, A-A and B-B, with $\epsilon = 0k_B T$. The free energy variation is then negative, which means that the mixing is more favorable than the phase separation. In this situation the entropy dominates and thus favors the mixing, as in the 1-dimension example. To the contrary, when the interactions are very different such as $\epsilon = 5k_B T$, the free energy variation is positive and the phase separation is more favorable. In this situation the energy dominates and favors separation, as in the 1-dimension example.

If we take an intermediate value, such as $\epsilon = 3k_B T$, the free energy variation has two minima and the situation is intermediate. The equilibrium state will be a phase separation but each phase will be a mixture of A and B, at the fraction given by each minimum. This illustrates that there is always a partial solubility of one species in the other (this is in fact also the case at the higher $\epsilon = 5k_B T$ value, but the solubility is extremely small and not distinguishable on the drawing).

The general conclusion is that the energy term favors phase separation, whereas the entropy term favors the mixing. Several examples will illustrate this principle in the rest of this thesis.

1.2 Phase separation implies interfaces

As stated in the previous section, the driving force for phase separation is the energy difference $\Delta E = 2.E_{A-B} - E_{A-A} - E_{B-B}$. It competes with the driving force for mixing, which is the entropy. If we consider a situation where two interactions A-B are weaker than one interaction A-A and one interaction B-B, such as the case of oil and water, phase separation is more probable than mixing. However there is always a residual solubility of some A in the phase B and of some B in the phase A. This solubility can be important for relaxation to equilibrium, which will be discussed in the next chapter.

If we take a system strongly dominated by the energy difference, phase separation occurs and we can at first-order neglect this solubility and assume domains of each pure compounds are formed. We have however not said anything on the number of domains formed. The intuitive idea that comes to mind is that we form only two domains, which means we are minimizing the contact between the two compounds. Such a picture comes to mind when considering the outcome of mixing oil and water where the number of domains, i.e. oil droplets, quickly decrease to form a single domain of oil over water.

The surface minimization stems from an energy cost of the unavoidable region where the two compounds interact, the interface. Assuming an infinitely thin interface, i.e. that contact occurs only on a surface, the energy cost per unit area is $\gamma = \sigma.[2.E_{A-B} - E_{A-A} -$

$E_{B-B}]$, where σ is the surface number density of molecules at the interface. In the case of two pure liquids, the energy cost usually largely dominates the entropy cost and can thus be assimilated to the thermodynamic potential (usually named free energy) cost. γ is named the interfacial tension and ($\gamma \cdot \text{Area}$) is thus the free energy cost of the interface. For a given interfacial tension, i.e. interactions, minimizing the thermodynamic potential is thus equivalent to minimizing the interfacial area. This is the driving force for two droplets to merge and form a bigger one.

1.3 Reducing the interfacial cost with amphiphiles

Methods to reduce the free energy cost of interfaces have been found relatively early in mankind history. The use of soap solutions in water to clean oil layers on skin goes back to the ancient Babylon and Egypt (3000 BC/2000 BC). To decrease the interfacial cost we must prevent the contact between the two phases at the interface. If we use molecules composed of two parts, one that would mix with water (hydrophilic) and one that would mix with oil (lipophilic), they will preferentially populate the interface and indeed prevent the direct contact between the phases. A popular amphiphilic molecule used in surfactant science is Sodium Dodecyl Sulfate (SDS). SDS is constituted of a twelve carbon linear alkane chain covalently linked to a sodium sulfate ion. Let's consider the interface between water and dodecane oil, a linear alkane with twelve carbon atoms and thus the same structure as the hydrophobic part of SDS. The sodium sulfate salt is very insoluble in the alkane, since there are no dipolar interactions to favor ions solvation. To the contrary water, which is constituted of strongly correlated dipoles, is a good solvent of salts. The hydrophobic tail should mix very well with the oil, which has the same structure, but not with water since dodecane oil and water do not mix. The SDS meets our definition of an amphiphilic molecule, does it lower the interfacial tension of the dodecane/water interface?

Results from Bonfillon and Langevin[4] are redrawn in Figure 1.4 for pure water and slightly salty water. We observe a decrease of the interfacial tension when adding amphiphilic molecules. This property has earned such molecules the name of surfactants (contraction of surface active agents). The collapse of the interfacial tension demonstrates that the main contribution to the thermodynamic potential of the system is the adsorption of surfactant at the oil/water interface to reduce the contacts. The energies involved are larger than the thermal energy $k_B T$ and the area per surfactant molecule is not easily tuned.

However, one could have naively hoped that the interfacial tension would reach a constant zero value if enough surfactant is added. Instead the interfacial tension reaches a constant non-zero value that we can term as a residual tension. What is the origin of this residual cost if we have suppressed the direct contact between the oil and the

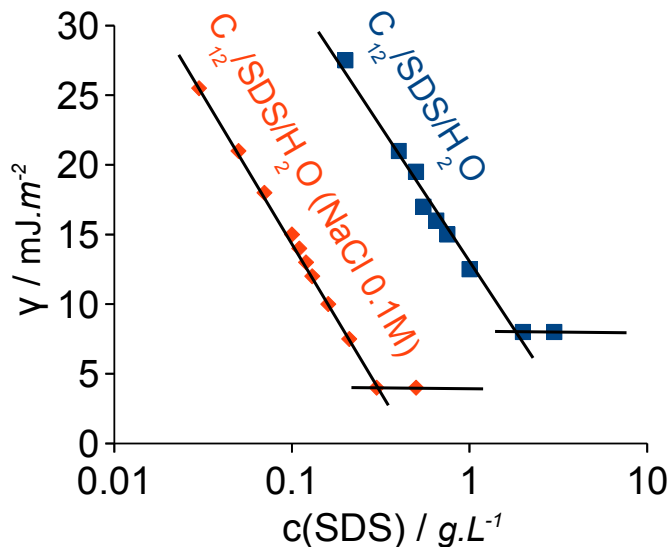


Figure 1.4: Variation of the interfacial tension of a water/dodecane interface with the concentration of SDS and two salt concentrations. The results are taken from Bonfillon and Langevin[4]. The interfacial tension decreases up to a residual non-zero value at a given surfactant concentration.

water? At this point it is useful to zoom on the interface and examine the balance of interactions. We have mentioned so far the interaction between the hydrophilic group and water and the hydrophobic group and oil. We have forgotten the crossed interactions hydrophilic group/hydrophilic group, hydrophobic group/hydrophobic group, hydrophobic group/water, hydrophilic group/oil and hydrophobic group/hydrophilic group. Residual tensions originate from the the sum of all these contributions. Since SDS is a charged surfactant, the addition of sodium chloride salt to the water modifies the interaction and indeed the residual tension value changes, as shown in Figure 1.4.

1.4 Preferred curvature

A microscopic analysis of the interactions and conformations of the molecules at the interface is a difficult problem that has not been solved. The approach has been rather to meet the problem halfway at the mesoscopic scale and look for a mesoscopic variable that changes the balance of microscopic interactions and conformations. Let's consider a few amphiphilic molecules densely packed at an interface and interacting with oil and water molecules as schematically drawn in Figure 1.5. Hydrophilic heads are schemed as red spheres, solvated by water molecules as smaller green spheres, while the hydrophobic chains and the oil chains are pictured by a black curve.

A flat line to separate the oil and water phases may seem the most natural since the macroscopic measurements of the interfacial tension are always performed on objects of low curvature, i.e. planar, at the microscopic scale. What happens however if we were to curve that interface on a microscopic scale? We can curve the interface towards the water and

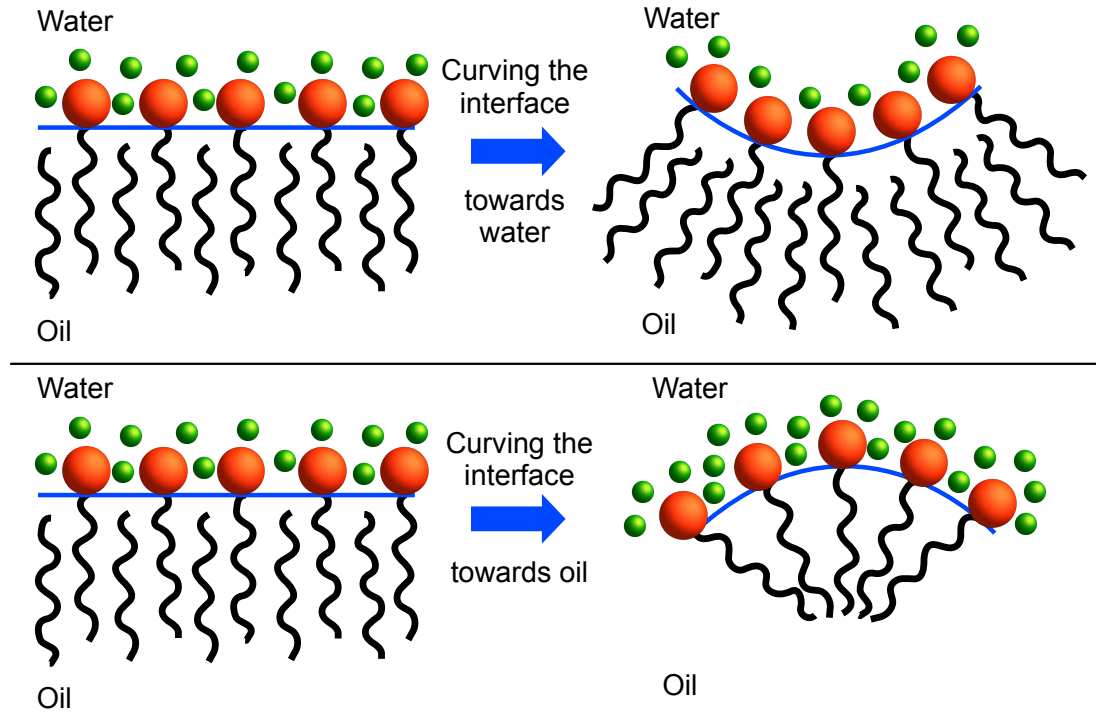


Figure 1.5: Curving the interface changes the balance of interactions between water, oil and surfactant.

understand from Figure 1.5 why the balance of interactions and conformations (energy and entropy) changes upon curving the interface. This is pictured as a decrease of the number of water molecules per hydrophilic head and an increase of the number of oil molecules per lipophilic chain. We can alternatively curve the interface towards the oil and the result will be opposite. There must thus exist a curvature that optimizes the interactions and conformations. This optimal curvature is termed the preferred curvature. However while this one dimensional representation is sufficient to grasp the main concepts, the interface is a two-dimensional surface and so are its deformations. We must thus quantify the free energy (energy + entropy) change associated with curving the interface.

The approach stems from the liquid crystals field with the earliest contribution by Oseen in 1933[27]. The theory was extended and refined by the work of Frank on the theory of liquid crystals in 1958[12]. He considers three types of deformations in respect to the vector normal to the surface, splay, twist and bend, which correspond to 6 coefficients. He postulates that the free energy can be described as a quadratic function of these 6 coefficients and associate constants to each. The examination of the constraints of the system then allows him to reduce the number of unknown constants and coefficients. This approach was later applied successfully to the case of bilayers by Helfrich in 1973[14] (and in a simplified version by Canham in 1970[6]). The current second-order expansion, although a reformulation from the original paper, of the Helfrich equation writes as :

$$g_c(H,K) = \kappa(H - H_0)^2 + \bar{\kappa}K \quad (1.21)$$

where g_c is the surface curvature free energy density, H the mean curvature, K the gaussian curvature, H_0 the spontaneous curvature, κ and $\bar{\kappa}$ are curvature-elastic moduli (note that in some definitions the first moduli is defined as 2κ). This corresponds to the splay and twist (saddle splay) terms of the Frank analysis. If we name c_1 and c_2 the two principal curvatures of the surface at the point considered, the mean curvature is $H = (c_1 + c_2)/2$ and the Gaussian curvature is $K = c_1.c_2$. The Helfrich equation relates directly the mean curvature to the spontaneous curvature for a cylindrical deformation ($K=0$). In addition, the Gauss-Bonnet theorem states that the surface integral of the gaussian curvature is an invariant for a given topology, which is then particularly useful in problems of known topology.

However relating the coefficients κ and $\bar{\kappa}$ to derivatives of the curvature free energy, i.e. physically related quantities, is difficult though achievable[30]. More importantly the reference surface in the colloidal domain is the sphere since it minimizes the area for a given volume. It is thus more natural to consider an expansion associated with a spherical deformation ($\Delta c = c_1 - c_2 = 0$). Indeed the optimal curvature that minimizes the curvature free energy of a sphere is not $H = H_0$ but $H = \frac{\kappa}{\kappa + \bar{\kappa}}H_0$, according to the Helfrich equation. This quantity is the preferred curvature, c_0 , and it is thus natural to expand the free energy around a point ($H = c_0, \Delta c = 0$) using the symmetry adapted coordinates H and Δc as suggested by Wennerström and Anderson in their work on vesicle stability [38]. A second order expansion can be written for this function of two variables as :

$$g_c(H, \Delta c) \approx g_c(c_0, 0) + (H - c_0) \frac{\partial g_c}{\partial H}(c_0, 0) + \Delta c \frac{\partial g_c}{\partial \Delta c}(c_0, 0) + \Delta c (H - c_0) \frac{\partial^2 g_c}{\partial H \partial \Delta c}(c_0, 0) \\ + \frac{1}{2} (H - c_0)^2 \frac{\partial^2 g_c}{\partial H^2}(c_0, 0) + \frac{1}{2} \Delta c^2 \frac{\partial^2 g_c}{\partial \Delta c^2}(c_0, 0)$$

The preferred curvature c_0 is defined so that $\frac{\partial g_c}{\partial H}(c_0, 0) = 0$. By symmetry the terms in Δc must be zero. This yields a more compact form of the free energy expansion :

$$g_c(H, \Delta c) = a(H - c_0)^2 + b\Delta c^2 + d \quad (1.22)$$

where $a = \frac{1}{2} \frac{\partial^2 g_c}{\partial H^2}(c_0, 0)$, $b = \frac{1}{2} \frac{\partial^2 g_c}{\partial \Delta c^2}(c_0, 0)$ and d a constant term.

The two expressions can be made equivalent by choosing $a + b = 2\kappa$, $b = -\bar{\kappa}$, $H_0 = c_0 a / (a + b)$ and by setting the constant term to $-c_0^2 ab / (a + b)$. As planned, this expression is intrinsically associated to a spherical geometry for which $\Delta c = 0$ and the minimum is then obtained for $H = c_0$. We obtain consistently that $c_0 = \frac{\kappa}{\kappa + \bar{\kappa}} H_0$. The Anderson-Wennerström expansion, through clear and simple arguments, treats the free energy as a two variable function and operates simplifications by a judicious choice of coordinates and expansion point. This contrasts with the Helfrich formulation and contrarily to H_0 , c_0 is also directly measurable in the case of spherical objects at equilibrium, to which we will now turn, through the measurement of their radius.

1.5 Macroemulsions vs. microemulsions

Despite these equilibrium considerations we know how to produce oil droplets in water. This emulsion corresponds to an increase of interfacial area and the cost is typically paid by a part of the mechanical energy (shaking, stirring). We have seen above that this energy cost could be decreased through addition of surfactants but not cancelled. Indeed, macroscopic droplets have low curvatures, close to that of planes, and the surfactant layer is thus not at its preferred curvature. The equilibrium state of the system will thus still consist in a phase separation of oil and water, with amphiphilic molecules at the interface. We are stating that emulsions, dispersions of liquid droplets in another liquid, are intrinsically *unstable* systems.

One feature of the interfacial tension curves displayed in Figure 1.4, that we have not explained, is the surfactant concentration value at which the interfacial tension reaches its residual value. It could be tempting to identify this critical concentration to the full coverage of the interface by a dense monolayer. However, if we double the interfacial area for a given volume (for example change the shape of the measuring vessel) the critical concentration should also be doubled, since we need twice more surfactant to cover the interface. Experimentally the interfacial tension actually depends on the type of interface and the structure of the surfactant. Indeed, covering the planar interface requires anyway a ridiculous amount of surfactant. For example a 1 m^2 surface is fully covered by $2 \cdot 10^{18}$ surfactant molecules (taking an area per surfactant molecule of $50 \cdot 10^{-20} \text{ m}^2$). If we consider that it separates a layer of 10 cm of water from a layer of 10 cm of oil, this corresponds to a concentration in water of $2 \cdot 10^{16}$ molecules/liter, i.e. $3.3 \cdot 10^{-8} \text{ mol.L}^{-1}$. This is several orders of magnitude lower than the observed critical concentrations.

Let's have a closer look at the choices available to amphiphilic molecules. Starting from a "pristine" oil/water interface, the most favorable choice for one molecule is to adsorb at this interface. This states again that the primary contribution to the free energy is the formation of a dense surfactant layer with a given area per molecule. As more molecules are added, the monolayer gets denser and it progressively becomes less and less favorable for a surfactant molecule to reach the interface, since the oil/water contacts are decreasing. Due to the mixing entropy, the surfactant molecules also have a solubility in water (for a hydrophilic surfactant) and as the interface gets close to dense packing more and more surfactant thus flee into water. However the hydrophobic tail is poorly water soluble and this hydrophobic interaction hinders the solubilization. The surfactant molecules are then facing two poor choices : packing at a nearly saturated interface or solubilizing despite unfavorable interactions. The molecular solubility of the surfactant in water must be small, due to the hydrophobic interaction similarly to an oil. Phase separation of a surfactant phase should then occur for relatively low concentrations in water. This third surfactant phase could first be pictured at the oil water interface and we

could picture a multilayer structure. However the surfactant layers would then be at zero curvature, although the preferred curvature is a priori non-zero. Optimally the surfactant phase should rather correspond to interface at the preferred curvature. This particular type of phase separation, constrained at the mesoscopic scale, is a self-assembly process. The surfactant objects are called micelles (latin : micae "grain") and their curvature is the preferred curvature c_0 , determined by the interactions and conformations. Adding more surfactant will result in the formation of more micelles, which does not change the total free energy. If we introduce the chemical potential of the surfactant, which is the partial derivative of the thermodynamic potential in respect to the amount of this specie, we can state that the formation of micelles sets a constant chemical potential condition (there is in fact a small variation that is not observable). This sets conditions on the physical quantities and this is the reason for the interfacial tension to reach its constant value at the critical micellar concentration (CMC). The value of the CMC corresponds then to the molecular solubility of the surfactant and is determined by the competition between energy (gain of interaction through self-assembly) and entropy (loss of conformational degrees of freedom through self-assembly).

The mean curvature of a micelle is set at c_0 to minimize the curvature free energy but this tells us nothing about its shape. The spherical shape minimizes the area of contact for a given volume and this would seem the most favorable geometry. However, if the preferred curvature is low enough, the micelles can not adopt a spherical geometry since the molecules have a finite length that would be smaller than the radius of the sphere corresponding to this preferred curvature. A change of geometry is then the only option and cylindrical micelles are then obtained. They can reach very large length and are then termed giant micelles. Another option is to feed the micelles with hydrophobic material that will fill up the inside of the sphere. For example adding an oil layer to an aqueous solution of micelles will result in a solubilization of the oil. Indeed, the micelles will swell with oil to adjust their curvature to the preferred curvature while retaining their spherical optimal shape. For a given amount of oil, there is a given preferred curvature value that is small enough to solubilize all the oil in swollen micelles. Such a system is intrinsically *stable*, since there are no oil/water contacts nor any curvature cost, and is named a microemulsion.

The solubilization curve corresponds to the equation $R_{geo}c_0 = 1$, where R_{geo} is the geometric radius associated with oil droplets of the same radius covered by all the surfactant. We can introduce the surfactant length l_s , which is the ratio of its volume by its area per head and, using the relation between volume and area for a sphere, we obtain :

$$R_{geo,sphere} = 3 \frac{\text{Volume}}{\text{Area}} = 3l_s \frac{v_{oil} + \alpha v_{surfactant}}{v_{surfactant}} \quad (1.23)$$

where v_{oil} is the volume fraction of oil, $v_{surfactant}$ the volume fraction of surfactant and $\alpha v_{surfactant}$ the volume fraction of the surfactant hydrophobic tail. $R_{geo}c_0 > 1$ corresponds

to swollen micelles in equilibrium with excess oil, i.e. the domain below the solubilization boundary (termed emulsification failure boundary by Safran). This allows to draw a phase diagram plotting the preferred curvature as a function of the oil/surfactant ratio, as displayed in Figure 1.6.

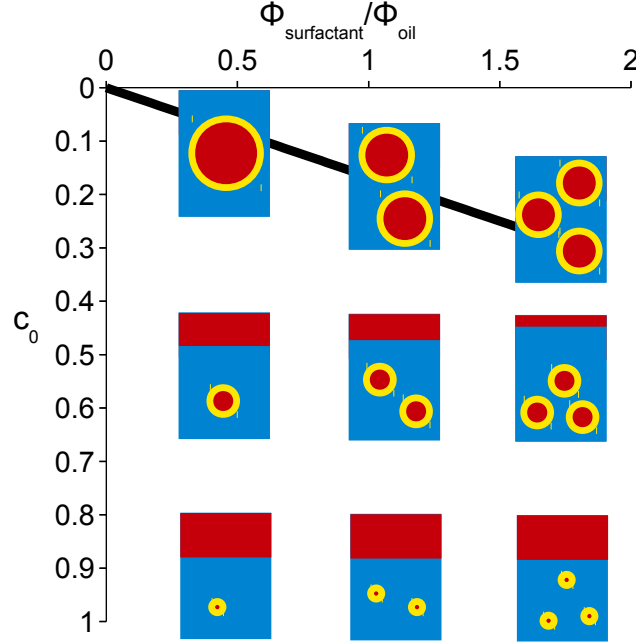


Figure 1.6: Calculated Phase diagram considering only spherical micelles swelling with oil ($l_s = 2$ nm). The solubilization boundary corresponds to the equation $R_{geo}c_0 = 1$.

1.6 Many self-assembly structures at low preferred curvatures

We may now wonder what occurs upon further decreasing the preferred curvature so that $R_{geo}c_0 < 1$. By definition the curvature free energy of a spherical structure must increase, which means such a structure is less and less favored. It is then possible to break the spherical symmetry and look for other structures. If we make Δc , the difference between the two principal curvatures, departs from 0, we have a cylindrical deformation and if we take the length of the cylinder much longer than its radius :

$$R_{geo,cylinder} = 2 \frac{\text{Volume}}{\text{Area}} = 2l_s \frac{v_{oil} + \alpha v_{surfactant}}{v_{surfactant}} \quad (1.24)$$

We can go further in deformation to reach a plane, Δc_{plane} then goes back to zero but the geometrical radius is now infinite, $R_{geo,plane} = \infty$.

We can calculate the curvature free energy density from Equation (1.22), for the spher-

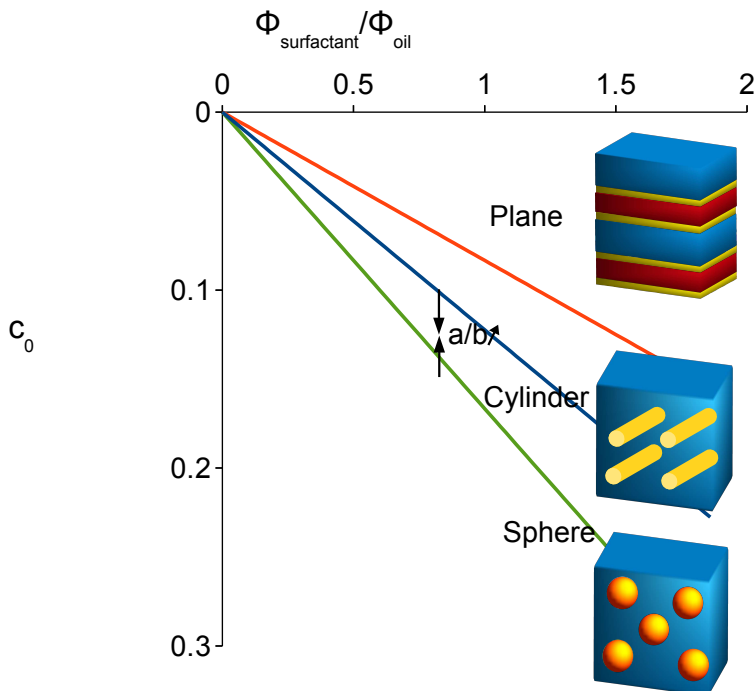


Figure 1.7: Calculated phase diagram according to the second-order expansion of the curvature free energy. The parameters are $a = 4$ and $b = 0.5$ defined in Equation (1.22).

ical, cylindrical and planar structures, for a given oil/surfactant ratio as a function of the preferred curvature. The calculation depends on the choice of a and b defined in Equation (1.22), which we can estimate from the literature or postulate. The additional boundaries are displayed in Figure 1.7 (i omitted the two-phases regions that must lay in between two one-phases regions). It is clear that the spherical structure is replaced by cylindrical and then planar structures when decreasing the preferred curvature above the solubilization boundary. At high a/b ratios, the cylindrical structure is unstable and the transition is then directly from spheres to plane. The analysis was done using more complex tools by Safran et al and yields the same conclusions[29].

Such a phase diagram is calculated from relatively simple approximations but is well followed at high surfactant/oil ratios. However it largely breaks down when lowering this ratio and a different type of structure is observed, as displayed in Figure 1.8. It consists of interconnected domains of oil separated by the surfactant layer from interconnected domains of water and is thus termed bicontinuous. This structure is encountered in a limited range of composition and curvatures and destabilized under dilution, which leads to a three-phase separation of that bicontinuous structure which contracts and expels oil and water. This constitutes the main complication of the phase behavior of oil/water/surfactant ternary system and has been the focus of many works between 1980 and 1995[26, 2, 40, 15, 39, 35, 21, 7]. This type of structures is in competition with other structures of similar curvature free energy and it was argued that additional terms should then be included in the free energy such as entropy, fluctuations and higher order terms.

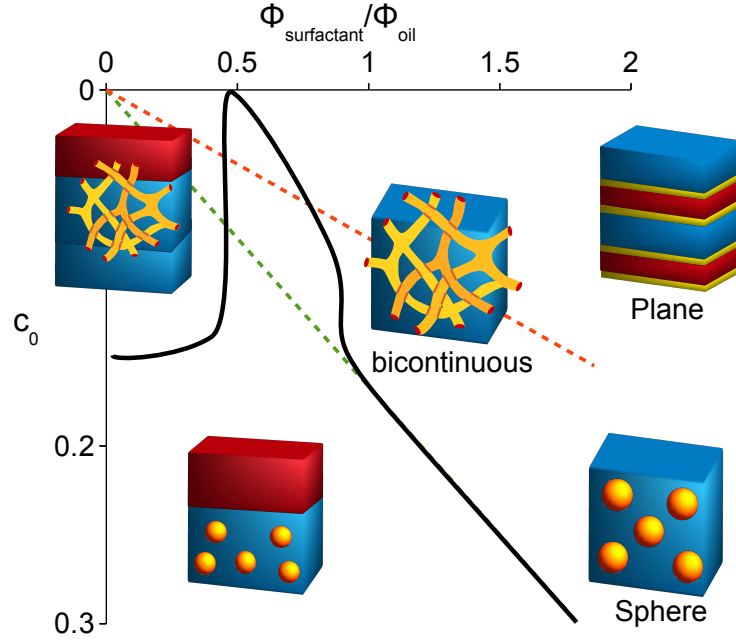


Figure 1.8: Qualitative correction of the previous phase diagram with the formation of bicontinuous networks.

The main research effort has focused both on the sponge phase, a bicontinuous swollen bilayer turned towards the solvent with $c_{0,bilayer} = 0$, and the balanced microemulsion, a bicontinuous network of equal volume in oil and water separated by a monolayer with $c_{0,monolayer} = 0$. Indeed for these two particular cases we can use a scaling invariance of the curvature free energy $G_c = \int_{\Sigma} g_c dA$. Indeed if one uses a length scale factor λ , the area scales as λ^2 , while each curvature scales as λ^{-1} . Only if $c_0 = 0$, the curvature free energy density scales as λ^{-2} and the free energy is scale-invariant. This leads then to an expression of the free energy[28] as a function of a simple invariant quantity :

$$G_c = \alpha(\kappa, \bar{\kappa}, T) \frac{A^3}{V^2} \quad (1.25)$$

This expression is monotonic in the area/volume ratio, A/V , and can not explain any phase transitions. The research was thus focused on extending this scaling law to a non-monotonic expression. Two major approaches were used and conflicted (and i will not enter the battlefield here), one that used a renormalization of the elastic constants and one based on inclusion of higher order terms. The latter is more consistent with the experimental knowledge of phase behavior but the two approaches are difficult to distinguish experimentally[16]. The "swedish" school has supported a scaling for the bicontinuous structure using a higher order expansion :

$$\frac{G_c}{V} = \alpha(\kappa, \bar{\kappa}, T) \left(\frac{A}{V} \right)^3 + \beta(\kappa, \bar{\kappa}, T) \left(\frac{A}{V} \right)^5 \quad (1.26)$$

Experimentally it is observed that at low A/V a phase separation with excess oil and water is observed, while at high A/V lamellar structures are formed. This expression can be made consistent with those observations if we take $\alpha(\kappa, \bar{\kappa}, T) < 0$, which destabilizes the structure going to lower concentrations, and $\beta(\kappa, \bar{\kappa}, T) > 0$, which destabilizes the structure going to higher concentrations. The curvature free energy of the bicontinuous structure is then represented as a bell shaped function of A/V . Attempts have been made to express α and β as explicit functions, with more success for the sponge phase than the balanced microemulsion. However the mesoscopic approach seems to reach its limits to go into more details.

1.7 From droplets to bicontinuous networks

At this stage we are drifting away from droplets and it's time to come back. If we consider the case of an aqueous solution of micelles swelling with oil, with more water than oil in the system, the complete solubilization could be achieved if the preferred curvature is decreased to a low enough value. However, the spherical microemulsions vanishes when this value needs to be too low (i.e. at large oil/surfactant ratios) and bicontinuous structures are formed instead. These highly asymmetrical (unbalanced) microemulsions have been even less investigated than their balanced counterparts, although a detailed attempt to provide some geometrical description was made by Anderson et al[1]. Understanding the transition from spherical droplets (eventually with excess oil) to bicontinuous networks (eventually with excess oil and/or water) remains a challenge and is a good final consideration for this section on equilibrium self-assembly.

As summarized by Olsson and Wennerström[26], the formation of bicontinuous structures arising in the ternary systems correlates with the phase separation of the binary system surfactant water[25, 13] into a surfactant-rich and a surfactant-poor phase. This observation lies on the study of phase diagrams that display clearly that the bicontinuous structures arise when this two phase region of the binary system touches the one-phase microemulsion region of the ternary system, leading to the three phase region. The formation of bicontinuous networks, and the binary phase separation, occur at low preferred curvatures, when the hydrophilicity is reduced. Structurally it is reasonable that bicontinuous structures can only be formed for low enough curvatures. However, as we saw from the comparison between spheres, cylinders and lamella, the spheres always win the contest at the solubilization line, in terms of curvature free energy. Since it is reasonable to suppose that the asymmetric bicontinuous network is an intermediate between cylinders, lamella and spheres (one argument is that at high surfactant/oil ratio a bicontinuous cubic phase is detected between an hexagonal cylindrical phase and a lamella phase), there does not thus seem to be a specific reason for bicontinuous structures to replace spheres at the solu-

bilization boundary $R_{geo.c_0} = 1$ (although by a similar argument it should indeed probably replace the spherical structure at $R_{geo.c_0} < 1$).

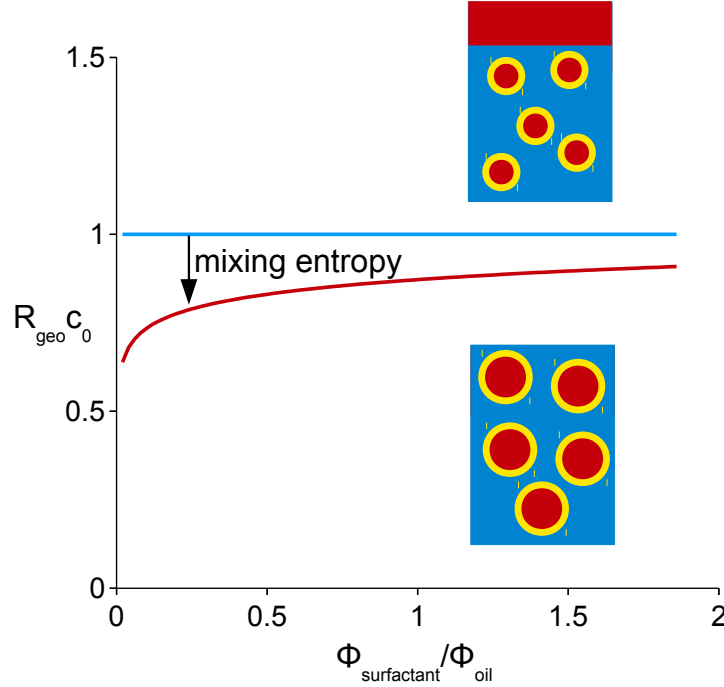


Figure 1.9: Mixing entropy correction to the free energy leads to a change of the solubilization boundary equation ($a = 4$ and $b = 0.5$).

Two explanations can be put forward. The first is that the cylinders are favored by an additional term to the free energy when they connect, i.e. form the bicontinuous network. This argument is derived by Tlustý, Safran and coworkers[36, 3] and is supported by calculations and cryo-TEM experiments. Still it must probably require the second explanation, which is that the spherical structure is destabilized at low surfactant/oil ratios, i.e. when $R_{geo,sphere}$ increases. One interesting argument raised by Olsson and Wennerström[26] is the need to consider the mixing entropy of the droplets in the fluid. This mixing entropy is of the same family as the one encountered when dealing with the problem of oil and water mixing. However, while molecules can be considered of similar sizes, this problem is more complicated since we are looking at the number of choices for big spheres (the oil swollen micelles) dispersed with small spheres (the water molecules). The most robust approach originates from the Carnahan-Starling equation but a work by Meroni et al[24] suggests that the mixing entropy does not deviate significantly from the ideal gas mixing entropy, i.e. as if the droplets and water molecules were of the same size. The ideal gas mixing entropy is simply the number of choices of distributing $N_{droplets}$ in $N_{droplets} + N_{water}$ boxes and we can write :

$$\Delta S_{mixing} = k_B \cdot \ln \frac{(N_{droplets} + N_{water})!}{N_{droplets}! N_{water}!} \quad (1.27)$$

Using Stirling approximation and introducing the mole fractions $X_{droplets}$ and X_{water}

$$\Delta S_{mixing} = -k_B(N_{droplets} + N_{water}).(X_{droplets} \ln X_{droplets} + X_{water} \ln X_{water}) \quad (1.28)$$

We deal with droplets much larger than the water molecules and not too concentrated we can thus simplify the mixing entropy as :

$$\frac{-T.\Delta S_{mixing}}{k_b T.V_{droplets}} \approx \frac{1}{v_{droplet}} \ln \frac{V_{droplets}.v_{water}}{V_{water}.v_{droplet}} \quad (1.29)$$

We can add this entropic contribution to the curvature free energy as a correction and the new equation of the solubilization boundary is thus (relatively) simply obtained :

$$R_{geo.c_0} = 1 + \frac{k_B T}{4\pi a} \left(\ln \frac{V_{droplets}.v_{water}}{V_{water}.v_{droplet}} + \frac{3}{2} \right) \quad (1.30)$$

Only $v_{droplet}$ varies and we can see that the correction is negative so that $R_{geo.c_0} < 1$ at the solubilization boundary. The entropy of mixing becomes more and more predominant as the droplets grow in size and thus hinder the solubilization of the oil through swelling. This contribution is thus a destabilizing factor for spheres to solubilize the oil. Indeed since $R_{geo.c_0} < 1$, the curvature free energy is not minimized (as it is minimal for $R_{geo.c_0} = 1$). The system may play on R_{geo} as a structural change or on c_0 as an interaction change. The structural change can consist in a ellipsoidal/cylindrical deformation. The change of interaction can be performed by bringing surfaces close to another, through attractions. These two levers are probably both used as suggested by the study on binary systems, and also the studies by Tlustý and Safran[36, 3] but a full description remains elusive so far.

Chapter 2

Non-equilibrium pathways and barriers

Contents

| | | |
|------------|---|-----------|
| 2.1 | Coalescence | 28 |
| 2.1.1 | Approach of charged droplets | 28 |
| 2.1.2 | Hole opening between droplets | 32 |
| 2.1.3 | Hole growth between droplets | 34 |
| 2.1.4 | Relaxation | 36 |
| 2.2 | Ostwald Ripening | 37 |
| 2.2.1 | Laplace pressure | 37 |
| 2.2.2 | Pathway : solubilization | 39 |
| 2.2.3 | Flux | 40 |
| 2.2.4 | Inhibiting Ostwald Ripening | 44 |

After a presentation of the most favorable states of a ternary oil/water/surfactant system, i.e. the equilibrium states, it is important to realize that most of them consist in a macroscopic phase separation of oil and water. Indeed, the system state is a single phase of a given self-assembly structure only in a limited range of concentrations and preferred curvatures. It is however possible to form a non-equilibrium state such as droplets of oil in water, covered by surfactant and with excess micelles, through for example stirring. This system is an emulsion and it is unstable, i.e. it reaches quickly its equilibrium state. The important question at this stage is how does it evolve? Directly related is the question, how to hinder the relaxation and trap the system in a metastable state, which is an unstable state prevented by barriers to reach the equilibrium state?

For emulsions the drive towards equilibrium will always be the reduction of interfacial area for a given volume. Two well-established pathways are known for relaxation, coalescence and Ostwald ripening.

2.1 Coalescence

If we consider two droplets, a straightforward way for the system to reduce its area for a given volume is through merging of the two droplets to form a new one. This new process is termed coalescence. Coalescence simply takes place when two droplets encounter, which results in an extremely fast destabilization (as fast as the collision rate of two droplets) : the emulsion quickly relaxes to equilibrium. However there are ways to drastically reduce the coalescence process such as the adsorption of amphiphilic molecules. We have discussed in detail how these molecules lower the cost of creating new interfaces and we can thus understand why it cost less energy to produce the emulsion. However we have no tools so far to explain the difference in lifetime for the emulsion with and without surfactant.

Let's consider the details of the coalescence process, which can be summarized in four steps :

1. Approach : The droplets get closer to each other. This step is determined by inter-droplet interactions
2. Hole opening : An oil bridge is established between the two drops.
3. Hole growth : The bridge grows and eventually the droplets completely merge.
4. Shape relaxation : the new non-spherical droplet changes shape to minimize its interface.

Each of these step can limit the coalescence process and to identify the limiting one we must study their characteristics.

2.1.1 Approach of charged droplets

The earliest use of amphiphilic molecules has been that of long chain carboxylates (soaps) synthesized through the basic hydrolysis (saponification with carbonates) of triglycerides (fats). These amphiphiles are negatively charged and it is a remarkable fact that most surfaces are negatively charged in natural systems. It could be thought that an electrostatic repulsion occurs between two negatively charged droplets, similarly to the repulsion between two charged surfaces in vacuum. However while a repulsion indeed occurs in most cases, it exists for altogether different reasons. This is a perfect example that in complex systems most so-called energies (potentials) are actually free energies (thermodynamic potentials) at a shorter length-scale than the one studied. These effective potentials thus comprise an energetic term and an entropic term. This "coupling" is important to keep in mind when discussing qualitatively the thermodynamic quantities of a colloidal system.

For example, if we consider the interaction of charges in vacuum, we can write a true interaction energy given by Coulomb expression. However when these charges are in a

solvent, called a dielectric medium, the interactions between the charges and the solvent molecules must be considered. This problem is highly difficult to treat and the common mean-field approach is to include the charges-solvent interactions, energy and entropy, in the dielectric constant. A new Coulomb expression is obtained, which is the same as in vacuum except for a factor (the dielectric constant). Although this looks innocent, there are deep consequences since the "energy" then has, for example, a temperature dependence. The Coulomb potential between two charges in a dielectric medium is actually an effective potential, it derives from a free energy rather than a simple energy.

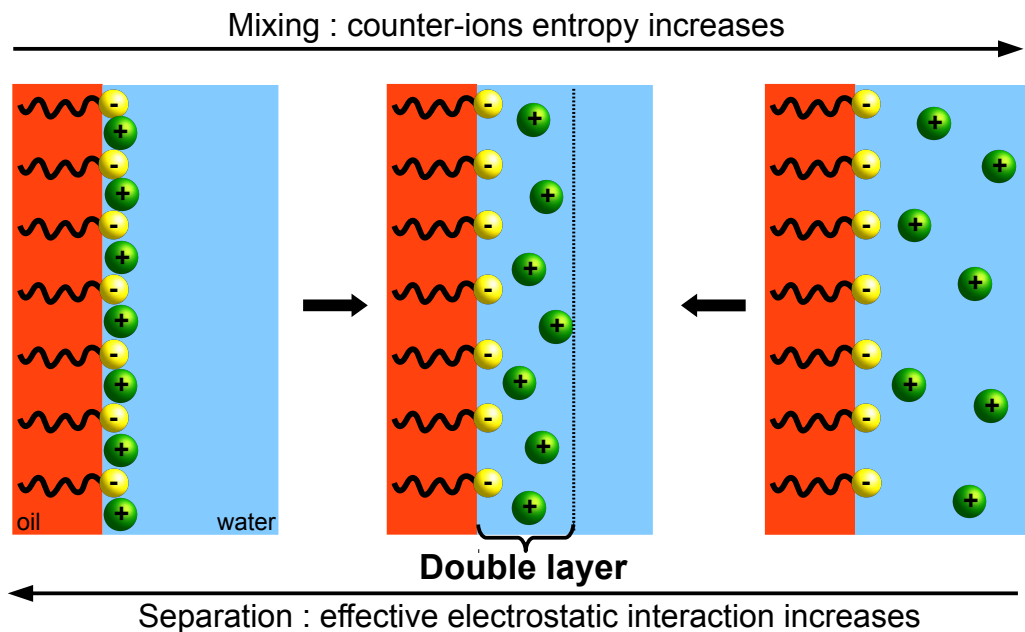


Figure 2.1: A charged surface is globally neutralized by the counter-ions. While the electrostatic interactions lead to a ion/counter-ion layer, the mixing entropy favors a distribution of the counter-ions over the whole volume. Since the electrostatic interaction decreases with length, the compromise is the so-called double layer. This can also be viewed as a special type of constrained phase separation.

Let's now consider the surface of a droplet, that we can assume as locally planar, if the droplet dimensions are much larger than the molecules. At the surface of the droplets are adsorbed anionic amphiphiles, which results in a negative surface charge. The anions are compensated by an equal number of cations due to electroneutrality, assuming a monovalent salt. The "electrostatic" (free) energy leads to the binding of the counter cations on the surface anions, consistently with our discussion on mixing vs. phase separation where was stated that the energy leads to phase separation. As in the mixing problem, the interaction competes with the mixing entropy that would lead to a complete mixing of the counter-ions in the volume. The important difference with the liquid/liquid mixing problem is the distance dependence of the interaction potential. The effective Coulomb interaction is weakened as the distance between the charges increase. The equilibrium state of the system can be viewed as a length-limited mixing (or equivalently phase separation) with a layer of counter-ions of an extension given by the energy/entropy competition.

It is named the double-layer and a schemed version is displayed in Figure 2.1. The most common description of the double-layer is achieved through the combination of the Poisson equation, which relates the effective electrostatic potential to the density of charges, with the Boltzmann equation, which embodies the competition between effective energy and mixing entropy. Combining the two equations lead to the Poisson-Boltzmann equation, using the major assumption that the position of the ions can be averaged so that the potential in the Poisson-Boltzmann equation is a mean potential, which means a new effective potential. It notably includes the entropy of the counter ions. Replacing the true ion distribution by the distribution in the mean potential is a mean-field approximation that can potentially break.

The addition of an electrolyte, which dissociates in anions and cations, leads to an increase of the ion concentration in the bulk, as schemed in Figure 2.2. The concentration difference in ions between the bulk and the double layer thus decreases. This results in a decrease of the entropy variation with the double-layer length and the double-layer reaches a new equilibrium state by contracting and thus increase the interactions.

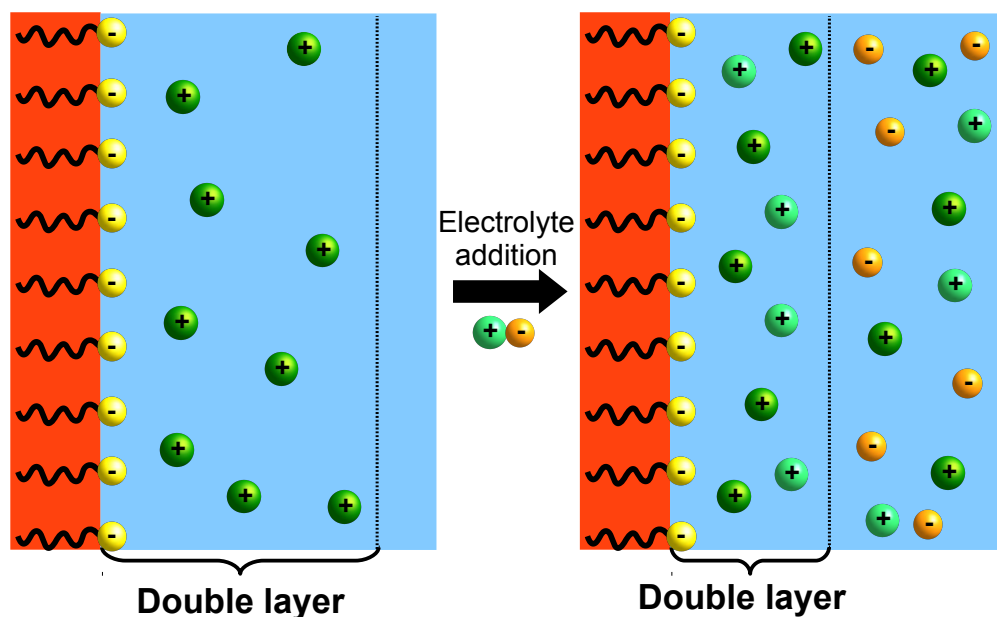


Figure 2.2: The addition of an electrolyte leads to the collapse of the ionic double-layer.

The approach of two droplets with a anionic surface charge is thus the approach of two ionic double-layers. What occurs when the two layers start to overlap? An elegant way of approaching the problem is to consider that each layer is compressed by the approach of a neutral layer. The sum of these two sub-problems then describes the full problem if the superposition approach holds. The equations are fully derived by Evans and Wennerström[9] and the approximation holds when the two layers are uncorrelated, as displayed in Figure 2.3. Approaching a neutral plane to compress the double layer force a change in the double layer length, which resulted from the competition between interaction energy and mixing

entropy. Energetically decreasing the length is favorable but entropically it is unfavorable, while the free energy balance must be unfavorable since we push the system out of its equilibrium state. The entropy of the double layer is an entropy of mixing in a limited volume and not all configurations are equiprobable, they depend on the distance. It is then composed of the ideal mixing entropy plus a modification due to the charged surface. We can intuitively understand, but also demonstrate exactly as shown by Evans and Wennerström[9], that the entropy modification due to the charged surface is balanced by the gain in energy. The total free energy cost of approaching a neutral plane is thus only the reduce in ideal mixing entropy, evaluated at the neutral plane since there all the charges are screened. By superposition the same conclusion apply for the two charges double-layer overlap. We make the important conclusion that the repulsion of two charged colloids is due to the decrease in mixing entropy of the counter ions when their double layers overlap. The effective repulsive potential is entropic. This is also termed in the literature as an osmotic pressure in some contexts or an entropic force in some others.

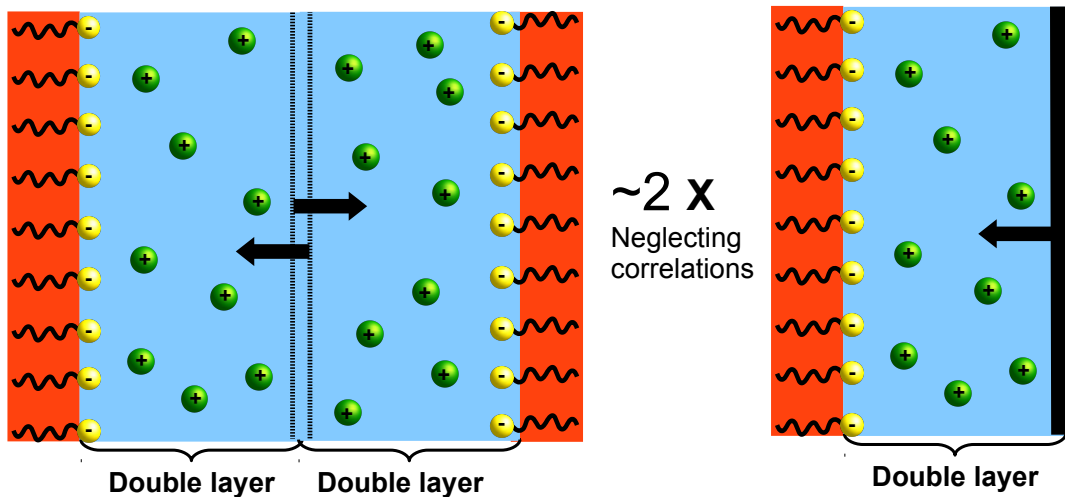


Figure 2.3:

This mechanism can break down in situations when the superposition approximation, and thus the mean-field approach, are not valid anymore. This occurs when the correlations between ions, neglected when dealing with mean quantities, have a large magnitude. This is typically the case in situations of high surface charge, multivalent ions, low dielectric constants. Correlations have two effects, first they induce an attractive term between the double-layers and second they reduce the entropy evaluated in the Poisson-Boltzmann theory due to the interactions. Cement paste are an important illustrations of this effect but an effect exists in the emulsion field, for example when concentrating an emulsion. The work of Sonnevile-Aubrun et al[32, 31] shows that if the droplets are forced to contact (for example through centrifugation), the double layers first compress to the Common Black Film and then jump to the Newton Black Film at higher centrifugation rates. This jump

is possible due to the correlations. It is remarkable that in the Newton black film then corresponds to a much lower area per ionic head and a higher order of the surfactant layer. In such cases the concentrated emulsions are reported to resist coalescence, although the oil domains come to contact. It is then important to remember that coalescence is not synonym of bringing the droplets close to each other (as they would through creaming or flocculation). This is equivalent to stating that the first step of a coalescence process, the approach to contact of droplets, is not necessarily the limiting step.

2.1.2 Hole opening between droplets

The droplets are now in contact and the next necessary step is the opening of a bridge between them. The smallest bridge is the molecular interaction between an oil molecule of the first droplet with another oil molecule of the second droplet. The hole opening free energy, ΔF_{hole} , is composed of two terms.

First is the cost of leaving a surface bare of surfactant on each droplet[10, 9]. The denser the surfactant monolayer, the higher this cost. This can be quantified using the interfacial tensions of the bare surface, γ_{bare} , and the covered surface, $\gamma_{covered}(c_{surfactant})$, the latter one depending on the surfactant concentration, $c_{surfactant}$, up to the Critical Micellar Concentration where it reaches its residual value γ_0 :

$$\Delta F_{hole} = F_{bare} - F_{covered} = (\gamma_{bare} - \gamma_{covered}).2S_{hole} \quad (2.1)$$

The cost is zero when no surfactant is present and reaches its maximal value when $\gamma_{covered} = \gamma_0$, for $c_{surfactant} > CMC$. However this equation assumes that the surfactant coverage (and thus the interfacial tension) is homogeneous. This is obviously the case for an isolated droplet but as two droplets approach the coverage may become heterogeneous. One example would be the approach of charged droplets, which may lead to a depletion of the charged surfactant from the droplet surface close to the other droplet approaching. This redistribution is hindered by dense monolayers.

Second is the cost of redistributing the surfactant that was covering the two bare surfaces. To evaluate this cost it is necessary to investigate where the surfactant is relocated. Three cases can be considered as displayed on Figure 2.4.

1. A relocation at the interface, which leads to a compression of the monolayer. If the surfactant concentration is below the Critical Micellar Concentration, the monolayer is not densely covered and the interfacial tension can be decreased by adding more surfactant. This can also be achieved by a compression of the monolayer, which is then favorable. The relocation is then a gain in free energy. To the contrary if the surfactant monolayer is already dense, the relocation at the interface is a cost.
2. A relocation in the continuous phase. As the Critical Micellar Concentration is

reached, the chemical potential of the surfactant sets to a (nearly) constant value and the surfactant rather self-assemble into micelles than compress the monolayer. This is the hypothesis chosen by Exerowa et al.

3. A relocation in the droplet phase. If the surfactant is more soluble in the droplet phase than in the continuous phase, it can solubilize at a lower cost.

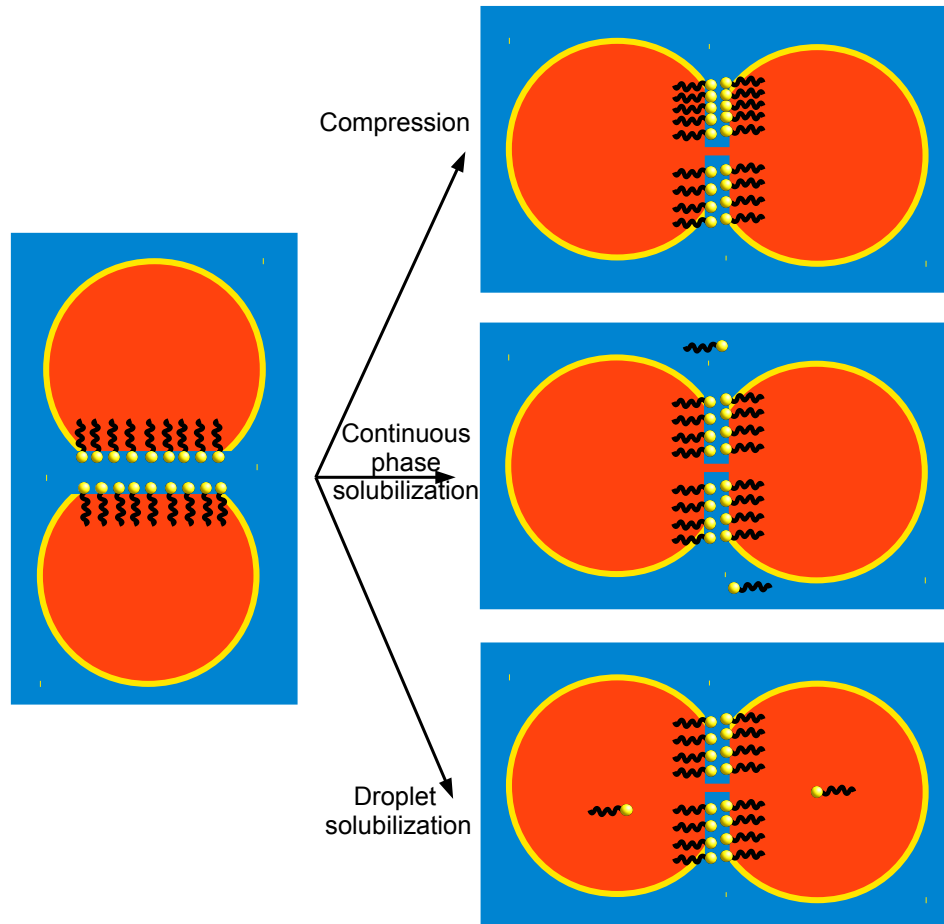


Figure 2.4: The opening of a hole between droplets covered by a surfactant layer requires a redistribution of the surfactant removed from the hole and three locations can be envisioned.

The first case clearly dominates for surfactant concentration below the CMC, where the coverage is sparse, since the relocation is actually favorable. The third case will dominate if the surfactant is highly soluble in the droplet phase and the monolayer dense. As to the second case, it is important to note that the surfactant can not desorb and self-assemble in the interfacial aqueous layer between two droplets. It must compress first the film and then desorption can take place outside of the contact area. This is not possible when all the interface is in contact with another interface such as concentrated emulsions. If additionally the surfactant is poorly soluble in the droplet, the only relocation available is the first case, i.e. compression. This can be especially difficult in the case of ultra-compact

layers such as in the Newton Black Film configuration observed by Sonneville et al, and probably explains the resistance to coalescence.

2.1.3 Hole growth between droplets

After seeing criteria for opening a hole we must investigate the growth of this hole until the droplets are truly merged. In the case of sparse surfactant coverage this does not seem problematic and this step is likely not limiting. If we now consider the case of a dense monolayer it is important to include additional observations. One key observation in the emulsion field is the empirical Bancroft's rule. It states that the type of emulsion (oil droplets in water or water droplets in oil) is determined by the solubility of the surfactant. A rather oil soluble surfactant would then lead to water droplets, while a rather water soluble surfactant would lead to oil droplets. A popular model to explain this observations has been the surfactant mass-flow model. This model is based on the argument that if the surfactant is more soluble in the droplet phase than in the aqueous phase, the hole can be quickly stabilized by a covering layer and then grow. It could be understood also from the relocation cost explained previously.

However, i will not go in deep details of these explanations since the Bancroft's rule is broken in some situations. This was recognized by Kabalnov and Wennerström [18]. They note that a valid empirical rule is that, above the CMC and for not too extreme volume fractions, the type of emulsion is determined by the sign of the surfactant layer spontaneous curvature. A priori this is a strange observation since macroscopic emulsions are composed of droplets with very low curvature, close to that of a plane, whether oil in water or water in oil. The curvature free energy cost should thus be similar between one type of emulsion and the other. Kabalnov and Wennerström have pointed out that the important region, the hole, is highly curved and that while the curvature cost was constant for the rest of the droplet, the curvature cost of opening a pore was deeply dependent on the spontaneous curvature. We can calculate the total cost of growth of the hole, following the presentation of Evans and Wennerström[9]. The variation of free energy from the two flat films in contact to the hole, schemed in Figure 2.5, can be written as the sum of four terms :

$$\Delta F_{growth} = \Delta F_1 + \Delta F_2 + \Delta F_3 + \Delta F_4 \quad (2.2)$$

ΔF_1 and ΔF_2 are related to changes in area. The flat part of the film decreases in area, which results in the following free energy change :

$$\Delta F_1 = -2.\gamma.\pi(r_{in} + r_{ext})^2 \quad (2.3)$$

To the contrary, a curved interface is created and assuming a revolving semi-circle geometry

we have the free energy change :

$$\Delta F_2 = -2\gamma\pi[\pi(r_{in} + r_{ext})^2 - 2r_{ext}^2] \quad (2.4)$$

ΔF_3 and ΔF_4 are related to the change in curvature free energy. Using the Helfrich formulation we can write :

$$\Delta F_3 = \kappa \int_{neck} ((H - H_0)^2 - H_0^2) dA \quad (2.5)$$

$$\Delta F_4 = \bar{\kappa} \int_{neck} K dA \quad (2.6)$$

Analytic expressions are obtained through nontrivial geometrical relations [18] and yield :

$$\Delta F_3 = 2\pi\kappa \left(2\pi H_0 r_{int} + \frac{2(r_{int} + r_{ext})^2}{r_{ext}[r_{int}(r_{int} + 2r_{ext})]^{1/2}} + 2(\pi - 4)r_{ext}H_0 - 4 \right) \quad (2.7)$$

$$\Delta F_4 = -4\pi\bar{\kappa} \quad (2.8)$$

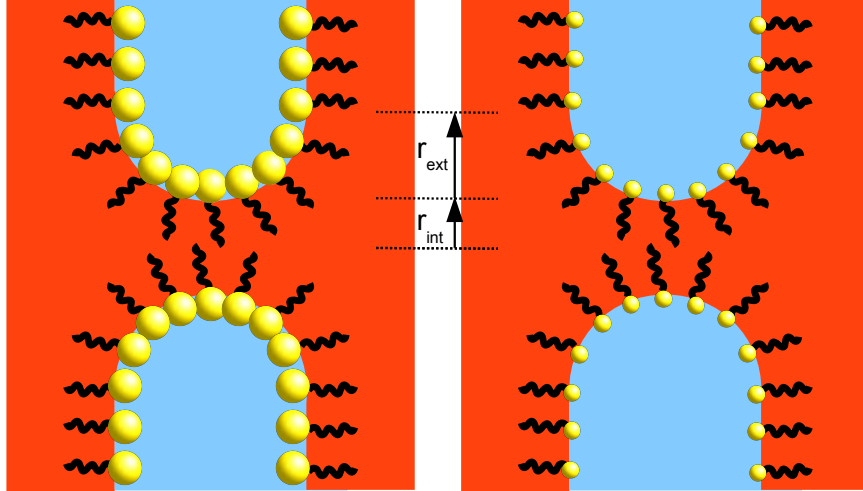


Figure 2.5: The hole growth is directly related to the preferred curvature. On the left the preferred curvature is towards the oil, which is the opposite of the hole curvature and is thus unfavorable. To the contrary on the right the preferred curvature is towards the water like the hole and there is no barrier to the growth.

The total free energy cost is obtained as a function of the variables r_{int} and r_{ext} and the parameter H_0 . Through an optimization procedure it is possible to find the lowest maximum of this function (similarly to the transition state theory) and plot this barrier height to growth of the hole as a function of the spontaneous curvature H_0 for a given set

of elastic constants [18].

This was performed by Kabalnov and Wennerström and validated quantitatively on a pure ternary system, n-octane/ $C_{12}E_5$ /water, by Kabalnov and Weers[17]. In this system the spontaneous curvature is controlled through the dehydration of the hydrophilic ethylene oxide head through temperature increase. Similar systems are used in half the experiments described in this thesis and will be described in more details later. Strey[33] showed that the dependence was linear on a large temperature interval and there we can transform the temperature scale to a curvature scale. Taking the raw data from Kabalnov and Strey, this adaptation leads to Figure 2.6. On the left side, the spontaneous curvature is towards the oil and the emulsion is oil in water. On the right side, the spontaneous curvature is towards the water and the emulsion is water in oil. Close to zero spontaneous curvature the emulsions are very unstable. This correlates to a collapse of the curvature free energy barrier to the growth of the hole.

The Kabalnov-Wennerström theory is the most complete theory (qualitatively and quantitatively) available to describe the growth of the hole. However, as we saw before, other steps of the coalescence process may be the limiting (and thus "important") ones in some conditions. Furthermore the theory has not been checked for mixtures of surfactants at the interface. In that case there might be a segregation effect with potentially large effects on the spontaneous curvature. Indeed the surfactant layer composition of the hole, and thus its spontaneous curvature, may be different from the composition on the rest of the droplet. This is an open question that has not been addressed to my knowledge and would require some serious investigation.

2.1.4 Relaxation

I will not dwell on the final shape relaxation of the two merged droplets. For surfactant-stabilized emulsions consisting of spherical droplets, this step is never problematic. This is obviously not true when the stabilizer is strongly adsorbed such as with particles-stabilized emulsions. This may also become relevant in concentrated emulsions and polymer particles dispersions (latex).

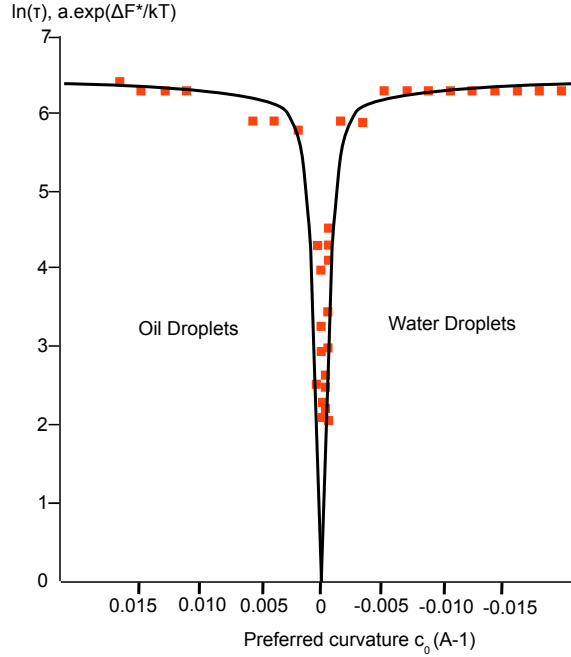


Figure 2.6: Taking the data from Kabalnov[17] (lifetime as a function of temperature) and Strey[33](preferred curvature as a function of temperature) we can recalculate the raw data and display the lifetime as a function of preferred curvature. The experimental dots are logarithm of the emulsion lifetime as a function of the preferred curvature. The black line is the result of a calculation using the Kabalnov Wennerström model. The prefactor a is adjusted to match the data at high preferred curvatures.

2.2 Ostwald Ripening

Even if droplets never encounter each other directly and are protected against every coalescence step, there exists one other relaxation mechanism to equilibrium. The drive is the same as for coalescence, the reduction of the interfacial area, but the pathway differs. Let's consider oil droplets dispersed in water and covered by a surfactant layer and assume no coalescence takes place. Due to the mixing entropy the oil has a finite solubility in water. This provides a pathway for oil exchange, the content of each droplet can dissolve in the continuous phase, driven by the reduction of the interfacial area. To describe quantitatively the process we need to write an expression for the drive and for the path.

2.2.1 Laplace pressure

The drive is the reduction the interfacial area, expressed as the free energy $F_{interfacial} = \gamma A$, where γ is the interfacial tension and A the interfacial area. Since Ostwald ripening is a molecular process it is convenient to look at the contribution of an oil molecule to this free energy. This can be achieved by taking the partial derivative to the free energy in respect to the number of oil molecules in the droplet, $\partial F_{interfacial}/\partial N_{oil}$, which is the interfacial contribution to the oil chemical potential. The interfacial tension is determined by the structure of the interface and thus does not depend on the number of oil molecules in the

droplet. The chemical potential thus writes as $\gamma \cdot \partial A / \partial N_{oil}$. If we define the molecular volume of oil, v_{oil} , the total volume is $N_{oil} v_{oil}$ and is also $(4\pi/3) \cdot (R)^3 = (4\pi/3) \cdot (A/4\pi)^{3/2}$. The radius R is $(3/4\pi)^{1/3} \cdot v_{oil}^{1/3} \cdot N_{oil}^{1/3}$. Through simple derivation we obtain :

$$\frac{\partial F_{interfacial}}{\partial N_{oil}} = 2\gamma \cdot \frac{4\pi}{3} N_{oil}^{-\frac{1}{3}} \cdot v_{oil}^{\frac{2}{3}} = 2 \frac{\gamma}{R} \cdot v_{oil} \quad (2.9)$$

We recognize the product of a pressure by a volume and we can define this pressure as the Laplace pressure :

$$p_{Laplace} = \frac{2\gamma}{R} \quad (2.10)$$

This logical sequence differs largely from what is found in most textbooks, where strange assumptions are made to introduce magically the Laplace pressure and calculate it (typically the "at equilibrium but not really" method is largely obscure to my opinion). The methods also fail when considering a radius dependence of the interfacial tension $\gamma(R)$. The method presented above is straightforward and conceptually simple. It also demonstrates that it is possible to completely bypass the notion of Laplace pressure in the thermodynamic approach. The advantage of the Laplace pressure is that it relates to a macroscopic quantity we intuitively grasp. For example, we readily understand that a small droplet will be swallowed by a large droplets since its Laplace pressure is higher. Predicting evolution from pressure gradients clearly originates from mechanic, often thought more accessible than thermodynamic. The Laplace pressure goes to zero for an infinite radius, which corresponds to equilibrium and the maximal reduction of interface.

Since we made no assumption on γ , except that it does not depend on N_{oil} , which is always verified, it is possible to incorporate the radius dependence in the interfacial tension. This dependence appears when the interface is saturated by a monolayer of surfactant and the droplet curvature is high. We have described previously that the residual interfacial tension was linked to the difference between the curvature of the monolayer and its preferred curvature. For large droplets this contribution is nearly constant and equal that of a plane. For smaller droplets the interfacial tension, which is then the curvature free energy density, depends on the radius through :

$$\gamma_0(R) = g_c(R) = a \left(\frac{1}{R} - c_0 \right)^2 - c_0^2 \frac{ab}{a+b} \quad (2.11)$$

This leads to the Laplace pressure :

$$p_{Laplace} = \frac{2}{R} \left[a \left(\frac{1}{R} - c_0 \right)^2 - c_0^2 \frac{ab}{a+b} \right] \quad (2.12)$$

The variations of this corrected Laplace pressure as a function of the droplet radius are displayed in Figure 2.7. As for the simpler expression this pressure asymptotically goes to zero as the radius goes to infinity, however it has a (global) minimum for $R \cdot c_0 = 1$.

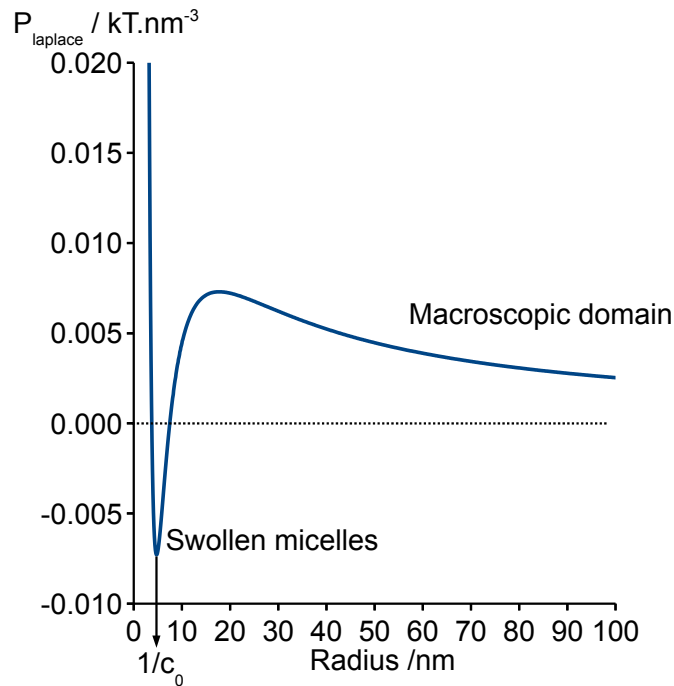


Figure 2.7: Variations of the Laplace pressure with the Radius taking into account the curvature free energy correction. A global minimum is obtained for the preferred curvature and swollen micelles are formed. Alternatively the pressure goes to zero for a macroscopic domain.

There the Laplace pressure is slightly negative! It is important to remember that what it really means is that the interfacial contribution to the chemical potential is negative, which is not a problem. When discussing the equilibrium self-assembly processes, we have seen that $R.c_0 = 1$ corresponds to the equilibrium swelling of micelles. Swollen micelles are equilibrium objects with no interfacial free energy cost since oil/water contacts are prevented by the surfactant layer, which is at the preferred curvature and thus the curvature free energy is minimal. This is the meaning of "negative" Laplace pressures. However swollen micelles at the constrained preferred curvature can geometrically solubilize only a given amount of oil. Excess oil can not be solubilized into such objects and the systems then chooses the second best option, which are infinitely large domains where the Laplace pressure goes to zero. This is a slightly alternative description in terms of Laplace pressure of the self-assembly process described in the previous chapter.

2.2.2 Pathway : solubilization

As we demonstrated above the oil molecules in a droplet have an excess chemical potential due to the interface, expressed as $p_{laplace}v_{oil}$. If we include the energy reference and the ideal mixing entropy we can write the full chemical potential for oil molecules inside the

droplets and outside the droplets :

$$\mu_{oil}^{inside} = \mu_{oil}^{o,inside} + kT \ln(c_{oil}^{inside}/c^o) + p_{laplace}v_{oil} \quad (2.13)$$

$$\mu_{oil}^{outside} = \mu_{oil}^{o,outside} + kT \ln(c_{oil}^{outside}/c^o) \quad (2.14)$$

At local equilibrium, these two chemical potentials must be equal (there is no discontinuity for the chemical potential from one phase to the other) and this writes as $\mu_{inside}^{oil} = \mu_{outside}^{oil}$, which leads to :

$$\frac{c_{oil}^{outside}}{c_{oil}^{inside}} = \exp(-[\mu_{oil}^{o,outside} - \mu_{inside}^{o,oil}]/kT) \cdot \exp(p_{laplace}v_{oil}/kT) \quad (2.15)$$

We can introduce the oil solubility in the continuous phase, s_{oil} , which is the outside concentration for a plane (i.e. $p_{laplace} = 0$) :

$$\frac{s_{oil}}{c_{oil,plane}^{inside}} = \exp(-[\mu_{oil}^{o,outside} - \mu_{inside}^{o,oil}]/kT) \quad (2.16)$$

This leads to :

$$c_{oil}^{outside} = s_{oil} \cdot \exp\left(\frac{2\gamma v_{oil}/kT}{R}\right) = s_{oil} \cdot \exp\left(\frac{\alpha}{R}\right) \quad (2.17)$$

This expression is known as the Kelvin equation. It means that the oil solubility at the surface of the droplet is higher than the equilibrium solubility, due to the interfacial energy of the droplet. This oil supersaturation in water is a signature of a relaxation process towards equilibrium, since it will decrease to zero to reach the equilibrium state : a gradient of concentration is produced, which must lead to an evolution.

2.2.3 Flux

The last step is to calculate the rate of evolution of a droplet at a given size in the presence of a collection of other droplets. We can first calculate the flux density from one droplet. This can be done through the Fick's first law:

$$\vec{J}_{oil} = -\frac{D_{oil}}{kT} \cdot c_{oil} \cdot \overrightarrow{grad}(\mu_{oil}) \quad (2.18)$$

The driving force is the gradient of chemical potential and the pathway is linked to diffusion, hence the diffusion coefficient, D_{oil} and concentration c_{oil} . When the chemical potential contains only the ideal mixing entropy, $kT \ln(c_{oil}/c^o)$, this expression immediately simplifies to :

$$\vec{J}_{oil} = -D_{oil} \cdot \overrightarrow{grad}(c_{oil}) \quad (2.19)$$

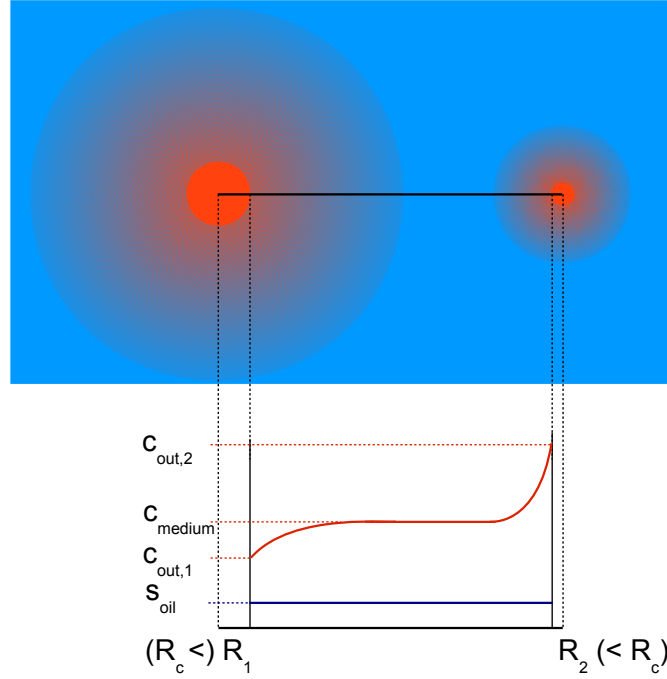


Figure 2.8: Ostwald ripening is a non-equilibrium phenomenon and as a result the oil concentration in water, c^{medium} , is higher than the equilibrium solubility, s_{oil} . Around each droplet there is a concentration gradient directly determined by the size of the droplets. Droplets larger than the mean size correspond to a smaller supersaturation than droplets smaller than the mean size.

Using the equation of continuity in steady-state conditions (i.e. time independent) leads immediately to Fick's second law :

$$\Delta c_{oil} = 0 \quad (2.20)$$

where Δ is the Laplace operator. This equation is easily solved in a spherical geometry with the two limit conditions schemed in Figure 2.8 :

$$c_{oil}(r = R) = c_{oil}^{outside} \quad (2.21)$$

$$\lim_{r \rightarrow \infty} c(r) = c_{oil}^{medium} \quad (2.22)$$

We obtain the expression of the radial flux density :

$$J_{oil}(r) = D_{oil} \cdot \frac{R(c_{oil}^{outside} - c_{oil}^{medium})}{r^2} \quad (2.23)$$

We then obtain the flux :

$$\Psi_{oil} = 4\pi r^2 \cdot J_{oil}(r) = 4\pi D_{oil} R(c_{oil}^{outside} - c_{oil}^{medium}) \quad (2.24)$$

We can notice that the flux does not depend on the radius where it is evaluated. This flux expression is often obtained in articles from a calculation in planar geometry with a diffusion length taken as the particle radius. While it leads to the same result due to this arbitrary

choice, it is necessary to consider the spherical problem for a proper demonstration.

Through the Kelvin equation we can define a critical radius, R_c as :

$$c_{oil}^{medium} = s_{oil} \cdot \exp\left(\frac{\alpha}{R_c}\right) \quad (2.25)$$

We then obtain the expression of the flux of a droplet of radius $R(t)$:

$$\Psi_{oil} = -4\pi R(t) D_{oil} s_{oil} \left[\exp\left(\frac{\alpha}{R(t)}\right) - \exp\left(\frac{\alpha}{R_c}\right) \right] \quad (2.26)$$

All works on Ostwald ripening use a first order expansion of both exponentials. This can be justified by the value of α . We can estimate the volume of a hexadecane molecule as $4.9 \cdot 10^{-28} m^3$, the surface tension for a surfactant covered interface as $10^{-3} J.m^2$, which is fairly small, and taking the temperature at $25^\circ C$, we obtain $\alpha \simeq 0.24 nm$. This is always much smaller than the radius of the droplets considered. The smallest size we could consider in this problem would be an unswollen micelle, with a radius around 2 nm, the error of the expansion is then 7%. For a slightly swollen micelle of radius 5 nm the error falls down to 1%. The expansion leads to :

$$\Psi_{oil} = \frac{4\pi}{3} \frac{dR^3(t)}{dt} \approx 4\pi D_{oil} s_{oil} \alpha \left[\frac{R(t)}{R_c} - 1 \right] \quad (2.27)$$

With this simplified expression, we can identify the critical radius to the mean radius of the size distribution, at any instant t . Following the argument by Finsy [11], we can consider a normalized distribution of radius $\rho(R,t)$ (the time dependence originates from the time dependence of each radius $R(t)$). The total volume is constant with time and this yields :

$$\int_0^\infty \rho(R,t) \frac{dR^3(t)}{dt} dR = 0 \quad (2.28)$$

This integral can also be evaluated from the flux expression :

$$\int_0^\infty \rho(R,t) \frac{dR^3(t)}{dt} dR = \int_0^\infty \rho(R,t) \left[\frac{R(t)}{R_c} - 1 \right] dR \quad (2.29)$$

The mean radius is defined as :

$$R_{mean}(t) = \int_0^\infty \rho(R,t) R(t) dt \quad (2.30)$$

Since the distribution is normalized we obtain :

$$\frac{R_{mean}(t)}{R_c(t)} = 1 \quad (2.31)$$

This relation demonstrates that for any shape of the size distribution, the mean radius is

the critical radius, provided that the mean volume is constant. This condition holds in the absence of chemical reactions (and any other source/sink term).

We obtain the final expression for the Ostwald ripening flux of a droplet of radius $R(t)$:

$$\Psi_{oil} = \frac{4\pi}{3} \frac{dR(t)^3}{dt} \approx 4\pi D_{oil} s_{oil} \alpha \left[\frac{R(t)}{R_{mean}(t)} - 1 \right] \quad (2.32)$$

This expression allows to describe completely the Ostwald ripening process. At a given instant t , droplets with a radius smaller than the mean size will shrink ($R(t) < R_{mean}(t) \rightarrow \Psi_{oil} < 0$), while droplets with a radius larger than the mean size will grow ($R(t) > R_{mean}(t) \rightarrow \Psi_{oil} > 0$). This leads to a change in the size distribution $\rho(R,t)$ and thus to a change of the mean radius $R_{mean}(t)$. Unfortunately evaluating the growth rate of the mean radius is not straightforward since equation (2.32) has no analytic solutions.

An analytical approach of this problem was undertaken by Lifshitz and Slyozov in their 1961 paper [22], and simultaneously by Wagner (However I have not found the german paper). The LSW theory is the cornerstone of the description of Ostwald ripening and is the reference to which numerous works compare. The approach is to use scaled variables, such as $R(t)/R_{mean}(t)$, and examine constraints in the asymptotic regime. The main result is that a self-similar distribution of sizes is obtained, which propagates with time, and the mean radius of this distribution scales as $R_{mean}(t) \sim t^{\frac{1}{3}}$.

With the advent of computers, numerical solutions to the growth equation can also be easily obtained[8]. The main conclusion is that the asymptotic regime of LSW is not reached even at extremely long times, which has also been suggested experimentally. The growth law $R_{mean}(t) \sim t^{\frac{1}{3}}$ is however observed, except at the earliest times.

A third method is to recall that the problem is mean field and that the growth law can be obtained through mean field arguments. All droplets exchange with the continuous phase at the concentration in oil c_{medium} , which is also the concentration at the surface of droplets at the mean radius $R_{mean}(t)$. If we take one droplet at the mean radius and put it in a continuous phase in equilibrium with an infinite oil reservoir, the concentration in the continuous phase far from the droplet is by definition the solubility s_{oil} . The flux of dissolution of this droplet writes then as :

$$\Psi_{oil} = \frac{4\pi}{3} \frac{dR_{mean}(t)^3}{dt} = -4\pi D_{oil} R_{mean}(t) (c_{medium} - s_{oil}) \quad (2.33)$$

This can be rewritten in an approximate form, as done above :

$$\Psi_{oil} = \frac{4\pi}{3} \frac{dR_{mean}(t)^3}{dt} \approx -4\pi D_{oil} s_{oil} R_{mean}(t) \frac{\alpha}{R_{mean}(t)} = -4\pi D_{oil} s_{oil} \alpha \quad (2.34)$$

This equation can be solved easily and yields :

$$R_{mean}^3(t) - R_{mean}^3(t=0) = -3D_{s_{oil}}\alpha t \quad (2.35)$$

This solution differs by a factor $-4/27$ with the LSW expression. However this approach clearly contains the same key element that leads to the same growth law as in asymptotical solutions and numerical calculations.

2.2.4 Inhibiting Ostwald Ripening

From the rate of Ostwald ripening, it is straightforward to understand what can hinder this relaxation process.

The first option is to change the pathway, which is the diffusion of oil molecules in the continuous phase. Larger molecules have a smaller diffusion coefficient and this will slow down ripening. Another effect of larger magnitude is the solubility of the oil in water : oils with extremely small solubilities will cause a collapse of the exchange rate.

The second option is to change the drive. This can be easily done by trapping a nearly insoluble specie in the oil droplet. Solubilization of the oil (i.e. ripening) due to the interfacial energy is then competing with the decrease in mixing entropy when removing oil, which corresponds to an increase of the concentration of the insoluble specie in the oil. This is also written as an osmotic pressure that competes with the Laplace pressure. A full treatment is provided by Webster and Cates[37] based on an idea of Kabalnov et al[19]. There is no specific difficulty to this extension.

The other extreme is to mix two population of droplets with the same size but different oil composition. If the two oils mix, the mixing entropy drives an homogenization in composition of the droplets. This drive is much more powerful than the interfacial reduction, i.e. the osmotic pressure dominates the Laplace pressure. This is then termed composition ripening. A complete description is provided in the work of Taisne[34].

Chapter 3

Experimental designs

Contents

| | | |
|------------|-----------------------------------|-----------|
| 3.1 | Scattering | 45 |
| 3.1.1 | Scattering and eye sight | 45 |
| 3.1.2 | Scattering equations | 47 |
| 3.1.3 | Small-Angle and static scattering | 49 |
| 3.1.4 | Dynamic light scattering | 50 |
| 3.2 | Phase Diagrams | 53 |
| 3.2.1 | The equilibrium is our reference | 53 |
| 3.2.2 | Griding the sample : a bad idea | 53 |
| 3.2.3 | Choosing the starting point | 54 |
| 3.2.4 | Identify metastability barriers | 55 |
| 3.2.5 | Observation | 55 |

3.1 Scattering

3.1.1 Scattering and eye sight

Eye sight is one of our main tools to probe the world around us. Shadows are perceived through a decrease of the light intensity. Colors, i.e. wavelength, are selected by absorbing materials. However, except by looking directly to the sun, our world would still look dark without scattering. A observer in the International Space Station sees mostly dark except for the stars and planets. Scattering requires changes in propagation medium composition and structure. It then changes the propagation of light and allows each material to send back some light in our direction. It can also select colors of a polychromatic beam, a property used by the sky and some parrots.

Often scattering is considered as a separate issue from geometrical optics, i.e. propagation of light rays, eventually deviated by medium changes. However, again we must realize that a description by geometrical optics would only allow to see the world from a direct beam or from reflecting surfaces. Geometrical optics is in fact a part of the scattering processes associated with objects large compared to the wavelength of the light. Going down in size will lead to other scattering processes. They can all be described by solving the Maxwell set of equations for a propagating wave and the solution is termed the Mie solution. Some programs are available to compute the scattering solution from a sphere in a dielectric medium.

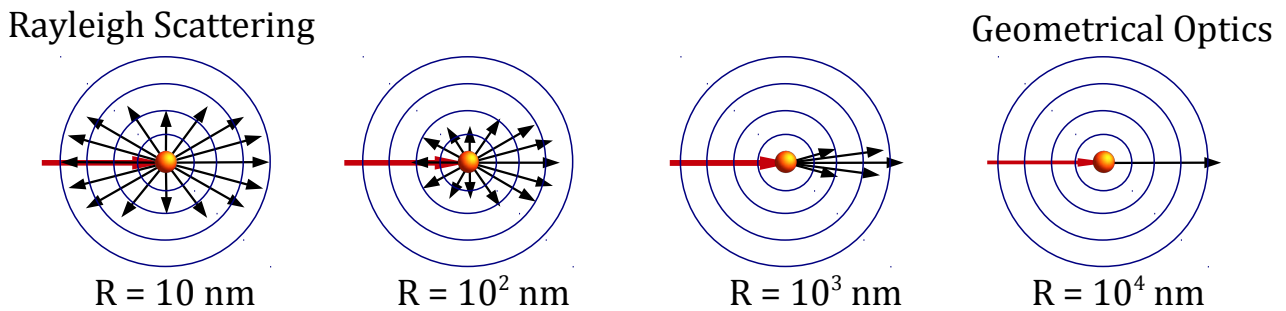


Figure 3.1: Scattering of a light beam ($\lambda = 600 \text{ nm}$) by a sphere of hexadecane oil in water for several droplets radius. The calculation is performed using the program from Zakharov. Small particles lead to Rayleigh scattering with a symmetric pattern, while large particles lead to geometrical optics and the ray model of light.

Taking the program by Zakharov[41] we can follow the scattering pattern as a function of the size of the object. At large sizes, the scattering is essentially the propagation of a light ray, this is the description by geometrical optics. At small sizes, the scattering is symmetric forward and backward and is termed Rayleigh scattering. The larger wavelength are less scattered than the smaller wavelength (blue light is scattered more than red light) and the intensity goes as the power sixth of the size. In the intermediate regime, the scattering is asymmetric between forward and backward and there is little wavelength selection. The result of a calculation for $\lambda = 600 \text{ nm}$ and hexadecane droplets in water is displayed in Figure 3.1.

Let's take a look at the sky. It is composed of very small molecules that we can assimilate to spheres much smaller than the wavelength. We are in the area of Rayleigh scattering, blue is scattered more than red and thus the sky is blue. Now some water droplets from evaporation/condensation process, a cloud, are also scattering light. They are of comparable dimensions to the wavelength and scatter in the intermediate regime, the scattering is mostly forward and does not select any wavelength, hence white light stays white and the clouds are white. We can finish by considering a balloon. This sphere is considerably larger than the wavelength and it is well described by geometrical optics.

Eye sight is thus a powerful tool to assess sizes of objects, even those we do not "see".

Very small droplets will scatter little and blue will be scattered more and red. Looking in parallel to the light beam the emulsion will appear reddish. Looking perpendicular to the light beam the emulsion will appear bluish. Increasing the size will lead to an increasingly whitish aspect. Much larger increase in size (oil flake) will result in clear phase separation and vision through our common geometrical optics. This is then useful to evaluate the number of phases in a system (layers, grains, precipitate...). Polarized light can also be used to obtain information on anisotropic samples.

3.1.2 Scattering equations

Other sources beside light can be used, they are X-rays and neutrons. The physical processes are different, light is concerned with polarization, X-ray by electron densities and neutron by nuclei. However they can be described under the same formalism, the Rayleigh-Debye-Gans approximation[23] (which is the scattering application of the first Born approximation) :

- Most of the beam particles (photons or neutrons) pass through the sample undeviated. A few are scattered once and multiple scattering is neglected
- The incident beam is not distorted significantly by the medium

This approximation holds when particles are much smaller than the wavelength (as discussed for light scattering) and/or have a low contrast with the surrounding medium. An important notion is the scattering vector defined as from the propagation vectors \vec{k} as :

$$\vec{q} = \vec{k}_{scattered} - \vec{k}_{incident} \quad (3.1)$$

We are assuming the scattering to be elastic and the wavelength is thus unchanged :

$$\|\vec{k}_{scattered}\| = \|\vec{k}_{incident}\| \quad (3.2)$$

We can then express the norma of the scattering vector :

$$q = \|\vec{q}\| = \frac{4\pi}{\lambda} \sin \frac{\theta}{2} \quad (3.3)$$

where λ is the wavelength in the medium and θ is the scattering angle, as displayed in Figure 3.2.

Let's consider a collection of N scattering particles. A particle i is positioned from the detector with a vector \vec{R}_i . The position of the sample to the detector is indexed by the distance R_d , much larger than distances between particles.

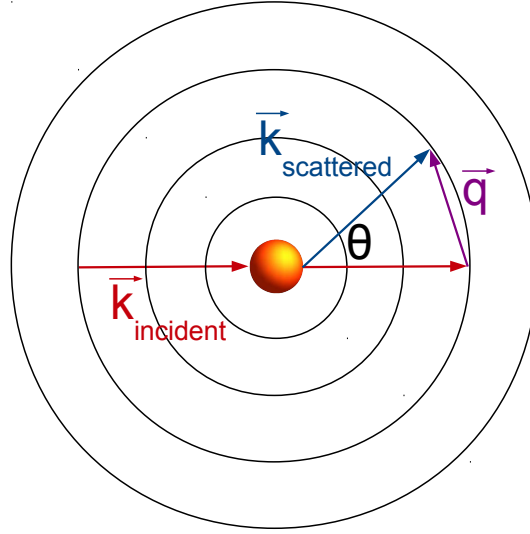


Figure 3.2: Definition of the scattering vector.

Each particle can be decomposed in sub-domains j of homogeneous contrast ρ and the index is \vec{r}_j . We define the scattering length of the particle i as :

$$b_i(\vec{q}, t) = \int \int \int_{V_i} \Delta\rho(\vec{r}_j, t) \cdot \exp(-i\vec{q} \cdot \vec{r}_j) d^3r_j \quad (3.4)$$

where $\Delta\rho(\vec{r}_j, t)$ is the contrast difference between the volume element indexed by \vec{r}_j and the continuous phase. This contrast is given by difference in polarizabilities for light scattering, electronic densities for X-ray scattering and nuclei for neutron scattering.

The expression of the scattered intensity, using particles indexes i and k is then :

$$I_s(q, t) = \frac{I_0}{R_d^2} \sum_{i=1}^N \sum_{k=1}^N b_i(\vec{q}, t) b_k^*(\vec{q}, t) \cdot \exp[-i\vec{q} \cdot (\vec{R}_i(t) - \vec{R}_k(t))] \quad (3.5)$$

This expression is given here without demonstration but we can rationalize the different terms. I_0/R_d^2 is the reference intensity without scattering divided by an area quantity corresponding to the detector position, it's a normalization factor that is important (and measured) when working on absolute scale. The product $b_i(\vec{q}, t) b_k^*(\vec{q}, t)$ contains the difference of contrast between the particle and the medium and is linked to the heterogeneity of the particle, its shape and its size. It is the key quantity for so-called static scattering. $\vec{q} \cdot (\vec{R}_i(t) - \vec{R}_k(t))$ contains the information on the movements of the particles with time. It is the key quantity for so-called dynamic scattering. The double summation is linked to the hypothesis that the total scattered intensity can be calculated from the sum of small homogeneous elements scattering.

3.1.3 Small-Angle and static scattering

If we focus first on static scattering, light, x-ray or neutrons, we can examine the conditions necessary for the Reyleigh-Debye-Gans theory to hold. The assumption that the incident beam is not distorted significantly by the medium is an important constraint. It requires the scattering object investigated to be much smaller than the wavelength (which requires sizes around 10-50 nm in light scattering) and/or to have a small contrast with the surrounding medium (usually true in the case of neutron and x-ray scattering).

We can calculate the typical q range for both light and x-ray/neutron for angles ranging between 0.01 and 1°. For X-ray we choose a wavelength of 0.1 nm, which yields a q interval of [0.011 - 1.11] nm⁻¹ and, taking the reverse, a distance interval of [91 - 0.91] nm. For light we choose a wavelength of 600 nm, which yields a q interval of [0.0000018 - 0.00018] nm⁻¹ and, taking the reverse, a distance interval of [547000 - 5470] nm. While X-ray (and neutrons) small angle scattering gives access to the desired length scale, this is not the case for light.

The analysis of small-angle scattering data can be performed through three main approaches :

- Model-independent analysis using general theorems and calculation of scattering invariants
- Inversion from the scattering (reciprocal) space to the real space
- Model-fitting assuming a given geometry

Each of them has its own merits and limitations and are thus potentially useful.

The model-independent analysis is based on the use of two quantities, the geometrical invariant and the Porod limit.

The geometrical invariant writes as :

$$Q = \int_0^\infty q^2 I(q) dq = 2\pi^2 (\Delta\rho)^2 \phi(1 - \phi) \quad (3.6)$$

where ϕ is the volume fraction.

The Porod limit writes as :

$$P = \lim_{q \rightarrow \infty} q^4 I(q) = 2\pi (\Delta\rho)^2 \phi A/V \quad (3.7)$$

where A is the total area of scattering material and V is the total volume of scattering material. A characteristic size is easily obtained in the dilute limit :

$$\frac{\langle R^3 \rangle}{\langle R^2 \rangle} = \frac{3}{\pi} \int_0^\infty q^2 I(q) dq / \lim_{q \rightarrow \infty} q^4 I(q) \quad (3.8)$$

The model-independent analysis is powerful to extract the mean size of objects without any assumptions.

The inversion procedure proposed by Botet et Cabane used in this work is based on the Shannon analysis of deviations to the Porod law. This method is powerful to extract size distributions. Other inversion methods are available but the formalism will not be presented here.

Finally the model-fitting method, quite popular, is based on a particular writing of the scattered intensity that is given below. The quantity measured is the time-average of the scattering intensity $I_s(q) = \langle I_s(q,t) \rangle_t$. Assuming homogeneous spheres, which is the main situation we encountered we can write :

$$I_s(q) = \frac{I_0}{R_d^2} \cdot b^2(q) \sum_{i=1}^N \sum_{k=1}^N \langle \exp[-i \vec{q} \cdot (\vec{R}_i(t) - \vec{R}_k(t))] \rangle_t \quad (3.9)$$

We can introduce the form factor, which describes the shape :

$$P(q) = \frac{b^2(q)}{b^2(0)} \quad (3.10)$$

and the static structure factor, which describes the positions correlation between the particles :

$$S(q) = \frac{1}{N} \sum_{i=1}^N \sum_{k=1}^N \langle \exp[-i \vec{q} \cdot (\vec{R}_i(t) - \vec{R}_k(t))] \rangle_t \quad (3.11)$$

We then obtain the time-average of the scattered intensity for monodisperse homogeneous spheres :

$$I_s(q) = \frac{I_0}{R_d^2} \cdot N b^2(0) P(q) S(q) = \frac{I_0}{R_d^2} \cdot NV \Delta\rho^2 P(q) S(q) \quad (3.12)$$

This expression contains from left to right, the setup parameters, the number of particles, the volume of a particle, the contrast, the form factor (shape) and the structure factor (positions).

A final point should be made in favor of neutron scattering. While light and X-ray scattering to change the contrast without changing the properties of the system, in neutron scattering the contrast can be changed through simple deuteration of the molecules. This drastically changes the contrast while leaving mostly unchanged the other properties of the system. This is the basis of contrast variations methods that have been used in this work.

3.1.4 Dynamic light scattering

Another very powerful scattering technique used extensively throughout this work is Dynamic Light Scattering (DLS). This technique is based on the analysis of the scattered intensity fluctuations. We thus analyze the deviations of the scattered intensity to its

mean value. The fluctuations are due to Brownian diffusion of the droplets with time and this movement leads to a speckle scattering pattern.

The key quantity is the intensity correlation function, which compared the signal $I(q, t)$ with its delayed version $I(q, t + \tau)$, for all starting times t and for a range of delay times τ :

$$\langle I(q, 0)I(q, \tau) \rangle = \lim_{T \rightarrow \infty} \frac{1}{T} \int_0^T I(q, t)I(q, t + \tau) dt \quad (3.13)$$

The two limits of this quantity are easily obtained :

$$\lim_{\tau \rightarrow 0} \langle I(q, 0)I(q, \tau) \rangle = \langle I^2(q) \rangle \quad (3.14)$$

$$\lim_{\tau \rightarrow \infty} \langle I(q, 0)I(q, \tau) \rangle = \langle I(q) \rangle^2 \quad (3.15)$$

From the expression of the scattered intensity in the Rayleigh-Debye-Gans approximation, we discussed that the key quantity for dynamic scattering was :

$$\sum_{i=1}^N \sum_{k=1}^N \exp[-i \vec{q} \cdot (\vec{R}_i(t) - \vec{R}_k(t))] \quad (3.16)$$

We can define the normalized time correlation function of the scattered field and the scattered intensity :

$$g^{(1)}(q, \tau) = \frac{\langle \vec{E}(q, 0) \vec{E}^*(q, \tau) \rangle}{\langle I(q) \rangle} = \langle \exp[-i \vec{q} \cdot (\vec{R}(0) - \vec{R}(\tau))] \rangle \quad (3.17)$$

$$g^{(2)}(q, \tau) = \frac{\langle I(q, 0)I(q, \tau) \rangle}{\langle I(q) \rangle^2} \quad (3.18)$$

Since the field is a complex Gaussian variable the factorization properties of the correlation function can be used to yield the Siegert relation :

$$g^{(2)}(q, \tau) = 1 + [g^{(1)}(q, \tau)]^2 \quad (3.19)$$

If the droplets are undergoing Brownian motion, the mean-square displacement in time τ is :

$$\langle \Delta R^2(\tau) \rangle = \langle [|\vec{R}(\tau) - \vec{R}(0)|^2] \rangle = 6D_0\tau \quad (3.20)$$

where the free-droplet diffusion constant is given by the Stokes-Einstein equation :

$$D_0 = \frac{kT}{6\pi\eta R_d} \quad (3.21)$$

where kT is the thermal energy, η the viscosity of the dispersing fluid and R_d is the

hydrodynamic radius of the droplet. We then obtain :

$$g^{(1)}(q, \tau) = \sqrt{g^{(2)}(q, \tau) - 1} = \exp(-q^2 D_0 \tau) \quad (3.22)$$

The measurement of the intensity time correlation function can thus give access through fitting to the diffusion coefficient and thus to the droplet radius. Dynamic light scattering is a sizing method for objects undergoing Brownian motion. The instruments often display directly $g^{(1)}(q, \tau)$ and this function should depart from 1 at initial time (perfect correlation) to reach zero at infinite time (no correlation). The speed of decay of the auto-correlation function is directly related to the diffusion speed of the particles, i.e. their size.

For experimental purposes, it is important to understand how the correlation function is measured. Theoretically, one time measurement would be enough to obtain the function. However, the measurements are necessarily polluted by signal noise, caused by all the imperfections of the device and sample. It is then necessary to repeat a large number of times the measurement to reduce the experimental error. For quality data obtention of a correlation function of colloidal objects, which diffuse slowly, this would be too time consuming. A better option is to use a correlator, which could be pictured as a wheel with C slots (or channels) (see Figure 3.3). The intensity is measured over time intervals of duration τ . The total duration of a measurement is thus $C \cdot \tau$. The interest of a correlator lies in the observation that measuring $\langle I(q, \tau) I(q, 2\tau) \rangle$ is the same as measuring $\langle I(q, 0) I(q, \tau) \rangle$. This is just a matter of changing the time reference and the correlator thus allows multiple measurements of a given value of the correlation functions by comparing the intensities stored in the different channels.

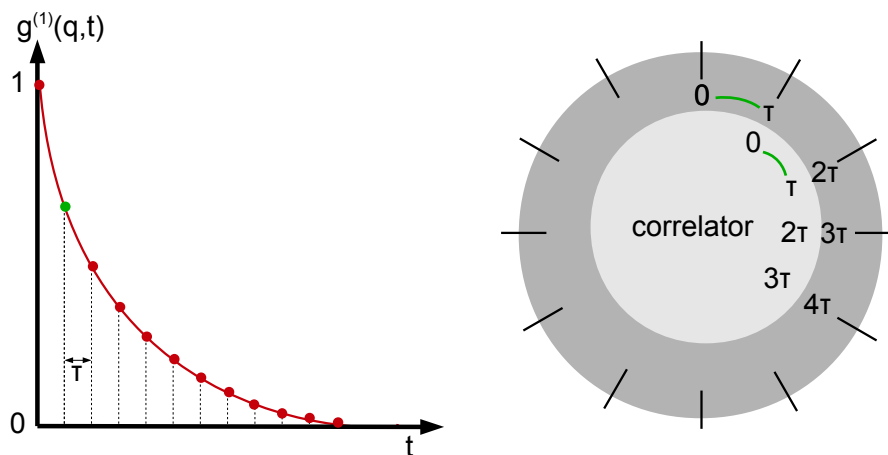


Figure 3.3: The correlation function decays with time. A correlator is used to obtain several repetitions of each experimental point through a simple initial time change as illustrated by the wheel drawing.

3.2 Phase Diagrams

3.2.1 The equilibrium is our reference

The equilibrium state of a system is the reference to which non-equilibrium states are compared. Tricking and trapping the system away from equilibrium thus requires a good understanding and characterization of the equilibrium behavior. This can be mapped on a phase diagram, which represents the optimum of the energy/entropy competition.

Throughout this work the establishment of phase diagrams has been a powerful tool to the study of non-equilibrium transformations. The main opposition against phase diagrams that every reasonable experimentalist should consider is that they are potentially tedious and time-consuming to establish. I would like to present a short overview of a personal method to probe phase diagrams in a hopefully more dynamic way.

3.2.2 Griding the sample : a bad idea

Establishing a phase diagram is very similar to drawing a map of an unknown territory. The hard method would be to use a long-range cannon and throw bullets to this territory. Each bullet contains a camera that can record its surroundings. Clearly, many bullets should be sent to have a proper map. Furthermore, the cameras can very well be trapped by the landscape and the observation difficult. A gentler method would be to walk into that new land and record the observations along the path taken. Clearly this requires to think about which path should be taken and this requires an understanding on how paths are designed in the first place.

Ending the metaphor, the method for establishing phase diagrams that frightens (rightfully) many experimentalist is the preparation of a large collection of samples to grid the whole range of parameters. This is typically the approach taken in "experimental design" but most often this approach is severely hindered by kinetics. Indeed metastability barriers are common (charges, viscosity, density match, resistance to coalescence or exchange etc...) and may prevent the system from reaching its equilibrium state. The more components in the system the more unsuccessful is this dominating approach.

I want to support a different way of exploring phase diagrams, which relies on starting from well-identified states and take clever paths. A few practical tools are presented below and although they are splitted for the sake of clarity they should all be considered simultaneously. Clearly an understanding of what triggers the phase transition in the system is a tremendous help but is often the aim of establishing the phase diagram in the first place. A constant interplay between expectations and answers from the system must be operated in addition to these principles. The two approaches are illustrated in Figure 3.4 on a real example taken from the work on emulsification through water addition

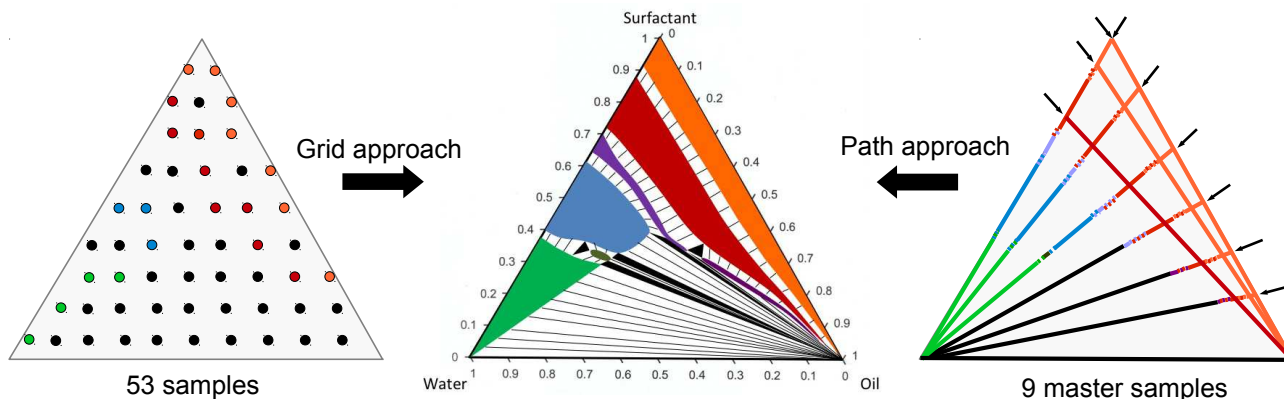


Figure 3.4: Comparison of the grid approach with the path approach to establish a phase diagram

3.2.3 Choosing the starting point

The first step in a trip is to start from the good base. There are three main ideas to keep in mind.

First, we are often interested in the study of multicomponents systems. It is often interesting to downgrade the number of components and study the equilibrium behavior and then add back the additional components. Practically if we consider a rather simple ternary system it is often clever to study the binary systems beforehand. They will often provide interesting initial states from which we can add the third compound. The decomposition is experimentally straightforward when the system is prepared from mixing of pure compounds. However most often multi components systems are prepared from unsure sources and it is then necessary to undertake separation steps before preparing the system. While it is a potentially difficult task, it is probably worth the effort in respect to the mapping of phase diagrams.

Second, it is often interesting to start from a one-phase region. This can be understood from the so-called Gibbs phase rule. It is more instructive to derive it directly from thermodynamics. Let's consider a ternary system with three components A, B and C. If there is only one phase, then A, B and C are in the same homogeneous volume. The amounts of A, B and C can be described for example by their molar fractions. Since the total amount of molecules is set, the sum of these fractions is 1. Only two fractions are thus independent. We can state that there are two composition degrees of freedom (we can set constant the external parameters such as pressure and temperature which would also count as degree of freedom). Let's now consider the line of contact between two one-phase regions (different structure). Each phase can be described as before by 3 molar fractions and a mass conservation relation yielding each 2 degrees of freedom. However there are additional constraints due to the equilibrium between the two phases. The chemical potential of each component must be equal in each phase at equilibrium. This yields three additional constraints. There is thus only one composition degree of freedom.

This degree can not be restricted to a separation point between the two one-phases region and therefore the two-phase coexistence region must consist in a set of lines. We derive the strong conclusion that for any system with more than two components one-phases regions can not touch. The identification of a one-phase region is thus a strong solid base to start the exploration.

Third, if it is the non-equilibrium transformations that are of interest for the study, it is probably smart to start from the same initial states as for the non-equilibrium transformations and then take a slow pace along the same path. This offers an interesting comparison and reference.

3.2.4 Identify metastability barriers

As stated above, the main difficulty of the gridding method arise from metastability barriers. Often interesting systems for non-equilibrium transformations will contain triggers for metastability. Understanding the origin of the metastability is often a good help. Typically we can try to address the following questions : which component or combination of components yield metastability? which structures are prone to yield metastability? can we lower the barrier through addition of another compound or through a different path? I stated above that equilibrium pathways similar to non-equilibrium transformations were interesting to study but they are also the most dangerous ones due to the metastability barriers expected for non-equilibrium transformations to be of interest.

Clearly this may contradict directly the idea presented above that pathways similar to the non-equilibrium transformations were the best. They can also be the most dangerous ones.

It is worth mentioning that these issues strongly manifest when one pure compound (or one type of compound) separates from the rest (for example oil separating out the a ternary oil/water/surfactant system). Removal of part of this compound can then be a solution to reach simpler phases.

3.2.5 Observation

Practical establishment of the phase diagrams is based on a careful visual inspection. Boundaries between separated phases are usually easy to observe. When phases are not macroscopically separated the separation can be restrained to the colloidal scale, which results in scattering. Large domains will typically gives whitish scattering, while small colloidal self-assembly objects will scatter reddish/bluish depending on the angle. The intensity of the scattering, i.e. the turbidity, is well-assessed by our eyesight and tells us about the concentration or the size of these colloidal objects. The visual inspection is completed by an observation under crossed polarizer/analyser. If the sample is isotropic

the light is filtered and the sample looks dark, whereas anisotropic structures lead to birefringence and the sample will look bright. Some wavelength selection can also occur and colorful pattern can then be observed.

It is often a good complement to manipulate the sample a bit and observe the changes through rotation (to assess viscosity), shear (to assess hydrodynamic stability and the possible presence of metastability barriers) or external parameters changes (temperature, ionic strength, pH ...).

The first aim is to identify the one-phase regions where the sample is always transparent (some Rayleigh scattering may be observed, as well as birefringence). If the regions are known then the rest is a combination of these phases and this helps greatly in the identification.

The analysis can be refined with quantitative methods such as calorimetry, NMR and small-angle scattering.

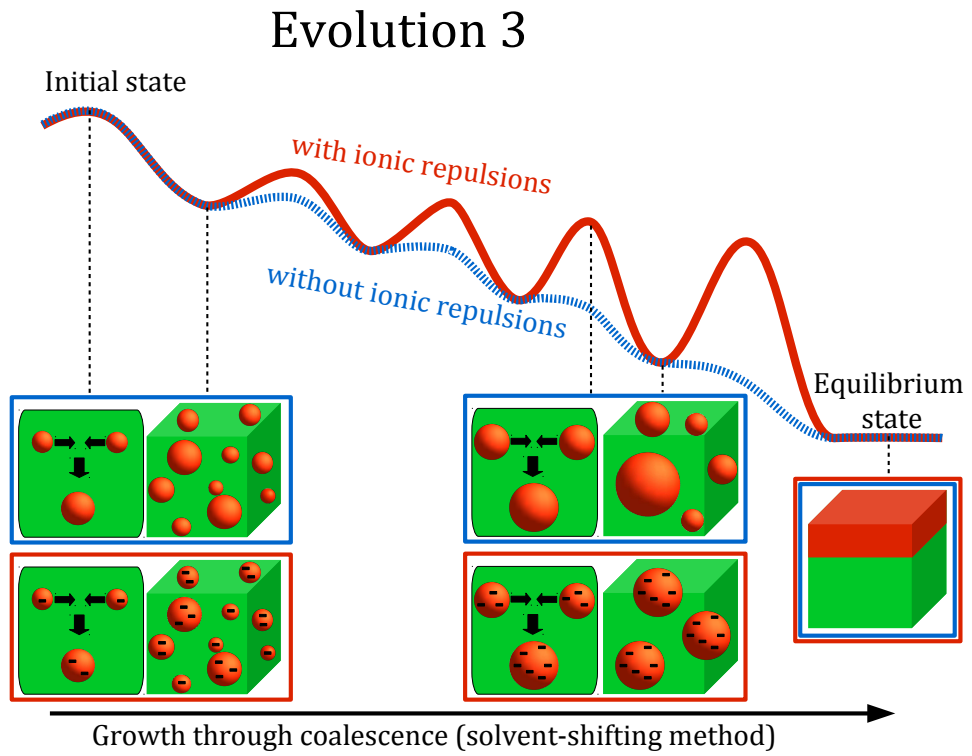
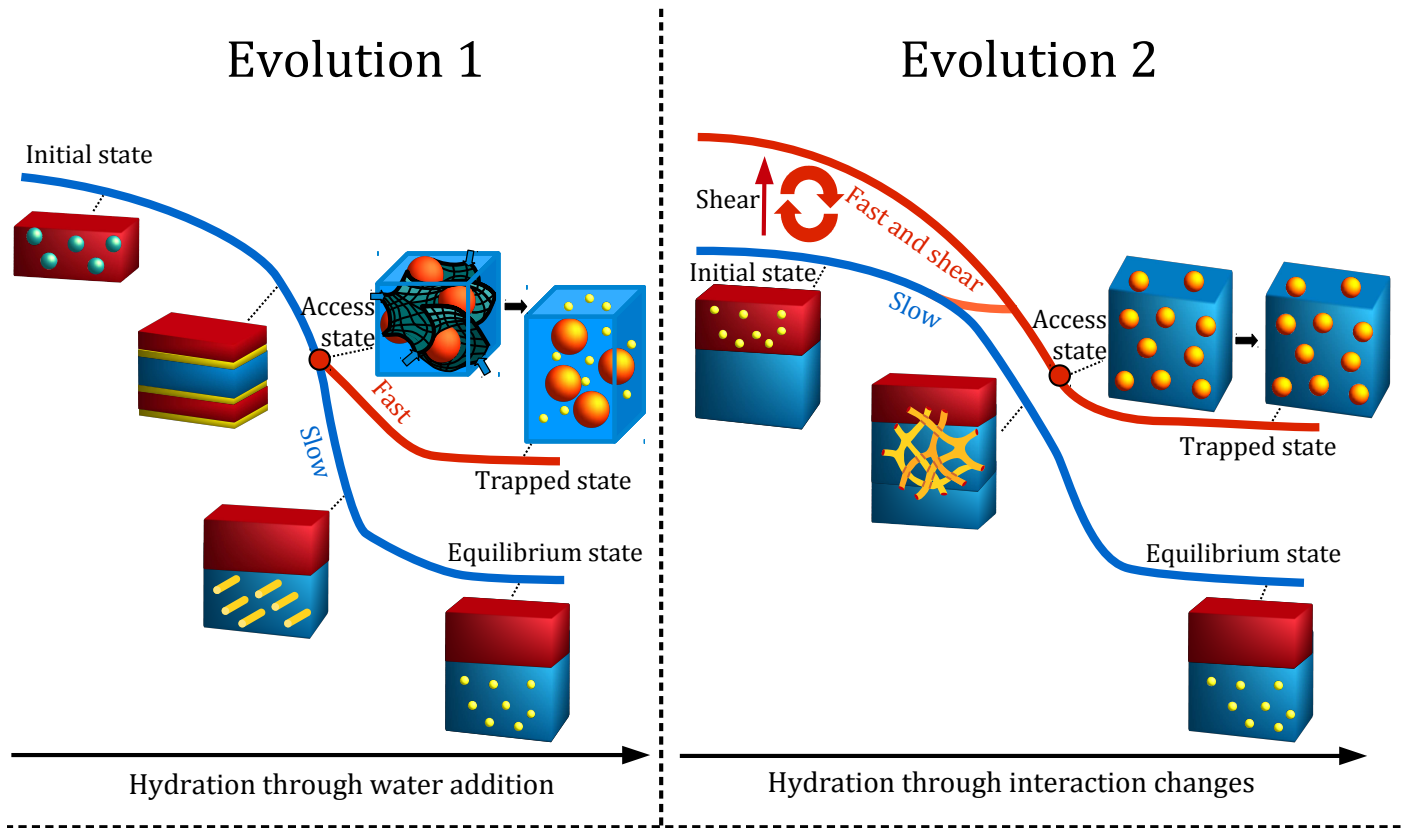
Chapter 4

Summary

Contents

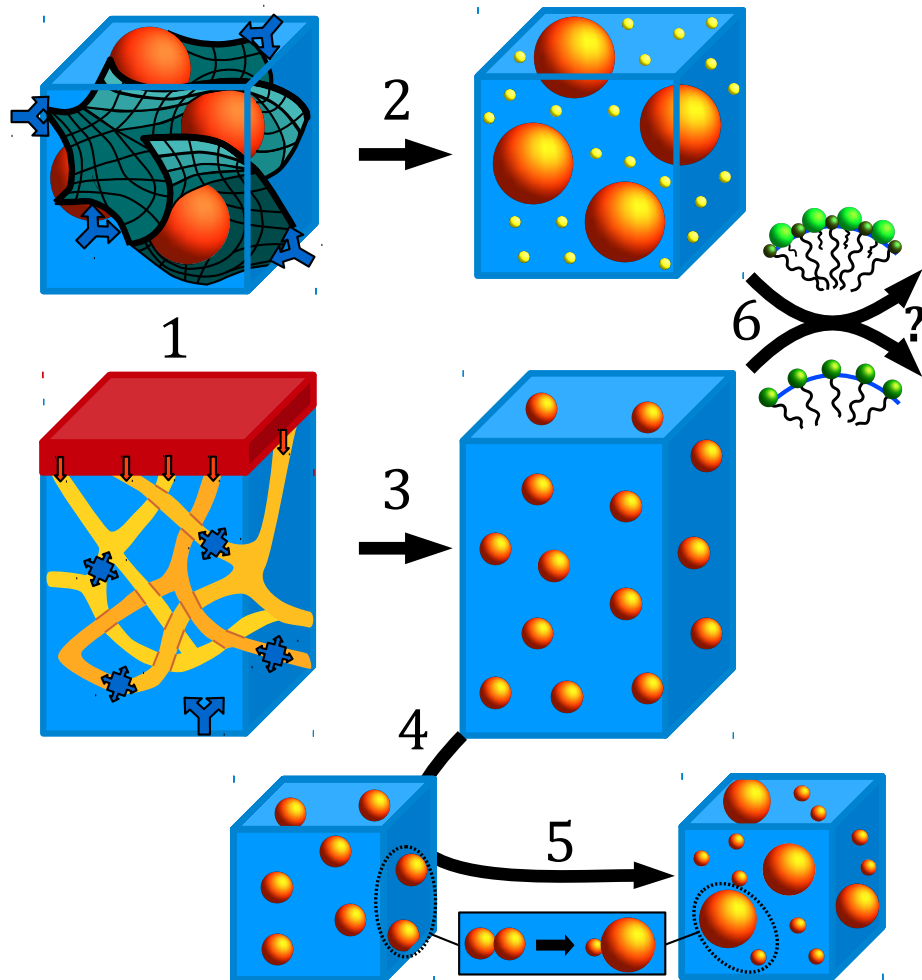
| | | |
|------------|--|-----------|
| 4.1 | Physicochemical methods | 58 |
| 4.2 | Main Findings | 60 |
| 4.3 | Non-equilibrium self-assembly through surfactant fast hydration | 62 |
| 4.3.1 | Rapid quench from access states rather than phase inversion . . . | 62 |
| 4.3.2 | Hydration through interaction changes | 63 |
| 4.3.3 | Hydration through addition of water | 65 |
| 4.3.4 | Systems investigated | 66 |
| 4.4 | Non-equilibrium self-assembly through Solvent-Shifting . . . | 67 |
| 4.5 | Destabilization pathways and barriers | 68 |
| 4.5.1 | Contact Ripening | 68 |
| 4.5.2 | Repulsion controlled coalescence | 69 |
| 4.5.3 | Origin of repulsions in "surfactant-free" conditions | 71 |

4.1 Physicochemical methods

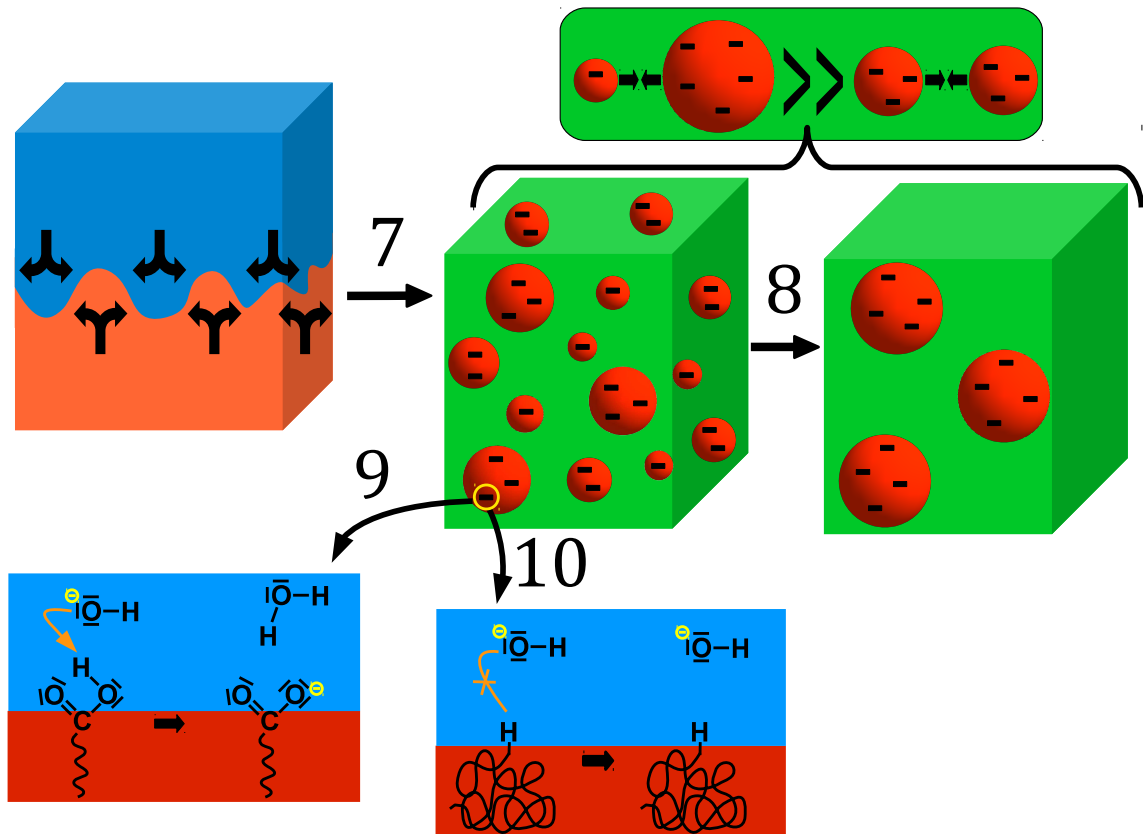


| | Evolution 1 | Evolution 2 | Evolution 3 |
|---------------|--|--|--|
| System | Oil+ Surfactant+ Water | Oil+ Surfactant+ Water | Polymer or oil+ good solvent+ bad solvent |
| Initial state | Water poor system : dehydration of the surfactant head | Water rich system, dehydration by weak solvent/head interaction | Oil or polymer in good solvent |
| Trigger | Hydration through water addition | Hydration through interaction changes : T, ionic strength, pH | Addition of bad solvent |
| Pathway | Oil nucleation templated by a sponge phase | Formation of a superswollen microemulsion | Repulsion hindered coalescence |
| Trap | Surfactant layer preferentially curved towards the oil | Surfactant layer preferentially curved towards the oil | Ionic repulsions between surface charges |
| Trapped state | Nanoemulsion with excess surfactant Typical size range : 100-300 nm | Monodisperse nanoemulsion with no excess surfactant Typical size range : 10-100 nm | Nanodispersion of polymer particles or nanoemulsion Typical size range : 50-200 nm |

4.2 Main Findings



1. Fragmentation as the system undergoes phase inversion is found to be irrelevant for the production of fine nanoemulsions (Papers 1 & 2).
2. Nanoemulsions are obtained through water dilution of a surfactant/oil solution, through a templated phase separation in a bicontinuous sponge phase (Paper 2)
3. A bicontinuous to spherical transition is observed under shear and leads to non-equilibrium superswollen microemulsions (Paper 3).
4. Monodisperse size-controlled nanoemulsions, with no excess surfactant, are obtained through trapping of superswollen microemulsions (Paper 1).
5. A novel pathway for emulsion destabilization is identified and characterized : Contact Ripening, which occurs through molecular exchange at contact (Paper 8).
6. The nanoemulsification methods are successfully extended to surfactant mixtures and the range of validity is characterized (Paper 9).



7. Nanoprecipitation through the solvent-shifting route has been fully characterized (mechanism, mixing effects, importance of repulsions) (Papers 6 & 10)
8. Experimental and theoretical demonstration that coalescence limited by repulsions lead to narrow populations of droplets (Paper 6)
9. An hydroxide ion adsorption mechanism on pure hydrophobic surfaces is opposed and countered by an explanation through fatty acid contamination (Papers 4 & 5).
10. Colloidal properties of polymers particles made from neutral units are controlled by the end-groups of the macromolecules (Paper 7)

4.3 Non-equilibrium self-assembly through surfactant fast hydration

4.3.1 Rapid quench from access states rather than phase inversion

Oil/surfactant/water systems display a large variety of equilibrium self-assembly structures and the selection is mainly performed by the preferred curvature of the surfactant layer. At low preferred curvature, the obtention of size-controlled droplets through oil swelling of micelles is compromised by the formation of bicontinuous networks. In such conditions the formation of droplets through equilibrium self-assembly is impossible and we must then take non-equilibrium pathways.

Still, since we aim for uniform collections of size-controlled droplets, we must retain strong constraints typical of self-assembly. This requires taking the system away from its equilibrium states but not too far, which corresponds to maintaining the predominance of the preferred curvature. We can either take the system along barriers separating it from the equilibrium states, which corresponds to strong structural similarity, or further away, which requires not only barriers but structural changes.

Practically the preferred curvature is tuned by the hydration of the hydrophilic head. A highly hydrated head will tilt the balance of interactions at the interface in favor of hydrophilicity, which results in a preferred curvature towards the oil, while a poorly hydrated head will favor hydrophobicity and results in a preferred curvature towards the water. Changes in hydration will trigger a modification of the preferred curvature and thus structural changes. If the curvature turns from water to the oil, we qualify the changes as a phase inversion. Also high values of the spontaneous curvature of the surfactant layer yield high barriers against droplet coalescence.

Two different triggers have been used to perform rapid hydration changes. One relies on a sudden change of the interaction between water and the hydrophilic head, through a change in a physico-chemical parameter (temperature, ionic strength, pH). Another is based on a rapid water addition to a water poor system.

In both cases, we have identified a state that determines the final properties of the nano-emulsion we obtain. This access state has a well-defined structure, corresponding to a precise preferred curvature, and controls the outcome of the non-equilibrium pathway. This access state corresponds to non-equilibrium self-assembly. We have shown that the access state is monophasic and corresponds to a preferred curvature turned towards the oil, as in the final nano-emulsion. The composition and hydration required to form these states are strongly constrained to a line. Experimentally the access states are easily detected as a minimum in scattering and the solubilization line has thus been named Clearing Boundary.

Starting from these access states, a sudden increase of the preferred curvature, through hydration, triggers the formation of the final nanoemulsion. Macroscopic phase separation

is prevented by a fast preferred curvature increase, which erects high barriers against coalescence, thus preventing the system from reaching its equilibrium state.

The mechanism of non-equilibrium self-assembly in oil/water/surfactant systems is guided by the preferred curvature variations, as its equilibrium counterpart. Access states contain this major structural constraint and transfer it to the final nanoemulsion through templating. The non-equilibrium pathway can then be described in two steps, first the formation of the access state, second the rapid evolution (quench) to the final nanoemulsion, which provides metastability barriers.

This novel mechanism dispels the previous literature claims that the emulsification takes place through fine fragmentation at the phase inversion. Such phase inversion mechanism rely on low interfacial tensions values as the preferred curvature turns from the water towards the oil. Since we show the process is determined by the crossing of access states, which correspond to structures already located after the phase inversion, phase inversion is irrelevant.

Despite their similarities, differences between access states obtained upon hydration through interaction changes or water addition have been identified. Hydration through interaction changes correspond to structural changes, while hydration through water addition operates closer to equilibrium. The differences in the access state structures lead to differences in the final properties of the nanoemulsion and the main characteristics are given in the following two sub-sections, while the systems are explicated in the last sub-section.

4.3.2 Hydration through interaction changes

Hydration changes can be performed at constant amount of water, through changes of the interactions between the aqueous phase and the surfactant head. The preferred curvature, c_0 , can then be adjusted to match the geometrical radius, R_{geo} , which writes as $R_{geo} \cdot c_0 = 1$. As described in chapter 1 on equilibrium self-assembly, this equation corresponds to the formation line of spherical microemulsions, collections of uniform swollen micelles of radius $R_{geo} = 1/c_0$. At low surfactant concentration, we observe experimentally that the spherical microemulsion is replaced by a bicontinuous network in equilibrium with excess oil and water. We have performed the reverse transition by shearing the system. Shearing disrupts the bicontinuous network and, at the line $R_{geo} \cdot c_0 = 1$, the system thus forms a collection of spherical droplets. These steady-states under shear are microemulsions with a size range higher than achievable in equilibrium conditions and are thus named superswollen microemulsions. Their radius is the geometrical radius, $R_{geo} = 3l_s(\phi_{oil}/\phi_{surfactant})$, thus determined by a single composition parameter, which is the oil to surfactant ratio or said otherwise the volume to area ratio. If shear is stopped, the system leaves the superswollen microemulsion state to reach its equilibrium bicontinuous state.

However, a rapid increase of the preferred curvature from this superswollen microemul-

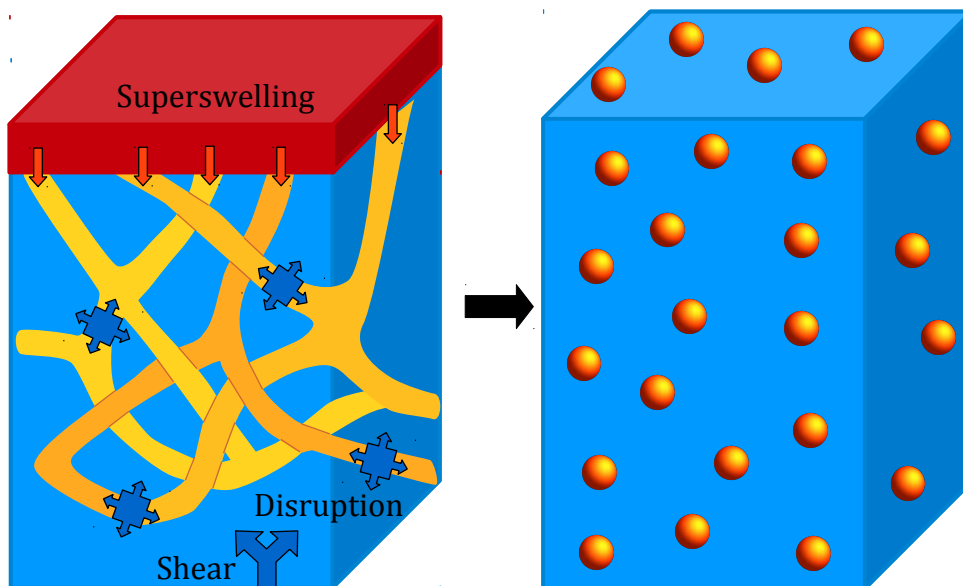


Figure 4.1: Bicontinuous networks in equilibrium with oil and water are disrupted by shear. If the preferred curvature matches the curvature of monodisperse spheres, the formation of a superswollen microemulsion is observed. This steady-state can then be trapped in a metastable state through a rapid curvature change.

sion, leaves no time for structural reorganization. As the fast increase of the preferred curvature provides protection against coalescence, the droplets encounters are hindered. The rapid curvature quench thus transforms the steady-state superswollen microemulsion into a metastable nanoemulsion. This emulsification method is unique in three ways :

- It makes a fully efficient use of the surfactant, i.e. all the surfactant is at the interface.
- A narrow population of droplets is obtained, i.e. a monodisperse emulsion.
- The size of the droplets is tunable in the 10-100 nm range through a single composition parameter

However it requires crossing the superswelling line, $R_{geo} \cdot c_0 = 1$. It is thus necessary to know the variations of the preferred curvature c_0 . The simplest method is to establish an equilibrium phase diagram, from which we can extract such variations. The identification of the superswollen microemulsion as an access state should simplify the use of this nanoemulsification method. Indeed, the requirement to undergo phase inversion, which is troublesome industrially due to fast properties changes, is lifted. This should lead to a wider industrial use of this method. On the lab scale this method is very useful to produce size-controlled and monodisperse emulsions, which are good model systems to study colloidal properties. This potential has been partly explored in this work through the study of a relaxation process, contact ripening.

4.3.3 Hydration through addition of water

Another way to change the surfactant hydration is to directly add water. If the initial state is water-poor, the surfactant layer is curved towards the water to maximize its poor hydration. Addition of water will relax this constraint and the preferred curvature will turn progressively towards the oil as the surfactant heads swell with water. A few equilibrium monophasic states, where all the oil is solubilized, are obtained at low water content. The most hydrated monophasic state correspond to a preferred curvature already turned towards the oil, at water content higher than the phase inversion composition. The structure of this equilibrium state is a bicontinuous sponge phase, which is a surfactant bilayer network swollen by water, with each monolayer curved towards the oil.

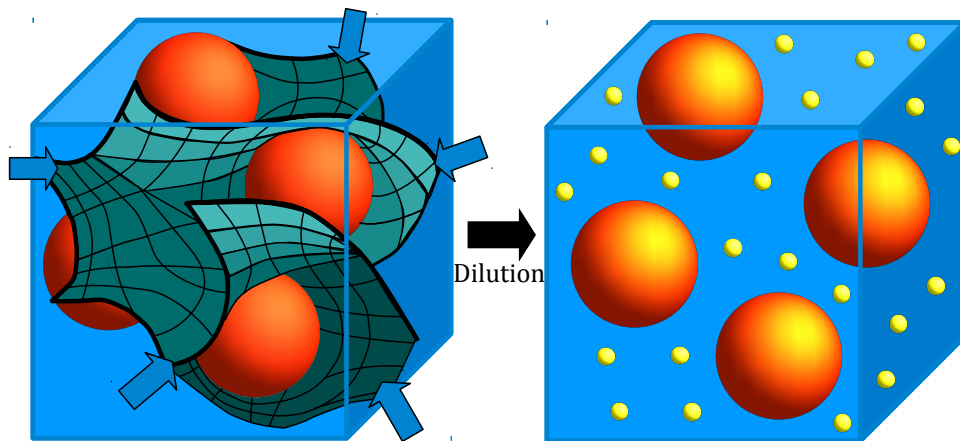


Figure 4.2: Rapid water addition to a bicontinuous sponge phase leads to nucleation of oil templated by the surfactant monolayers. The mean curvature of the monolayer determines the final droplet size.

At equilibrium, this structure is destroyed with further addition of water, which leads to macroscopic oil phase separation. However, if the addition of water is rapid, the surfactant layer has no time to change its curvature to match the preferred curvature. The oil phase separates in the sponge phase but is templated by the sponge phase monolayers. The droplets self-assemble to a radius that matches the curvature of the sponge phase layer. They are subsequently protected against coalescence by large values of the preferred curvature.

Since the curvature of the sponge phase is much lower than in the superswollen microemulsions, which correspond to the optimal structure, some surfactant is wasted and the droplets are larger than in the previous hydration method. The typical size range is 100-300 nm droplets, coexisting with surfactant micelles. However, this method is extremely easy to scale up and use. Also it can be readily extended to any type of surfactant systems. One important industrial application is the on-site emulsification to produce lubricating fluids.

4.3.4 Systems investigated

So far the presentation was focused on mechanistic aspects with the introduction of the access state concept. However, the experimental identification of these mechanisms is based on a careful choice of system. Purified ($> 99\%$) oxyethylenated surfactants have been extensively used. They consist of a hydrophobic alkane chain linked to a hydrophilic ethylene oxide (EO or EG) chain. Water is a good solvent for EO chains at low temperatures but the solvent quality decreases upon increasing the temperature. This peculiar property allows to tune the hydration of the surfactant head, hence the preferred curvature, through temperature changes. This is a way to change hydration through changing the water/head interaction. The associated emulsification was named Phase Inversion Temperature (PIT) method since phase inversion was thought to be the operating mechanism. Since we identified an access state, the superswollen microemulsion, at lower temperatures, this method is in fact a sub-PIT method (with no links with phase inversion).

The same system can also be used for hydration through water addition. The temperature range is then always sub-PIT to ensure the preferred curvature is towards the oil at high water content. If we start to the contrary at low water content, the hydrophilic heads are not sufficiently hydrated and the preferred curvature is towards the water. Addition of water swell the hydrophilic layer, turning the curvature towards the oil. The inversion composition is named the Phase Inversion Composition (PIC) and also lead to the incorrect denomination PIC emulsification method. However it is also not related to phase inversion since the sponge phase occurs at water fractions above the phase inversion, the emulsification is thus a sup-PIC method.

The non-equilibrium self-assembly concepts have been based on the use of such model systems but their applicability to more complicated systems can be questioned. Since only mixtures of surfactants are of practical use it is essential to extend the single surfactant results to more complex systems. One important extension performed in this work is the use of two pure surfactants as a good intermediate between a model system with a single surfactant and real systems with several.

One two-surfactant system investigated was a mixture of a pure oxyethylenated surfactant with a fatty acid. The fatty acid is a weak lipophilic surfactant at low pH but is a strongly hydrophilic surfactant at high pH. Starting at low pH the temperature can be tuned to reach the Clearing Boundary line. Under shear a superswollen microemulsion was obtained, as in the single surfactant case. The preferred curvature was then rapidly increased by a pH increase, at constant temperature. This trapped the system in a metastable, a size-controlled monodisperse nanoemulsion, as in the single surfactant case. However one major difference was observed : while any states of lower hydration than the access state yielded the same result in the single surfactant case, this is not true when using surfactant mixtures. This is due to segregation of the different surfactants in

different phases, which prevents the formation of the access state during the rapid quench. It is then essential to start directly from the access state to obtain the nanoemulsion. This highlights the importance of the concept of access states developed in this work.

The same conclusion was reached for systems of octylglucoside/span or SDS/oxyethylenated surfactants. In these cases the preferred curvature was adjusted through addition of water to water poor initial states. Similarly to the single phase case, the access state is a bicontinuous sponge phase, which templates the oil phase separation and yield the final droplets. However it was also found essential to start from the access states or any upstream monophasic states.

We state that the emulsification mechanisms when the surfactant layer is rapidly hydrates are extendable to a large variety of systems while their practical design rests solely on the identification of the access states and use of application-tailored triggers.

4.4 Non-equilibrium self-assembly through Solvent-Shifting

Emulsification through hydration is based on the interfacial free energy modification. There is another set of methods that rely on the bulk free energy modification. Several denominations exist but we will choose to name them as nano-precipitations. Indeed a good description is a precipitation restrained to the colloidal ("nano") scale. Consider a solute in a solvent, the mixing is favored by the mixing entropy that dominates over the interaction energy. If this interaction energy is modified it can win over the mixing entropy and lead to phase separation. Such a modification can be performed through a modification of the solute by a chemical reaction, or a modification of the solvent such as addition of a non-solvent, or a temperature change, or a ionic strength change. Narrow populations of droplets or particles are typically obtained, which means that the system is strongly constrained. Nanoparticles dispersions of metals and oxides are usually produced through such a method using a chemical reaction to change the solute/solvent interactions.

In this work, we investigate in details a route that does not involve chemical reactions. It leads to either oil droplets or polymer particles and is based on the addition of a miscible bad-solvent to a solute/good-solvent mixture. Water has been used a bad-solvent, acetone as good-solvent and either an oil or a polymer have been used as solutes. This solvent-shifting leads to a precipitation of the solute. The method involves two steps : the hydrodynamic of the mixing and the precipitation of the solute.

The relative speed of each step determines whether they are coupled or not. We have used a setup in which the mixing can be precisely monitored. At high mixing rates, the hydrodynamic step is rapid compared to the precipitation step and they are thus uncoupled. In this case the diameter of the final droplets does not depend on the concentration of solute and is solely determined by the interdroplets repulsions. If mixtures of charged

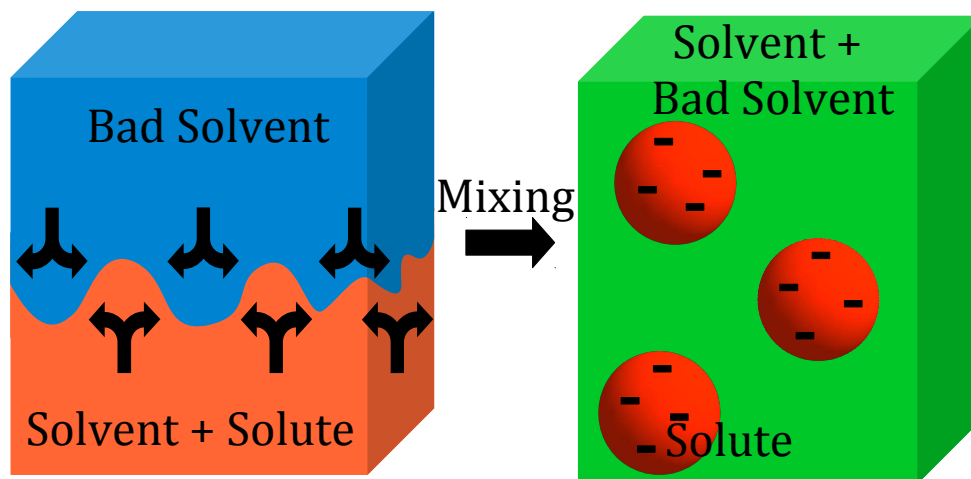


Figure 4.3: Mixing a solute/solvent mixture with a miscible bad solvent can lead to formation of solute droplets or particles. This solvent-shifting route couples a hydrodynamic step with a physicochemical step

and uncharged macromolecules are used, the particles are homogeneous. At lower mixing rates, the hydrodynamic step couples with the precipitation step. The diameter then increases with the solute concentration but still depends on the interdroplets repulsions. If mixtures of charged and uncharged macromolecules are used, the particles tend to have a core-shell structure as the different macromolecules start to precipitate at different water concentrations. This knowledge allows a better control of the solvent-shifting technique to elaborate model systems or more complex ones.

4.5 Destabilization pathways and barriers

4.5.1 Contact Ripening

Coalescence and Ostwald ripening are the two well-established mechanisms responsible for the destruction of emulsions. A few works have indicated that this textbook description did not seem to cover some experimental evidences. Contact ripening was postulated as an intermediate mechanism. Like coalescence the droplets must come at contact and like Ostwald ripening oil molecules are exchanged. This third mechanism is then clearly difficult to prove since it resembles the two other processes.

The existence of Contact Ripening is demonstrated in this work : using a very water-insoluble oil we monitored a fast exchange of isotopic oil molecules at constant droplet size. The study took great advantage of the emulsification method presented above since model monodisperse emulsions with no excess surfactant can be easily obtained. A fine structure variation of the oil and the surfactant structure was also easily performed thanks to the use of purified compounds.

Contact ripening is hindered by inter-droplets repulsions and thus favored in non-ionic

and/or concentrated systems. In the dilute regime a mean field approach is successful since the process is concentration independent. Like Ostwald ripening, a growth law $R_{mean}(t) \sim t^{1/3}$ is observed, although by different physical arguments. This is the reason for difficulties to distinguish between the two processes and probably explains many reported experimental deviations to the theory of Ostwald ripening for non-ionic systems. We show that Contact ripening is activated by dehydration of the surfactant, so that the oil can effectively permeates through the surfactant layers. It is also favored by short oil or surfactant chains.

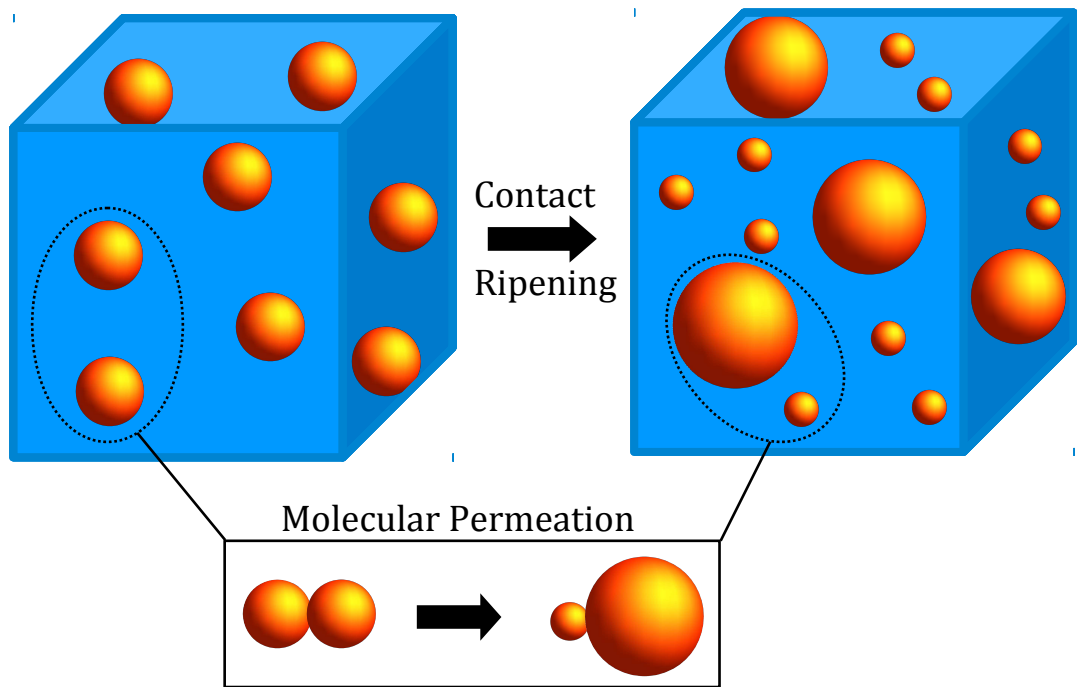


Figure 4.4: Contact ripening operates through permeation of oil molecules at contact of two droplets.

The identification and characterization of this new destabilization mechanism is essential to improve the formulation of emulsions. Even when the experimentalist takes great care to protect the emulsion from coalescence, with a strong surfactant barrier, or Ostwald ripening, with the use of long insoluble oils, contact ripening may still occur and destroy the emulsion.

4.5.2 Repulsion controlled coalescence

The field of nanoparticles synthesis covers a wide range of compositions and conditions but revolves around one goal : obtaining narrow populations. Indeed, the original properties at the nanoscopic scale are related to the size of the objects. To select a precise property, it is then necessary to select accurately the size. Low polydispersities are also a requirement to obtain colloidal crystals. Despite some experimental criticisms, the dominant frame to

design nanoparticles synthesis remains the nucleation and growth scheme. In this approach the solute will precipitate to form critical nuclei of a given size, which grow by molecular capture of solute.

To avoid the complications of chemical reactions we have used the solvent-shifting method to investigate the formation of nano-objects through precipitation. The hydrodynamics step was uncoupled using fast mixing. The first direct observation of the droplets recombinations was achieved. Through ultra-fast time-resolved scattering we observe that the number of droplets decreases with time, while they grow in size. This observation demonstrates that the droplets grow through a coalescence mechanism while it rules out a nucleation and growth mechanism. A novel growth law is identified :

- Logarithmic growth of the radius with time : $R_{mean}(t) \sim \ln(t)$
- Decreasing polydispersity with time : $\sigma R/R_{mean} \sim R_{mean}^{-1/2}$

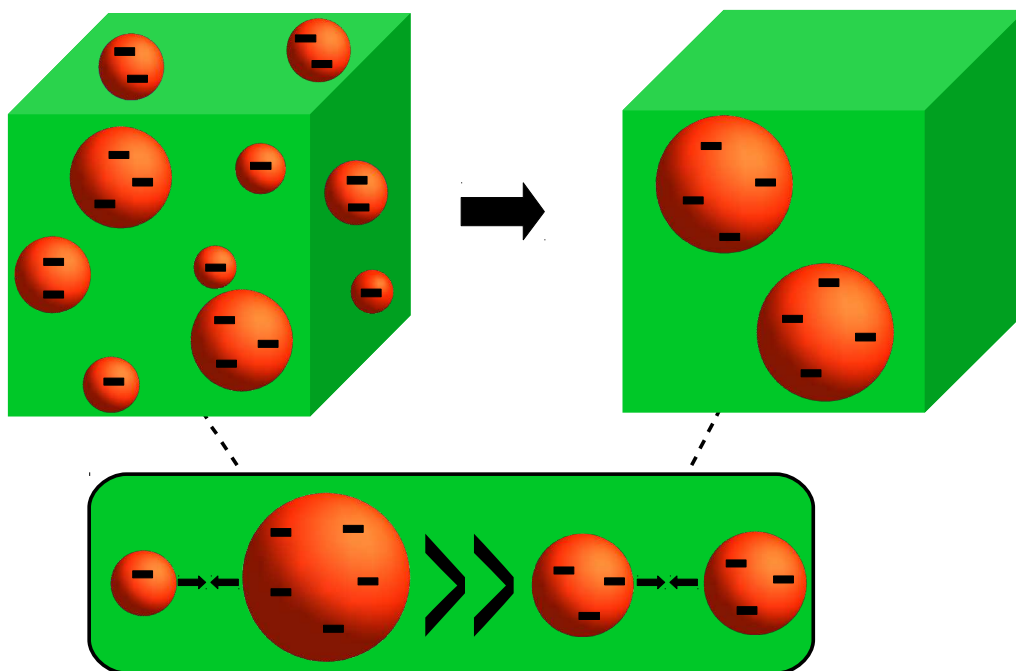


Figure 4.5: Coalescence limited by the approach of droplets follow an original growth law. The radius grows logarithmically with time at decreasing polydispersity. This is explained by a more probable small+large coalescence event than medium+medium.

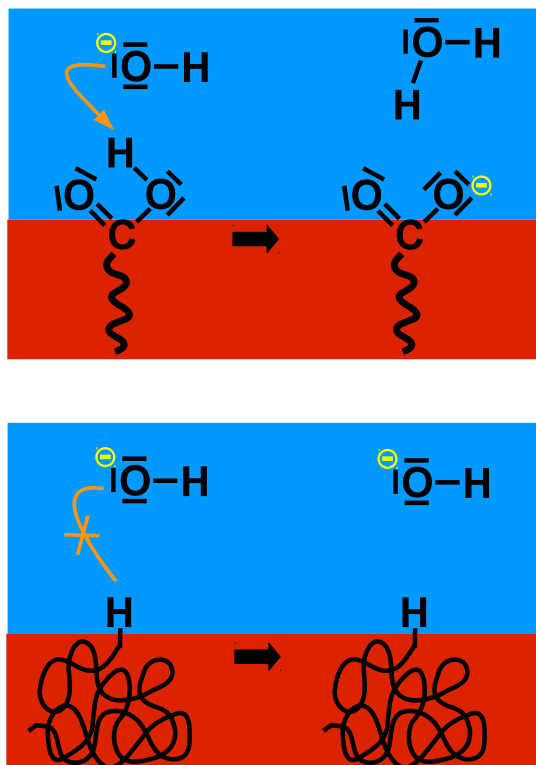
We thus demonstrate that coalescence can lead to narrow populations, if the limiting step is the approach of the droplets. This is the case for sparsely covered droplets which merge at contact. Though not very common in emulsions, it matches usual conditions of nanoparticles dispersions. A fully quantitative model is developed in this work. The core idea is that repulsions increase with increasing the size of the droplets. Encounters between a small and a large droplet are thus more probable than between two medium

droplets. As a result, the small droplets quickly coalesce and the short sizes tail of the distribution moves towards the large sizes tail faster than the mean size growth. This sequence is displayed in Figure 4.5 and leads to narrow populations.

In the colloidal domain diffusion-limited processes lead to a self-similar behavior of the size distribution (constant polydispersity during the growth), which corresponds in the theory of critical phenomena as the first-scaling law. In this work we identify for the first time in the colloidal domain the second-scaling law (decreasing polydispersity during the growth). This bridge between different domains of physics is also the key to reasoned designs of synthesis of nano-objects through precipitation methods.

4.5.3 Origin of repulsions in "surfactant-free" conditions

In a surfactant-poor regime, droplets are sparsely covered by surfactants. At contact there is thus no barrier to coalescence. However, if the surfactants are charged, ionic repulsions between droplets hinder coalescence. In the ultimate limit, the surfactant-free regime, the repulsion barrier should vanish and coalescence should just be limited by the rate of collisions of droplets.



However, for more than a century, observations of a pH-dependent and negative surface charge at supposedly pristine interfaces have been accumulated. The typical examples are air bubbles in water, purified oil droplets in water and polymer particles in water. Two communities have fought over a possible explanation. Both corresponding theories differ

in vocabulary but rest on subtle modifications of the water properties at an hydrophobic interface. One dominant expression has been the adsorption of hydroxide ion, another the unbalance in hydrogen-bonding.

In this work, we have entered the controversy by showing that all the experimental evidence could be explained by considering minute amounts of fatty acids impurities. This statement can be rephrased as the impossibility to reach surfactant-free conditions in emulsions. This conclusion has received two comments to which we have offered a reply where we demonstrate that polymer surfaces, build from uncharged macromolecules, are not charged and that the corresponding particles can never be stabilized. We thus prove that no alteration of the water structure next to a hydrophobic interface can provide sufficient ionic repulsions between colloidal objects.

Surfactant-free conditions can be obtained for dispersions of polymer particles in water. In this case, we have demonstrated that the surface charge is determined by the end-groups of the macromolecules. The end-groups are created at the initiation step, when the initiator react with a monomer. They are often ionizable functions (sulfate or carboxylate). Controlling the end-groups is usually not important for macroscopic properties of polymer materials but we have demonstrated that it is essential for colloidal properties, i.e. encounters between the particles. We also show that the number of end-groups is determined by the self-assembly process and thus measuring this number gives information on the formation process.

Chapter 5

Articles

1. Formation of 10-100 nm size-controlled emulsions through sub-PIT cycles,
Langmuir **2010**, K. Roger*, B. Cabane and U. Olsson
2. Emulsification through surfactant hydration : The PIC process revisited,
Langmuir **2011**, K. Roger*, B. Cabane and U. Olsson
3. Superswollen microemulsions stabilized by shear and trapped by a temperature quench,
Langmuir **2011**, K. Roger*, U. Olsson, M. Zackrisson, P. Lindner and B. Cabane
4. Why are hydrophobic/water interfaces negatively charged?,
Angewandte Chemie **2012**, K. Roger* and B. Cabane
5. Uncontaminated interfaces are uncharged : a reply,
Angewandte Chemie **2012**, K. Roger* and B. Cabane
6. Coalescence of repelling colloidal droplets : a route to monodisperse populations,
Langmuir **2013**, K. Roger*, R. Botet and B. Cabane
7. Surface charge of polymer particles in water : The role of ionic end-groups,
Langmuir **2013**, K. Roger*, M. Eissa, A. Elaissari and B. Cabane
8. Destabilization of emulsions through molecular permeation : Contact Ripening
Manuscript unpublished, K. Roger*, B. Cabane, R. Schweins and U. Olsson
9. The link between preferred curvature and nanoemulsion formation
Manuscript unpublished, K. Roger* and B. Cabane
10. Solvent-Shifting : hydrodynamics vs. precipitation
Manuscript unpublished, K. Roger*, C. Tang, B. Cabane and R. Prud'homme

Formation of 10–100 nm Size-Controlled Emulsions through a Sub-PIT Cycle

Kevin Roger,^{*,†,‡} Bernard Cabane,[†] and Ulf Olsson[‡]

[†]*PMMH, CNRS UMR 7636, ESPCI, 10 rue Vauquelin, F 75231 Paris cedex 05, France, and*

[‡]*Physical Chemistry, Lund University, P.O. Box 124, Lund S 22100, Sweden*

Received September 9, 2009. Revised Manuscript Received October 19, 2009

We have re-examined the phase inversion temperature (PIT) emulsification process. This is a low-energy method that uses a physicochemical drive to produce very fine oil/water emulsions in the absence of high shear flows. We used the polyoxyethylene 8 cetyl ether (C₁₆E₈)/hexadecane/water system, which has a PIT of 76.2 °C. We find that successful emulsification depends on two conditions. First, the mixture must be stirred at low speed throughout the whole process: this makes it possible to produce emulsions at surfactant concentrations that are too low to form an equilibrium microemulsion. Second, the stirred mixtures must be heated above a threshold called the clearing boundary (CB) and then quenched to lower temperatures. The clearing boundary is determined experimentally by a minimum in the turbidity of the stirred mixture, which results from solubilization of all the oil into swollen micelles. This matches the emulsification failure boundary, and it is expressed mathematically by the condition $R^*C_0 = 1$, where R^* is the radius that results from the oil/surfactant composition for monodisperse spheres and C_0 is the spontaneous spherical curvature of the surfactant. Thus, we show that such cycles do not need to cross the PIT. In fact, sub-PIT cycles and cross-PIT cycles give exactly the same result. These conditions lead to emulsions that have a narrow size distribution and a mean diameter controlled by the oil/surfactant ratio. The typical range of those diameters is 20–100 nm. Moreover, these emulsions have an excellent metastability, in contrast with emulsions made with shorter oil and surfactant molecules.

Introduction

Emulsions are usually dispersions of oil-in-water or water-in-oil. These dispersions are unstable, unless a surfactant is present. If surfactant molecules are adsorbed at the oil/water interfaces of an emulsion, they form a monolayer that opposes the recombination of interfaces and in this way they provide some metastability to the emulsion.¹ One of the most interesting questions in this field is the relation between the properties of the surfactant layer and those of the emulsion. For instance, the extension of the surfactant layer determines the spatial scale at which oil and water domains can be dispersed: if the emulsion is made by fragmenting large volumes of oil and water into very small droplets, these droplets will coalesce until they are fully covered by the surfactant layer (“surfactant limited regime”).² Moreover, the spontaneous curvature of the surfactant layer determines the probability of coalescence events involving oil droplets separated by a water film, or vice versa.³ There is a method for making emulsions that uses the properties of the surfactant layer in a particularly ingenious way. It is called the phase inversion temperature (PIT) method, because it employs surfactant layers that have a phase inversion temperature, such as the polyoxyethylene surfactants. At temperatures below the PIT, the spontaneous curvature of these surfactants is turned toward the hydrocarbon chain. In this condition, if surfactant/oil/water mixtures are dispersed by hydrodynamic forces, the Kabalnov-Wennerström (KW) theory³ demonstrates that oil droplets covered with surfactants will be

metastable, whereas water domains will coalesce to form a continuous aqueous phase. Conversely, at temperatures above the PIT, the spontaneous curvature of the surfactant layers is turned toward the polyoxyethylene chain. In this condition, water droplets covered with surfactants will be metastable, and a water/oil emulsion will be formed. The PIT method consists of making a water-in-oil emulsion at a high temperature, where it is metastable, and quenching that emulsion to a low temperature, where the spontaneous curvature of the surfactant yields metastability only to oil/water emulsions.^{4,5} It has been found by many workers that this process can yield oil/water emulsions made of extremely small droplets, sometimes in the 100 nm range.^{6–8} This is an extremely efficient way of dispersing oil-in-water, compared with the much coarser emulsions that are produced by the use of hydrodynamic shear (sizes in the 1–10 μm range) or even by the use of elongational flows (sizes in the 100–1000 nm range).⁹

Despite the fact that the PIT method is widely and successfully used, there is no real understanding of its mechanism. A common view is that the process uses a direct transformation of the high temperature water-in-oil emulsion into an oil-in-water emulsion: the temperature quench would cause the surfactant layer around the water droplets to invert its curvature, and this inversion would produce a fragmentation of the continuous oil phase into

*To whom correspondence should be addressed. E-mail: kevin.roger@ens-cachan.fr.

(1) Bibette, J.; Leal-Calderon, F.; Schmitt, V. *Emulsion Science*; Springer-Verlag GmbH: Heidelberg, Germany, 2007.

(2) Taisne, L.; Walstra, P.; Cabane, B. *J. Colloid Interface Sci.* **1996**, *184*, 378–390.

(3) Kabalnov, A.; Wennerström, H. *Langmuir* **1996**, *12*, 276–292.

(4) Shinoda, K.; Saito, H. *J. Colloid Interface Sci.* **1968**, *26*, 70–74.

(5) Shinoda, K.; Kunieda, H. In *Encyclopedia of Emulsion Technology*; Becher, P., Ed.; Marcel Dekker: 1983.

(6) Morales, D.; Gutiérrez, J. M.; Celma, M. J. G.; Solans, Y. C. *Langmuir* **2003**, *19*, 7196–7200.

(7) Morales, D.; Solans, C.; Gutierrez, J. M.; Garcia-Celma, M. J.; Olsson, U. *Langmuir* **2006**, *22*, 3014–3020.

(8) Förster, T.; Rybinski, W. V.; Wadle, A. *Adv. Colloid Interface Sci.* **1995**, *58*, 119–149.

(9) Walstra, P. *Chem. Eng. Sci.* **1993**, *48*, 333–349.

nanometer size droplets. There is, however, no direct evidence that would explain how this fragmentation would take place. Moreover, most PIT processes do require some hydrodynamic motions (stirring), which does not seem to make sense if the spontaneous curvature of the surfactant layers is the sole driving force for the inversion.

There is a variant of the PIT method that seems to be easier to understand. It takes place in mixtures that contain a higher surfactant concentration (volume fraction > 0.1). Then the surfactant may form small globular micelles that dissolve a substantial fraction of the oil; the radius of these swollen micelles is determined by the spontaneous curvature of the surfactant, and at temperatures near the PIT it may become so large that all the oil is solubilized in this micellar phase. Alternatively, the ternary system may form, near the PIT, a so-called microemulsion in which the surfactant film separates bicontinuous water and oil domains. When this single-phase state is quenched to temperatures much below the PIT, the micellar structure is retained, or the microemulsion is fragmented into small micelles.¹⁰ In either case, the final state after the quench is a metastable emulsion with a droplet size that matches the characteristic length of the initial microemulsion.

In this study, we wanted to find out whether there are really different mechanisms for the PIT processes that take place at low and at high surfactant concentrations. Thus, we used different initial conditions, with both high and low surfactant concentrations, and temperatures above and below the PIT. We also examined the effect of hydrodynamic shear and the effect of the rate of the quench. We did obtain emulsions with droplet sizes that could be prescribed by the composition of the ternary systems. Moreover, these emulsions had excellent metastability. There was only one condition for the success of the process, which was the selection of an initial temperature that had to be above a particular line in the phase diagram. With these results, we aimed to answer the following questions: (i) What is the nature of the line that separates successful from unsuccessful processes? How does it depend on the composition of the ternary system? (ii) What happens to the ternary surfactant/oil/water system upon crossing this line? (What transient states are formed at this stage, and what is the effect of hydrodynamic motions in these states?) (iii) Does the quench retain the structure of these transient states, and how does it provide them with metastability?

Experimental Section

Materials. The surfactants polyoxyethylene 5 dodecyl ether ($C_{12}E_5$) and polyoxyethylene 8 cetyl ether ($C_{16}E_8$) were obtained from Nikko Chemicals. The oils decane, dodecane, and hexadecane were bought from Aldrich. The purity of all those products was at least 99%. It must be emphasized that the use of very pure surfactants is extremely important. Indeed, less pure surfactants are mixtures of molecules with different alkyl and polyoxyethylene chain lengths, which may segregate in different parts of the systems or in regions of different interface curvature. In such cases, the phase behavior and the response to temperature changes could be completely different from that of the pure system. Deionized water (Milli-Q) was produced in the laboratory and controlled at regular intervals.

The surfactant/oil/water mixtures were prepared as follows. The components were weighed in a small 4 mL glass bottle, and a small magnetic stirrer was added. The closed bottle was immersed in a temperature regulated water bath and stirred at 100 rpm. The precision of the temperature regulation was ± 0.2 °C.

Methods. The experiments consisted of temperature cycles (heating, steady state, quench) for stirred and unstirred samples. The conditions for a successful cycle were as follows: (i) spatial variations of the composition must be kept small, in the steady state and during the quench, and (ii) the quench must be fast. These conditions were met by using small samples, with a constant volume, and keeping them stirred during the steady state and also during the quench. In a typical cycle, the sample (1 mL) was equilibrated at a chosen temperature in the water bath, with constant stirring. Then it was quickly transferred (≤ 1 s) to an ice-salt bath that had a temperature of -10 °C. It was stirred in this cold bath until its temperature was approximately 25 °C. Finally, it was removed from the bath, stirring was stopped, and it was transferred to a small plastic cell for visual observation, turbidity, and light scattering measurements. In this last case, most samples were diluted before the measurement (typically by a factor 100).

During the cycles and immediately afterward, visual observations made it possible to assess the turbidity or opalescence of the samples and obtain a rough estimate of their mean droplet sizes, provided that these sizes were not too polydisperse. Indeed, samples containing small droplets (20 nm) were transparent. Larger droplets (80 nm) gave a typical Rayleigh scattering (blue when scattered in the perpendicular direction and red in the transmitted direction). Still larger ones (150 nm) gave Mie scattering (milky). In samples equilibrated at rest, visual observations were also made to count the number of phases. We could distinguish between one-phase (microemulsion or lamellar phase), two-phase aqueous micellar solution plus excess oil (Winsor I), two-phase oil continuous microemulsion plus excess water (Winsor II), or three-phase (Winsor III) coexistences. Turbidity measurements were performed with a Varian spectrophotometer through the comparison of the incident light intensity I_0 to the transmitted light intensity I . Dynamic light scattering measurements were performed using a Malvern Zetasizer NS instrument. This instrument analyzes the autocorrelation of the backscattered intensity. The software uses this autocorrelation function together with a model for the diffusion of Brownian particles to calculate a distribution of particle diameters. The size distributions given in the Results section were taken directly from the intensity averaged distribution calculated by the instrument and in one case from the number averaged distribution. For broad or bimodal distributions, this intensity average has the disadvantage of weighting heavily the contribution from the large particles. For unimodal distributions, we calculated the following averages: (i) The mean diameter: $d_{\text{mean}} = \sum_i d_i I_i / \sum_i I_i$, where I_i is the percentage of intensity for a diameter d_i . (ii) The polydispersity which is defined as the standard deviation divided by the mean diameter: $e = (\sum_i d_i^2 I_i / \sum_i I_i - d_{\text{mean}}^2)^{1/2} / d_{\text{mean}}$. The reproducibility of our results was excellent (error typically below 2%).

Results

In this section, we first describe the equilibrium states of the water/hexadecane/ $C_{16}E_8$ system. Some of these states are used as starting points to produce the nanometric emulsions, and some are the end points toward which the system tends to evolve. Then we present the effect of shear (stirring), which produces unexpected results (fragmentation to nanometric sizes) in the region near the PIT. Next, we report experiments in which these transient nanometric emulsions have been quenched to temperatures far below the PIT, and we provide a full characterization of these emulsions. Finally, we report how these quenched emulsions evolve in time. These results are summarized in Figure 1, which shows images of this water/oil/surfactant system at each one of these stages.

Equilibrium Phases. The classical way to describe the equilibrium states of a multicomponent system is to draw a phase diagram, in which the locations of the thermodynamic phases and

(10) Taisne, L.; Cabane, B. *Langmuir* **1998**, *14*, 4744–4752.

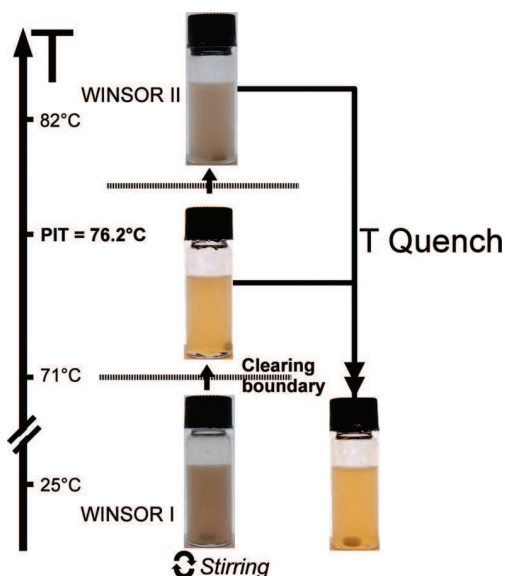


Figure 1. Photographs of the main states for a sample made at oil/surfactant $S = 3$ and oil/water $W = 0.2$, according to stirring, temperature, and thermal history. The left row presents the steady states of systems that were equilibrated at a set temperature and stirred continuously. The middle one has a low turbidity. The sample on the right-hand side had been equilibrated at a temperature above the “clearing boundary” under constant stirring and quenched to a low temperature; it has the same low turbidity as the samples just above the “clearing boundary”.

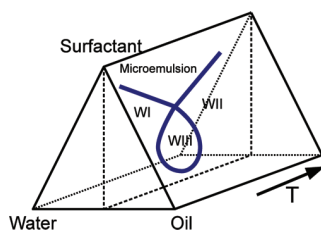


Figure 2. Phase prism and its section at a constant oil/water ratio. In this section, the phase boundaries, indicated as thick blue lines, have the classic fishlike pattern.

of their boundaries are traced according to the composition variables and to temperature. For a water/oil/surfactant system, there are two independent composition variables, that is, the oil/water mass ratio, W , and the oil/surfactant mass ratio, S . In this work, we chose to remain at a constant oil/water ratio $W = 0.2$, for it yields emulsions that are concentrated enough yet not too viscous. This corresponds to the selection of one plane cut across the phase prism (Figure 2). In this plane, the states of the system are determined by the oil/surfactant ratio and by temperature. Extensive studies by Kahlweit and co-workers of systems containing a polyoxyethylene surfactant have shown that their phase diagrams have a common shape, the so-called Kahlweit fish.¹¹ We have determined the corresponding phase diagram for the water/hexadecane/ $C_{16}E_8$ system through visual inspection of the samples (Figure 3).

A practical way to read this phase diagram is to follow the experimental paths, that is, choose a surfactant concentration and examine the effect of temperature. If a low surfactant fraction is chosen, below 0.054 for our system, then at low temperature the system separates into a normal micellar phase and an oil phase

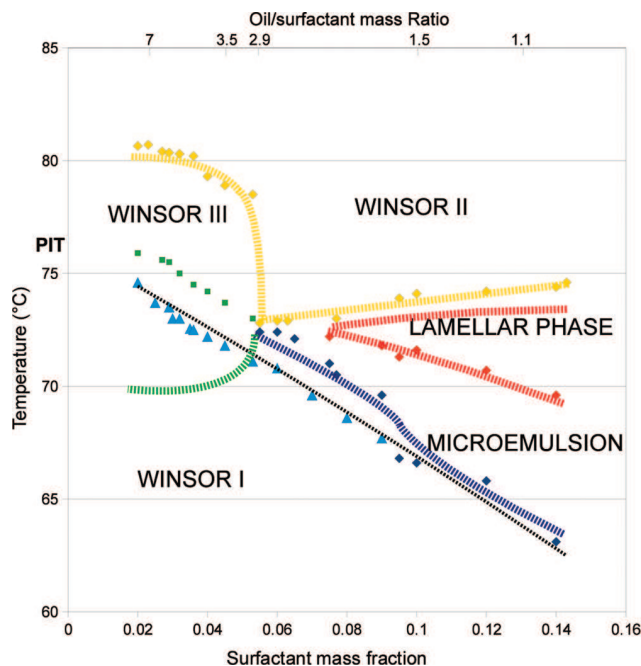


Figure 3. A cut through the phase prism of the water/hexadecane/ $C_{16}E_8$ system at constant oil/water ratio $W = 0.2$. The red, blue, and yellow tilted squares indicate phase boundaries of samples at rest, determined visually with a precision of 0.4 °C. The dashed lines indicate the usual locations of the boundaries. The blue triangles indicate the position of the “clearing boundary”, determined according to the turbidity minimum of the stirred samples (see text). The green squares correspond to the fast separation into a three phase coexistence.

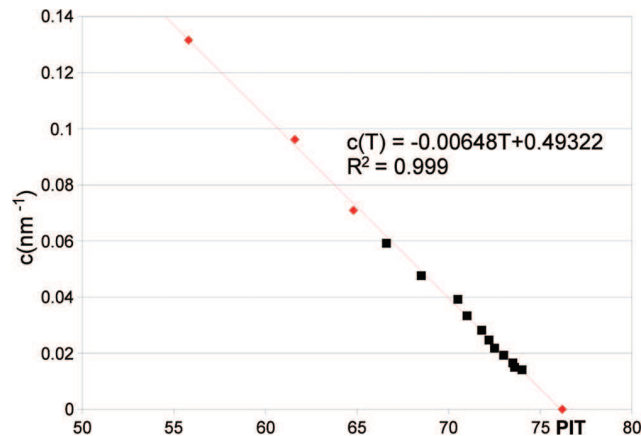


Figure 4. Temperature variation of the spontaneous spherical curvature of the surfactant. Horizontal scale: temperature (°C); the PIT has been determined as the temperature of the critical point for a composition such that the oil/water ratio equals 1. Vertical scale: curvature C calculated as $2/D$, where D is the equilibrium hydrodynamic diameter of the swollen micelles (Winsor I). The black squares are calculated from the diameters of the nanometric emulsions formed by stirring at temperatures above the clearing boundary (see text below).

(Winsor I). At intermediate temperatures, near the PIT, three separate phases coexist, that is, an aqueous phase, a microemulsion, and an oil phase (Winsor III). Finally, at high temperature, there are again two phases in coexistence, a reverse micellar phase and an aqueous phase (Winsor II). If a high surfactant concentration is chosen, above 0.054 for our system, the sequence is similar, but at intermediate temperatures the system is in a single

(11) Kahlweit, M.; Strey, R.; Haase, D.; Firman, P. *Langmuir* **1988**, *4*, 785–790.

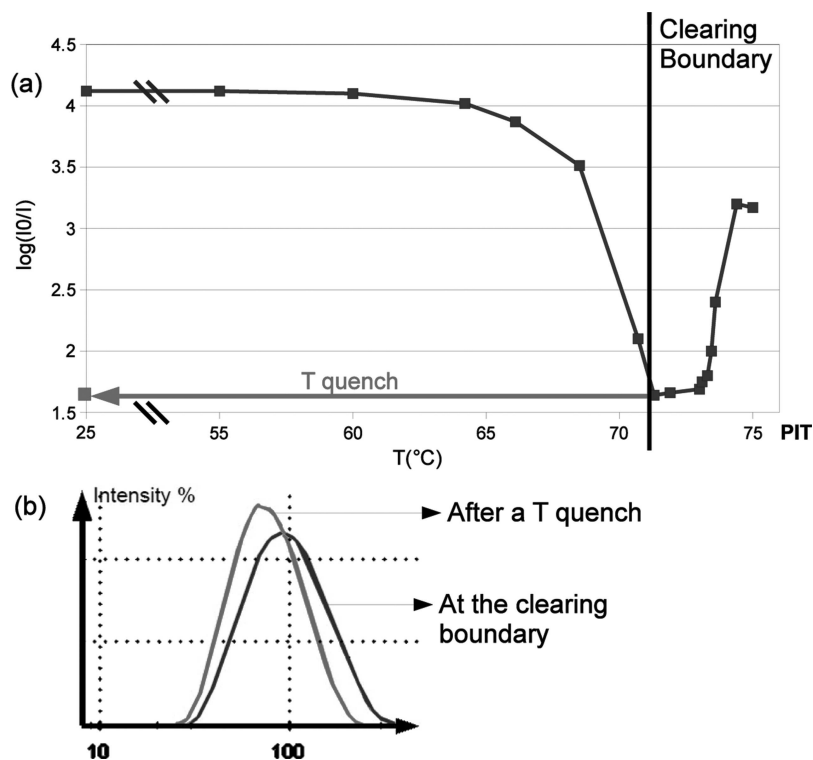


Figure 5. (a) Turbidity of stirred mixtures made at $S = 3$. Horizontal scale: temperature ($^{\circ}\text{C}$). Vertical scale: $\log(I_0/I)$. High turbidity at low temperatures reflects a micellar solution in equilibrium with big droplets, whereas low turbidity reflects a homogeneous population of droplets with nm sizes. (b) Size distributions measured at the clearing boundary and after the quench from this boundary to 25 $^{\circ}\text{C}$. Both states have similar size distributions and identical turbidities as indicated by the lower arrow in (a). The small shift in the size distributions is due to the fast destabilization when stirring is stopped for the dynamic light scattering measurement and nondiluted conditions for this measurement at T_{CB} .

microemulsion phase (Winsor IV) or a single lamellar phase, or else in a mixture of these two phases. There is one surfactant concentration, at the boundary of these two ranges, for which the system crosses directly from a Winsor I coexistence to a Winsor II coexistence. According to Kahlweit, the point at which this transition occurs is the unique connection between the Winsor III and Winsor IV regions of the phase diagram. Finally, at very low surfactant concentrations, the system also crosses directly from Winsor I to Winsor II coexistence. If the PIT is defined as the temperature of the critical point for a composition such that the oil/water ratio equals 1, then similar experiments can be realized to obtain this value from the corresponding phase diagram. It indicates that $\text{PIT} = 76.2 \pm 0.4^{\circ}\text{C}$. This method is generally valid when using a pure surfactant, since the PIT is then independent of the surfactant concentration.

In the micellar phase that separates out of the Winsor I region, we used dynamic light scattering to measure the diameter of swollen micelles, assuming that they retain a spherical shape at all temperatures. Since these swollen micelles coexist with excess oil, their equilibrium diameter D is determined by the spontaneous spherical curvature C of the surfactant monolayer. Therefore, we can determine C as $2/D$. We found that $2/D$ varies linearly with temperature and that the variation extrapolates to zero curvature at the PIT defined as above (Figure 4).

Steady State of Stirred Samples. The key to the mechanism of emulsion formation at nanometer scales was provided by experiments in which the equilibrium mixture (e.g., micellar phase plus oil phase) was stirred with a simple magnetic stirbar. As shown in Figure 1, stirring the mixture at low temperature produced a coarse emulsion, recognized by its high turbidity. However, stirring the mixture (micellar phase plus oil phase) at

temperatures near the upper boundary of the Winsor I region produced a nearly transparent liquid, indicating that the large emulsion drops have been fragmented. Figure 5 presents systematic measurements of the turbidity of a stirred mixture as a function of temperature. It shows that the turbidity becomes 300 times smaller upon approaching a temperature T_{CB} . Therefore, the droplet sizes become nanometric (below 100 nm, by comparison with the turbidity of quenched nanometric emulsions, see below). This experiment was repeated at different oil/surfactant ratios, and we define an additional boundary which we call the “clearing boundary”; its location is indicated in the phase diagram (Figure 3).

Quenched Emulsions. The nanometer-size emulsions produced by stirring at temperatures above the “clearing” boundary T_{CB} were *unstable*: when stirring was discontinued, they separated spontaneously into a set coexistence of two or three phases, as indicated by the phase diagram. However, we found that these emulsions could become *metastable* if they were quenched to a temperature that was at least 17 $^{\circ}\text{C}$ below the PIT for this system, according to the general scheme indicated in Figure 1. The “standard” quench process was performed by selecting a sample stirred at a temperature above T_{CB} , quickly transferring the stirred sample to an ice-salt bath and keeping it stirred in the bath until its temperature was below 25 $^{\circ}\text{C}$, as described in the Methods subsection. These quenched emulsions remained nearly transparent (they had the same turbidity, see Figure 5, and size distributions as the sample at the clearing boundary), and their droplet size distributions could be measured using dynamic light scattering. These measurements required a dilution of the samples with water, since the light scattering from concentrated emulsions measures a collective diffusion coefficient that differs

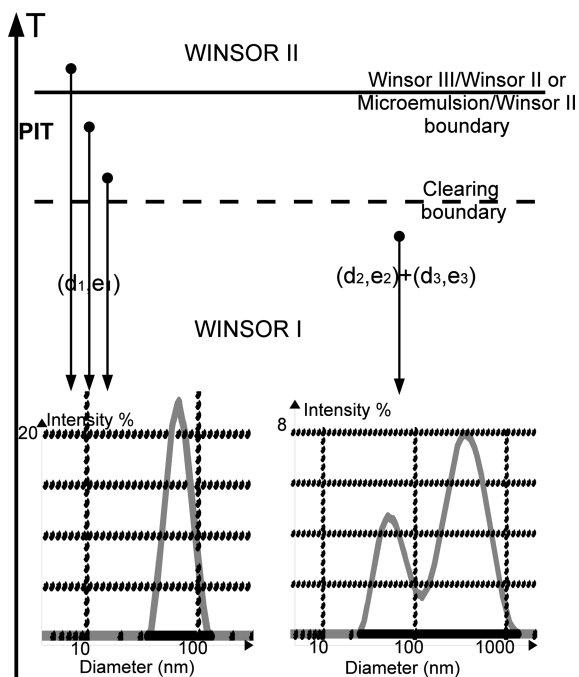


Figure 6. Comparison of the droplet size distributions for samples stirred at temperatures above T_{CB} and below T_{CB} and quenched to a temperature approximately $50\text{ }^{\circ}\text{C}$ below the PIT. Composition $W = 0.2$, $S = 3.5$. Systematic measurements of the final size distribution and polydispersity were performed for a set of samples prepared at composition $W = 0.2$, $S = 3.5$ (Figure 7). They show that the same final state was obtained regardless of the initial temperature as long as (a) the initial temperature was above T_{CB} and (b) stirring was continued during the quench. If the initial temperature was below T_{CB} , then the quenched samples contained two populations, one with sizes comparable to those of the equilibrium micelles formed at the initial temperature and the other one with much large sizes, which creamed very quickly.

from the single droplet self-diffusion. Measurements on diluted emulsions gave results that were stable, reproducible, and independent from the final oil/water ratio, thereby demonstrating that the stir-quenched emulsions were made of oil-in-water droplets. The droplet size distributions of emulsions that were stir-quenched and diluted reflected the initial state of the stirred emulsion, which was set by composition and initial temperature. Figure 6 presents the size distributions of emulsions that were prepared at a composition to the left-hand side of the phase diagram, stirred at different temperatures and stir-quenched to a temperature approximately $50\text{ }^{\circ}\text{C}$ below the PIT. A single population of droplets, with sizes below 100 nm , is obtained for all quenches that started from a temperature above T_{CB} (Figure 7).

The importance of stirring before and during the quench was demonstrated by an experiment in which the sample was placed in a very thin flat cell ($\sim 1\text{ mm}$), equilibrated at rest at a temperature above T_{CB} , and then quenched without any agitation. In this case, a coarse emulsion was obtained regardless of the initial temperature. This failure to fragment the original state was also observed if the initial state was a water/oil emulsion, against expectations that the change in spontaneous curvature would cause a spontaneous “inversion” of the emulsion structure.

Similar results were obtained with samples that had different compositions. Experiments with different oil/water ratios show that the emulsions have exactly the same size distributions if typically $W \leq 0.5$. Hence, it was interesting to find out how the droplet size varied with the other composition variable which is the

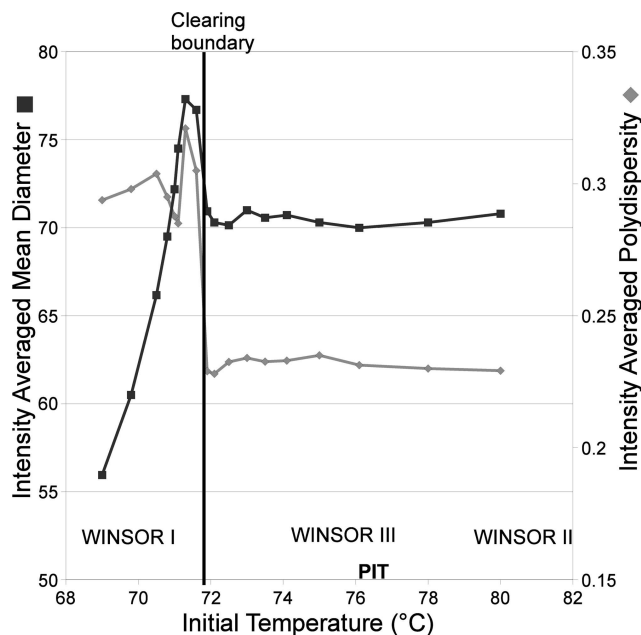


Figure 7. Mean size and polydispersity of emulsions stir-quenched from different initial temperatures to $T = 25\text{ }^{\circ}\text{C}$. Composition $W = 0.2$, $S = 3.5$. For initial temperatures below the clearing boundary, a bimodal distribution is obtained after the quench, whereas for initial temperatures above the clearing boundary a unimodal distribution is obtained after the quench, as shown in Figure 6.

oil/surfactant ratio. For this purpose, a set of samples were prepared with very different ratios, ranging from $S = 1$ to 7 (unimodal distributions were not obtained if $S > 7$). Since this set contains compositions that form a single phase microemulsion and others that separate according to the Winsor III coexistence, they were stirred at $T = 80\text{ }^{\circ}\text{C}$, above the PIT, in the Winsor II region where all of them formed water/oil emulsions, and then quenched to $25\text{ }^{\circ}\text{C}$. Figure 8 presents the variation of the number averaged mean diameter with the oil/surfactant ratio S . This variation is linear and does not show any discontinuity between samples that form a single phase microemulsion at intermediate temperatures and others that separate according to the Winsor III coexistence.

Metastability of Quenched Samples. The quenched emulsions were metastable, in contrast to their initial state that was unstable. Hence, there was a strong temperature dependence of the stability. In order to evaluate this dependence in a quantitative way, four quenched emulsions ($S = 2, 2.5, 3,$ and 3.5) were heated slowly ($0.5\text{ }^{\circ}\text{C}/\text{min}$), and the turbidity was measured during each temperature scan. In each case, the turbidity remained low and nearly constant up to $T = 59\text{ }^{\circ}\text{C}$, and then, above $T = 59\text{ }^{\circ}\text{C}$, the turbidity rose rapidly, indicating a fast coarsening of the emulsion (Figure 9).

In the range of temperatures below $59\text{ }^{\circ}\text{C}$, where a good metastability was obtained, the quenched emulsions made with $C_{16}E_8$ and hexadecane evolved very slowly. Quantitative measurements of this ripening were performed using samples containing dodecane as the oil, since the ripening time scales were hours in this case, instead of days for those containing hexadecane (see Figure 10). Quenched emulsions prepared at $W = 0.2$ and $S = 1$ were kept at $25\text{ }^{\circ}\text{C}$ in the light scattering instrument after dilution. Figure 10 presents the evolution of the mean size and of the polydispersity. This evolution occurs in two stages: there is a first stage in which the mean size remains approximately constant and the polydispersity increases, and then a second stage in which the mean sizes grows and the polydispersity decreases. The law for the

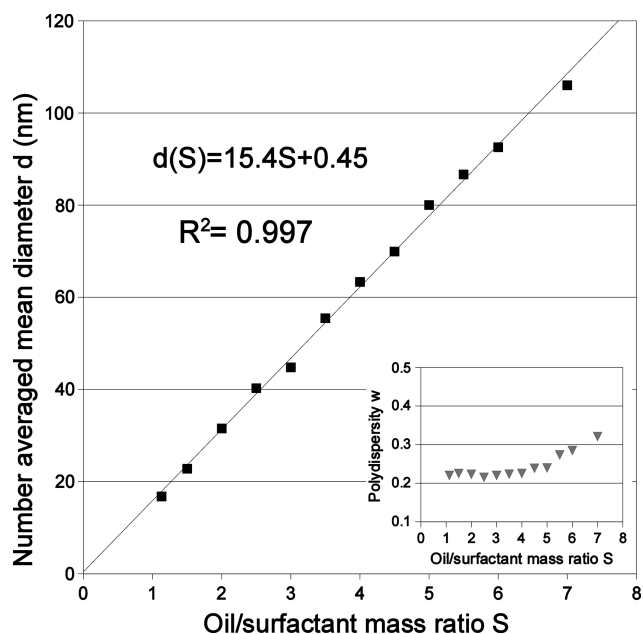


Figure 8. Mean diameter of the stir-quenched emulsions according to oil/surfactant ratio S . All samples were stirred at 80 °C, above the PIT, in the Winsor II region where all of them formed water/oil emulsions, and then quenched to 25 °C. During the quench, samples at $S < 2.9$ went through a single phase micro-emulsion, whereas samples at $S > 2.9$ went through a Winsor III coexistence. The absence of any discontinuity between these ranges indicates that the “transient state” that determines the final structure is the same in both cases.

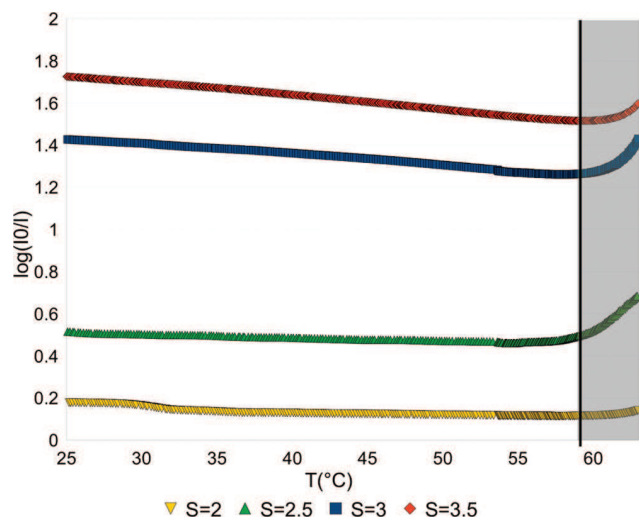


Figure 9. Turbidity of emulsions that were stir-quenched at 25 °C and then heated at 0.5 °C/min, as indicated on the horizontal scale. Vertical scale: $\log(I_0/I)$.

growth of the mean diameter appears to be a power law, though the exponent is not the one expected for the Ostwald ripening mechanism. The induction time increases with droplet size and in every case the absolute rate of growth is much too fast for a mechanism that depends on the transfer of dodecane molecules across the aqueous phase.

Comparison with Other Water/Oil/Surfactant Systems. Similar experiments were performed with systems containing shorter oil molecules (decane or dodecane instead of hexadecane) and/or shorter surfactants ($C_{12}E_5$ instead of $C_{16}E_8$). The equilibrium

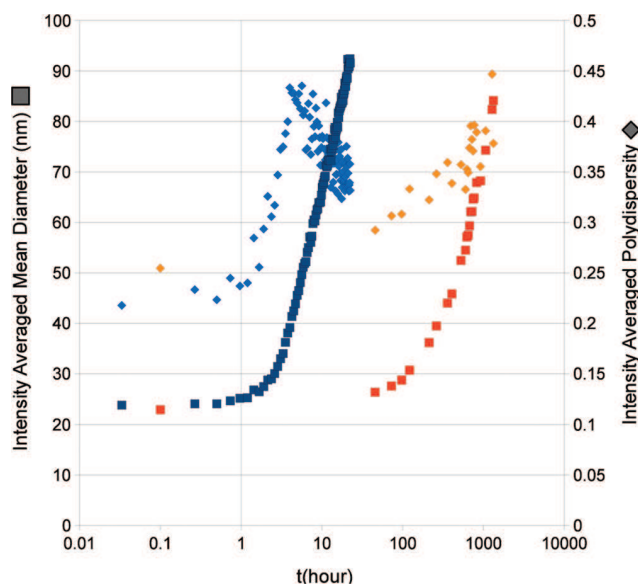


Figure 10. Evolution of the mean size and polydispersity of an emulsion made of water, dodecane, and $C_{16}E_8$ (blue/black symbols) and of an emulsion made of water, hexadecane, and $C_{16}E_8$ (red/gray symbols), stir-quenched to 25 °C and stored at 25 °C.

Table 1. Temperatures of the “Clearing” and “Metastability” Boundaries for Systems with Different Oils or Surfactants at $S = 3$, $W = 0.2$

| boundary | dodecane/ $C_{12}E_5$ | dodecane/ $C_{16}E_8$ | hexadecane/ $C_{16}E_8$ |
|---------------|-----------------------|-----------------------|-------------------------|
| metastability | 25.5 | 55 | 59.3 |
| clearing | 40.7 | 62.6 | 71.1 |

phases were the same (excepted for the lamellar phase, which was absent in the case of $C_{12}E_5$), and the phase diagram was essentially shifted to lower temperatures. Table 1 presents the values of the clearing and metastability boundaries for different systems at $S = 3$. The key experimental observations were the same. The phase mixtures formed at T_{CB} , slightly below the PIT, were fragmented to nanometer scales by the application of simple stirring. Thus, it is possible to extend to those systems the clearing boundary concept. This fragmented state was an unstable emulsion, since it was maintained only under stirring. However, these emulsions could also become metastable if they were quenched to sufficiently low temperatures, thus making it possible to also extend to those systems the metastability boundary concept. The metastability that was achieved through the quench was determined essentially by the length of the surfactant and the oil molecule: longer oils and longer surfactants yielded emulsions that had a much better metastability, for example, weeks for hexadecane, days for dodecane, and hours for decane (see Figure 10). Accordingly, all our results on the hexadecane/ $C_{16}E_8$ system can be transposed to similar oil/ C_nE_j systems, with different temperatures scales and different kinetics.

Discussion

The aim of this discussion is to decide on a mechanism, that is, a succession of nonequilibrium states that bring the system from its initial state to its final state. For this purpose, we first examine the range of final states that we can reach and the types of pathways or “cycles” that make it possible to reach them. This leads us to discriminate between the mechanisms that require sub-PIT cycles and those that require cross-PIT cycles, and also those that require shear and those that do not.

Size-Controlled Nanometric Emulsions. We have obtained nanometric-size emulsions with prescribed droplet diameters and a low polydispersity by tuning a single composition parameter: the oil/surfactant ratio S . Indeed, Figure 8 shows that the mean diameter evolves linearly with S , and the insert shows that the distribution of droplet sizes around the prescribed diameter is narrow, and similar experiments (not reported here) show that the oil/water ratio W has no effect on the mean size. In order to obtain these emulsions, we only need to stir-heat the samples just above the “clearing boundary”, which is defined by the minimum in turbidity (see Figure 5), and then stir-cool it quickly far below this boundary (temperature quench, see Figure 1). Since the “clearing boundary” is located a few degrees below the PIT, we call this process a sub-PIT cycle, in contrast with the cross-PIT cycles that were used in previous work.^{4–8} Figure 7 shows that identical final states are obtained regardless of the upper temperature of the cycle, provided that it is above the “clearing boundary”. Therefore, the PIT process does not require an inversion of the spontaneous curvature, nor a “phase inversion” from water-in-oil to oil-in-water. However, the processes that we have used do require the use of hydrodynamic shear. Moreover, the “final states” have the required metastability only if sufficiently long oil and surfactant molecules are used (see Figure 10). In the following discussion, we try to understand how these conditions (upper temperature > “clearing boundary”, shear) are related to molecular parameters of the system.

The Clearing Boundary. First, we investigate the nature of this boundary, which separates successful cycles (upper temperature $T_{\max} > T_{\text{CB}}$) from unsuccessful ones. Experimentally, it corresponds to the turbidity minimum of the steady state obtained under stirring. This turbidity minimum must originate from a particular size distribution of oil droplets (since results obtained at very low oil/water ratios are the same, we know that all samples are made of oil droplets in an aqueous phase). From Figure 5, we see that the turbidity and the size distribution of this steady state are the same as those of the emulsion obtained after a temperature quench. In particular, the mean radii are the same:

$$R_{\text{CB}} = R_{\text{quenched}} \quad (1)$$

This relation is helpful, because we have measured R_{quenched} with a very good precision. According to Figure 4, the mean radii of the quenched emulsions (black squares) are exactly equal to the equilibrium radii R_{eq} expected from measurements on equilibrium micelles, extrapolated to the PIT (red tilted squares). Hence, the following relation must hold:

$$R_{\text{CB}} = R_{\text{quenched}} = R_{\text{eq}} \quad (2)$$

Through this relation, we can determine the position of the clearing boundary in the phase diagram. On the one hand, we have determined how R_{quenched} varies with the oil/surfactant mass ratio $S = m_o/m_s$, where m stands for mass fraction. According to Figure 8, this variation is

$$R_{\text{quenched}} = K \frac{m_o}{m_s} = K' \frac{(1 - m_s)}{m_s} \quad (3)$$

On the other hand, we know that the equilibrium curvature of the surfactant varies linearly with temperature. The coefficient of this relation has been determined in Figure 4:

$$1/R_{\text{eq}} = C_0 = \beta(\text{PIT} - T) \quad (4)$$

If the temperature T is that of the clearing boundary T_{CB} , then both eqs 3 and 4 must hold, and therefore, there must be the

following relation between T_{CB} and m_s :

$$K'\beta(\text{PIT} - T_{\text{CB}}) = \frac{m_s}{(1 - m_s)} \quad (5)$$

Since m_s is small, this is practically a linear relation. We have traced the corresponding curve in the phase diagram (Figure 3). By construction, this line goes through the temperatures T_{CB} measured with stirred samples that have different surfactant concentrations, and it extrapolates at the PIT for $m_s = 0$. More interestingly, at higher surfactant concentrations, it matches the lower boundary of the microemulsion phase.

$$R^*C_0 = 1$$

These relations are so simple that they must have a geometrical interpretation. This can be derived from the assumption that the samples at the clearing boundary consist of a monodisperse population of oil droplets, covered with surfactant (i.e., swollen micelles). For a spherical oil droplet covered with a thin surfactant layer of thickness l_s , the radius R^* is determined by the surfactant and oil concentrations:

$$R^* = 3l_s \frac{V_o}{V_s} = 3l_s \frac{m_o}{m_s} \frac{\rho_s}{\rho_o} \quad (6)$$

where V is the volume, m is the mass, and ρ is the density. This equation describes the data presented in Figure 8 quite accurately; the measured slope is 15.4 nm, compared with an expected value of 15.1 nm according to data from ref 12, indicating that the area per surfactant molecule remains constant. Hence, eqs 2 and 6 express the fact that the system at the clearing boundary has become a collection of nearly monodisperse spheres, and that these spheres are covered by surfactant at a constant area per surfactant molecule (l_s is constant). Then relation 2 expresses the fact that, at the clearing boundary, the radius of these spheres matches the equilibrium curvature:

$$R^*C_0 = 1 \quad (7)$$

Then what happens at other temperatures, where C_0 changes? At lower temperatures, C_0 is higher, which imposes a smaller value of R :

$$R_{\text{eq}} = 1/C_0 < R^*$$

Then, according to the first part of eq 6, the volume of oil per swollen micelle must be reduced. Since the total amount of oil is constant, some oil must be released to another population of drops: this is the origin of the double population shown in Figure 6 for samples quenched from $T < T_{\text{CB}}$. This population must have very large diameters, since very little surfactant is available to cover their surfaces, and hence, their contribution to the turbidity must be large. According to this interpretation, the clearing boundary is indeed the temperature at which the population of large drops vanishes, due to increased solubilization of oil by the micelles. It is the same as the “emulsification failure” boundary defined by Safran and Turkevich.^{13,14} Another interesting question is what happens at temperatures higher than T_{CB} , where C_0 is lower, and a larger value of R would be needed to minimize the curvature free energy. However, there is no excess oil available; hence, the micelles must retain the sizes set by eq 6 (which is again

(12) Hamada, N.; Einaga, Y. *J. Phys. Chem. B* **2005**, *109*, 6990–6998.

(13) Safran, S.; Turkevich, L. *Phys. Rev. Lett.* **1983**, *50*, 1930–1933.

(14) Safran, S. *Statistical Thermodynamics of Surfaces, Interfaces and Membranes*; Westview Press: Boulder, Colorado, 1994.

the behavior predicted by Safran), and the turbidity must remain constant. We conclude that the relation $R^*C_0 = 1$, modeling the clearing boundary, shows that the stirred steady state at the clearing boundary is obtained from the equilibrium state by a solubilization process into spherical micelles with a radius that matches the spontaneous spherical curvature.

The Effect of Shear. The phenomenon described in the previous sections is a complete solubilization of the oil by swollen micelles at the clearing boundary. This phenomenon takes place in stirred samples only. In samples kept at rest, at the clearing boundary, the swollen micelles release some oil to a macroscopic oil phase (and at very long equilibration times, this might yield to a three-phase coexistence). Thus, hydrodynamic shear is necessary to prevent phase separation. A really interesting question is how shear achieves this result: does it break up the macroscopic phases into drops that have a size determined by the intensity of the shear (a simple mixing effect) or does it shift phase boundaries so that the single phase microemulsion replaces the two- or three-phase coexistence regions? The first option can be expressed in other terms: is the very low surface tension, as we are close to the PIT, responsible for the formation of the state obtained under stirring at T_{CB} ? There are three pieces of experimental evidence that can be used to answer these questions. (1) At all temperatures below T_{CB} , the system is composed of two populations: swollen micelles and large oil droplets. Upon approaching the clearing boundary, these two populations do not merge. In particular, the average size of the large oil droplets remains above 500 nm (see Figure 6). (2) If the formation of unimodal emulsions through temperatures cycles (sub-PIT or cross-PIT) was the result of fragmentation in conditions of low interfacial tensions, then it would be expected that the mean droplet diameter would depend on the shear rate. This is not the case. (3) For systems with very low surfactant concentrations ($S > 7$), the clearing boundary no longer exists and there are no temperature cycles that yield unimodal emulsions, regardless of shear rates, even though interfacial tensions are still vanishingly low near the PIT.

Only the second option (shear extends the domain where the microemulsion is the favored state) is consistent with the observation that all the oil can be solubilized, at the clearing boundary, by a monodisperse population of swollen micelles with sizes that are determined by the condition $R^*C_0 = 1$.

Transient State. It is now important to explain why the same final states (nanometric emulsions) have been obtained using cycles that heat up the sample above the clearing boundary only (sub-PIT cycles), compared with cycles that heat up above the PIT (cross-PIT cycles). Indeed, Figure 7 shows that the mean diameters of the quenched emulsions are the same regardless of the upper temperature T_{max} of the cycle, provided that $T_{max} > T_{CB}$. Moreover, the size distributions are also the same, as indicated in Figure 5. These results demonstrate that all these cycles go through a common transient state and that the structure of this transient state is conserved in the final state. The only state that meets these conditions is the stirred steady state at the clearing boundary. Therefore, when quenching a sample from $T_{max} > T_{CB}$, its structure reverts to the droplet structure of the transient state that meets the condition $R^*C_0 = 1$. This structure is conserved through the quench. A summary of the different significant microstructures that occur at different temperatures is presented in Figure 11.

Quench and Metastability. The only difference between the transient state (stirred steady state at T_{CB}) and the quenched

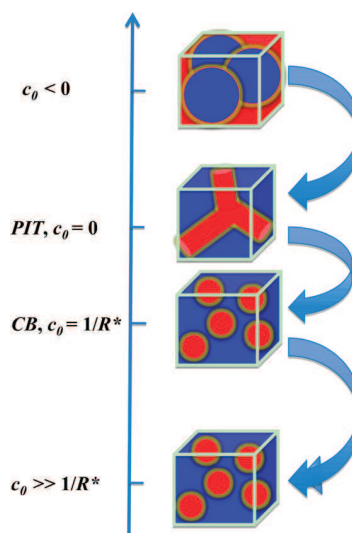


Figure 11. Summary of the different significant microstructures that occur at different temperatures. Above the PIT, the system forms a water-in-oil emulsion. When this emulsion is cooled, a rapid droplet coalescence results in a bicontinuous structure around $T = PIT$. Upon further cooling, the preferred curvature increases and the surfactant film closes around the oil, forming globular oil-in-water droplets. This occurs around $T = T_{CB}$, corresponding to $R^*C_0 = 1$. In this state, the droplets may still experience some coalescence when C_0 is small. However, upon cooling quickly (quenching) this state to lower temperatures, corresponding to $R^*C_0 \gg 1$, coalescence is essentially blocked and the oil-in-water emulsion has significant metastability. Note that the transient structures, both the bicontinuous structure around $T = PIT$ and the droplet structure around $T = T_{CB}$, correspond to a true steady state when the system is stirred or sheared and thus can be reached from lower temperature as well as from above the PIT. Hence, it is sufficient to homogenize the system at $T = T_{CB}$ in order to obtain an oil-in-water emulsion with low polydispersity at $R = R^*$.

emulsion is their thermodynamic nature. The transient state is unstable with respect to coalescence and separation of a macroscopic oil phase. The quenched emulsion is metastable with respect to coalescence, as long as its temperature is kept below 59 °C (see Figure 10). This metastability originates from the high spontaneous curvature of the surfactant at low temperatures, as explained by the KW theory.³ Moreover, this high spontaneous curvature also limits the rate of other degradation processes, such as ripening through exchange of oil molecules during collisions of droplets.¹⁰ Therefore, the function of the quench is to provide metastability in a temperature range that is adequate for the later uses of these emulsions.

Conclusion

Metastable emulsions with controlled size droplets, in the 20–100 nm range, can be produced reliably through sub-PIT cycles with stirring. The mechanism of this emulsification is a solubilization of the oil into swollen micelles, above the R^*C_0 boundary (where R^* is the radius defined by the oil/surfactant ratio and C_0 is the spontaneous spherical curvature of the surfactant). Cross-PIT cycles yield exactly the same result. Hence, their mechanism of emulsification is also solubilization into swollen micelles and not, as was previously thought, transformation of a structure through curvature inversion.

Emulsification through Surfactant Hydration: The PIC Process Revisited

Kevin Roger,^{*,†} Bernard Cabane,[†] and Ulf Olsson[‡][†]*PMMH, CNRS UMR 7636, ESPCI, 10 rue Vauquelin, F 75231 Paris Cedex 05, France, and* [‡]*Physical Chemistry, Lund University, POB 124, Lund S 22100, Sweden**Received October 23, 2010. Revised Manuscript Received November 30, 2010*

We have performed sudden composition changes on a (surfactant + oil + water) system by adding water to a (surfactant + oil) solution. This composition change quenches the system into a metastable oil-in-water emulsion with a population in the 100 nm range. The conditions for a successful quench are as follows: the initial water content should be below a boundary called the “clearing boundary” (CB), the final water content should be sufficiently beyond CB, and the quench should be fast. We have used high purity components to avoid the complex phase separation patterns that occur with low purity ingredients: the surfactant is octaethylenhexadecyl ether (C₁₆E₈) and the oil is hexadecane (C₁₆). Under these conditions, we show that the pathway for this type of quench proceeds through the swelling of the reverse micellar phase by the added water and the formation of a sponge phase. Then, further water addition causes the nucleation of oil droplets in this sponge phase, with a size that matches the spontaneous curvature of the sponge phase. Part of the surfactant remains adsorbed on these droplets, and the rest is expelled as micelles that coexist with the droplets. It is concluded that a PIC emulsification will always lead to a bimodal size distribution with surfactant “wasted” in small micelles. This is in contrast with the more efficient PIT emulsification.

Introduction

Emulsions are usually dispersions of oil in water or water in oil. These dispersions are unstable, unless a surfactant is present. If surfactant molecules are adsorbed at the oil/water interfaces of an emulsion, then they form a monolayer that opposes the recombination of interfaces; in this way, they provide some metastability to the emulsion.¹ One of the most interesting questions in this field is the relation between the properties of the surfactant layer and those of the emulsion. For instance, the extension of the surfactant layer determines the spatial scale at which oil and water domains can be dispersed: if the emulsion is made by fragmenting large volumes of oil and water into very small droplets, then these droplets will coalesce until they are fully covered by the surfactant layer (surfactant-limited regime²). Moreover, the spontaneous curvature of the surfactant layer, H_0 , determines the probability of coalescence events involving oil droplets separated by a water film or vice versa.³

It is often advantageous to make emulsions with small droplets in the 100 nm range. Such emulsions will have a very large area of interfacial film, on the order of $60 \text{ m}^2 \cdot \text{g}^{-1}$ for an average droplet diameter $D = 100 \text{ nm}$, and therefore a large amount of surfactant. However, it turns out to be difficult to create such a large area of interface, unless extremely strong elongational flows are applied to break all droplets that are larger than the required size.⁴ Otherwise, the system remains inhomogeneous, with some surfactant in the interfacial films and the rest in micelles. This is indeed, for the surfactant, a more favorable situation because the micelles have a curvature that matches the spontaneous curvature of the surfactant films.

There is a set of methods that avoids this difficulty by starting from a homogeneous state for the surfactant, which is at its spontaneous curvature. These methods use a sudden change in this spontaneous curvature to incorporate a large amount of either oil or water and reach a metastable emulsion state. The change in the spontaneous curvature of the surfactant is caused by a jump in a physical parameter (e.g., temperature) or a composition parameter (e.g., hydration). Historically, these methods are related to the use of the C_{*m*}E_{*n*} amphiphiles because the spontaneous curvature can then be tuned according to temperature and to water content, and the total area can be easily estimated. The best known example is the phase inversion temperature (PIT) method, which uses a jump in temperature to produce metastable emulsions, with nearly monodisperse sizes in the 50–100 nm range. We have recently demonstrated that the mechanism of the PIT process is the formation of an oil/water microemulsion that can incorporate all of the oil, followed by a quench to a temperature where this microemulsion becomes a metastable emulsion.⁵ We now turn to the phase inversion composition (PIC) method, which uses a composition (water content) jump to produce metastable emulsions. This method has a greater potential for large-scale applications because it is easier to add water than to change suddenly the temperature of a large volume of emulsion. Furthermore, it could in principle be extended to other types of surfactants, whereas the PIT method is restricted to the use of the C_{*m*}E_{*n*} amphiphiles.

The starting point of the PIC method is a water-in-oil micellar phase, which is an equilibrium phase of the ternary system, in which the surfactant is already at the water/oil interfaces with a curvature turned toward water. The method then proceeds with a large addition of water, which causes an inversion of the spontaneous curvature of the surfactant film, now turned toward the oil. It is found that for certain compositions and with some constraints on the process a homogeneous metastable emulsion, with diameters in the 100 nm range, can be obtained.

*To whom correspondence should be addressed. E-mail: kevin.roger@espci.fr.

(1) Bibette, J.; Leal-Calderon, F.; Schmitt, V. *Emulsion Science*; Springer: New York, 2007.

(2) Taisne, L.; Walstra, P.; Cabane, B. *J. Colloid Interface Sci.* **1996**, *184*, 378–390.

(3) Kabalnov, A.; Wennerström, H. *Langmuir* **1996**, *12*, 276–292.

(4) Walstra, P. *Chem. Eng. Sci.* **1993**, *48*, 333–349.

(5) Roger, K.; Cabane, B.; Olsson, U. *Langmuir* **2010**, *26*, 3860–3867.

At present, there is no satisfactory understanding of this process because we do not know what pathways the system takes to invert its curvature and incorporate a large amount of water. It may go through a succession of equilibrium states⁶ before falling into the metastable emulsion state. However, the equilibrium states of a ternary system usually involve the separation of macroscopic phases, which may preclude the formation of a homogeneous emulsion, or the system may proceed through the formation of a nonequilibrium mesophase with zero curvature, as recently observed.⁷ However, this observation appears to be limited to a particular surfactant system and a narrow range of compositions. Alternatively, the system may proceed through the formation of a multiple emulsion (water/oil/water).⁸ However, there is no explanation of how the water/oil globules of such an emulsion would yield an oil/water emulsion.

Moreover, the efficiency of this process is not optimal, in the following ways:

- The emulsion droplets are too large, compared with the amount of surfactant in the system. This means that the area of final interfacial film is not large enough, which implies that some of the surfactant is not in the interfacial film but in excess micelles. Therefore, the system is locally heterogeneous.
- There are strong constraints on the composition (the amount of surfactant is in a narrow range) and on the process (the mixing must be fast). If these constraints are not met, then macroscopic phases separate out, and the system becomes heterogeneous on large scales.

In the present work, we propose a new approach to understand the nonequilibrium phenomena that take place in such phase inversion methods. The aim is to describe the structural transformations taking place when water is poured quickly in an (oil + water) solution, which results in the formation of a 100 nm oil/water emulsion. The approach was to investigate the phase diagram to find homogeneous states that contain high amounts of both oil and water and to relate those “access states” to the final emulsions.

Experimental Section

Materials. The surfactant octaethylenhexadecyl ether ($C_{16}E_8$) was obtained from Nikko Chemicals. The oil hexadecane was bought from Aldrich. The purity of all of those products was at least 99%. It must be emphasized that the use of very pure surfactants is extremely important. Indeed, less pure surfactants are mixtures of molecules with different alkyl and polyoxyethylene chain lengths, which may segregate in different parts of the systems or in regions of different interface curvature. In such cases, the phase behavior and the response to temperature and hydration changes could be completely different from that of the pure system. Deionized water (Milli-Q) was produced in the laboratory, and its purity was controlled at regular intervals.

The surfactant/oil/water mixtures were prepared as follows. The components were weighed in a small 4 mL glass bottle, and a small magnetic stir-bar was added. (For some samples that were very viscous, we used stir-bars with strong magnets to achieve proper shear.) The closed bottle was immersed in a temperature-regulated water bath and stirred at 200 rpm. The precision of the temperature regulation was ± 0.2 °C.

We used a Bruker Nanostar instrument for the small-angle X-ray scattering (SAXS) measurements, a Bruker 200 MHz

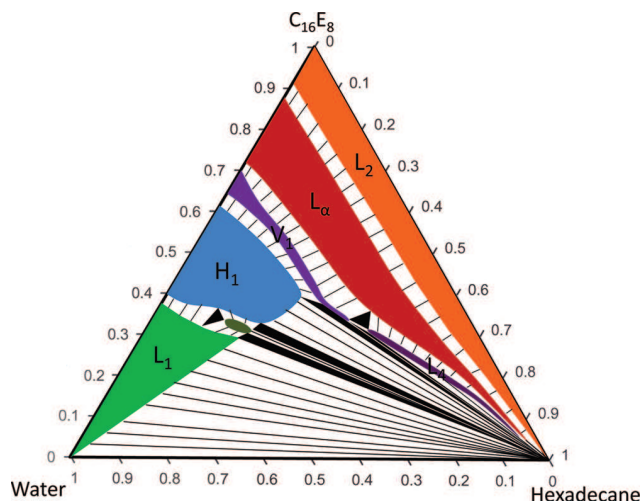


Figure 1. Ternary phase diagram of the $C_{16}E_8$ /hexadecane/water system at 50 °C. L_1 : oil/water micellar solution. L_2 : water/oil micellar solution. L_4 : water swollen sponge phase. L_α : lamellar phase. V_1 : bicontinuous cubic phase. H_1 : hexagonal phase.

NMR instrument for self-diffusion experiments, and either a Malvern Nanosizer or a Cordouan Vasco for dynamic light scattering (DLS) measurements.

Methods. One kind of experiment consisted of varying the water fraction at constant temperature and oil/surfactant ratio for several values of these parameters. Another kind of experiment consisted of quickly pouring water (fast dilution or composition quench) in a (oil + surfactant) mixture eventually containing some water for several values of those parameters. We achieved the temperature control by immersing the vial in a thermostatted water bath; the precision of the temperature control was ± 0.2 °C. Visual observation was used to determine whether the sample was homogeneous. We performed SAXS on the viscous samples to determine their length scales and also on metastable samples that were reaching equilibrium to see which equilibrium phases were forming. We used DLS to obtain the mean diameter and polydispersity of the emulsions resulting from the dilution of concentrated states. We used NMR self-diffusion to determine the topology (oil/water, water/oil, or bicontinuous) of the access states though self-diffusion measurements.⁹

Results

In this section, we report experiments through which we identified a set of homogeneous states located on the water swelling pathways that lead to PIC emulsification. Indeed, because the PIC emulsification results from the addition of water, it is appropriate to study water swelling lines, as shown in Figure 1. These lines start at points located on the (oil| surfactant) axis and end at the water corner. Each line is specified by a set value of the oil/surfactant ratio $O|S$. Upon slow addition of water to the (oil + surfactant) solution, the ternary systems separate with an aqueous phase that contains most of the surfactant and an oil phase. However, at smaller water contents, we identified some homogeneous states that hold large amounts of both water and oil. Moreover, we also discovered that fast addition of large amounts of water to these states produced an abrupt transition to oil/water emulsions. In the following, we first report where these homogeneous states are located (compositions, temperature, shear) in the phase diagram. Then, we present experiments that determine the general structure of these states and their location as a function of temperature.

(6) Pey, C.; Maestro, A.; Solé, I.; González, C.; Solans, C.; Gutiérrez, J. *Colloids Surf., A* **2010**, *361*, 1–196.

(7) Sonneville-Aubrun, O.; Babayan, D.; Bordeaux, D.; Lindner, P.; Rata, G.; Cabane, B. *Phys. Chem. Chem. Phys.* **2009**, *11*, 101–110.

(8) Lin, T. J.; Kurihara, H.; Ohta, H. *J. Soc. Cosmet. Chem.* **1975**, *26*, 121–139.

(9) Lindman, B.; Olsson, U. *Ber. Bunsen-Ges.* **1996**, 344–363.

Finally, we show how these states can be quenched by water swelling to give oil/water emulsions with droplet diameters of ~ 100 nm, and we examine how the surfactant molecules are distributed in this final state.

Equilibrium Phase Diagram. When studying a given oil/surfactant/water ternary system, it is very useful to know its phase behavior, that is, the phases that are formed at equilibrium for given values of both composition and intensive parameters. Furthermore, in this case, the Gibbs' phase rule indicates how to connect the regions with respect to the number of phases present. Because the spontaneous curvature of the surfactant layer depends on both the temperature and the water fraction, the phase diagram is in fact a phase prism. In this section, we report a cut of this phase prism for $T = 50$ °C, which is the usual range for the PIC process, that is, ~ 25 °C below the PIT of this system, which was measured to be 76.2 °C. The typical experiment was to prepare samples in small 2 mL vials and let them equilibrate, after proper stirring, at $T = 50$ °C. Their state was then assessed by visual observation and observation under polarized light. Some samples were also analyzed by SAXS to verify the nature of the phases present. The phase sequence of the water/surfactant binary system was also used in this phase diagram.¹⁰ The main feature is that three single-phase regions extend to high oil content. Those phases are, with increasing water fraction, the reverse micellar solution, the lamellar phase, and an isotropic fluid phase. The distinction between those two last phases is not possible through simple visual observation, but they can be easily distinguished under polarized light, the lamellar phase being birefringent. Of particular interest is the fact that this fluid isotropic phase is a homogeneous state that can contain simultaneously large amounts of oil and water. Therefore, it is the last homogeneous state along the dilution line at high oil fractions. At lower oil fractions, it connects through a two-phase region to the bicontinuous cubic phase. Both cubic phase and isotropic fluid phase are isotropic, but they can be distinguished easily because the cubic phase has a much higher viscosity than the isotropic fluid phase. In the next subsection, we investigate the precise structure of these last homogeneous states and their position on the phase prism, that is, for several cuts at different temperatures.

Clearing Boundary. The cubic and fluid isotropic phase are the last single-phase states that the ternary system encounters along a water swelling line, before entering a region that separates into an aqueous phase and an oil phase. We used a temperature-step method to determine precisely the location of this boundary beyond which oil separates from the surfactant. In a typical experiment, an (oil + surfactant) solution was made with a given oil/surfactant ratio O/S; then, a small fraction of water was added. The bottle was then equilibrated in a thermostatted water bath and stirred constantly. The temperature was then increased until the sample appeared visually homogeneous and nearly transparent. Then, another small amount of water was added, which led to the apparition of a white gel phase. The temperature was then increased until the sample was transparent and homogeneous again. We reiterated the procedure by adding small water fractions until the temperature no longer depended on the water fraction. This yields a curve indicating the temperature at which the mixture is homogeneous, which we call the "clearing boundary" (CB), as a function of the water/surfactant ratio (W/S), as shown in Figure 2. This name comes from the visual appearance of the sample on either side of this boundary: When the water/surfactant ratio is lower than the clearing boundary, the system is

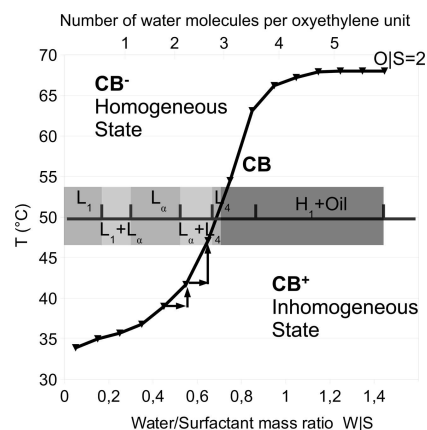


Figure 2. Clearing boundary for O/S = 2 and the equilibrium structures at $T = 50$ °C. This line separates homogeneous states CB^- from inhomogeneous states CB^+ .

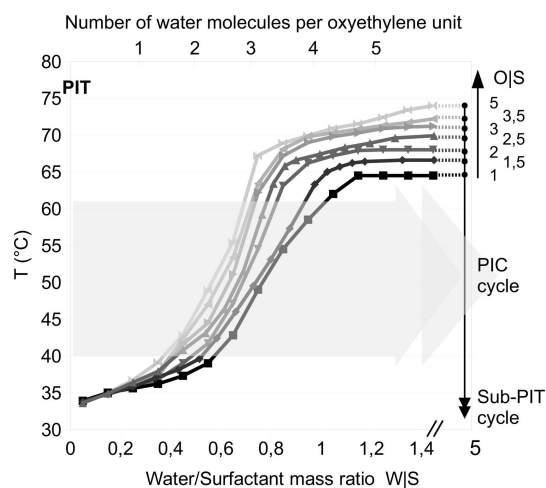


Figure 3. Clearing boundary for several oil/surfactant ratios O/S. Dilution lines involved in PIC emulsification are horizontal lines on this diagram, whereas temperature quenches are vertical lines.

homogeneous, monophasic, and nearly transparent; we name such states CB^- . When the water/surfactant ratio is higher, the system always undergoes fast phase separation; we name those states CB^+ .

The experiment was done for several oil/surfactant ratios O/S, and similar boundaries were always observed, as shown in Figure 3. At low water/surfactant ratios, the clearing boundary temperature, T_{CB} , slightly increases with the water/surfactant ratio but does not depend on the oil/surfactant ratio. This temperature is in fact the temperature at which the system can still form a water/oil microemulsion. When the water fraction increases, T_{CB} depends on both the oil/surfactant and water/surfactant ratios.

It was also considered to be important to determine the structure of those CB states and, in particular, to determine whether water or oil was the continuous phase or whether the structure was bicontinuous. For this purpose, we performed NMR self-diffusion experiments in which we measured the self-diffusion coefficients of water, oil, and surfactant molecules in the CB states. We then compared these self-diffusion coefficients with those of a water/oil micellar phase (oil is the continuous phase and water is confined) and with those of a oil/water nanoemulsion (opposite topology). The results are presented in Tables 1 and 2. This comparison shows that the self-diffusion coefficients of oil

(10) Mitchell, D.; Tiddy, J.; Waring, L. *J. Chem. Soc., Faraday Trans.* **1983**, *1*, 975–1000.

Table 1. Diffusion Coefficients ($\text{m}^2 \cdot \text{s}^{-1}$) of the Species for Several Compositions at the CB and Two Constrained Reference States^a

| sample | $D_{\text{H}_2\text{O}}$ | D_{EO} | D_{CH_2} | D_{CH_3} |
|--|--------------------------|------------------------|------------------------|------------------------|
| oil/water $T = 25\text{ }^\circ\text{C}$ | 2.29×10^{-9} | 1.33×10^{-11} | 8.76×10^{-12} | 8.14×10^{-12} |
| water/oil $T = 50.5\text{ }^\circ\text{C}$ | 3.55×10^{-10} | 8.10×10^{-11} | 6.53×10^{-10} | 6.92×10^{-10} |
| clearing boundary $T = 50.5\text{ }^\circ\text{C}$ | 1.36×10^{-9} | 2.67×10^{-10} | 4.86×10^{-10} | 4.62×10^{-10} |
| clearing boundary $T = 56.5\text{ }^\circ\text{C}$ | 1.05×10^{-9} | 1.52×10^{-10} | 4.95×10^{-10} | 4.69×10^{-10} |
| clearing boundary $T = 61.5\text{ }^\circ\text{C}$ | 1.04×10^{-9} | 1.02×10^{-10} | 4.94×10^{-10} | 4.55×10^{-10} |

^a All samples correspond to O|S = 3, and W|S can be read on the associated CB line in Figure 3.

Table 2. Comparison of Several Diffusion Coefficients of the Species for Several Compositions at the CB with Constrained Reference States

| sample | $D_{\text{H}_2\text{O}}/D_{\text{H}_2\text{O}}^{\text{bulk}}$ | $D_{\text{CH}_2}/D_{\text{CH}_2}^{\text{bulk}}$ |
|--|---|---|
| oil/water $T = 25\text{ }^\circ\text{C}$ | 1.0 | 0.01 |
| water/oil $T = 50.5\text{ }^\circ\text{C}$ | 0.16 | 1 |
| clearing boundary $T = 50.5\text{ }^\circ\text{C}$ | 0.59 | 0.74 |
| clearing boundary $T = 56.5\text{ }^\circ\text{C}$ | 0.46 | 0.76 |
| clearing boundary $T = 61.5\text{ }^\circ\text{C}$ | 0.45 | 0.76 |

(CH_2 and CH_3 ^1H NMR lines) in the **CB** state are comparable to those of a water/oil micellar phase. Therefore, the oil phase of the **CB** state is continuous. Similarly, the self-diffusion coefficients of water in the **CB** state are comparable to those of an oil/water emulsion. Therefore, the aqueous phase of the **CB** state is continuous. Consequently, the **CB** states must have bicontinuous structures. If the O|S ratio is low enough, then this is a cubic phase, which is followed at higher O|S ratios by a bicontinuous isotropic phase, which is therefore a L_4 phase or “sponge” phase.¹¹

Finally, SAXS experiments were performed on samples that were prepared in the sponge phase and examined after transfer in the X-ray cell before phase separation took place. These SAXS spectra have a broad peak at a q value that corresponds to a repeat period of 12 nm. Therefore, the structure can be described as an array of cells with this average size, which are connected both through the oil and through water, as has been described in the literature on bicontinuous sponge phases.¹²

It can be seen on the phase diagram that all **CB**⁻ states are either monophasic states (reverse micellar, lamellar, cubic, or sponge) or biphasic states resulting from the phase transition between the monophasic states. This means that no oil phase separates from the system in the **CB**⁻ region. On the contrary, upon crossing the **CB**, the system always falls into either a two- or a three-phase region, one of the phases being pure oil. Therefore, oil always phase separates from the **CB**⁺ states. This allows us to draw a simplified phase diagram for our purpose in Figure 4. In the next section, we show that the emulsification leads to either stable or unstable emulsion, depending on whether the initial composition is chosen in the **CB**⁻ region or in the **CB**⁺ region. We also characterize the emulsions as a function of their initial composition.

Quenched Emulsions. In this section, we report the nature and characteristics of the final states that were prepared by quenching along the water swelling lines two different kind of samples:

- Samples at given O|S ratio but different water fraction, that is, samples along a given dilution line.
- Samples at the **CB** for several O|S ratios.

The main characteristics are the number of coexisting droplet populations, their metastability, their mean diameters, and the

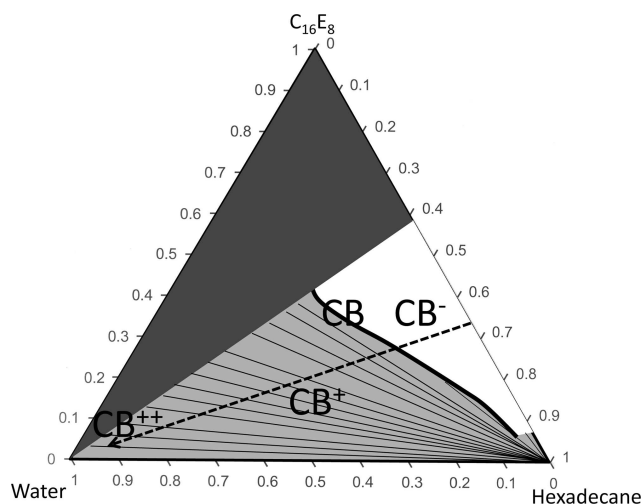


Figure 4. Schematic phase diagram at $T = 50\text{ }^\circ\text{C}$ for the C_{16}E_8 /hexadecane/water system. The **CB** line separates the **CB**⁻ area, with a sequence of homogeneous phases that solubilize all of the oil from the **CB**⁺ area, where weakly oil-swollen micelles coexist with excess oil. The **CB** line essentially corresponds to the location of the sponge phase.

overall emulsification efficiency defined as

$$E = R_c/R_{\text{emulsion}} \quad (1)$$

where R_c is the composition radius, that is, the radius obtained if the system consists of a monomodal dispersion of oil spheres in water,⁵ and R_{emulsion} is the radius of the emulsion droplets.

$$R_c = \frac{3\phi_o l_s}{\phi_s} \quad (2)$$

where ϕ_o is the oil volumic fraction, ϕ_s is the surfactant volumic fraction, and l_s is the “surfactant length” defined as

$$l_s = v_s/a_s \quad (3)$$

where v_s is the surfactant volume and a_s is the area per molecule at the defined monolayer interface. For C_{16}E_8 , $l_s \approx 2\text{ nm}^5$.

In the first approach, we start from different states in **CB**⁻, **CB**, or **CB**⁺ regions and dilute them quickly to the water-rich area, which we will call **CB**⁺. A typical experiment consisted of preparing several samples for several O|S ratios and temperatures at different initial water fractions. This corresponds to a horizontal line in Figure 2 and a dilution line in Figure 1. Then, a large amount of water at the same temperature was added, and the resulting emulsion was analyzed by DLS. When the initial sample had a water fraction below **CB**, the quench yielded a nanoemulsion that had the same droplet size distribution regardless of the initial water fraction. Figure 5 shows size dispersions of an emulsion obtained through PIC emulsification and PIT

(11) Olsson, U.; Jonströmer, M.; Nagai, K.; Söderman, O.; Wennerström, H.; Klose, G. *Prog. Colloid Polym. Sci.* **1988**, *76*, 75–83.

(12) Olsson, U.; Wennerström, H. *Adv. Colloid Interface Sci.* **1994**, *49*, 113–146.

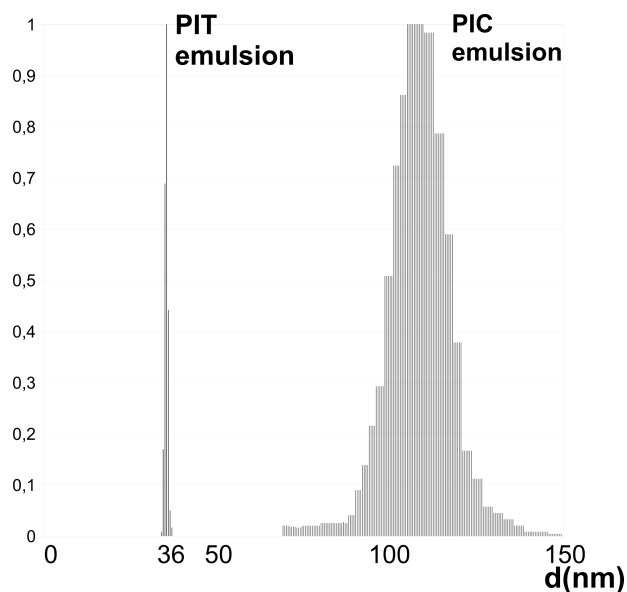


Figure 5. Size statistical dispersions obtained through the Padé-Laplace algorithm and a multiacquisition procedure. Each peak correspond to several measurements. The composition of the sample was identical in both cases to $O/S = 2$. Emulsions obtained through the PIC process have a higher mean diameter and polydispersity compared with emulsions obtained through the PIT process.

emulsification at $O/S = 2$. When the initial sample had a water fraction beyond **CB** and was therefore nonhomogeneous, the quench yielded a coarse emulsion that creamed rapidly.

The other approach consisted of comparing different swelling lines, defined by different values of O/S (oil/surfactant ratio) and T (temperature) (Figure 1). Because the final state does not depend on the amount of water (W/S) in the initial state, providing it is below **CB**, it was sufficient to use surfactant/oil solutions ($W/S = 0$) as initial states. This was done by preparing several oil/surfactant solutions with different values of O/S and by quickly adding water at the same temperature T . The resulting emulsion was analyzed by DLS. We used both the cumulants method and the CONTIN algorithm to obtain mean diameters and size distributions.

This leads to three distinct situations, which are indicated in Figure 6 and described below:

1. At $O/S < 1.5$, we obtained two large coexisting populations: a population of oil droplets (mean diameter < 100 nm) and a very numerous population of swollen micelles (mean diameter ≈ 13 nm).
2. In the range $1.5 < O/S < 3$, we obtained a single population of droplets with a diameter $100 \text{ nm} < d(\text{PIC}) < 160$ nm. The emulsification efficiency was almost constant at $E \approx 0.35$: This is indicated in Figure 6 by the relative values of $d(\text{PIC})$ and $d(\text{composition})$. Because $E < 1$, some surfactant was not at the interfaces of the droplets. This surfactant must form micelles, but these micelles were not detected by light scattering, presumably because they were less numerous than those in the low O/S case.
3. At high O/S , we obtained coarse emulsions that creamed quickly.

Three observations from this diagram should be emphasized:

- The maximal O/S is quite small, which is a limitation for this method to be used.

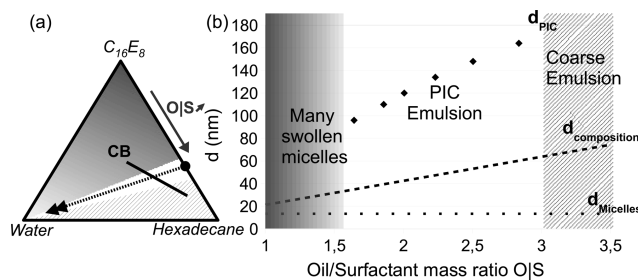


Figure 6. (a) Composition triangle at $T = 50^\circ\text{C}$ showing the three types of dilution lines. The corresponding emulsions are classified in part b. On the left part of this diagram, many swollen micelles with a diameter d_{micelles} are coexisting with the emulsion droplets and are detected by DLS. In the middle of the diagram, only a population of droplets with a diameter d_{PIC} were obtained. On the right part of this diagram, it was impossible to achieve proper emulsification, and only coarse emulsions were obtained. We also plotted the diameter $d_{\text{composition}}$ we obtained in a sub-PIT emulsification,⁵ which corresponds to a monomodal population of oil droplets covered by a surfactant layer.

- Using large amounts of surfactant is useless because in that case we will mainly obtain a population of equilibrium swollen micelles.
- Whatever composition is used, $E < 1$, which means that the PIC emulsification is not optimal because surfactant is wasted and micelles always coexist with oil/droplets.

Finally, we tried several geometries and procedures of dilution such as thin films experiments, low volumes, and intensity of shear. This was done when the initial state was either an oil/surfactant solution or a state at the clearing boundary. In all of those cases, no important dependence was found with our system.

Comparison with Other Water/Oil/Surfactant Systems.

To check the generality of the results obtained with our particular system, we tested two other surfactants, $C_{12}E_5$ and $C_{16}E_5$, and three other oils, decane, dodecane and tetradecane. All resulting systems were found to give similar results and conclusions so that our reasoning can be in fact extended to the generic C_nE_j /oil/water pure system. As an example, we drew a **CB** line for the water/tetradecane/ $C_{12}E_5$ system and $O/S = 2.5$ in Figure 7. This curve is perfectly similar to those obtained in the water/hexadecane/ $C_{16}E_8$ system both qualitatively and quantitatively if the X axis is the number of water molecules per oxyethylene unit. Fast dilution from the **CB** area at $O/S = 2.5$ yields emulsions with the a typical diameter of 148 nm, which is also similar to the data shown in Figure 6. Also, as for the water/hexadecane/ $C_{16}E_8$ system, comparison with the phase diagram¹³ shows that this **CB** line is still the limit before oil phase separation.

Discussion

The aim of this discussion is to identify a mechanism, that is, a succession of nonequilibrium states, that defines the pathway that the system follows from its initial state to its final state. For this purpose, we first examine the homogeneous states along the dilutions lines and then relate them to the final emulsions. This allows us then to draw the detailed sequence of events that occurs when adding water to an oil/water solution.

CB States As "Access" States. The existence of the homogeneous states called **CB** states appears to be central for the identification of the PIC emulsification pathways. Indeed, according

(13) Kunieda, H.; Shinoda, K. *J. Dispersion Sci. Technol.* **1982**, *3*, 233–244.

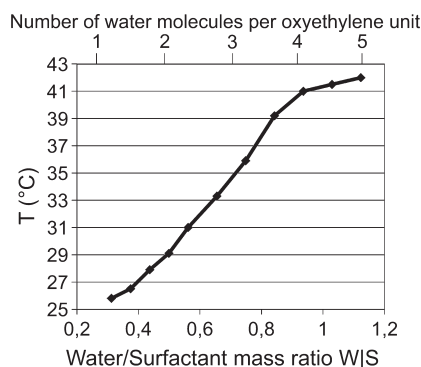


Figure 7. CB line for the water/tetradecane/ $C_{12}E_5$ system and O|S = 2.5, in Figure 7. Notice the similarity with Figure 3, particularly when using the number of water molecules per oxyethylene unit to describe its features.

to the experiments reported above, these states can be transformed to PIC emulsions by the addition of appropriate amounts of water. Therefore, each one of these states is a part of an emulsification pathway. We make the hypothesis that at a given composition if a system is constrained to remain homogeneous, then its free enthalpy $G(T, p, n_i)$ has a single minimum corresponding to a certain state of the water/oil/surfactant system; therefore, the system will evolve to or through this homogeneous state. Conversely, according to this hypothesis, an emulsification pathway at the same O|S ratio must go through this CB state. Because this state is the last homogeneous state that can be maintained on this pathway, it has the characteristics of an “access state”. We must now answer three questions regarding these states: how are they formed, what is their structure, and how are they transformed?

CB Boundary: Hydration versus Temperature. Here we turn to the location of the CB boundary. As shown in Figure 2, the boundary beyond which the spontaneous curvature causes the decomposition of the homogeneous bicontinuous structure depends on both hydration and temperature. There are two ranges where the effect of hydration is dominant, and one central range where the both effects compete:

- When there is less than one water molecule per oxyethylene unit, the system crosses directly from a reverse micellar solution to a multiphase equilibrium state (small water addition) or to the metastable emulsion (large water additions). In this range, the system is poorly hydrated, and changes in hydration are much more important than changes in temperature (Figure 2). Moreover, the oil content does not matter because the micelles are separated by excess oil (Figure 3).
- Between one and four water molecules per oxyethylene unit, the system forms at equilibrium a lamellar phase or cubic phase and then a hexagonal phase (Figure 2). Hence the effects of hydration are still strong because the spontaneous curvature changes from nearly zero to positive. However, they are shifted by changes in temperature: indeed, the slope of the CB line shows that a larger hydration is required at higher temperature to produce the decomposition of the homogeneous state. Moreover, the oil content does matter because the curvature is turned toward oil (Figure 3).
- When there are more than four water molecules per oxyethylene unit, there are enough water molecules to hydrate the oxyethylene chains regardless of

temperature (Figure 2). Under these conditions, the CB boundary merges with the clearing boundary that was identified in PIT experiments.⁵ Moreover, the oil content still has the same effect as before because the curvature is turned toward oil (Figure 3).

CB Curvature. The CB states have a bicontinuous structure in the range $40 < T < 65$ °C. According to the corresponding compositions, the oil content is also always higher than the water content, and the surfactant hydration (three water molecules per oxyethylene unit) indicates that the curvature of the surfactant layers must be turned toward the oil. This allows us to estimate their average curvature.

We consider a water swollen reverse bilayer structure, as shown in Figure 8.^{14,12} At the bilayer midplane, $\bar{H} = 0$, the monolayers on the average curve toward the oil with magnitude¹⁵

$$\bar{H} = \frac{\phi_B^2}{1.1\delta} \quad (4)$$

where ϕ_B is the bilayer volume fraction and δ is the bilayer thickness. The exact definition of ϕ_B is coupled to the strict definition of δ and the location of the interfaces where we evaluate H . Defining $\phi_B = \phi_W + \gamma\phi_S$, where γ (~ 0.5) is the volume fraction of oxyethylene units in the surfactant molecule, we have defined the monolayer interface to lie between the oxyethylene groups and the alkyl chains. For the corresponding bilayer thickness, δ , we have

$$\delta = \frac{2\phi_B l_s}{\phi_S} \quad (5)$$

where δ is the distance between the two parallel monolayer interfaces. Those relations yield the expression of the average curvature \bar{H}

$$\bar{H} = \frac{\phi_S(\phi_W + \gamma\phi_S)}{2.2l_s} \quad (6)$$

which we can use to calculate \bar{H} for such a spongelike structure as a function of its composition.

This expression was used to calculate \bar{H} for each point of each CB curve drawn in Figure 3. Figure 9 shows the corresponding (T, \bar{H}) diagram for several O|S values.

A striking feature of those curves is that the curvature does not depend on the temperature along the CB line, whatever the O|S. This means that the competition between hydration by water and the dehydration by the temperature is closely matched. Also increasing O|S leads to a decrease in the curvature, which is consistent with the fact that the curvature is turned on the average toward the oil, and values of the curvature are much smaller than typical spherical curvatures, which is consistent with the bicontinuous structure. Therefore, we can conclude that the CB is a line of constant curvature, which depends solely on the composition of the sample.

Evolution from the CB State. According to the phase diagram, crossing the CB states leads to a phase separation where pure oil is expelled. Furthermore, emulsification experiments show that starting from those CB^+ states leads to a coarse emulsion. This contrasts with initial compositions in the CB^- region, which

(14) Olsson, U.; Würz, J. U.; Strey, R. *J. Phys. Chem.* **1993**, *97*, 4535–4539.

(15) Anderson, D.; Wennerström, H.; Olsson, U. *J. Phys. Chem.* **1989**, *93*, 4243–4253.

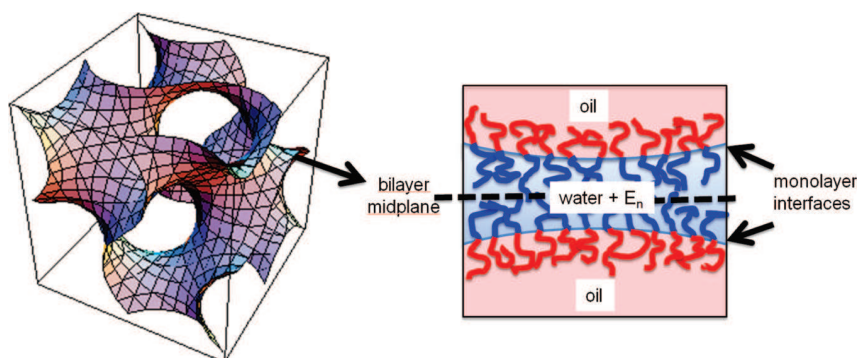


Figure 8. Illustration of the structure of an oil-rich sponge phase. A reverse, water swollen, multiply connected bilayer forms a dividing surface between two separate 3D-continuous oil labyrinths, of equal volume. By symmetry, the average mean curvature of the bilayer midplane is zero. The two monolayers, on the other hand, have an average mean curvature toward the oil.

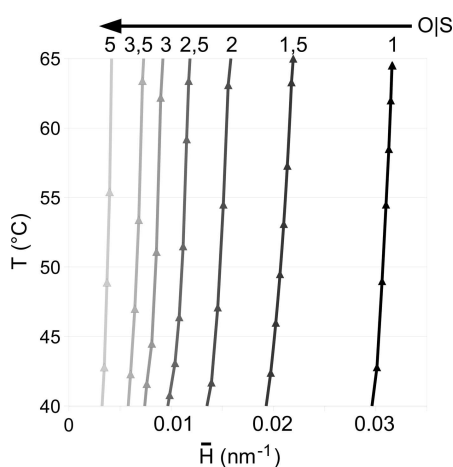


Figure 9. Calculation of the average curvature of the surfactant layer \bar{H} , calculated for a bicontinuous structure, for each CB line of Figure 3. Each line corresponds to a constant O/S but to several water fractions, which are given by the temperature.

lead to a metastable emulsion if the O/S is not too high. In both cases, oil phase separates from the homogeneous state; however, in the first case, a macroscopic phase separation takes place, whereas in the second case, the phase separation occurs on a given length scale.

This length scale is given by the diameter of the final emulsion droplets. To find out how this size is controlled, we worked with curvatures. Figure 10 compares the emulsion droplet curvature to the CB curvature, the composition curvature, and the swollen micelle curvature. As noticed before, the droplets curvature is lower than the composition curvature. Therefore, the emulsion consists of swollen micelles and larger droplets. It is very interesting to notice that the curvature of the emulsion droplets is very close to the curvature of the CB state. Therefore, the length scale of the oil phase separation is imposed by the CB state.

This can be understood by a kinetic phase separation in the sponge phase upon fast water addition. Consider a large (1–10 μm) drop of this phase, surrounded by water. Diffusion of water in that bicontinuous structure will occur within a few milliseconds, and it will increase the curvature of the surfactant layer. As a result, some connections between oil domains will break, and the system will separate into large domains and a phase that is enriched in water. However, at the beginning of the phase separation, the spontaneous curvature is still close to that of the CB state. Nucleation of the oil droplets in the drop occurs, and

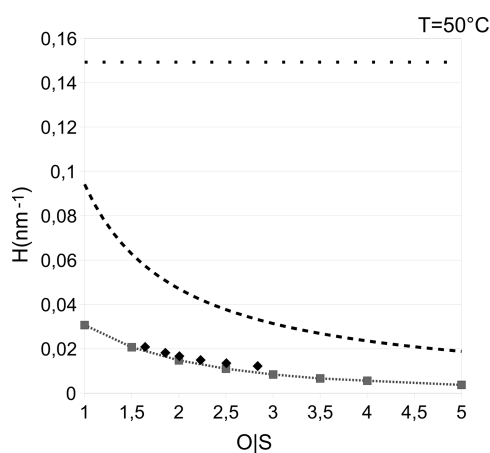


Figure 10. Curvature as a function of O/S for several structures. Dotted line: swollen micelles. Dashed line: oil droplets at the composition radius. Gray square: bicontinuous phase at the CB, as calculated in Figure 9. Black diamonds: PIC emulsion. The curvature is then calculated as two over the diameter of the droplets.

their size matches the spontaneous curvature. Of course, as high fluctuations of the composition take place during the process, the polydispersity is quite high, as observed. This process leads to the bimodal emulsion with big droplets at a curvature given by the O/S value. This allows us to understand why the droplets size is unchanged with temperature because the curvature at the CB does not depend on this parameter. Also, at high O/S values, the curvature is very low, and droplets would be very large; in such a case, oil droplets are so close to each other that they may coalesce before the change in curvature make them metastable, and they dissolve in a water-continuous phase. In this case, the macroscopic phase separation cannot be prevented.

Overview of the PIC Emulsification Mechanism. To conclude the discussion, we return to the complete sequence of events that take place when adding water to an (oil + surfactant) solution. The main idea that was developed above is that the PIC emulsification results from a mesoscopic phase separation on a length scale, given by the chosen composition. Therefore, the system follows the sequence from the phase diagram but on a different length scale. The main steps of this sequence are schematized in Figure 11.

The first step consists of the hydrodynamic fragmentation of the (oil + surfactant) solution in water. The resulting drop size ($\sim 1\text{--}10 \mu\text{m}$) is not crucial in this process because further

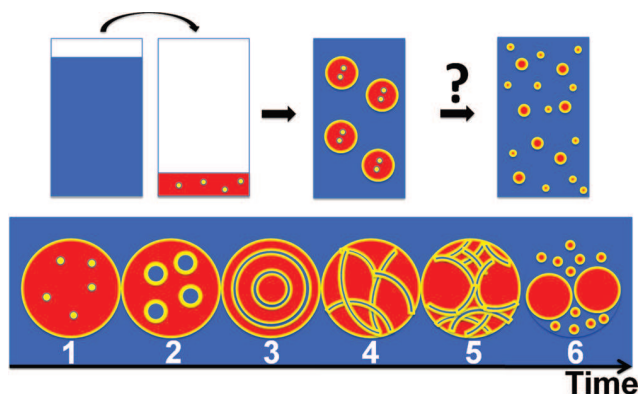


Figure 11. Sequence of events occurring when large amounts of water are quickly added to an (oil + surfactant) solution. First, the hydrodynamic fragmentation of the (oil + surfactant) solution in water results in the formation of big drops ($\sim 1\text{--}10\ \mu\text{m}$). Each of these drops undergoes a sequence of six main transformations as water diffuses in. (1) The (oil + surfactant) drop is surrounded by water. (2) The drops swells with water, resulting in the formation of swollen reverse micelles. (3) Further swelling leads to a decrease in the curvature and thus the formation of a lamellar phase. (4) The lamellar phase connects to form a sponge phase as the curvature turns toward the oil. (5) Emulsion droplets nucleate within the sponge phase with a diameter that matches the spontaneous curvature. (6) What is left of the sponge phase transforms into a collection of very small micelles, and the large droplets are released.

evolution takes place through diffusion of water in the drop (1). Then, reverse swollen micelles are formed as water diffuses in, and the curvature is toward the water (2). As the curvature continues to decrease, the lamellar phase is obtained (3). Eventually, this leads to the phase inversion, which results in the formation of the sponge phase as the spontaneous curvature turns toward the oil (4). Upon further addition of water, the oil droplets nucleate in the sponge phase, and their sizes match the spontaneous curvature of this sponge phase (5). In this biphasic state, oil droplets are still trapped in a sponge phase. Eventually, what is left of the sponge phase transforms into cylindrical or spherical micelles/droplets, as observed in the equilibrium sequence. These structures are water-soluble. Therefore, as the final event (6), the

swollen micelles and oil droplets disperse in the continuous water phase, forming the bimodal size distribution. These droplets are now metastable as a result of the high spontaneous curvature of the surfactant, which prevents the inversion of the surfactant film.³ We would like to highlight the fact that the bimodal size distribution is a fundamental property of the PIC method, resulting from the formation of the emulsion droplets by nucleation at a low spontaneous curvature.

Comparison with the PIT Emulsification. Observation of Figure 5 shows that for a given composition, the PIC emulsification is not efficient, in contrast with the PIT emulsification ($E_{\text{PIC}} \approx 0.35$ and $E_{\text{PIT}} \approx 1$). This reveals that the two processes do not take place through similar mechanisms. Indeed, although similar sequences of the curvature changes are observed in both cases, the structures of their respective access states are different.

In the PIC emulsification, the access state is a bicontinuous sponge phase. The emulsification results from the nucleation of the oil in this low curvature phase, and a bimodal size distribution is obtained. On the contrary, when this access state has an oil/water droplet-like structure, as identified in sub-PIT emulsification,⁵ no surfactant is wasted, and the size obtained results from the best geometric compromise between the volume of dispersed phase and the area that can be covered by surfactant molecules (i.e., the composition curvature). This state is, however, geometrically impossible to obtain in PIC emulsification, where there is just not enough water to produce droplets of oil in water.

Therefore, whereas in the PIT mechanism the emulsification proceeds through the formation of an homogeneous state where all oil is solubilized and that is kept metastable through the quench, in the PIC mechanism, the emulsification proceeds through the expulsion of oil from an homogeneous state, where it was solubilized during the quench. This intrinsic difference makes it impossible to produce emulsions at the composition diameter through the PIC process

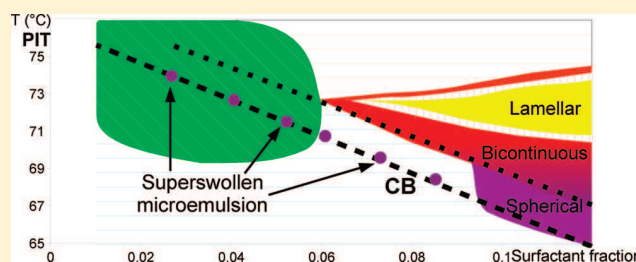
Acknowledgment. We would like to thank D. Durand for her help while performing SAXS and I. Åslund for her help in NMR experiments. This work was supported by the Swedish Research Council.

Superswollen Microemulsions Stabilized by Shear and Trapped by a Temperature Quench

Kevin Roger,^{*,†} Ulf Olsson,[‡] Malin Zackrisson-Oskolkova,[‡] Peter Lindner,[§] and Bernard Cabane[†][†]PMMH, CNRS UMR 7636, ESPCI, 10 rue Vauquelin, F 75231 Paris cedex 05, France[‡]Physical Chemistry, Lund University, POB 124, Lund, S 22100, Sweden[§]Institut Laue-Langevin, 6 rue Jules Horowitz, F-38042 Grenoble cedex 09, France

Supporting Information

ABSTRACT: We studied the solubilization of oil in the $C_{16}E_8$ /hexadecane/ H_2O system. Close to the phase inversion temperature (PIT), the system, at equilibrium, can form either homogeneous states (i.e., microemulsions) at high surfactant concentrations or three-phase states at lower concentrations. We show that, under gentle shear, at a line we named the clearing boundary (CB), located a few degrees below the PIT, the system is homogeneous regardless of the surfactant concentration. We relate this shift of the microemulsion boundary to shear-induced disruption of the asymmetric bicontinuous structure. Although this state quickly relaxes to equilibrium when shear is stopped, we show that it is still possible to trap it into a metastable state through a temperature quench. This method is the sub-PIT emulsification that we described in a previous work (Roger et al. Langmuir 2010, 26, 3860–3867).



INTRODUCTION

Although oil and water are immiscible, it is possible to obtain homogeneous equilibrium states by adding surfactant. Such systems are called microemulsions and have remarkable properties such as solubilization of various molecules and low surface tensions. However, their usefulness is somehow limited by their low capacity to solubilize oil. Typically, the amount of oil cannot exceed 3 times the amount of surfactant. Indeed, multiphase states are favored when more oil is added to such systems. A good example is given by the nonionic amphiphiles of the polyoxyethylene type, whose hydration depends on temperature. At a temperature called the phase inversion temperature, the surfactant layer has zero mean spontaneous curvature. Far below the phase inversion temperature (PIT), the system, at equilibrium, consists of high-curvature objects, namely, oil-swollen micelles, and excess oil. It could be expected that, upon increasing the temperature, the excess oil would be solubilized as the spontaneous curvature decreased and the micelles grew in size. However, at low surfactant concentrations and at temperatures close to the PIT, the system rather forms bicontinuous structures coexisting with excess oil (and possibly water).¹ Understanding and describing the transition from bicontinuous structures to spherical structures is one of the outstanding questions in this field.

The aim of this work was to address this question by triggering transitions between bicontinuous and spherical structures, at a set composition and spontaneous curvature. In a previous work, we studied a low-energy emulsification process that relies on temperature-induced transitions, the sub-PIT method.² The PIT

method³ is traditionally related to easy fragmentation at temperatures close to the PIT, where interfacial tensions are very small,^{4,5} and subsequent rapid cooling to keep the system metastable. We challenged this point of view by identifying, below the PIT, intermediate homogeneous states under gentle shear that completely determined the outcome of the emulsification process. Furthermore, their structural length was the spontaneous curvature of the surfactant layer as in typical microemulsions. These states were, however, unstable at low surfactant concentrations, and phase separation occurred quickly when shear was stopped, at constant temperature (i.e., spontaneous curvature).

In this study, we systematically investigated phase behavior under shear and below the PIT, using mainly small-angle neutron scattering, and compared it to the equilibrium phase behavior.

Our goal was to answer the following questions:

- (1) How can one obtain homogeneous states under shear, below the PIT? What pathways lead to their formation? What are their structures?
- (2) Do these homogeneous states originate from the fragmentation of a continuous oil phase, facilitated by ultralow interfacial tensions? Otherwise, is the effect of interfacial tensions restricted to the immediate vicinity of the PIT?

Received: May 6, 2011

Revised: June 28, 2011

Published: June 29, 2011

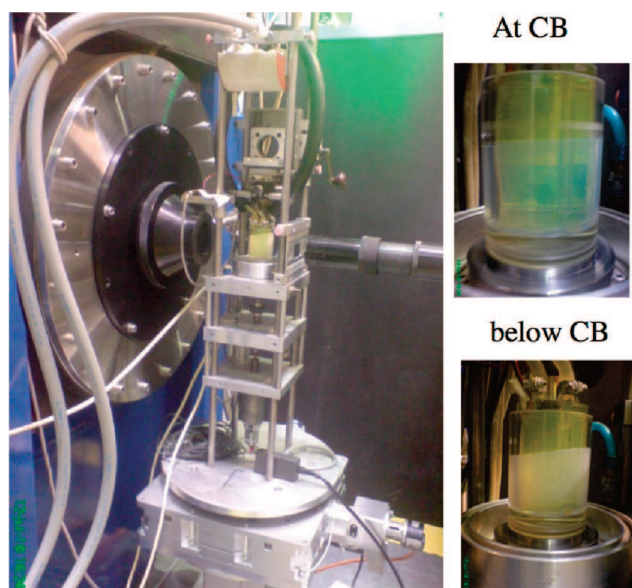


Figure 1. Experimental setup: thermostatted Couette cell in front of the neutron beam. Visual inspection allows the clearing boundary to be distinguished as the minimum of turbidity.

- (3) Can the phase behavior under shear and at equilibrium be related in terms of structural transitions? Can shear rather be described as a trigger between possible structures?
- (4) Is it possible to keep these intermediate states, which are superswollen microemulsions, in metastable states that retain the same structure?

EXPERIMENTAL SECTION

Materials. The surfactant octaethylenehexadecyl ether ($C_{16}E_8$) was obtained from Nikko Chemicals. Hexadecane, deuterated hexadecane and D_2O were purchased from Aldrich. The purity of all these products was at least 99%. It must be emphasized that the use of very pure surfactants is extremely important. Indeed, less pure surfactants are mixtures of molecules with different alkyl and polyoxyethylene chain lengths that can segregate in different parts of the systems or in regions of different interface curvature. In such cases, the phase behavior and the response to temperature and hydration changes could be completely different from that of the pure system. The use of hexadecane was motivated by the low rate of ripening processes when this oil is used. Furthermore, the $C_{16}E_8$ /hexadecane/ H_2O system was extensively studied in a previous study on sub-PIT emulsification² and allows comparison between sets of data. D_2O was used for small-angle neutron scattering (SANS) experiments, whereas H_2O was used in all other cases. Indeed, when D_2O was used instead of H_2O , the boundaries were typically shifted down by 2 °C, but we verified that no shift occurred along the surfactant axis.

Methods. The phase diagram of the $C_{16}E_8$ /hexadecane/ H_2O system was established by weighing components in 4 mL vials and using visual inspection, under normal or polarized light, to determine the number and nature of phases. We investigated the effect of shear as a means to prevent phase separation but not as an emulsifier tool; therefore, we did not use high shear. Typically, we used small magnetic stir bars for glass vials. We performed small-angle neutron scattering (SANS) at the Institut Laue-Langevin on the D11 instrument, using a Couette cell⁶ that allows observation of the system under shear (Figure 1). This cell had a 1-mm gap that was crossed twice by the neutrons. It was modified by applying small spots of glue ($0.5 \times 1 \times 1$ mm) to the surface of the

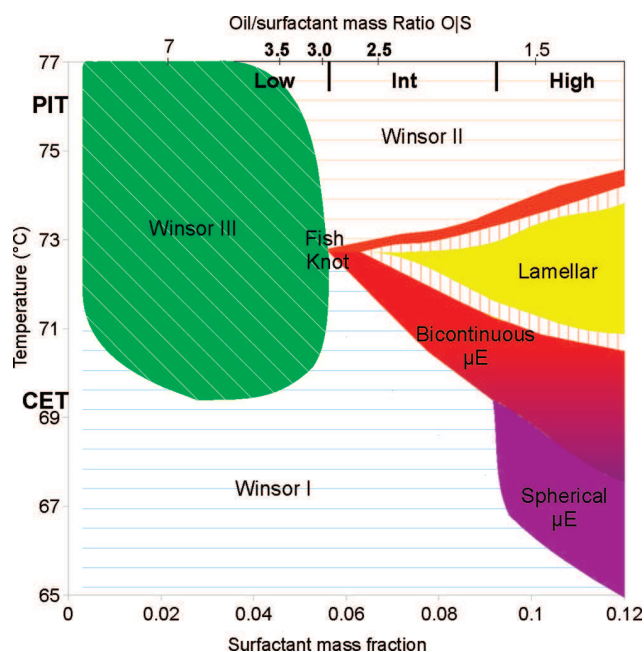


Figure 2. Cut of the phase prism for $O|W = 0.2$ in the hexadecane/ $C_{16}E_8$ / H_2O system. Redrawn from ref 2. When D_2O is used instead of H_2O , this cut is shifted to lower temperatures by 2 °C. The fish knot separates microemulsions coexisting with excess oil and water from single-phase microemulsions. The critical end-point temperature (CET) separates spherical from bicontinuous structures.

nonrotating inner cylinder. This disturbed the laminar flow and ensured mixing of the top and bottom layers of the cell. By using dispersions of larger reflecting anisotropic particles, we verified that these modifications did result in proper mixing of the top and bottom layers. The temperature was regulated by a water bath from 25 to 75 °C. The temperature was read from a probe on the inner cylinder, and it was also checked from time to time with a manual probe inside the gap. The shear rates ranged from 200 to 1200 s^{-1} .

Turbidity measurements were performed with a Varian spectrophotometer through a comparison between the incident light intensity I_0 and the transmitted light intensity I . A small stir bar was placed in the cell to provide agitation during turbidity measurements.

RESULTS

Equilibrium Phase Boundaries. In this work, we aimed to understand and shift phase boundaries. Hence, we needed an adequate way to trace and display these boundaries. In ternary systems, a phase diagram can be displayed in a triangular representation. However, for polyoxyethylene surfactants, temperature is the most important variable, because it largely controls surfactant hydration and, hence, the spontaneous curvature of the surfactant layer. Therefore, an appropriate representation is a vertical slice of the phase prism at a constant oil/water ratio, which was chosen as 0.2 in this work. This yields a Kahlweit “fishlike” plot.¹ This cut for the $C_{16}E_8$ /hexadecane/ H_2O was determined in ref 2 and is redrawn in Figure 2. When D_2O was used instead of H_2O , the boundaries typically shifted downward by 2 °C, but we verified that no shift occurred along the surfactant axis. This cut is therefore accurate for the $C_{16}E_8$ /hexadecane/ D_2O system provided that the temperature is shifted upward by 2 °C. Two features are of particular interest with respect to oil

solubilization and structural changes. The first is the “fish knot” that separates the microemulsion area from the three-phase region (Winsor III). For an equilibrium system, this point gives the largest amount of oil that can be solubilized in a homogeneous single phase (microemulsion).¹ Second, the critical end-point temperature (CET) can be visualized here by the change in slope in the microemulsion boundary. At the CET, there is a droplet-to-bicontinuous transition in the microemulsion structure, displayed in Figure 2 by a change in color from purple to red.

To examine swelling processes that might lead to a microemulsion, it is useful to keep the composition constant but increase the temperature. These paths are vertical lines in the phase diagram. All paths start from the Winsor I state, namely, swollen micelles coexisting with excess oil. Three possible transitions from this state, with respect to the two particular points described above, can be observed at temperatures close to the PIT and are shown in Figure 2:

- At high surfactant fractions (denoted high), there is a temperature, below the critical end-point temperature, at which all of the oil is solubilized in a spherical microemulsion.
- At intermediate surfactant fractions (denoted int), there is a temperature, above the critical end-point temperature, at which all of the oil is solubilized in a bicontinuous microemulsion.
- At low surfactant fractions (denoted low), there is a temperature, above the critical end-point temperature, at which the system forms a bicontinuous microemulsion coexisting with excess oil and water.

Therefore, at equilibrium, only the high part of the phase cut yields an equilibrium single phase made of oil droplets. It was shown that this state could be trapped in a metastable state through fast cooling.⁷ However, the question of interest here is: how does shear change these transitions?

Clearing Boundary. To assess the influence of shear on the low-curvature states, we performed visual inspections of samples that were constantly stirred with stir bars. At low temperatures and at rest, the equilibrium state was observed to consist of an equilibrium micellar solution coexisting with excess oil. This resulted in an emulsion with a milky appearance due to Mie light-scattering. Increasing the temperature caused the solubilization of the oil into surfactant-rich objects, such as micelles. Indeed, the sample appeared much clearer at higher temperature, as shown in Figure 1, as large objects were solubilized and only small objects then contributed to the light scattering. This procedure was used for samples at various surfactant concentrations. Typically, samples corresponding to the three equilibrium behaviors described above (high, int, and low) were studied. This resulted in the determination of a line, that we denote as the clearing boundary (CB) drawn in Figure 3. In the high area, this line overlaps the equilibrium boundary. However, at the critical end-point temperature, the microemulsion boundary and this line split. The clearing boundary then continues into the Winsor I and Winsor III areas. Therefore, under shear, it was not possible to distinguish, through visual observations, any differences in the oil solubilization behavior between the different parts of the equilibrium cut (high, int, and low). The phase diagram is thus considerably simpler.

SANS Experiments under Shear. To follow the structural changes induced by shear, we performed small-angle neutron scattering experiments using a bulk contrast with the system $C_{16}E_8$ /hexadecane/ D_2O . The sample was placed in the Couette cell, with a 500 s^{-1} rotation speed, and scattering curves were recorded as the temperature was increased. The scattering

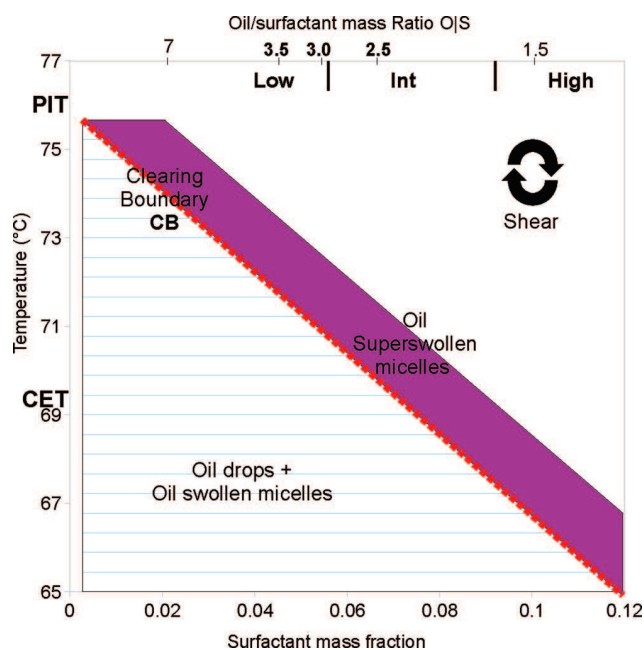


Figure 3. Cut of the phase prism under shear for $O|W = 0.2$ in the hexadecane/ $C_{16}E_8$ / H_2O system. When D_2O is used instead of H_2O , this cut is shifted to lower temperatures by $2\text{ }^\circ\text{C}$.

patterns consisted of a small region of very intense scattering next to the beam, confined to q values below $3 \times 10^{-3}\text{ \AA}^{-1}$, corresponding to distances beyond 200 nm, and a large region of less intense scattering away from the beam, extending to q values reaching $2 \times 10^{-2}\text{ \AA}^{-1}$, corresponding to distances around 10 nm. No anisotropic scattering was detected in either region; therefore, we performed azimuthal regrouping to obtain scattering curves of the scattered intensity versus the magnitude of the scattering vector q . Anisotropic scattering was detected only in the immediate vicinity of the PIT ($\pm 1\text{ }^\circ\text{C}$).

Figure 4 presents sets of scattering curves obtained upon raising the temperature, in which these two components appear clearly. In each set, the relative magnitudes of the two components vary in opposite directions, and the scattering curves intersect at an isosbestic point. These features indicate that the scattering is produced by two coexisting populations, which we call micelles (10 nm) and drops (>200 nm). According to these observations, the complete set of scattering curves can be reproduced on the basis of eqs 1–7, as discussed next.

Assuming that the large drops and small micelles are uncorrelated, the total intensity, I_{total} , is the sum of the two contributions from large drops, I_{drops} , and small micelles, I_{micelles}

$$I_{\text{total}} = I_{\text{drops}} + I_{\text{micelles}} \quad (1)$$

Because polydispersity is quite low and can be taken into account in the form factor only, we calculate the scattered intensity from spherical micelles of radius R_{micelles} using a decomposition into a form factor and a structure factor. We use a spherical form factor with a Schultz distribution, $P_S(q)$, and a hard-sphere structure factor, $S_{HS}(q)$, derived from the Percus–Yevick integral equations, because the surfactant coronas repel each other, at temperatures below the PIT

$$I_{\text{micelles}} = \phi_{\text{micelles}} (4\pi/3) R_{\text{micelles}}^3 S_{HS}(q) P_S(q) \quad (2)$$

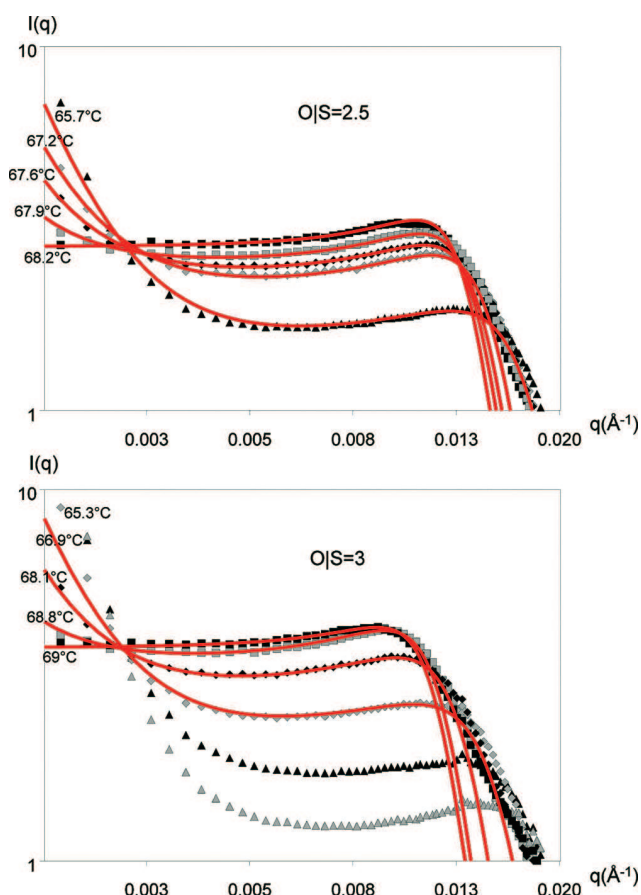


Figure 4. Scattering curves of samples sheared in a Couette cell (shear rate = 500 s^{-1}) upon increasing temperature. Two compositions for the $\text{D}_2\text{O}/\text{hexadecane}/\text{C}_{16}\text{E}_8$ system were used, namely, $\text{O|S}=2.5$ and $\text{O|S}=3$, corresponding to an int path and a low path, respectively, according to Figure 2. Two components are visible, one at low q values that corresponds to large drops (distances beyond 200 nm) and one at higher q values that corresponds to small micelles (distances around 10 nm). Upon increasing the temperature, the intensity scattered by the micelles increases, and the position of the micelle structure peak shifts toward lower q values, which shows that they grow in size. In contrast, the intensity scattered by the drops decreases to 0. This occurs at the clearing boundary temperature, where the scattering is produced only by the micelles. Red lines are fits obtained using the model detailed in this section.

The scattered intensity from spherical large droplets of radius R_{drops} can be expressed with a modified Fisher–Burford expression⁸ for the form factor $P_{\text{FB}}(q)$. This expression allows one to reproduce simply the asymptotic scattering of objects that are extremely polydisperse

$$I_{\text{drops}} = \phi_{\text{large}} (4\pi/3) R_{\text{drops}}^3 P_{\text{FB}}(q) \quad (3)$$

As the surfactant sets the spontaneous curvature of the micelles, their radius is given by a linear variation with temperature. Assuming that this relation is not changed by shear, one can write

$$1/R_{\text{micelles}} = K(\text{PIT} - T) \quad (4)$$

The dispersed phase consists of the drops and the micelles and the total volume of this phase is constant, which yields a sum rule for the volume fractions

$$\phi_{\text{drops}} + \phi_{\text{micelles}} = \phi_{\text{total}} \quad (5)$$

Another sum rule results from the fact that drops and micelles contain the oil and the surfactant, respectively. Therefore

$$\phi_{\text{total}} \approx \phi_{\text{oil}} + \phi_{\text{surfactant}} \quad (6)$$

We approximate that all of the surfactant was localized on the micelles and assume that the $N_{\text{surfactant}}$ molecules, with a constant area per head of a_0 , were localized on the micelles. Indeed, the specific area of the micelles is 100 times larger than that of the large drops; hence, the micelles have nearly all of the surface area

$$\phi_{\text{micelles}} \approx \frac{R_{\text{micelles}} a_0 N_{\text{surfactant}}}{3V_{\text{total}}} \quad (7)$$

Equations 1–7 contain many parameters, and it is useful to see which ones are in fact constrained. For this system, $a_0 = 62 \text{ \AA}^2$, $K = 6.5 \times 10^{-3} \text{ K}^{-1} \text{ nm}^{-1}$, and $\text{PIT} = 74.2 \text{ }^\circ\text{C}$. For a given composition, ϕ_{oil} and $\phi_{\text{surfactant}}$ are set. Therefore, ϕ_{total} is set by eq 7. For a given temperature, R_{micelles} is set by eq 4. Hence, ϕ_{micelles} is set by eq 7. Finally, ϕ_{drops} is set by eq 5. This leaves only two unconstrained parameters: R_{drops} and the polydispersity of the micelles, contained in the form factor $P_{\text{S}}(q)$. R_{drops} has little physical significance; indeed, it depends on the shear rate and relates to a very high polydispersity. Typically, R_{drops} is taken to be around $100 \text{ }\mu\text{m}$. Concerning the polydispersity, it is easily obtained by fitting the phase diagram curves, which yields $\sigma_{R_{\text{micelles}}}/R_{\text{micelles}} = 0.10$ far from the PIT and 0.18 at higher temperatures, which is the typical order of magnitude for micelles.

The two-component model reproduces the whole set of scattering curves over most of the q range, although all of the significant parameters are constrained, which shows a good adequacy between the model and the experimental data. At high q values, the model exhibits a significant deviation from the experimental scattering curve. This occurs at q values where the form factor for spherical micelles has a strong oscillation, which is an indication that the “micelles” in the CB states have structures that are not perfectly spherical.

Whatever the composition (i.e., the equilibrium behavior, low and int), there exists one temperature at which all of the oil is solubilized in swollen micelles under shear. From these scattering curves, it is possible to define the clearing boundary in an alternate way: It is the solubilization boundary under shear where only one population of small objects is detected in the scattering patterns. It is worth noticing that this boundary is in good agreement with that obtained through visual inspections. (This was verified on the same samples and can be visualized on the phase cuts of Figures 2 and 3 provided that a $2 \text{ }^\circ\text{C}$ shift is applied to account for the replacement of H_2O by D_2O .)

Clearing Boundary As a Minimum in Turbidity. To understand the visual inspections and the SANS experiments in the same model, we performed light scattering experiments. The sample was placed in a quartz cell, and a small stir bar was added as described in the Methods section. The temperature was controlled with a Peltier device. The variations of turbidity with temperature are shown in Figure 5a. The clearing boundary is then defined as the temperature where the turbidity reaches its lowest value. This makes it possible to draw a master curve by plotting the turbidity [i.e., the logarithm of the ratio of the initial intensity to the transmitted intensity, $\log(I_0/I)$] as a function of $T - T_{\text{CB}}$. This can be related to the SANS results by plotting the volume fractions of micelles and drops as functions of temperature. Again, a master curve can be obtained by plotting the volume fractions as functions of $T - T_{\text{CB}}$, as is done in Figure 5b for $\text{O|S}=2.5$ and $\text{O|S}=3$. One can see that, as the temperature

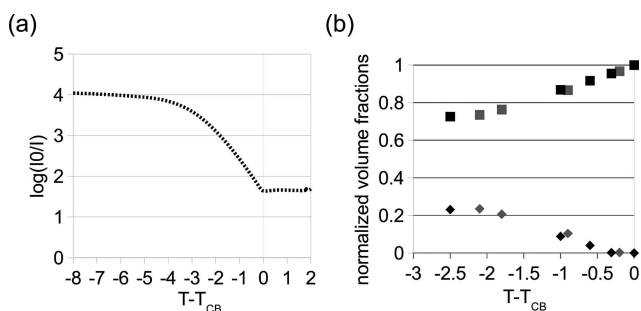


Figure 5. Evolution with temperature of (a) the turbidity of samples for the H_2O /hexadecane/ $C_{16}E_8$ system under shear and (b) $\phi_{micelles}$ (squares) and ϕ_{drops} (diamonds) for $O|S = 2.5$ (black) and $O|S = 3$ (gray) for the D_2O /hexadecane/ $C_{16}E_8$ system, as deduced from the fitting procedure of Figure 4. As the temperature approaches the clearing boundary, solubilization of the oil into the micelles increases (i.e., $\phi_{micelles}$ increases), and large drops vanish (i.e., ϕ_{drops} decreases). As the drops scatter light much more strongly than the micelles, this leads to a sharp decrease in the turbidity of the sample.

increases, the turbidity and the volume fraction of drops decrease, whereas the volume fraction of micelles increases. This is because the light scattering is produced mainly by the drops. Therefore, at the clearing boundary, where drops disappear and only micelles are present, the turbidity is minimal. Therefore, turbidity measurements are also a good way to visualize shear-induced solubilization processes.

CB States and Quenched Emulsions. As observed above, regardless of which pathway is considered (i.e., low, int, or high surfactant concentrations), the shear-induced behavior is similar. However, when shear is stopped at the clearing boundary, only in the high situation does the system retain its structure. In the low and int situations, when shear is stopped, some oil is expelled within a few minutes. Therefore, it is impossible to keep and use these states as such. However, it is known⁷ that, in the high case, the system can be quenched by rapid cooling and retains its structure while acquiring metastability. Therefore, we investigated similar processes in the low case for two compositions using the previous SANS setup in the CB and separate cells for the quenched emulsions.

The first composition was $O|S = 3$ for the D_2O /hexadecane/ $C_{16}E_8$ system, which gives a “bulk” contrast. The CB-state scattering curve was the same as that shown in Figure 4 for the highest temperature of the set at $O|S = 3$. The “quench” scattering curve was obtained from the same sample after it was cooled rapidly to 25 °C. The scattering curves of the CB state and of the quenched emulsion are compared in Figure 6. The fit was obtained from the model presented in the section SANS Experiments under Shear.

The second composition was $O|S = 3.5$ for the D_2O /deuterated hexadecane/ $C_{16}E_8$ system, which gives a “shell” contrast. The sample was prepared in a vial and then transferred to the Couette cell. Its scattering curve was recorded when the sample appeared to be visually homogeneous (see Figure 1). Then, the sample was transferred back to a vial, kept at the CB temperature, and then cooled quickly by putting the vial in an ice/salt bath. The sample was then transferred to a 1-mm cuvette, and its scattering curve was again recorded. The scattering curves of the CB state and of the quenched emulsion are compared in Figure 7. The two scattering curves were fitted using the procedure using a core–shell model for polydisperse hard spheres with a Schulz distribution as described by Nayeri et al.⁹

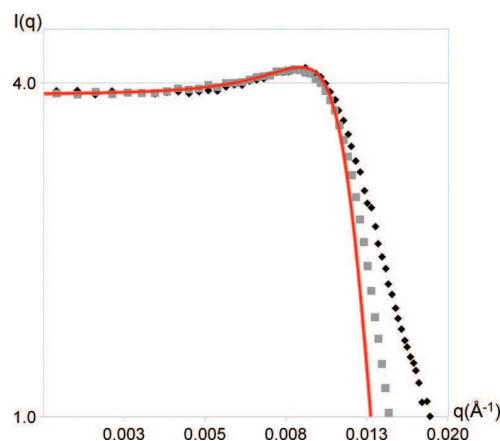


Figure 6. Comparison of two SANS scattering curves for a sample at $O|S = 3$ for the D_2O /hexadecane/ $C_{16}E_8$ system. Black diamonds correspond to the scattering curve at $T = 69$ °C, shown in Figure 4, that is, when the sample was stirred at the clearing boundary. Gray squares correspond to the sample after a temperature quench and in the absence of shear. The fit was done using the model presented in Figure 4.

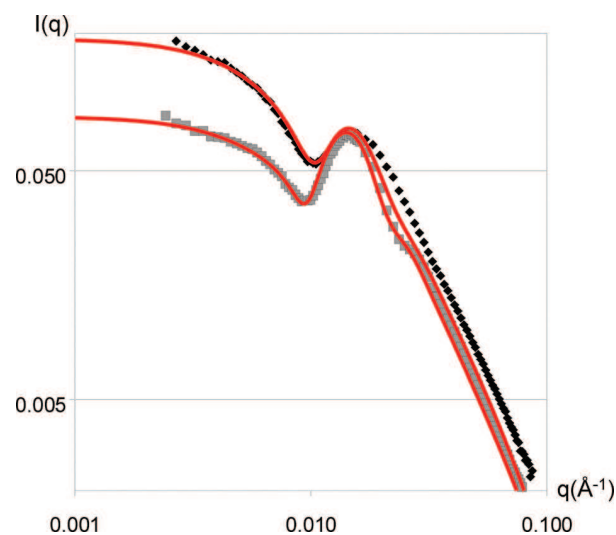


Figure 7. Comparison of two SANS scattering curves for a sample at $O|S = 3$ for the D_2O /deuterated hexadecane/ $C_{16}E_8$ system. Black diamonds correspond to the scattering curve of the sample under shear at the clearing boundary. Gray squares correspond to the sample after a temperature quench and in the absence of shear. Fits were realized using a core–shell model, described by Nayeri et al.,⁹ with the parameters provided in the Supporting Information.

In the bulk contrast, the peaks are at the same position for the CB state and the quench state. In shell contrast, the oscillations due to the contrast inversion between core and shell are also at the same position for the CB and quench states. This shows that the numbers of droplets are the same in the two states and, therefore, that the volumes per droplet are the same.

DISCUSSION

Throughout this work, we have identified a line, the clearing boundary, where the system is a superswollen microemulsion, that is, a microemulsion swelled with excess oil, when shear is

applied. Because the CB temperatures are a few degrees below the PIT, it could be argued that this boundary is related to very low values of the interfacial tension. The formation of super-swollen microemulsions would therefore result from the fine fragmentation of an excess oil layer in the microemulsion. In our SANS experiments, the clearing boundary was defined as the line where a population of swollen micelles and a population of large oil drops merge together to form a homogeneous system, which is a superswollen microemulsion. This is displayed in Figures 4 and 5 by the vanishing of the scattering from the large drops and the shift of the peak for the swollen micelles. This leads to the conclusion that such states result from a solubilization process and not from a fragmentation process. Furthermore, if the CB states were obtained through fragmentation of the excess oil, the scattering pattern would show anisotropy. We observed that this was the case only in the immediate vicinity of the PIT, but not around the CB. This finding supports previous arguments² that rule out the effect of low interfacial tensions in our case.

Therefore, the first aim of this discussion is to understand how shear competes with phase separation to promote homogeneous states rather than multiphase ones. This is done by examining the different microemulsion structures at all of the relevant boundaries. The effect of shear is then discussed in terms of relative destabilization of these structures. Then, in a second subsection, we examine the possibility of keeping the superswollen microemulsions in a metastable state while retaining their structures.

Shear versus Phase Separation. In this section, we discuss the remarkable simplification of the phase behavior that takes place upon increasing the temperature when the system is constantly sheared. It consists of a striking extension of the spherical microemulsion phase to lower surfactant concentrations, as demonstrated by comparing Figure 2 with Figure 3.

First, it is useful to notice that the changes are restricted to areas a few degrees below the PIT. There, the spontaneous curvature is low enough to allow other structures in addition to spheres. Depending on the total interfacial area, which is linked to the amount of surfactant in the system, several structures can indeed be obtained. At high surfactant concentrations (i.e., high interfacial areas), spheres are favored. However, at intermediate and low surfactant concentrations, bicontinuous structures are preferred, as seen in Figure 2. Therefore, the rich phase behavior just below the PIT, visible in Figure 2, results from the composition-dependent choice between structures at the same curvature.

However, under shear, this complicated phase behavior collapses to a single possible structure, which consists of oil spheres covered by surfactant. In the following discussion, our aim is to answer four main questions arising from this shear-induced transition:

- (1) How can one understand the location of the shear-induced boundary that we named the clearing boundary?
- (2) How does shear promote spherical over bicontinuous structures?
- (3) How can one understand the shift of the phase boundary associated with bicontinuous structures?
- (4) Can a minimal shear rate for this transition be deduced?

Question 1 can be easily understood by considering the clearing boundary to be the direct extension of the equilibrium boundary between the Winsor I and spherical microemulsion regions. (This solubilization boundary is also called the emulsification

failure boundary,¹⁰ as it separates a single-phase spherical microemulsion from a spherical microemulsion coexisting with excess oil.) In the Winsor I region, far below the PIT, the system consists of oil-swollen micelles in water (spherical microemulsion) coexisting with excess oil. The first obvious effect of shear is the fragmentation of the oil layer into large drops, as in a classical emulsification process. These drops are responsible for the main light scattering, and turbidity, of the sample shown in Figure 5, as well as the strong neutron scattering near the beam stop (see Figure 4). Such drops have a very small area; hence, their contribution to the total free energy is very small. Observation of Figure 4 shows that, for each composition, there is a temperature at which the large drops are solubilized into the micelles, namely, the clearing boundary temperature. Indeed, upon increasing the temperature, the spontaneous curvature decreases, and thus, the micelles grow in size and solubilize more oil. At this boundary, the system is homogeneous, as shown in Figure 1, and its turbidity is minimal, as shown in Figure 5. Second, the spherical microemulsion is not disrupted by the low-intensity shear, and the droplets remain largely unchanged in sizes and shapes. The set of equations used to fit the curves of Figure 4 show that the micelles have a spherical spontaneous curvature of C_0 as their radius follows eq 4 and the typical diameter corresponds to the composition radius R^* , which is the radius associated with monodisperse spheres covered by surfactant for a given composition. This is in agreement with our previous work,² in which we proposed the following equation for the clearing boundary

$$R^*C_0 = 1 \quad (8)$$

This behavior is well-known in the high region, where it occurs at equilibrium (i.e., in the absence of shear). However, its extension to all compositions (i.e., the int and low regions) shows that shear induces structural transformations.

To answer question 2, we propose to describe these transformations in terms of the shear stabilities of bicontinuous and spherical structures. Small spherical structures are not influenced by the shear applied to the system in our experiments: the spherical microemulsion boundary does not shift when shear is applied. In the low and int regions, however, bicontinuous structures for microemulsions are favored at equilibrium, and shear-induced transitions take place. This demonstrates the instability of the bicontinuous structures in shear flow, which is consistent with the geometrical view of such structures, where the connections break under the flow, and with experiments performed in shearing sponge phases, which yield lamellar phases in a similar process.¹¹ Therefore, under shear, the system's only choice is to form spherical structures.

The issue now is to understand how this results in super-swelling behavior, which is question 3, as emphasized by the shift of the solubilization boundaries to lower surfactant concentrations. This super-swelling behavior is visible by the observation of the microemulsion boundary in Figure 2, which clearly shows a transition between spherical and bicontinuous structures at the critical end-point temperature. To make the reasoning easier, we focus on the int region of the phase diagram. For a given spontaneous curvature (i.e., temperature), a comparison of the clearing boundary (solubilization boundary under shear) and the microemulsion boundary (solubilization boundary at equilibrium) shows that the clearing boundary corresponds to a lower value of the surfactant concentration. This is consistent

with the observation that a system at the CB will separate into a bicontinuous microemulsion and excess oil when shear is stopped. We now demonstrate that this results from the geometrical difference between the two structures. The interface curvature for both geometries can be modeled by assuming a homogeneous system, namely, at the spontaneous curvature. Assuming saddle splay constant equals zero and a perfectly monodisperse structure, the curvature for spheres is given by²

$$H_{spheres} = \frac{\phi_s}{3l_s\phi_o} \quad (9)$$

where ϕ_s and ϕ_o are the surfactant and oil volume fractions, respectively, and l_s is the surfactant length. Describing the bicontinuous structure is obviously more difficult as many structures can be encountered. Furthermore we are dealing here with very asymmetric bicontinuous structures. In this case the structure can be described more conveniently by interconnected cylinders than surfaces of constant mean curvature.¹² Assuming the distance between branch points is long compared to the tube diameter, we can neglect the branch points in the calculation of the average mean curvature and obtain a simple expression of the mean curvature:

$$H_{cylinders} = \frac{\phi_s}{4l_s\phi_o} \quad (10)$$

If we set the temperature, i.e. the spontaneous curvature, we can calculate the composition difference between the spherical and bicontinuous structure by equating these two equations:

$$\frac{\phi_s^{sph}}{3l_s\phi_o^{sph}} = \frac{\phi_s^{cyl}}{4l_s\phi_o^{cyl}} \quad (11)$$

For a given temperature, the composition at the clearing boundary, which corresponds to a spherical structure, is known. Therefore, one can calculate from eq 11 the composition associated with a bicontinuous structure of the same mean curvature. In Figure 8, we display both calculated curves for the spherical structure and the bicontinuous structure boundaries and compare them to experimental data. This figure shows that the typical boundaries can indeed be reproduced based on simple and purely geometric considerations. This demonstrates that the superswelling behavior can be readily explained by a structural transition from bicontinuous to spherical structures.

Finally, we expect that a minimal shear rate is required to break the bicontinuous structure into spheres (question 4). Experiments performed in 4 mL vials with small stir bars showed that very gentle shear is sufficient. We expected the Couette setup to give a precise value, but unfortunately, in such a setup, low shear rates give rise to concentration gradients (due to differences in the densities of the oil and the water phases) and temperature gradients (as the heating device is placed in the middle of the cell). Therefore, it is possible to give only an upper limit: all experiments performed above 250 s^{-1} were successful in obtaining a spherical microemulsion. This upper limit is far below the shear rates required to obtain droplet diameters in the 10–100-nm range.¹³ We can conclude however, that this shear rate is sufficient to break the bicontinuous structure, which gives rise to the superswelling behavior and leads to the solubilization of the excess oil.

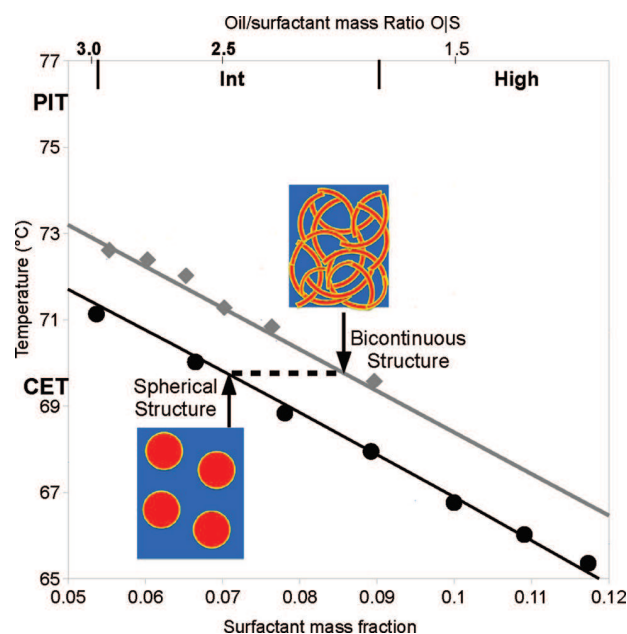


Figure 8. Calculated boundaries and experimental data corresponding to both spherical and bicontinuous structures. The black line corresponds to the calculation of the clearing boundary,² and the black dots are the experimental determinations of the clearing boundary displayed in Figure 3. The gray line was calculated from the black line using eq 11, and the gray diamonds are the experimental determinations of the bicontinuous microemulsion boundary displayed in Figure 2.

Quenching and Structure Conservation. The CB states have interesting properties, as they require lower amounts of surfactants than equilibrium microemulsions for a given amount of oil, as can be seen in the phase cuts in Figures 2 and 3. Therefore, they are superswollen microemulsions, namely, homogeneous oil/surfactant/water systems at surfactant concentrations below the fish knot. However, these shear-induced states quickly revert to the equilibrium structure at rest, and typically, the destabilization occurs within a few minutes. A possible description of their destabilization is that arms of bicontinuous structures quickly grow back from the stubs on the droplets and expel some oil. As it is not practical to keep a system under shear, it is of interest to put it in a metastable state while retaining its structure. We have shown above that this can be done by a rapid temperature quench that retains the main structures. Indeed, at low temperatures (i.e., high spontaneous curvatures), the driving force to form a bicontinuous structure no longer exists: the arms can no longer grow back.

The CB states thus provide access to metastable nanoemulsions. This is, in fact, the sub-PIT method as described in ref 2. Its main interest is in the possibility of obtaining quenched superswollen microemulsions, that is, states that cannot be obtained under equilibrium conditions. This makes it possible to quench microemulsions that have average diameters of up to 100 nm instead of 30 nm. In addition, the mean diameter can be simply tuned by the oil/surfactant ratio through eq 9, which yields a method to produce size-controlled emulsions. Furthermore, the simplification of the phase diagram provided by shear allows easier exploration of different systems. Also it is worth noticing that the nonequilibrium transformation taking place in this process is actually close to equilibrium, so that much knowledge about the

workability of a system in such a process can be deduced from equilibrium studies.

■ CONCLUSION AND PERSPECTIVES

One of the outstanding questions about the phase behavior of oil/water/surfactant systems is to understand why spherical microemulsions all have a maximum diameter of around 30 nm. In this work, we have emphasized the importance of the spherical-to-bicontinuous transition with respect to the swelling behavior. We show that shearing a bicontinuous microemulsion coexisting with at least excess oil gives rise to the formation of a superswollen spherical microemulsion, which results from simple geometric considerations. This allows the preparation of steady-state microemulsions of larger sizes and lower surfactant contents that can be kept in a metastable state by rapid cooling. A question that remains is a precise description of the structural pathway that leads to these homogeneous states.

■ ASSOCIATED CONTENT

S Supporting Information. Fit parameters used in Figure 7. This material is available free of charge via the Internet at <http://pubs.acs.org>.

■ AUTHOR INFORMATION

Corresponding Author

*E-mail: kevin.roger@espci.fr.

■ ACKNOWLEDGMENT

The authors thank David Bowyer for his help in the use and modifications of the Couette cell device and Professor Sam Safran for useful advice.

■ REFERENCES

- (1) Kahlweit, M.; Strey, R.; Haase, D.; Firman, P. *Langmuir* **1988**, *4*, 785–790.
- (2) Roger, K.; Cabane, B.; Olsson, U. *Langmuir* **2010**, *26*, 3860–3867.
- (3) Kunieda, H.; Shinoda, K. *J. Dispersion Sci. Technol.* **1982**, *3*, 233–244.
- (4) Wennerström, H.; Balogh, J.; Olsson, U. *Colloids Surf. A* **2006**, *291*, 69–77.
- (5) Kabalnov, A.; Wennerström, H. *Langmuir* **1996**, *12*, 276–292.
- (6) Lindner, P.; Oberthür, R. *Rev. Phys. Appl.* **1984**, *19*, 759–763.
- (7) Morris, J.; Olsson, U.; Wennerström, H. *Langmuir* **1997**, *4*, 606–608.
- (8) Fisher, M.; Burford, R. J. *Phys. Rev.* **1967**, *156*, 583–622.
- (9) Nayeri, M.; Zackrisson, M.; Bergenholtz, J. *J. Phys. Chem.* **2009**, *113*, 8296–8302.
- (10) Safran, S.; Turkevich, L. *Phys. Rev. Lett.* **1983**, *50*, 1930–1933.
- (11) Olsson, U.; Mortensen, K. *J. Phys. II France* **1995**, *5*, 789–801.
- (12) Olsson, U.; Würz, J. U.; Strey, R. *J. Phys. Chem.* **1993**, *97*, 4535–4539.
- (13) Walstra, P. *Chem. Eng. Sci.* **1993**, *48*, 333–349.

Why Are Hydrophobic/Water Interfaces Negatively Charged?*

Kevin Roger* and Bernard Cabane

Interfaces between water and apolar media (gases, liquids, or solids) have a high cost in free energy. Therefore they tend to recombine to reduce the total interfacial area: in water, oil drops coalesce and air bubbles recombine following collision. The metastability of emulsions, foams, and polymer dispersions is achieved through adsorption of amphiphilic molecules (ionic or non-ionic), macromolecules, or particles, which block the recombination. The mechanisms of this stabilization are well understood.^[1] Yet very fine emulsions made of pure oil droplets in pure water have also been found to be metastable in the absence of any added stabilizers.^[2–4] According to sum frequency generation (SFG) spectroscopy^[5] and electrophoretic mobility measurements,^[2,3] the droplets of these surfactant-free emulsions are ionized and carry a negative electrical charge. Similar results have been reported for the water/air interface.^[6–8] Moreover, this negative charge increases rapidly with pH value and therefore with the bulk concentration of hydroxide ions.^[2,4,9]

The most frequent explanation given for these phenomena is that hydroxide ions adsorb at hydrophobic/water interfaces. While consistent with the pH signature of these phenomena, this explanation requires high adsorption energies, more than 20 times the thermal energy $k_B T$ (about 50 kJ mol⁻¹),^[2,6] and an outstanding selectivity of hydroxide ions over other simple anions^[2,6,10,11] that do not adsorb at such interfaces. On the theoretical side, some models attempt to account for this unexpected adsorption,^[12–14] while others find no accumulation of hydroxide ions at hydrophobic interfaces;^[15] still, other models look for another origin of the surface charge.^[16] At present, there is no clear and straightforward understanding of this intriguing phenomenon.

The basic assumption of all previous experimental and theoretical studies has been that these systems have “pristine” oil/water interfaces, that is, oil molecules in contact with water molecules, although the possibility of contamination by anionic, surface-active impurities has been mentioned.^[17] This assumption is supported by the use of pure components (99%) with additional purification, thoroughly cleaned glassware and equipment, inert atmospheres, and good reproduc-

ibility of the data. Moreover, the same variation with pH value of the surface charge has been found by different research groups with various experimental systems. However, the question remains whether these results leave no other choice but to accept a specific adsorption of hydroxide ions at hydrophobic interfaces? We propose that an alternative mechanism could be a reaction of hydroxide ions with species that are confined to the interface.

We conducted systematic experiments to find out whether such alternative explanations could account for all the published experimental results. We used emulsions obtained through a solvent-shifting method.^[18–20] Solutions of hexadecane, of different purities, were prepared at a constant volume fraction of 10⁻³ in 99.9% pure acetone. They were then mixed with a much larger volume ($\times 20$) of Milli-Q water. The supersaturated solution separated spontaneously, yielding nanometer-sized hexadecane droplets (average diameter approximately 150–200 nm). This process is particularly well suited to the study of the stability of hydrophobic/water interfaces, because the droplets grow through a recombination mechanism that ends when their interfaces acquire a sufficient number of stabilizing ions. Hence, both final size and polydispersity of the nanometer-sized droplets decrease upon increasing the concentration of stabilizing ions. The final sizes of the droplets can also be controlled through the concentration of oil in acetone and the rate of addition of the acetone/oil solution into water.

We performed three types of experiments using these emulsions. First, we measured the electrophoretic mobility of oil droplets in emulsions made with different oils, as a function of the pH value of the aqueous phase (Figure 1). In these experiments, the emulsification process was adjusted so that the average droplet size was the same in each emulsion. The only difference between the three emulsions was the composition of the oil.

The first emulsion was made with 99% pure hexadecane in water at pH 6, ionic strength $I = 10^{-3}$ mol L⁻¹ (sodium chloride), and with a mean droplet diameter was 170 nm. Then we varied the pH value and measured the electrophoretic mobility of the oil droplets, using a Malvern Zetasizer. We found that the pH variation (Figure 1), reproduced the signature of the surface-charging process described in previous studies.^[2,4] The mobility was close to zero at pH 2–3, increased in magnitude until pH 8, and subsequently remained constant. If this variation was due to the adsorption of hydroxide ions, previously used models immediately show that their adsorption free energy would be above 20 $k_B T$.^[2,6] We checked that the addition of other small anions (halides or carboxylates) did not produce any changes in the electrophoretic mobility, as had been reported.^[6,11] Therefore the change in surface charge detected is specific to the concentration of hydroxide ions.

[*] K. Roger, Dr. B. Cabane
PMMH, CNRS UMR 7636, ESPCI
10 rue Vauquelin, 75231 Paris cedex 05 (France)
E-mail: kevin.roger@espci.fr

Dr. B. Cabane
Theoretical Chemistry, Lund University
222100 Lund (Sweden)

[**] This work was supported by ANR 2010 BLAN 942 03 “LimOuzIne”. We thank F. Ganachaud, B. Jönsson, G. Karlström, and H. Wennerström for useful discussions and input and C. Labbez and D. Bouttes for their help on the pH-dependence calculation of the surface potential.

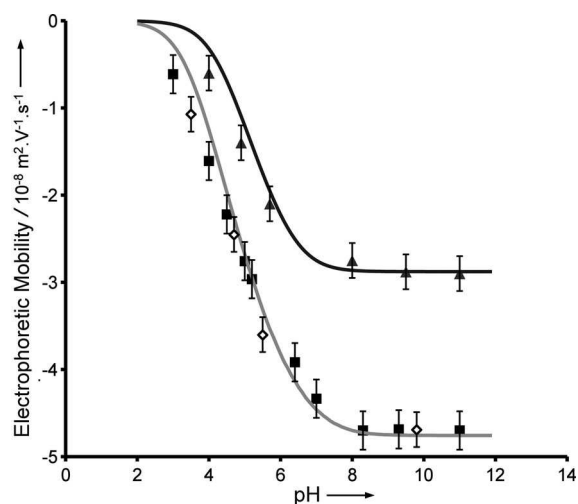


Figure 1. Variation of the electrophoretic mobility of hexadecane droplets with pH value, at a constant ionic strength of 1 mmol L^{-1} adjusted with NaCl. Emulsions were obtained through solvent-shifting using 99% pure hexadecane (■) or 99.8% pure hexadecane that was deliberately contaminated with oleic acid at a concentration of 5.8 mmol L^{-1} (◇) or also with fast mixing, using 99.8% pure hexadecane (▲). The mixing conditions were adjusted so that these three emulsions have the same mean diameter of 170 nm. Smooth lines are fit according to the model presented in the text, with a charging free energy of $20.7 k_B T$ or equivalently an acidity constant of $K_a = 10^{-3}$. The maximal surface densities of elementary charges are 0.25 nm^{-2} (■) and 0.034 nm^{-2} (▲), which correspond to stabilizer concentrations in the oil of 7.0 mmol L^{-1} (■) and 1.0 mmol L^{-1} (▲).

While the hydroxide ions are certainly important in the charging process, it is unlikely that they possess the amphiphilic behavior implied by high adsorption energies and ion specificity. To demonstrate that the surface charging is not caused by hydroxide ions alone, we performed solvent shifting using an oil with a different grade of purity: 99.8% pure hexadecane (also purchased from Sigma–Aldrich). The pH variation of the electrophoretic mobility of oil droplets in an emulsion made of 99.8% pure hexadecane is shown in Figure 1 (black triangles). With this oil, faster mixing conditions were needed to obtain the same mean droplet diameter of 170 nm. The curve is similar to the one obtained with 99% pure hexadecane, but the electrophoretic mobility has a smaller magnitude at each pH value. Since the ionic strength and the average droplet diameters are constant, this means that the surface charge density, and thus the concentration of stabilizing ions, was lower for the 99.8% pure hexadecane than for the 99% pure hexadecane.

In a second set of experiments, we compared the size distributions of emulsion droplets, using a Cordouan Vasco dynamic light scattering instrument (Figure 2). In this experiment, the emulsions were made using identical mixing conditions, and therefore in each emulsion the average droplet size was proportional to the amount of stabilizing ions available. While a low-polydispersity emulsion with nanometer-sized droplets was obtained using 99% pure hexadecane, a much coarser emulsion was obtained using 99.8% pure hexadecane. The respective interfacial areas are proportional to the amounts of stabilizing species available in

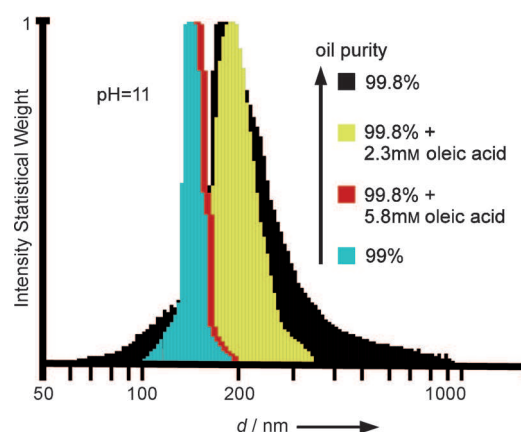


Figure 2. Normalized statistical size distributions obtained through dynamic light scattering measurements of emulsions at various oil purities and set hydroxide ion concentrations and mixing conditions.

either case, since the mixing conditions are the same. As the amount of hydroxide ions available was the same in both experiments, the difference shows immediately that another species was involved in the stabilization. Moreover, the mean diameter obtained with 99% pure hexadecane at pH 11 was smaller than that at pH 6. Accordingly, when a larger amount of hydroxide ions was available, more stabilizing molecules were also available. Therefore, the anionic stabilizers were not hydroxide ions but were produced by a reaction with hydroxide ions, which is a property of weak acids. Moreover, these weak acids are likely present as impurities in the oil and gradually removed during purification.

To quantify the traces of weak acids in both oils, we performed a third set of experiments, using a standard chemical titration method. We titrated 99% pure hexadecane and 99.8% pure hexadecane using a standard method for quantification of fatty acids in an oil.^[21] 10 mL of hexadecane were solubilized in 50 mL of a 1:1 mixture of 95% ethanol and diethylether and titrated by a 0.1 mol L^{-1} KOH solution in 95% ethanol. Phenolphthalein was used as a colorimetric indicator and the endpoint was obtained when the solution turned pink. The method was also checked against a hexadecane solution of known oleic acid concentrations and pure solvent. We obtained a weak acid concentration of $7.0 \pm 1 \text{ mmol L}^{-1}$ for 99% pure hexadecane and $1.0 \pm 1 \text{ mmol L}^{-1}$ for 99.8% pure hexadecane. This experiment therefore, provides a direct quantification of acid impurities in the oils. The value obtained for the 99% pure hexadecane compares well with the one that can be deduced from the electroacoustic titration experiment performed by Beattie and Djerdjev^[4] (9.0 mmol L^{-1} versus our measurement of 7.0 mmol L^{-1}).

To determine if the stabilizing species could be fatty acid ions, that is, surfactant with a carboxylate ion as the hydrophilic head, we added a common fatty acid, 99% pure oleic acid, to the 99.8% hexadecane at a concentration of 5.8 mmol L^{-1} (which, together with the intrinsic impurities of the 99.8% hexadecane, equals the concentration of impurities in the 99% hexadecane), and produced an emulsion through solvent-shifting with a mean diameter of

170 nm. The mobility/pH value curve of this contaminated emulsion (empty diamonds in Figure 1) was identical to that of the emulsion obtained with 99% hexadecane but different from the one obtained with the 99.8% hexadecane. This result means that the addition of oleic acid increases the surface charge density, and thus stabilizes the droplet, but does not change the pH signature of the electrophoretic mobility. Therefore the weak acids that are present in the oil, according to the titration experiment, are fatty acids. Another way to visualize this is to follow the evolution of the size distribution of the emulsion, prepared under identical mixing conditions, upon contamination with oleic acid. As shown in Figure 2, adding increasing amounts of oleic acid to the 99.8% hexadecane led to emulsions with progressively narrower distributions and smaller mean radii, matching the size distribution of the 99% hexadecane when the concentration of oleic acid in hexadecane reached 5.8 mmol L^{-1} . These two experiments support the idea that fatty acids react with hydroxide ions to yield the anionic stabilizing species.

We can now consider whether this model accounts quantitatively for all observations, particularly the variation of mobility with pH value, using a single parameter, which is the $\text{p}K_a$ value of fatty acids. For this purpose, we use the following relations: 1) pH to surface charge density, 2) surface charge density to surface potential, 3) surface potential to zeta potential, and 4) zeta potential to electrophoretic mobility.

To obtain relation 1, we must describe the acid–base equilibrium between fatty acids (RCOOH) and their anions (RCOO^-) at the oil/water interface. We use a mean field theory for calculating the activity of the fatty acid anions [Eq. (1)]

$$a_{\text{RCOO}^-} = \frac{\sigma}{\sigma_{\text{max}}} \exp\left(\frac{-e\psi_s}{k_B T}\right) \quad (1)$$

where σ is the surface density of elementary charges (m^{-2}), σ_{max} is the maximal surface density of elementary charges, ψ_s is the surface potential, k_B is the Boltzmann constant, T the temperature, and e the elementary charge. We define the acidity equilibrium constant, $K_a = (a_{\text{RCOO}^-} a_{\text{H}_3\text{O}^+})/a_{\text{RCOOH}}$ with $a_{\text{H}_3\text{O}^+} = 10^{-\text{pH}}$. The total amount of stabilizer being constant, $a_{\text{RCOOH}} = 1 - \sigma/\sigma_{\text{max}}$. This leads to Eq. (2)

$$\sigma = \sigma_{\text{max}} K_a / (K_a + 10^{-\text{pH}} \exp\left(\frac{-e\psi_s}{k_B T}\right)) \quad (2)$$

This expression contains only two parameters, the maximum surface charge density, σ_{max} , and a free energy $-k_B T \ln(K_a)$

In order to obtain relation 2, we use the Poisson–Boltzmann theory, as expressed in the Grahame Equation [Eq. (3)].^[1]

$$\frac{\sigma}{e} = \sqrt{8\varepsilon\varepsilon_0 k_B T I} \text{sh}\left(\frac{e\psi_s}{2k_B T}\right) \quad (3)$$

where $\varepsilon\varepsilon_0$ is the local dielectric constant and I is the ionic strength (number of ions per unit volume). There are no free parameters in this Equation, that is, the value of the surface charge uniquely determines the surface potential.

Obtaining relation 3 is more difficult since the zeta potential is defined at the shear plane, which is at a short distance, d , from the surface. The electrical potential at the shear plane is attenuated with respect to the surface potential by a factor that increases with the distance d between the surface and the shear plane. We calculate this factor using the Gouy–Chapman theory.^[1]

For relation 4, we did not use the simple linear Smoluchowski^[22] relation, since it holds only when the product of the Debye length and the droplet radius is much higher than unity, which is not the case in our experiments. Instead we used the analytical expression developed by O'Brien and Hunter,^[23] which is more accurate. There are no free parameters, and the mobility is uniquely determined by the zeta potential (note that the reverse is not true, and for this reason we present our results as mobility values rather than zeta potential values).

At this point, it is possible to calculate the electrophoretic mobility as a function of pH value, using all four relations. The free parameters are K_a , σ_{max} , and the distance between the surface and the shear-plane, d . Two fits were performed for the two hexadecane purities (99% and 99.8%). In both cases, we used $K_a = 10^{-5}$, which is the acidity constant for fatty acids and $d = 1 \text{ nm}$.^[24] Maximal surface densities of elementary charges were chosen according to the impurity concentrations determined through the titration experiments, $\sigma_{\text{max}} = 0.25 \text{ nm}^{-2}$ for 99% pure hexadecane and $\sigma_{\text{max}} = 0.034 \text{ nm}^{-2}$ for 99.8% (smooth lines in Figure 1). With these values of the parameters, this model provides a very good fit to the experimental data. However, it should be mentioned that only K_a is determined with excellent accuracy through this fitting procedure, whereas other acceptable fits are produced with simultaneously smaller values of d and larger values of σ_{max} . We therefore conclude that the variations in the surface charge with the hydroxide ion concentrations, as shown in Figure 1, can be explained by considering the acid–base reaction between hydroxide ions and fatty acids with an equilibrium constant $K = 10^9$, which corresponds to acids with an acidity constant of $K_a = 10^{-5}$. The free energy extracted from this curve is $20.7 k_B T$, which matches the free energy of a chemical reaction rather than that of an adsorption process.

These results demonstrate that hydroxide ions in water do not adsorb to hydrophobic interfaces, but rather react with traces of fatty acids, which have been dissolved in the oil and delivered to the interfaces. The accumulation of fatty acid anions through this acid–base reaction is at the origin of the negative charging of the hydrophobic/water interface and the cause of the metastability of surfactant-free emulsions.

The pH signature of this charging process is the acid–base titration curve of a carboxylic acid functional group, hence the similar pH value dependence observed for water/air interfaces may also be explained by the presence of fatty acid impurities. As those experiments were performed on large single bubbles, the available surface area was much smaller compared to our collection of nanometer-sized droplets.^[7] Consequently, the concentrations of trace carboxylic acids to produce a similar effect are much lower, and they are likely introduced from the glassware, water, and air. Moreover, if other surface-active species that possess ionized or ionizable

functional groups are also available, the charging will have a different origin, which will be displayed by a different pH signature. The procedures described in this work are thus an instructive way to examine any kind of hydrophobic/water interfaces to gain information on the origin of their surface charge.

Received: November 22, 2011

Revised: February 13, 2012

Published online: April 24, 2012

Keywords: carboxylic acids · colloids · electrophoresis · hydrophobic effect · interfaces

-
- [1] F. D. Evans, H. Wennerström, *The Colloidal Domain: Where Physics, Chemistry, Biology, and Technology Meet (Advances in Interfacial Engineering)*, Wiley-VCH, Weinheim, **1999**.
- [2] K. G. Marinova, R. G. Alargova, N. D. Denkov, O. D. Velev, D. N. Petsev, I. B. Ivanov, R. P. Borwankar, *Langmuir* **1996**, *12*, 2045–2051.
- [3] J. Stachurski, M. Michałek, *J. Colloid Interface Sci.* **1996**, *184*, 433–436.
- [4] J. K. Beattie, A. M. Djerdjev, *Angew. Chem.* **2004**, *116*, 3652–3655; *Angew. Chem. Int. Ed.* **2004**, *43*, 3568–3571.
- [5] R. Vácha, S. W. Rick, P. Jungwirth, A. G. F. de Beer, H. B. de Aguiar, J.-S. Samson, S. Roke, *J. Am. Chem. Soc.* **2011**, *133*, 10204–10210.
- [6] P. Creux, J. Lachaise, A. Graciaa, J. K. Beattie, A. M. Djerdjev, *J. Phys. Chem. B* **2009**, *113*, 14146–14150.
- [7] M. Takahashi, *J. Phys. Chem. B* **2005**, *109*, 21858–21864.
- [8] R. Vacha, V. Buch, A. Milet, J. P. Devlin, P. Jungwirth, *Phys. Chem. Chem. Phys.* **2007**, *9*, 4736–4747.
- [9] R. Zimmermann, U. Freudenberg, R. Schweiß, D. Küttner, C. Werner, *Curr. Opin. Colloid Interface Sci.* **2010**, *15*, 196–202.
- [10] G. V. Franks, A. M. Djerdjev, J. K. Beattie, *Langmuir* **2005**, *21*, 8670–8674.
- [11] J. K. Beattie, A. M. Djerdjev, G. V. Franks, G. G. Warr, *J. Phys. Chem. B* **2005**, *109*, 15675–15676.
- [12] R. Zangi, J. B. F. N. Engberts, *J. Am. Chem. Soc.* **2005**, *127*, 2272–2276.
- [13] A. Gray-Weale, J. K. Beattie, *Phys. Chem. Chem. Phys.* **2010**, *12*, 14364–14366.
- [14] K. N. Kudin, R. Car, *J. Am. Chem. Soc.* **2008**, *130*, 3915–3919.
- [15] R. Vacha, D. Horinek, M. L. Berkowitz, P. Jungwirth, *Phys. Chem. Chem. Phys.* **2008**, *10*, 4975–4980.
- [16] R. Vacha, D. Horinek, R. Buchner, B. Wintere, P. Jungwirth, *Phys. Chem. Chem. Phys.* **2010**, *12*, 14362–14363.
- [17] R. Vacha, V. Buch, A. Milet, J. P. Devlin, P. Jungwirth, *Phys. Chem. Chem. Phys.* **2008**, *10*, 332–333.
- [18] L. Taisne, P. Walstra, B. Cabane, *J. Colloid Interface Sci.* **1996**, *184*, 378–390.
- [19] H. Lannibois, A. Hasmy, R. Botet, O. A. Chariol, B. Cabane, *J. Phys. II* **1997**, *7*, 319–342.
- [20] J. Aubry, F. Ganachaud, J.-P. Cohen Addad, B. Cabane, *Langmuir* **2009**, *25*, 1970–1979.
- [21] ISO 660: 1983 E. *Animals and vegetable fats and oils—Determination of acid value and of acidity*, ISO, Geneva **1983**.
- [22] M. V. Smoluchowski, *Bull. Int. Acad. Sci.* **1903**, *8*, 182–200.
- [23] R. W. O'Brien, R. J. Hunter, *Can. J. Chem.* **1981**, *59*, 1878.
- [24] R. J. Hunter, *Zeta Potential in Colloid Science*, Academic Press, **1981**.
-

Uncontaminated Hydrophobic/Water Interfaces Are Uncharged: A Reply

Kevin Roger* and Bernard Cabane

carboxylic acids · colloids · interfaces · polymers · water

In our communication “Why are hydrophobic/water interfaces negatively charged?” we offer a simple explanation for the negative charge observed at hydrophobic interfaces with water.^[1] We demonstrate that traces of carboxylic acid surfactant at these interfaces account qualitatively and quantitatively for the properties of “surfactant-free” emulsions. This is a classic example of colloidal behavior where traces of surface-active substances can control the surface behavior and hence the macroscopic properties of the colloidal dispersion.^[2]

Our demonstration rests on three simple but solid experimental observations:

- 1) Through straightforward acid–base titrations we detect trace amounts of acids at a concentration of 7 mmol L^{-1} in 99 % pure hexadecane oil and 1 mmol L^{-1} in 99.8 % pure hexadecane oil. For 100 nm diameter droplets in an aqueous phase, with 99 % pure oil, the concentration that we detect yields a surface charge of 0.065 e nm^{-2} at pH 7.
- 2) We observe that these carboxylic acids accumulate at the interface of oil droplets in surfactant-free emulsions. Indeed, through electrophoretic mobility measurements we find a strong variation of the negative charge with pH, as reported by a large number of authors.^[5,6] The free-energy associated with this variation is 20 times the thermal energy kT , which matches exactly the reaction free-energy between hydroxide ions and carboxylic acids.
- 3) The key observation was obtained by comparing different emulsions made with the same method, at constant pH, but with two oils of different purity (99 % hexadecane and 99.8 % hexadecane). All other parameters being kept constant, the concentration of impurities changed dramatically the surface properties of the droplets and particularly their colloidal stability.

Roke et al.^[3] and Beattie et al.^[4] challenge our assessment of the concentrations of impurities in hydrocarbon oils. They both state that their own samples were pure, free of ionic

surfactant impurities. However, these two comments contradict each other since Roke et al. claim that they had no impurities in droplets made with 99 % hexadecane used as received, whereas Beattie et al. claim that their purification method is necessary to eliminate surfactant impurities from 99 % hexadecane.

At this stage the debate about hydrophobic/water interfaces has revolved mostly about the origin of surface charges carried by oil/water interfaces, with the assumption that these are “pristine” oil/water interfaces. However a central tenet of the models proposed by Beattie et al. and Roke et al. is that they apply to all hydrophobic/water interfaces. For Roke et al. the surface charge density originates from asymmetric charge transfer between the water molecules next to a hydrophobic interface.^[7] For Beattie et al. the surface charge originates from a Hamaker-like force driving the hydroxide ions to regions of low dielectric constant, such as hydrophobic interfaces.^[8] Both models predict a negative surface charge in the molecular layers next to the hydrophobic interface, irrespective of the precise chemical nature of the hydrophobic phase.

Therefore, according to both models, it should be possible to obtain metastable colloidal dispersions in water with other hydrophobic materials besides the hydrocarbon oils in which we found traces of carboxylic acids. In response, we repeated our previous experiments with hydrophobic polymers instead of hydrophobic oils. This method is indeed routinely used for synthesizing polymer nanoparticles.^[10] Polymethylmethacrylate (PMMA) was dissolved in acetone (good solvent), at a volume fraction of 10^{-3} , and then water (non-solvent) was added, which resulted in the formation of PMMA nanoparticles. We used two monodisperse PMMA: PMMA-COOH (weight average molecular weight $M_w = 9500 \text{ g mol}^{-1}$) where each endgroup of a macromolecule was a carboxylic moiety and PMMA-H ($M_w = 25000 \text{ g mol}^{-1}$) where each endgroup was a hydrogen atom. Through electrophoretic pH titrations we found that the nanoparticles of PMMA-COOH had surface charge densities in the order of 0.05 e nm^{-2} . This is far below what Beattie et al. predict for hydroxide ions at an interface (0.3 e nm^{-2}),^[4,6] and below what we obtained for 99 % hexadecane droplets (order of 0.15 e nm^{-2}).^[1]

The preparation method that we used^[1,10] is particularly well-suited for the study of interactions of hydrophobic/water interfaces, because the droplets grow through a recombination

[*] K. Roger, Dr. B. Cabane
PMMH, CNRS UMR 7636, ESPCI
10 rue Vauquelin, 75231 Paris cedex 05 (France)
E-mail: kevin.roger@espci.fr
Dr. B. Cabane
Theoretical Chemistry, Lund University
222100 Lund (Sweden)

mechanism that ends when their interfaces acquire a sufficient number of charges. Hence both final size and polydispersity of the nanoparticles decrease upon increasing the number of surface charges. We display in Figure 1 the variation of the

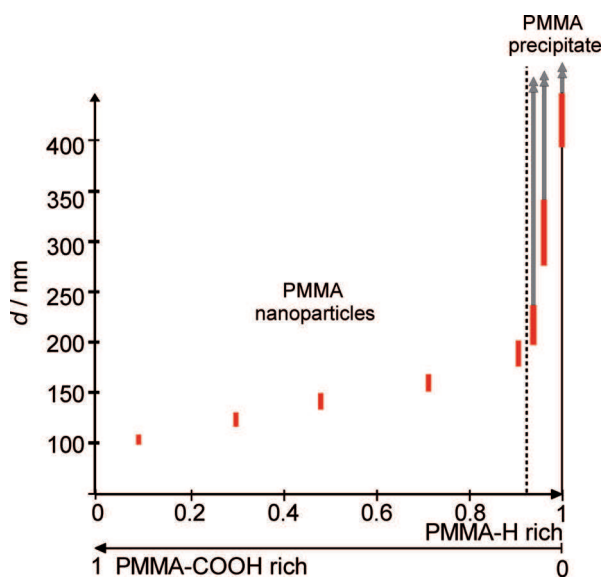


Figure 1. Diameter of nanoparticles prepared through solvent-shifting from solutions containing both PMMA with ionizable endgroups and PMMA with nonionizable endgroups. The pH was set at 10 and the ionic strength at $10^{-3} \text{ mol L}^{-1}$ with NaCl. At high fractions of the nonionizable PMMA-H, macroscopic aggregates coexisting with smaller particles were observed. If only PMMA-H was used, the nanoparticles formed macroscopic aggregates, indicating that their interfaces were not charged enough to provide colloidal stability.

PMMA particle diameter upon gradually replacing PMMA-COOH with PMMA-H, that is, decreasing the number of charged endgroups. The pH was set at 10 and the ionic strength was kept constant at $10^{-3} \text{ mol L}^{-1}$. First a regular increase of the diameter is observed, which follows from the decrease of the number of charged endgroups that stabilized the nanoparticles. A dramatic change occurs at higher fractions of PMMA-H where we observed the formation of macroscopic aggregates coexisting with smaller particles. If we used PMMA-H alone, the same method yielded only a macroscopic precipitate. Therefore the colloidal stability of the PMMA particles originated solely from the endgroups. This was confirmed by a colloidal stability calculation using the DLVO theory:^[2] the loss of colloidal stability with PMMA without charged endgroups was reproduced if the surface charge was below 0.005 e nm^{-2} . Therefore the surface charge of the PMMA-H/water interface is far below the surface charge of the hexadecane/water interface. This is incompatible with both models by Beattie et al. and Roke et al., each of which predicts similar surface charges for any type of hydrophobic interfaces.

We will now address separately the remaining points of the comments by Roke et al. and Beattie et al.

Roke et al.^[3] propose an explanation for the charging of the interface, caused by the orientation of water molecules at the interface. We disagree on the following grounds:

- 1) Through modeling of the charge transfer between water molecules near the interface, they estimate a surface charge density of -0.00014 to $-0.0028 \text{ e nm}^{-2}$. For 100 nm diameter droplets, this corresponds to (at the most) 9 charges per droplet, which is far too low to account for the colloidal stability of surfactant-free emulsions. On the contrary the traces of carboxylic acid we titrated in the oils correlate with the observed colloidal stabilities. Indeed, for 100 nm droplets of the 99% oil we find 2200 surface charges per droplet, which insures colloidal stability, as observed. Conversely, for 100 nm droplets of the 99.8% oil we find 315 surface charges per droplet, which yields marginal metastability, as observed.
- 2) They estimate quite different charge densities from electrophoretic mobility measurements, in the range of -0.008 to -0.42 e nm^{-2} . According to their theory, these surface charge densities should not depend upon the nature of the hydrophobe, and therefore the PMMA-H/water interface should carry the same surface charge, but it does not, as discussed above.
- 3) The spectroscopic observations of Roke et al. do not show any pH dependence. This is clearly stated in their comment:^[3] "Figure 1 A shows there is no change in the chemical surface structure at different pH values. We observe no additional interference, no new vibrational modes and no change in the water structure that would be reminiscent of the presence of ions upon changing the pH. Furthermore, spectra recorded with 99% and 99.8% pure oil showed the same results". This is in conflict with numerous reported electrokinetic measurements that show a strong pH dependence.^[5,6] We demonstrate that this pH dependence is the signature of the traces of carboxylic acids that we also find through acid–base titrations.
- 4) As cited above, Roke et al. did not find any difference between emulsions made with 99% pure oil or with 99.8% pure oil. This demonstrates that their method is not sensitive to traces of impurities adsorbed at the interface. They show that they can detect hexadecanoic acid at a concentration of 0.005 mol L^{-1} in water. With their oil volume fraction of 1%, the concentration of hexadecanoic acid in the oil must have been 0.5 mol L^{-1} . This concentration is enormous and much beyond the detection limit that they indicated.

To conclude, we think that the surface charge mechanism that is proposed by Roke et al. does not produce a charge of sufficient magnitude to account for the colloidal metastability of surfactant-free emulsions and does not reproduce the pH variation of this surface charge. Moreover, it is not consistent with the large surface charge differences between different hydrophobic interfaces such as PMMA and hydrocarbon oil. It may be that this surface charge mechanism exists, but in surfactant-free emulsions the corresponding surface charge is small compared with that from trace amounts of fatty acids, and in polymer nanoparticles it is small compared to that from the endgroups of the macromolecules.

Beattie et al. argue that our results describe the effects of both carboxylic surfactant impurities and hydroxide ions

adsorption. We disagree with their analysis on the following grounds:

- 1) Beattie et al. are “puzzled” that we did not try to purify our compounds, since they are confident in the purification method they use. We think that any purification method such as the exchange with an alumina column used by Beattie et al. reaches a limit in terms of the concentration of remaining impurities. In the first part of our response, we provided an example of uncontaminated hydrophobic/water interface, using hydrophobic polymer nanoparticles. As discussed above these uncontaminated interfaces must have surface charge densities at least two orders of magnitudes lower than those predicted by Beattie et al. for hydroxide ion adsorption.
- 2) Beattie et al. are concerned about the values of the surface charges we use. This is directed to our calculations of the number of surface charges from the concentration of impurities in the oil. The surface charge can be estimated through three different methods: titration, electrophoretic mobility, and colloidal stability. We agree with Beattie et al. that the determination of surface charges from electrophoretic mobility is imprecise. What matters is the relative magnitude of the surface charges for oils of different purity. We find a 7/1 ratio in the surface charges required to model the electrophoretic mobility of the two oils, which corresponds to a 7/1 ratio in the carboxylic acid concentration of these two oils. However we thank Beattie et al. for pointing out an imprecision in our communication: regarding electrophoretic mobility, the position of the slip-plane is unknown and thus the precise absolute value of the surface charge cannot be deduced from electrophoretic mobility measurements. Therefore the absolute surface charge values were not directly deduced from the titration experiment, only their relative values and an order of magnitude.
- 3) Beattie et al. state that for the 99% pure hexadecane, the surface charge density is 0.25 nm^{-2} , of which half (0.12 nm^{-2}) originates from fatty acids ionization and the other half (0.13 nm^{-2}) from hydroxide ions adsorption. This is based on an argument in which they compare the electrophoretic mobility of the 99% hexadecane with that of the 99.8% hexadecane. They argue that, since the

former contains 7 mmol L^{-1} of fatty acid, and the latter only 1 mmol L^{-1} fatty acid, the mobility ratio ought to be equal to the ratio of concentrations, that is, 7:1. This is of course wrong, since it is well-known that both the relation of mobility to surface charge density^[8] and the relation of the surface potential to the surface charge density^[2] are highly nonlinear. Their additional conclusion that the surface charge density of the 99.8% hexadecane originates mostly from hydroxide ions is then also in error.

To conclude, we believe that we provide a mechanism, which explains quantitatively the otherwise puzzling adsorption of hydroxide ions at hydrocarbon oil/water interfaces. Hydroxide ions react with fatty acids adsorbed on the interface. We also provide an example of uncontaminated hydrophobic/water interfaces, namely those of hydrophobic polymer particles, which are then uncharged.

Received: September 3, 2012

Published online: December 6, 2012

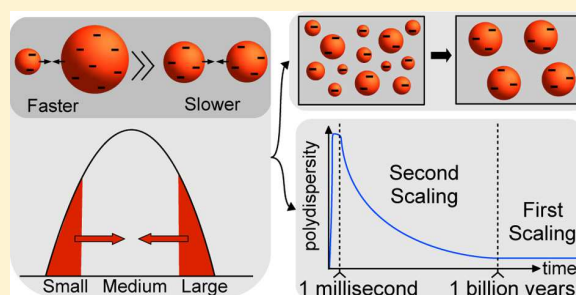
-
- [1] K. Roger, B. Cabane, *Angew. Chem.* **2012**, *124*, 5723–5726; *Angew. Chem. Int. Ed.* **2012**, *51*, 5625–5628.
 - [2] F. D. Evans, H. Wennerström, *The Colloidal Domain: Where Physics, Chemistry, Biology, and Technology Meet (Advances in Interfacial Engineering)*, Wiley-VCH, Weinheim, **1999**.
 - [3] K. C. Jena, R. Scheu, S. Roke, *Angew. Chem.* **2012**, *124*, 13112–13114; *Angew. Chem. Int. Ed.* **2012**, *51*, 12938–12940.
 - [4] J. K. Beattie, A. Gray-Weale, *Angew. Chem.* **2012**, *124*, 13115–13116; *Angew. Chem. Int. Ed.* **2012**, *51*, 12941–12942.
 - [5] K. G. Marinova, R. G. Alargova, N. D. Denkov, O. D. Velev, D. N. Petsev, I. B. Ivanov, R. P. Borwankar, *Langmuir* **1996**, *12*, 2045–2051.
 - [6] J. K. Beattie, A. M. Djerdjev, *Angew. Chem.* **2004**, *116*, 3652–3655; *Angew. Chem. Int. Ed.* **2004**, *43*, 3568–3571.
 - [7] R. Vácha, S. W. Rick, P. Jungwirth, A. G. F. de Beer, H. B. de Aguiar, J.-S. Samson, S. Roke, *J. Am. Chem. Soc.* **2011**, *133*, 10204–10210.
 - [8] A. Gray-Weale, J. K. Beattie, *Phys. Chem. Chem. Phys.* **2009**, *11*, 10994–11005.
 - [9] R. W. O'Brien, R. J. Hunter, *Can. J. Chem.* **1981**, *59*, 1878.
 - [10] J. Aubry, F. Ganachaud, J.-P. Cohen Addad, B. Cabane, *Langmuir* **2009**, *25*, 1970–1979.

Coalescence of Repelling Colloidal Droplets: A Route to Monodisperse Populations

Kevin Roger,^{*,†} Robert Botet,[‡] and Bernard Cabane^{†,§}[†]PMMH, CNRS UMR 7636, ESPCI, 10 rue Vauquelin, 75231 Paris cedex 05, France[‡]LPS, CNRS UMR 8502, Université Paris-Sud, 91405 Orsay, France[§]Theoretical Chemistry, Lund University, 222100 Lund, Sweden

Supporting Information

ABSTRACT: Populations of droplets or particles dispersed in a liquid may evolve through Brownian collisions, aggregation, and coalescence. We have found a set of conditions under which these populations evolve spontaneously toward a narrow size distribution. The experimental system consists of poly(methyl methacrylate) (PMMA) nanodroplets dispersed in a solvent (acetone) + nonsolvent (water) mixture. These droplets carry electrical charges, located on the ionic end groups of the macromolecules. We used time-resolved small angle X-ray scattering to determine their size distribution. We find that the droplets grow through coalescence events: the average radius $\langle R \rangle$ increases logarithmically with elapsed time while the relative width $\sigma_R/\langle R \rangle$ of the distribution decreases as the inverse square root of $\langle R \rangle$. We interpret this evolution as resulting from coalescence events that are hindered by ionic repulsions between droplets. We generalize this evolution through a simulation of the Smoluchowski kinetic equation, with a kernel that takes into account the interactions between droplets. In the case of vanishing or attractive interactions, all droplet encounters lead to coalescence. The corresponding kernel leads to the well-known “self-preserving” particle distribution of the coalescence process, where $\sigma_R/\langle R \rangle$ increases to a plateau value. However, for droplets that interact through long-range ionic repulsions, “large + small” droplet encounters are more successful at coalescence than “large + large” encounters. We show that the corresponding kernel leads to a particular scaling of the droplet-size distribution—known as the “second-scaling law” in the theory of critical phenomena, where $\sigma_R/\langle R \rangle$ decreases as $1/\sqrt{\langle R \rangle}$ and becomes independent of the initial distribution. We argue that this scaling explains the narrow size distributions of colloidal dispersions that have been synthesized through aggregation processes.



INTRODUCTION

The fate of unstable systems in the colloidal domain is determined by the outcome of encounters between colloidal objects, e.g., particles or droplets. This is the case of emulsions, made of droplets of one liquid dispersed into another nonmiscible liquid. Since the two liquid phases are nonmiscible, there is an interfacial free energy cost proportional to the area of interface. Droplets encounter each other through Brownian collisions and may then aggregate and coalesce, since this will reduce the area of interface and thus the total interfacial free energy. How will the population of droplets evolve through these coalescence events? In surfactant stabilized emulsions, it is usually found that encounters of two large droplets are more successful than those of a large and a small droplet. Indeed if the limiting step for coalescence is the rupture of the surfactant film that separates droplets, then the larger area of the film separating two large droplets will lead to a higher coalescence probability. Consequently, large droplets will grow faster than the rest of the population, and the distribution of droplet sizes will become more and more polydisperse as film rupture events occur. Thus, the effect of coalescence in emulsions is usually to

yield a few very large drops that grow at the expense of the rest of the population.¹ The same trend is predicted in dry foams.²

A similar fate is observed in dispersions of colloidal particles, where interfacial free energy or interfacial reactions may cause the individual particles to aggregate. Experimental observations and numerical observations show that in most cases these aggregates turn out to have disordered self-similar structures, and size distributions that are quite polydisperse. Indeed, during collisions interfacial forces maintain the particles in the configuration in which they stuck to each other. The repetition of such aggregation events yields clusters with branched, bushy structures where the branches are more likely to react than the inner surfaces of the aggregates. In the reaction limited cluster aggregation (RLCA) processes, where only a fraction of all encounters are successful, the larger clusters are more successful at reacting, again because they have a larger surface area available for reactions, and the population of clusters becomes

Received: February 7, 2013

Revised: March 22, 2013

Published: April 9, 2013

more and more polydisperse as the reactions proceed.³ In the diffusion limited cluster aggregation (DLCA), where all the encounters are successful, the population of clusters reaches a constant polydispersity,⁴ lower than for RLCA but often higher than what is desired in practical purposes.

The view that aggregation/coalescence processes always lead to polydisperse populations of disordered aggregates is so commonly held that it has often been taken as a universal trend. Consequently, colloid chemists who attempt to synthesize monodisperse collections of colloidal particles take great precautions to avoid aggregation/coalescence: a classical review by Sugimoto states that: "Thus, as a rule, inhibition of coagulation is necessary for the preparation of monodisperse particles".⁵ If possible, colloid chemists try to grow the particles according to the "nucleation and growth" scheme.⁶ In this scheme, the supersaturation of the solution is kept at a low value, so that the number of successful nuclei is small, and these nuclei are kept apart from each other, so that no aggregation takes place, while the nuclei grow through monomer addition.

However, a few authors such as Zukoski and co-workers⁷ and Matijevik and co-workers^{8–10} have reported that monodisperse populations of colloidal particles can be obtained at very high supersaturation, through processes in which a large number of very small nuclei are generated, which subsequently aggregate with each other to form the final particles. This view has recently received additional experimental support from the work of Polte and co-workers.^{11,12} Such reports contradict the idea that aggregation processes always lead to polydisperse populations. Furthermore, the possibility of using high supersaturations to produce the desired particles is attractive, since it opens the way to higher productivity and simpler processes.

In order for an aggregation/coalescence process to lead to a "monodisperse" population, it is necessary that the reactions of small objects with larger ones be more frequent than the reactions of large with large objects. This requires a particular type of interaction between these objects. In the present work, we show that colloidal droplets of a concentrated polymer solution, dispersed in a nonsolvent, may interact in this way if their surfaces carry electrical charges bound to the macromolecules, and the nonsolvent is water or a solution of water with a polar solvent. These droplets repel each other through ionic long-range interactions, and these repulsions are stronger for larger droplets, because they carry more electrical charges.

We use a model system comprising macromolecules of poly(methyl methacrylate) (PMMA) in a solvent (acetone) that is mixed quickly with water, using a stopped-flow device. We follow the kinetics of the droplet coalescence process through ultrafast small angle X-ray scattering (SAXS). Whereas previous works^{11–18} have used stopped-flow SAXS to study metal or oxide particle formation, involving reactive species, our work monitors for the first time the formation of organic particles without any chemical reaction (Ouzo effect). The SAXS spectra show that the droplet population evolves through coalescence events, and yet this population propagates to relatively narrow size distributions. We show that these results can be explained within the frame of coalescence events hindered by a size-dependent repulsive interdroplet potential.

The observation of coalescence events that decrease the polydispersity of a distribution of droplets is also important because it represents a new scaling of the solutions of the Smoluchowski equation.¹⁹ By scaling, we mean that the populations that result from processes that run according to

the Smoluchowski equation have size distributions that are all similar to each other, and can be deduced from each other by a simple transformation such as the application of a scale factor. The well-known first scaling is obtained for Brownian collisions and corresponds to a size distribution that keeps a constant relative width $\sigma_R/\langle R \rangle$, while the radius grows as the power 1/3 of time. Here we identify the second scaling through kinetic Monte Carlo simulations and comparison with the kinetic SAXS experiments. Ionic repulsions between droplets lead to this new scaling law where the relative width $\sigma_R/\langle R \rangle$ decreases as $\langle R \rangle^{-1/2}$, while the radius grows logarithmically with elapsed time. This brings a new perspective on the concept of colloidal metastability.

This paper is organized in the following way. At first, we present the phase diagram of the PMMA–acetone–water system, and we describe the solvent-shifting method that we used to produce droplets of concentrated PMMA solution dispersed in the nonsolvent mixture (water–acetone). Next we describe how the growth of these droplets was monitored through ultrafast SAXS, and how we extracted the size distributions of droplets through an inversion of the scattering curves. Then we write the kernel of the Smoluchowski equation according to the interactions between droplets, and compare the predictions from this equation between the case of no interactions and the case of repulsive interactions with the experimental evolution of the droplet populations observed through SAXS. We show that coalescence without repulsions leads to a high polydispersity with the first scaling law, whereas coalescence of repelling droplets leads to a low polydispersity with the second scaling law. Finally we show how the outcome of any process involving the coalescence of droplets or particles, limited by ionic repulsions, may be predicted through the Smoluchowski approach.

■ EXPERIMENTAL SECTION

Materials. Poly(methyl methacrylate) (PMMA) was purchased from Aldrich. Size exclusion chromatography in THF yielded a weight-average molar mass of 14700 g/mol with a polydispersity of 1.54. Acetone was purchased from Aldrich with an assessed purity of 99.9% and milli-Q water was adjusted to pH = 10 using a sodium hydroxide aqueous solution; the ionic strength of water was set with sodium chloride to 1.5×10^{-2} mol.L⁻¹.

Methods. Controlled and Rapid Solvent-Shifting with a Stopped-Flow Apparatus. We used a Bio-Logic SFM-400 stopped-flow instrument, consisting of four motorized syringes and three mixers. The last mixer was coupled to a thin-walled flow-through quartz capillary cell (1.3 mm in diameter with a wall thickness of approximately 10 μ m). The total dead time was estimated to below 5 ms. The first syringe was filled with a solution of PMMA in acetone at a mass fraction of 10^{-2} (volume fraction 0.66×10^{-2}). The last syringe was filled with water at a pH of 10 at an ionic strength of 1.5×10^{-2} mol.L⁻¹. The two middle syringes were filled with pure acetone.

One experiment consists of one injection; however, several experiments are necessary to perform a time-resolved sequence. It is thus essential to achieve an excellent reproducibility between the successive injections. The mixing reproducibility is ensured by the use of the stopped-flow apparatus; however, it is also important to prevent any mixing contamination of the syringes between two successive experiments. The main problem arises from Marangoni effects inside the device, which may cause contamination in the syringes, since they are opened to the whole device during an experiment.

We designed a strict protocol to avoid these difficulties. The PMMA/acetone solution was injected with the water in the final mixing cell and a set of spectra was acquired. Immediately after these measurements, pure acetone from the intermediate syringes was injected in order to create an acetone buffer between the PMMA/

acetone solution and the water syringes. Then the syringes of the stopped flow were closed manually until the next experiment was performed. We used a video camera to follow the macroscopic events taking place in the capillary cell and we checked that the cell was filled homogeneously with no turbid domains, within the experimental time frame.

Ultrafast Small Angle X-ray Scattering (SAXS) with a Stopped-Flow Apparatus. SAXS experiments were performed on samples prepared through rapid mixing of the PMMA/acetone solution with water, injected in the capillary flow-cell. SAXS patterns were collected at the European Synchrotron Radiation Facility, at the high-brilliance beamline ID02 (wavelength = 0.1 nm, detector distance 8 m, cross-section of the beam at the sample holder = 0.3 mm). The X-ray scattered intensity was recorded using a FReLoN (fast-readout low-noise) Kodak CCD detector in the q -range of 0.01–0.6 nm⁻¹ with a high sensitivity and count rate capability. This unique instrument with a monochromatic, highly collimated, and intense beam makes it possible to perform millisecond time-resolved stroboscopic experiments of SAXS.²⁰

The duration of each measurement was 5 ms and the minimal time interval between two measurements was 200 ms. To obtain data in the range 5–205 ms, we thus had to perform several experiments with various initial measurement times. This requires good reproducibility of all the processes, which is possible when using a stopped-flow device with the protocol detailed above.

The SAXS data was then reduced, i.e., normalized, grouped into one-dimensional spectra, and background-subtracted. The background was the mixture of acetone and water made through a stopped-flow experiment with the same parameters as for the PMMA/acetone solutions. The intensities were obtained on an absolute scale.

Experimental Coalescence Laws through Inversion of the SAXS Data. We used a numerical optimized inversion procedure,²¹ based on the Titchmarsh formula, to obtain the size distribution of the droplets from the SAXS data. This method computes the size distributions from the deviations of the scattering signal to the Porod law, using Shannon's theorem for the available amount of information. The procedure does not require extrapolation of the data beyond the experimental q -range, and it is known to provide a reliable and stable way to assess possible broad distributions. The quality of the inversion procedure was assessed by calculating the scattering curves from the inverted size distributions and comparing them with the experimental spectra.

Theoretical Coalescence Laws through Kinetic Monte Carlo Simulations of Charged Droplets. We realized a number of kinetic Monte Carlo simulations^{22,23} to solve the coalescence Smoluchowski equations¹⁹ including van der Waals and electrostatic interactions. Systems containing up to $N = 2 \times 10^6$ monomers, with monodisperse initial conditions, have been studied that way. The general algorithm for the simulations is as follows.

At each time step:

- All the probabilities per unit of time of possible coalescence events are listed. Probabilities are noted: K_{ij} with i and j the labels of the colliding droplets.
- The average time for the next coalescence event to occur is $\tau = 1/\sum_{ij} K_{ij}$. Then, the normalized event probabilities are τK_{ij} .
- A time increment, δt , is chosen randomly with the exponential distribution of parameter τ (i.e., $f(\delta t) = 1/\tau \exp(-\delta t/\tau)$).
- An event is chosen randomly in the list of all the possible coalescence events, according to the probabilities τK_{ij} . This event is realized, and the current time is incremented by δt .

The sequence of coalescence events goes on this way until the experimental times are reached. That way, we have access to the theoretical evolution of the physical observables, such as the average value and the standard deviation of the droplet radius.

RESULTS

Solvent-Shifting Produces a Collection of Droplets with Ionized Interfaces. Solvent-shifting is a mixing method that throws a solution into a state that is far from equilibrium,

and uses the subsequent evolution to produce a fine dispersion of the solute. Typically, a polymer/good solvent solution is rapidly mixed with a nonsolvent to cross the equilibrium phase separation boundary (binodal line). The equilibrium state is then the coexistence of two macroscopic phases, which is quantitatively described by the phase diagram of the ternary system. However, interactions between the separating domains may restrict the phase separation to the colloidal scale. The system is then conveniently described as a homogeneous colloidal system, i.e., a dispersion of droplets in a liquid. Nonetheless, since the phase diagram indicates the compositions of the dispersed phase and of the dispersing liquid, its study is valuable to understand the nonequilibrium pathways. We therefore first locate the solvent-shifting pathways in the phase diagram, describe the phase separation process, and then show that the system, trapped in a nonequilibrium state, can be described as a colloidal one-phase system.

We used the system PMMA/acetone (good solvent) + water (nonsolvent). The phase diagram of this ternary system has been determined experimentally by Aubry and co-workers²⁴ and analytically through the Flory–Huggins–Stockmayer theory by Cohen-Addad.²⁵ Figure 1 presents this phase

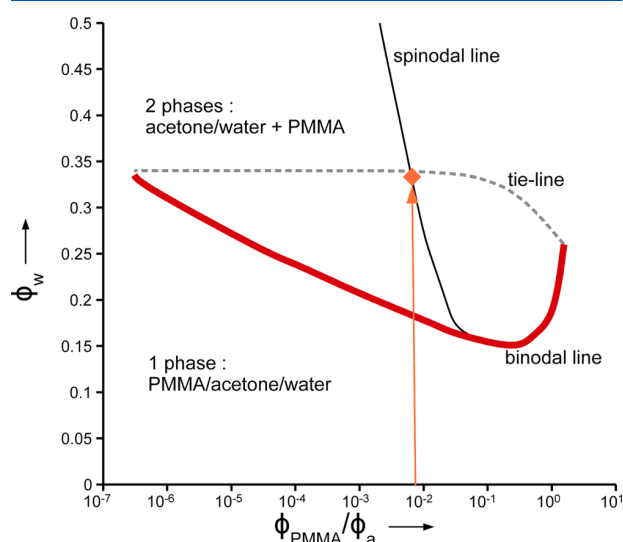


Figure 1. Phase diagram of the PMMA/acetone/water system. Horizontal axis: ratio of the PMMA volume fraction to the acetone volume fraction, $\phi_{\text{PMMA}}/\phi_a$ logarithmic scale. Vertical axis: water volume fraction, ϕ_w . The solvent-shifting path is the ascendant vertical line. When the system crosses the binodal line (red), phase separation takes place. High values of the supersaturation are quickly reached. The composition used in the present experiments is indicated by a filled diamond.

diagram in coordinates that are the ratio, $\phi_{\text{PMMA}}/\phi_a$ of PMMA volume fraction to acetone volume fraction, and the water volume fraction, ϕ_w . At low water volume fractions the homogeneous solution of PMMA in the acetone-rich solvent mixture is stable, whereas at high water volume fractions the stable state is the coexistence of a polymer-rich phase, which will constitute the droplets, with a water–acetone solution containing a small amount of polymer. These regions are separated by the equilibrium phase separation line, or binodal line. Most of this binodal line is located at very low volume fractions, and for this reason a log scale was used for the horizontal axis.

In a solvent-shifting experiment, the solution starts at $\phi_w = 0$ (no water) and follows a vertical path during solvent shifting (addition of water). With moderate water additions ($\phi_w = 0.2-0.5$), the system reaches the two-phases region where it is supersaturated with respect to the polymer. The supersaturation S is the ratio of the actual polymer concentration to its equilibrium concentration, which can be read at the intersection of the tie line with the binodal line. Since the binodal line is quite flat, a small water addition above the binodal line produces a huge supersaturation. The composition used in the present study is displayed on the phase diagram and corresponds to a PMMA/acetone volume ratio $\phi_{\text{PMMA}}/\phi_a = 6.6 \times 10^{-3}$ and water volume fraction $\phi_w = 0.33$. The supersaturation is above 3000. The phase diagram allows the calculation of the equilibrium swelling of a macromolecule in the mixed solvent water/acetone. Knowing the radius of a collapsed macromolecule from its molar mass and density, $R_{\text{collapsed}} = 1.7$ nm, we can deduce the radius of the macromolecule in the mixed solvent at equilibrium to $R_1 = 2.2$ nm.

In dilute conditions, metastable dispersions of PMMA droplets with sizes around 100 nm and low polydispersity are obtained. Metastability requires repulsive barriers between the droplets to prevent relaxation toward the equilibrium macroscopic phase separation. We found through electrophoretic mobility measurements that these droplets are negatively charged with a pH-dependent variation that is typical of carboxylic acid moieties (see Supporting Information). We have demonstrated in previous work that even macromolecules that have no ionizable monomers can carry a charge at their end groups, where the initiator started the polymerization during the synthesis of the macromolecules.²⁶ If the initiator does not bear any ionizable group, the macromolecules cannot provide any charge, and the surface charge of the polymer water interface vanishes. In that case, the dispersion does not show metastability, in contrast to the case of oil droplets that always carry a surface charge due to fatty acid impurity adsorption and reaction with hydroxide ions.²⁷ We can obtain the surface charge density from the variation with pH of the electrophoretic mobility of the final polymer droplets $\sigma = 0.025 \pm 0.005$ e.nm⁻². Assuming a simple geometrical model in which the macromolecules at the interface of the polymer droplet contribute to the surface charge, we can estimate the surface charge density $\sigma = 0.0236$ e.nm⁻².

Solvent-shifting is also sensitive to other parameters such as the PMMA/acetone ratio²⁴ and the mixing conditions.²⁸ In this work we kept these parameters constant, by choosing a set PMMA/acetone ratio and operating under fast mixing conditions. This was important since bad mixing leads to mixtures of regions of different compositions, which evolve at different rates, leading to larger sizes and broader distributions of the droplet population. The most favorable hydrodynamic situation is thus the fast, turbulent mixing of the two liquids, as achieved in the stopped flow device.

We investigate the mechanism through which monodisperse droplets are obtained in conditions where homogeneous solvent-shifting is achieved through fast mixing and the resulting colloidal droplets repel through ionic interactions.

Ultrafast SAXS Monitors the Droplet Population in Real Time. The PMMA/acetone solution was mixed with water and injected in the SAXS capillary cell in 5 ms. This step triggered the first measurement time, which took 5 ms. Measurements were performed using several initial times in

order to obtain time-resolved scattering patterns. In Figure 2, we plot $I(q) \cdot q^4$ as a function of q , for six measurement times. Such a plot displays efficiently the temporal evolution of the spectra.

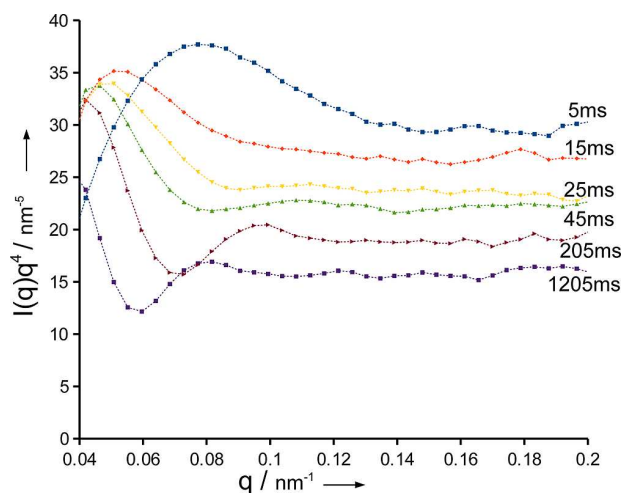


Figure 2. Evolution of the SAXS spectra during droplet coalescence. Each spectrum corresponds to a selected time after mixing the polymer solution with the nonsolvent. Additional spectra were consistent (see Figure 3) but are not displayed for clarity. Horizontal scale, magnitude of the scattering vector, vertical scale, $I(q) \cdot q^4$ (Porod plot). A decrease of the asymptotic value of the intensity at large q -values indicates a decrease of the area of interface of the droplets, whereas growth of oscillations in the intermediate q range corresponds to a decrease in their polydispersity.

Droplets Grow by Coalescence. The average size of the scatterers can be determined through model-independent analysis of the SAXS data. Indeed, when $\lim_{q \rightarrow \infty} q^4 I(q)$ is finite, the surface area of the scattering phase is given by the ratio of two invariants, namely

$$\frac{A}{V} = \pi \lim_{q \rightarrow \infty} q^4 I(q) / \int_0^\infty q^2 I(q) dq \quad (1)$$

with A the total interface area and V the total volume of the scattering phase.

In the case of an ensemble of spheres with distributed radii R , one has $3V/A = \langle R^3 \rangle / \langle R^2 \rangle$. Thus we can determine the Porod length, which is a measure of the mean radius through the formula

$$\frac{\langle R^3 \rangle}{\langle R^2 \rangle} = \frac{3}{\pi} \int_0^\infty q^2 I(q) dq / \lim_{q \rightarrow \infty} q^4 I(q) \quad (2)$$

in the dilute limit whatever the normalization of the SAXS intensity $I(q)$.

Furthermore, the Porod geometrical invariant is

$$Q = \int_0^\infty q^2 I(q) dq = 2\pi^2 (\Delta\rho)^2 \phi (1 - \phi)$$

and the Porod limit is

$$P = \lim_{q \rightarrow \infty} q^4 I(q) = 2\pi (\Delta\rho)^2 \phi A / V$$

with ϕ the volume fraction of the dispersed phase and $\Delta\rho$ the difference of the scattering length densities. Then, during an experiment, a variation of Q reflects essentially change in the

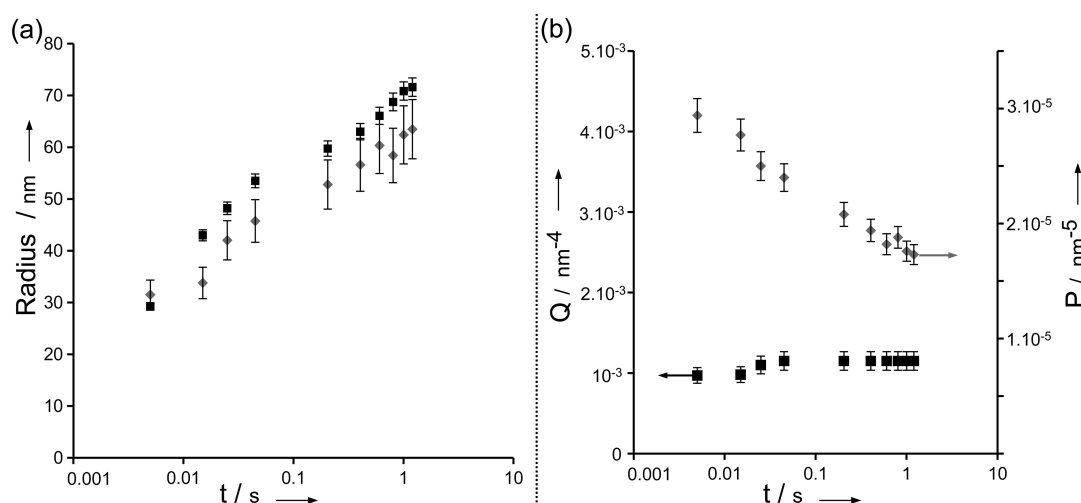


Figure 3. (a) Particle growth law as a function of elapsed time, t in semilogarithmic scale. Gray diamonds correspond to the average radius, $\langle R^3 \rangle / \langle R^2 \rangle$ calculated from eq 2. Black squares correspond to the mean radius, $\langle R \rangle$, obtained through inversion of the spectra. (b) The invariant Q (black squares) remains constant, which means that the total volume of droplets does not change. The Porod limit P decreases with elapsed time, which means that their total interfacial area decreases. Therefore the population evolves through coalescence of the droplets.

volume fraction ϕ of the dispersed phase, while a variation of P reflects changes in the total interfacial area of the dispersed objects.

The results of this simple analysis are as follows:

- First, one notes from Figure 2 that $q^4 I(q)$ reaches an asymptotic value for the largest available values of q , for every elapsed time. Then, the Porod invariants can be used.
- In Figure 3, we see that Q keeps a constant value independent of the elapsed time. We deduce that the amount of scattering matter is constant in the investigated period of time.
- The Porod limit P , and thus the total interfacial area, decreases with elapsed time.
- The variation of the radius defined in eq 2 is plotted in Figure 3. It shows a logarithmic growth with elapsed time (note the scale).

Therefore the droplets evolve through coalescence, since their average size grows while their total volume remains constant. Conversely, if the process was nucleation and growth, where nuclei grow into droplets by collecting single molecules, the volume of the dispersed phase would increase while the total interfacial area would increase as well, in contrast with the observed constancy of Q and the decrease of P .

Polydispersity Decreases with Elapsed Time. On the SAXS curves shown in Figure 2, oscillations of $q^4 I(q)$ in the intermediate q -range appear as the elapsed time grows. This is a strong sign that the width of the size distribution decreases with elapsed time. We can define a quantitative measure of this width through the nondimensional parameter $\sigma_R / \langle R \rangle$, with σ_R the standard deviation of the radius distribution. A perfectly monodisperse population has $\sigma_R / \langle R \rangle = 0$, and a population with $\sigma_R / \langle R \rangle \leq 0.1$ is sufficiently monodisperse to crystallize at high volume fractions.²⁹ In order to compute this parameter, we must determine the distributions of droplets sizes that produced the spectra shown in Figure 2. For this purpose we used an inversion method that relies on the deviations from Porod's law.²¹ This method is simple and does not require any assumption on the shape of the size distributions or on the

scattered intensity outside the experimental range of q . We checked the reliability of the inversion data in two ways: (a known distribution \rightarrow calculated scattering curve \rightarrow the inverted distribution) and (the experimental spectra \rightarrow calculated size distribution \rightarrow calculated spectra). Furthermore, the mean radii extracted from these distributions are in very good agreement with those determined through the model-independent analysis presented above.

Radius distributions, $f(R)$, are displayed in Figure 4 for various elapsed times. From them, moments of the radius R are readily obtained, and in particular, the mean radius, $\langle R \rangle$, and the polydispersity $\sigma_R / \langle R \rangle$.

In Figure 3, we plot the mean radius, $\langle R \rangle$, as a function of elapsed time. As we already found from the model-independent analysis, the variation of $\langle R \rangle$ is essentially logarithmic, which corresponds to a slower and slower increase with time of the mean radius. In Figure 5, we plot the polydispersity as a

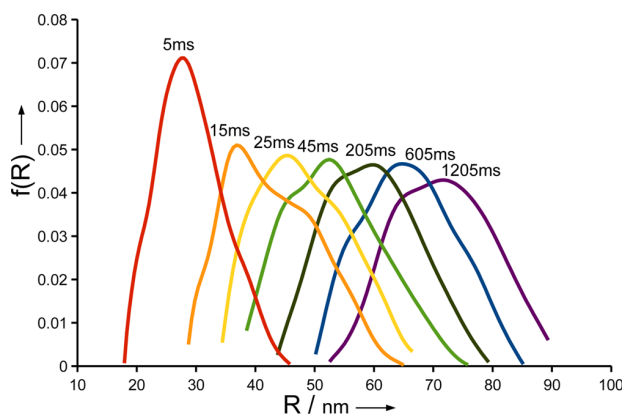


Figure 4. Distributions of droplet radii, calculated from the scattering curves displayed in Figure 2, through the inversion procedure. At larger elapsed times these distributions shift to larger radii but their width does not increase proportionally. Quantitative analysis shows that the relative width or polydispersity $\sigma_R / \langle R \rangle$ decreases continuously with time.

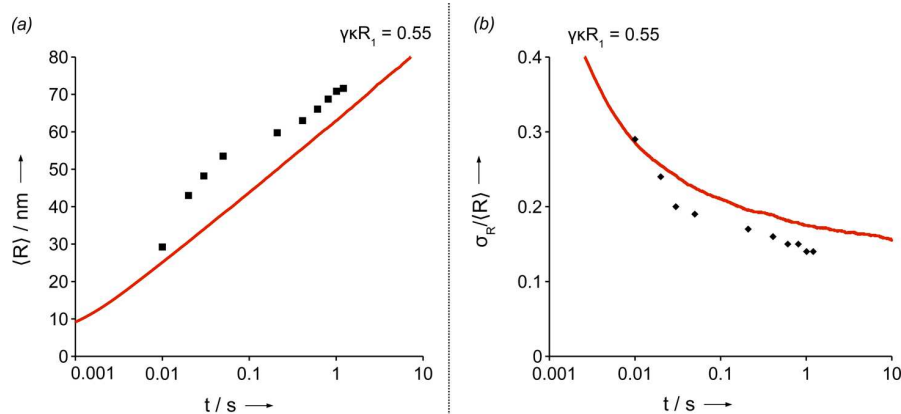


Figure 5. (a) Experimental mean radius as a function of elapsed time deduced from the inversion procedure (black squares) and simulation results for droplets with surfaces carrying one electrical charge per macromolecule (red line). (b) Experimental polydispersity as a function of elapsed time (black diamonds) and simulation results for the same droplets (red line).

function of elapsed time. We see that the polydispersity decreases with time, as the droplets become larger. This is consistent with appearance of an oscillation in the scattering curves displayed in Figure 2. Then, the system tends to become monodisperse. We will now focus on these observations and discuss how they can be explained.

DISCUSSION

Brownian Coalescence vs Hindered Coalescence.

Mean-field droplet-coalescence theory can be invoked as soon as it is possible to define unambiguously the probability of coalescence, K_{ij} , between a droplet of volume V_i and a droplet of volume V_j , per unit of volume and unit of time. This rate kernel, K_{ij} , gathers information about Brownian diffusion, interaction potential, and the coalescence rules when droplets come in contact.³⁰ For rigid droplets in a fluid, the kernel is written generally as

$$K_{ij} = \frac{4\pi}{w_{ij}}(R_i + R_j)(D_i + D_j) \quad (3)$$

where D_i is the diffusion coefficient of the droplet of radius R_i , and w_{ij} is the Fuchs stability ratio depending on the two-bodies interaction potential.³¹ Originated by Smoluchowski a century ago,¹⁹ this approach provides a unique and efficient tool to study dynamics of colloidal dispersions.³²

In this work we consider the general case of coalescence of spherical droplets carrying an electric surface charge density σ , dispersed in water. This corresponds to the experimental system, since the spherical shape of the swollen droplets was checked through TEM,²⁴ and since the surface charge density was determined through electrokinetic experiments (see Supporting Information). The droplet–droplet interaction potential, Φ_{ij} , is the sum of the repulsive ionic potential V_R and the attractive van der Waals potential V_A , as described in the Derjaguin–Landau–Verwey–Overbeek (DLVO) approach.³³ It results in the following stability ratio³⁴

$$w_{ij} = 1 + (R_i + R_j) \int_{R_i+R_j}^{\infty} [e^{\Phi_{ij}(r)/k_B T} - 1] \frac{dr}{r^2} \quad (4)$$

when hydrodynamics can be neglected.³⁵ Here, $\Phi_{ij}(r) = V_A(r) + V_R(r)$, with r the center-to-center distance, and the respective attractive and repulsive potential functions³⁶

$$\frac{V_A(r)}{k_B T} = -\alpha \left[2R_i R_j \left(\frac{1}{r^2 - (R_i + R_j)^2} + \frac{1}{r^2 - (R_i - R_j)^2} \right) + \ln \left(\frac{r^2 - (R_i + R_j)^2}{r^2 - (R_i - R_j)^2} \right) \right] \quad (5)$$

$$\frac{V_R(r)}{k_B T} = \gamma (2\kappa R_i \sinh \kappa R_i) (2\kappa R_j \sinh \kappa R_j) \frac{e^{-\kappa r}}{\kappa r} \quad (6)$$

The two nondimensional parameters are $\alpha = A_H/6k_B T$ (with A_H the Hamaker constant), and $\gamma = (2\pi\sigma)^2 l_B/\kappa^3$, where κ is the inverse of the Debye length and l_B the Bjerrum length. It is important to notice that both potentials are growing functions of the droplets sizes, i.e., the van der Waals potential becomes more attractive and the ionic potential more repulsive, as the droplets grow in size.

The potential expressions eq 5 and eq 6 are too complicated for analytical treatment of the stability ratio without approximation. For the charged droplets, several domains can be defined according to the number of electrical charges per droplet, the ionic strength and dielectric constant of the solution, and the Hamaker constant. In the present context, we will discuss only two important domains:

- the uncharged droplets, which corresponds to the usual reference case
- the moderately charged droplets with moderate ionic strength, which corresponds to the experiments

Coalescence without Repulsions: The First-Scaling Law. When the charge density $\sigma = 0$, the repulsive potential V_R vanishes and the Fuchs stability ratio is written as the exact function of the auxiliary parameter $a_{ij} = 4R_i R_j / (R_i + R_j)^2$:

$$w_{ij} = \int_0^1 e^{-\alpha \mathcal{F}(a_{ij} x^2 / (1-x^2))} dx \quad (7)$$

$$\mathcal{F}(z) \equiv z(1+z/2)/(1+z) + \ln(1+z)$$

Without van der Waals interaction (i.e., $\alpha = 0$), the Fuchs factor is $w_{ij} = 1$, whatever the droplet sizes, and we recover the usual Brownian kernel between noninteracting droplets, $K_{ij} = 4\pi(R_i + R_j)(D_i + D_j)$. For spheres, the Stokes–Einstein relation $D_i \propto 1/R_i$ gives a rate kernel that is a homogeneous function of the

volumes,³⁷ with homogeneity exponent 0 (i.e., K_{ij} is invariant for droplet volume rescaling $V_i \rightarrow \lambda V_i$, whatever the positive λ scaling factor).

When the Hamaker constant, A_H , is positive, eq 7 shows that the Fuchs factor is a decreasing function of α and thus of A_H , since the function \mathcal{F} is positive. It means that the corresponding coalescence probability increases with increasing the van der Waals interactions, and it results in a faster coalescence process. Importantly, one should note that the factor w_{ij} in eq 7 depends on the sizes R_i and R_j through the nondimensional parameter a_{ij} only. Then, the homogeneity exponent of the coalescence kernels K_{ij} is still 0. This has several profound consequences: the mean droplet radius grows as a power law of the time, $\langle R \rangle \sim (c + c' t)^{1/3}$, with c and c' two positive constants, and a self-preserving form of the size-distribution

$$\langle R \rangle f(R) \simeq \phi \left(\frac{R - \langle R \rangle}{\langle R \rangle} \right) \quad (8)$$

with ϕ a scaling function, is expected to build up for the large times. This assumption was first based on observations of regularities of experimental distributions,³⁸ then searched theoretically in the solutions of the corresponding Smoluchowski coalescence equations.³⁹ Nowadays a number of numerical results confirm the realization of this assumption.⁴⁰ However, the proper scaling function ϕ appears to belong to a full class of functions, and the asymptotic solution depends on characteristics of the initial distribution.⁴¹ For kernel with homogeneity exponent 0 and monodisperse initial conditions, the self-preserving size distribution is well documented.⁴²

The polydispersity $\sigma_R/\langle R \rangle$ keeps a constant value as long as the self-preserving form of the size distribution holds true.⁴³ This is the first scaling law.⁴⁴ For the pure Brownian kernel, one has $\sigma_R/\langle R \rangle \simeq 0.34$, as shown in Figure 6. For comparison, we plotted on the same figure the exact result for the constant kernel $K_{ij} = 1$, which is the simplest homogeneous function with homogeneity exponent 0, and monodisperse initial

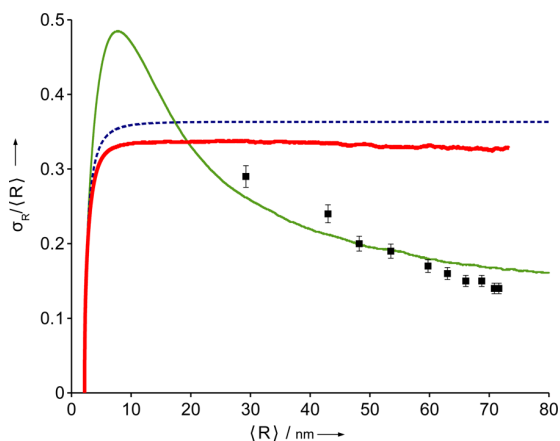


Figure 6. Comparison between the experimental evolution of the polydispersity (black squares), the simulation results for the Brownian kernel (thick red line), the exact result for the constant kernel (dotted blue line), and the simulation results for the kernel including ionic repulsions with $\gamma\kappa R_1 = 0.55$ (thin green line). The decrease seen experimentally contrasts with the saturation due to the self-preserving form of the size distribution associated with the Brownian kernel, but is properly described when ionic repulsions are added to the kernel.

conditions. The mean radius and the polydispersity function are then

$$\langle R \rangle = \frac{Li_{-1/3}(z)}{Li_0^2(z)} \quad \frac{\sigma_R}{\langle R \rangle} = \left(\frac{Li_{-2/3}(z)Li_0(z)}{Li_{-1/3}^2(z)} - 1 \right)^{1/2} \quad (9)$$

with the polylogarithm function⁴⁵ $Li_s(z) \equiv \sum_{k=1}^{\infty} z^k/k^s$, and the parameter $0 < z = (Nt/2)/(1 + Nt/2) < 1$, N being the total mass of the system. The limit value of the polydispersity is $\lim_{t \rightarrow \infty} \sigma_R/\langle R \rangle = 0.363$.

These results contrast both quantitatively and qualitatively with our experimental data, where a decrease of the polydispersity is observed and the mean radius increases logarithmically with elapsed time. Therefore the pure Brownian process (possibly with van der Waals attractions) does not describe the coalescence of charged droplets. Similarly we can rule out the Ostwald Ripening process since it corresponds to the same growth law,⁴⁶ $\langle R \rangle \sim t^{1/3}$, as the Brownian process. Reaction limited cluster aggregation is even more easily ruled out since the opposite growth law where the mean radius increases exponentially with elapsed time:³ $\langle R \rangle \sim \exp(t)$ is expected, and the polydispersity increases. We conclude that a key ingredient is lacking to describe the logarithmic growth of the mean droplet radius, as seen in the coalescence process studied in this work.

Coalescence with Repulsions: The Second-Scaling Law. An important ingredient that must be considered in the theory is the repulsive interaction between droplets. Indeed, in the experimental system, the droplets contain macromolecules with one ionized end group each.

Mean-Radius Logarithmic Growth Specifies a Class of Kernels. The logarithmic increase of the mean radius may serve as a guide to guess which special class of kernels K_{ij} to consider. Indeed, let us use the crude approximation where the droplet population is strictly monodisperse: at the time t all the droplets have volume $V_i = V$, and after the time increment Δt all the droplets have reached volume $V_j = 2V$. If we are looking for a mean radius, here $R \sim V^{1/3}$, that grows logarithmically with the elapsed time, the duration Δt should be $\sim \exp(cR)$, with c a positive constant. Since K_{ii} is the probability of coalescence of two droplets of volume V per unit of time, the duration Δt is $\sim 1/K_{ii}$ for all the droplets i , and then, the leading part of the coalescence kernel: $K_{ii} \sim \exp(-cV^{1/3})$. This class of kernels is characteristic of the logarithmic behavior $\langle R \rangle \sim c^{-1} \ln t$.

We will see now that this kind of coalescence kernel appears naturally for the charged droplets. Indeed, according to an argument by Reerink and Overbeek,⁴⁷ the stability ratio, w_{ij} can be approximated as $w_{ij} \simeq \exp(\Phi_{\max}/k_B T)$ for strong repulsive interaction potentials, in which Φ_{\max} is the height of the repulsive barrier resulting from the total potential $\Phi(r) = V_A(r) + V_R(r)$. According to eqs 5 and 6, the attraction between two neighboring droplets of same volume V and radius R , is $V_A(r) \simeq -\alpha R/(r - 2R)$, and the repulsive interaction is $V_R(r) \simeq \gamma\kappa R e^{-\kappa(r-2R)}/2$. Since both potentials scale as $V^{1/3}$, it will be the same for the maximum value of the sum $\Phi(r)$. Then, the coalescence kernel, which is inversely proportional to w_{ij} , is such that $K_{V,V} \sim \exp(-cV^{1/3})$, consistent with the logarithmic increase of the mean radius.

Interestingly, such a feature for the kernel leading to the logarithmic growth law, depends only on the charge characteristics of the droplets, while various fluid properties result simply

in different time scales (for example, when comparing diffusive and convective systems). Thus, the present conclusions about droplet distributions and growth laws for systems of Brownian droplets do apply in convective systems as well. That remark is important since most of the synthesis reactors work in convective flows.

Analytic Expression of the Coalescence Kernel. Since the cause of the logarithmic time behavior of the mean radius is now well established, we can proceed to discuss the behavior of the polydispersity. Actually, it requires much more careful analysis. In the Supporting Information, we complete in a more detailed way the argument of Reerink and Overbeek⁴⁷ that only the values around the repulsive barrier of the potential are relevant for the quantitative description of the process. We find that, in the case of charged droplets, the coalescence kernel can be written as

$$K_{ij} = \frac{1}{\tau} (u_i + u_j)^2 \left(\frac{1}{u_i} + \frac{1}{u_j} \right)^{1/2+\alpha} e^{-(1/u_i+1/u_j)^{-1}} \quad (10)$$

$$u_i \equiv \gamma\kappa R_i \quad (11)$$

using the scaled radius u_i . The characteristic time, τ , is of same order as the Brownian coagulation time for uncharged monomers, for values of the parameters $\alpha, \gamma \sim 1$ (a definite formula for τ is given in Supporting Information).

The special scaling on the radius, exhibited in eq 11, deserves a short comment here. In the Smoluchowski approach, volumes are the additive quantities, and they are all multiples of a common size, the monomer volume, defining the volume unit $V_1 \equiv 1$. A monomer should correspond here to the critical nucleus size as discussed within the framework of the nucleation theory. Moreover, the typical radius of a macromolecule, R_1 , gives the natural length scale for the droplet radius. Then, all the kinetic equations should be written in principle in terms of the droplet volumes, $V_i = (R_i/R_1)^3 V_1$ instead of their radius R_i . Equivalently, the auxiliary variable u_i , defined in eq 11, should be written $u_i = (\gamma\kappa R_1) V_i^{1/3}$, making apparent the nondimensional parameter $\gamma\kappa R_1 = (2\pi\sigma)^2 l_B R_1 / \kappa^2$. In conclusion, there are two nondimensional physical parameters in the system, namely, $\alpha = A_H / 6k_B T$, characteristic of the attraction, and $\gamma\kappa R_1$, which gathers the information about the ionic interactions in the system.

When Are (Large+Small) Recombination Events Favored? The function $i \rightarrow K_{i,n-i}/K_{n/2,n/2}$ represents the coalescence probability of a droplet of volume iV_1 and a droplet of volume $(n-i)V_1$, compared to the probability of coalescence of two identical droplets of volume $(n/2)V_1$. It gives essential information about the most probable coalescence events leading to the droplet of volume V_n . Three examples are shown in the Figure 7, for $\alpha = 1/3$ and $\gamma\kappa R_1 = 0.55$. These values correspond to the Hamaker constant $A_H = 2k_B T$, and a surface charge density of 0.021 e.nm^{-2} , slightly below the value deduced from electrophoretic mobilities, as exposed in the Results section.

For these values of the parameters, droplets of volume smaller than $43 V_1$ (i.e., $n = 43$, and $R < 3.5R_1$) are formed through coalescence of droplets of essentially random size (similarly to the Brownian case), whereas droplets of larger sizes (radius $> 3.5R_1$) are most probably formed by coalescence of a small droplet and a large droplet. Then, the coalescence kernel is related to the so-called “class-III” kernels³⁷ (i.e., kernels for which the values of the exponents μ and ν , defined

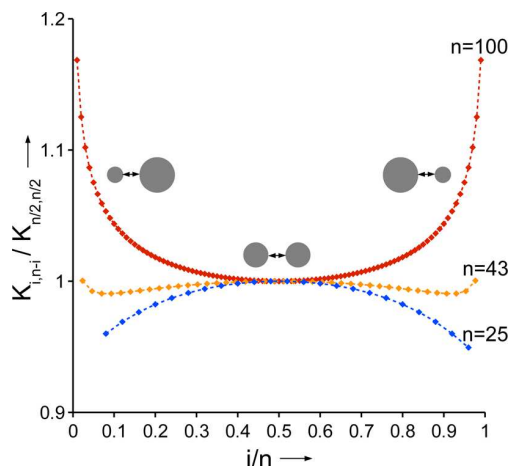


Figure 7. Ratio $K_{i,n-i}/K_{n/2,n/2}$ of the probability of coalescence of a droplet of volume iV_1 and a droplet of volume $(n-i)V_1$, compared to the probability of coalescence of two identical droplets of volume $(n/2)V_1$, as function of i/n . Lines are guides for the eyes. Three values of n are shown, namely, $n = 25$, $n = 43$, and $n = 100$. Parameters $\alpha = 1/3$, $\gamma\kappa R_1 = 0.55$. For the larger n value, the most probable event is coalescence of a large droplet with a small one.

by $K_{ij} \sim i^\mu j^\nu$ for $j \gg i$, are respectively positive and negative). For the class-III kernels, (large + small) events are dominant, and this results in bell-shaped distributions that have fast decay at small sizes. This is the key ingredient to explain the decrease in polydispersity as droplets coalesce.

Kinetic Monte Carlo Simulations Reproduce Quantitatively the Observed Evolution. We realized a number of numerical simulations of Smoluchowski systems with $N = 2 \times 10^6$ monomers and monodisperse initial conditions. Kinetic Monte Carlo algorithm was used.²² We calculated the temporal evolution of the mean radius and of the polydispersity for various values of the parameter $\gamma\kappa R_1$ over long times including the experimental range of times. In all the simulations below, the Hamaker constant is $A_H = 2k_B T$.

In Figures 5 and 6 the experimental data are compared to simulation results for $\gamma\kappa R_1 = 0.55$, which correspond to typical values in our system as explained above. Quantitative agreement of the time scale and length scale is obtained without using any adjustable parameters. Moreover, the overall behaviors of the mean radius and the polydispersity agree well. We conclude that the ionic potential we used in the Smoluchowski equations captures the essential physics of our experiments. However a still better agreement can be achieved by adjusting the parameter $\gamma\kappa R_1$. This will be done in the next sections.

An important question is whether or not the self-preserving form (eq 8) is recovered in this case, or expressed differently whether we reach the first-scaling law, as is often assumed, or not. Indeed, an analytic solution realizing eq 8 was found for the general Smoluchowski problem with high repulsive barriers increasing with the droplet sizes.⁴⁸ This solution writes, for the infinite system, in terms of the radius-distribution as

$$\langle r \rangle f(r) = 3\alpha^3 \left(\frac{r}{\langle r \rangle} \right)^4 \quad \alpha/2^{1/3} < r/\langle r \rangle < \alpha \quad (12)$$

with the numerical coefficient $\alpha = 2/(3(2^{2/3} - 1)) \simeq 1.1349$. Several points about this solution have to be highlighted: Physical parameters do not appear in the solution. This means

that this distribution is universal and characteristic of a general scenario, namely, kinetic coalescence of charged droplets, with repulsive barriers increasing with the droplets sizes. The solution is written in the first-scaling form. Then, the polydispersity factor, $\sigma_R/\langle r \rangle$ is a constant, independent of the elapsed time. Its numerical value is

$$\frac{\sigma_R}{\langle r \rangle} = \frac{\sqrt{2^{7/3} - 5}}{3} \approx 0.066402 \quad (13)$$

In our case, an example of numerical solution of the Smoluchowski equations including very long times is shown in Figure 8, in the representation $\sigma_R/\langle R \rangle$ versus elapsed time. The

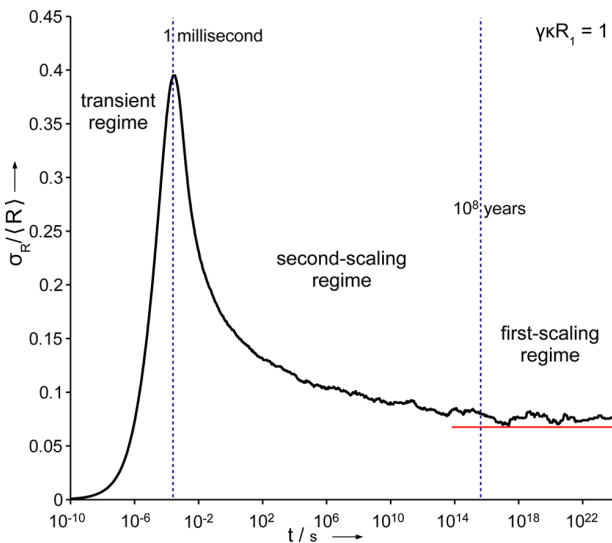


Figure 8. Different scalings as functions of elapsed time for a simulation with $\gamma\kappa R_1 = 0.55$. A burst in polydispersity is obtained for times below the millisecond, which are not experimentally accessible. The first scaling, corresponding to the self-preserving regime is obtained only after billions of years. The second scaling thus dominates for all the physically accessible times.

value in eq 13 appears indeed on the plot, but at physical times that are surprisingly long (several millions of years). Then, we do not expect the generic analytical solution 12 to be realized in our experiments which extend to the minute.

Second-Scaling Law Characterizes the Coalescence of Repelling Droplets. The quantitative agreement between the model and the experimental data can be improved by allowing small changes of the surface charge density during the coalescence process. Such changes could result from a reorganization of the charged end-groups within the droplets.

Rather than to postulate a time-law for this variation, we present below a method to *evaluate* the surface charge density within a fitting condition. We have seen that self-preserving scaling holds true for the uncharged droplets case. It results in large fluctuations characterized by a variance, σ_R^2 proportional to the *square* of the mean value, $\langle R \rangle^2$. Such a scaling is well-known in various domains of physics—sometimes under the terminology “first-scaling law”⁴⁴—and is generally characteristic of the disordered systems, that is an ensemble of droplets with irrelevant interactions (the first-scaling law is also valid at the critical point of a collective system, then for interaction marginally relevant).

When droplet interactions are strong, (such as in the ordered systems), the fluctuations are generally Gaussian,⁴⁹ that is, $\sigma_R^2 \propto \langle R \rangle$. It is called the second scaling law, and this is what we could expect for the charged droplets. This assumption is checked in Figure 9 where we plotted the results of the

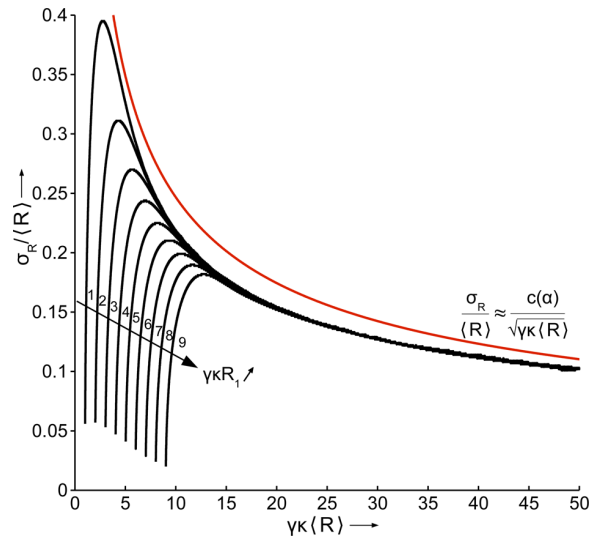


Figure 9. Polydispersity curves as functions of the variable $\gamma\kappa\langle R \rangle$ always collapse onto a single curve, characteristic of Gaussian fluctuations, after a maximum. This is the main feature of the second-scaling law. This collapse makes it possible to determine the experimental charge, the measured mean radius, and the polydispersity.

polydispersity, $\sigma_R/\langle R \rangle$ versus the scaled mean radius $\gamma\kappa\langle R \rangle$, obtained from the Smoluchowski model for various values of the parameter $\gamma\kappa R_1$ and a constant Hamaker coefficient $\alpha = 1/3$. For each value of the running parameter, the polydispersity departs from 0 (that corresponds to the initial system made of monomers), reaches a maximum, then decreases gently as the inverse of the squared root of the argument, as it should for the second scaling law.

Remarkably, all the data collapse on a single curve after the maximum, following the law

$$\frac{\sigma_R}{\langle R \rangle} \approx \frac{c(\alpha)}{\sqrt{\gamma\kappa\langle R \rangle}} \quad (14)$$

with the numerical constant $c(\alpha)$, such that $c(1/3) \approx 0.69$. The coefficient $c(\alpha)$ depends only slightly on α . For example, one finds $c(0.1) = 0.68$, $c(0.3) = 0.69$, and $c(1) = 0.71$. Changing the size of the system, one checks that this behavior, shown here for $N = 2 \times 10^6$ monomers, corresponds to the asymptotic $N \rightarrow \infty$.

Fitting the Experimental Data with the Second-Scaling Law Evaluates the Strength of Ionic Repulsions. With the experimental behavior of $\sigma_R/\langle R \rangle$ versus $\langle R \rangle$ (Figure 6) known, eq 14 can then be used to deduce the value of the actual surface charge density σ . Indeed, there is no sign of a maximum in the experimental data, and eq 14 can be rewritten

$$\sigma = \frac{c(\alpha)}{2\pi} \frac{\kappa}{\sqrt{l_B}} \frac{\sqrt{\langle R \rangle}}{\sigma_R} \quad (15)$$

With $c(1/3) = 0.69$, $\kappa = 0.41 \text{ nm}^{-1}$, and $l_b = 2.23 \text{ nm}$ known, the data for $\langle R \rangle$ and σ_R gives the value of the charge density. The results are shown in Figure 10. They show that the

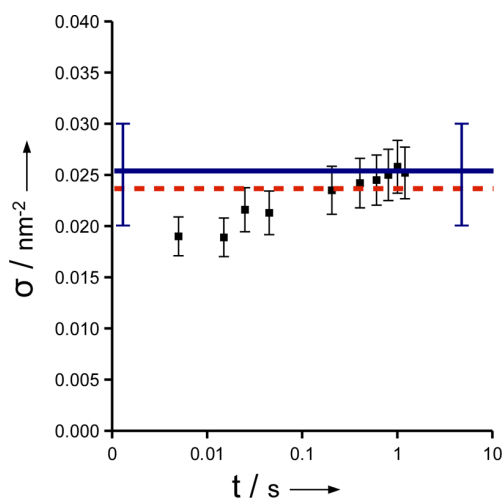


Figure 10. Surface charge densities deduced from eq 14 applied to the data displayed in Figure 3. The surface charge density increases only very slowly during the coalescence process. Its magnitude is consistent with electrophoresis measurements on final droplets (blue line) and a geometrical model where the macromolecules in the surface layer expose their end groups (red line).

variation of the surface charge is small (around 10%) and within the estimated values obtained through electrophoresis and estimation of the number of end-groups.

Smoluchowski Approach Predicts the Outcome of Droplets Encounters. The kinetic model based on the Smoluchowski approach reproduces quantitatively the experimental variations of the size distributions with elapsed time.

This suggests that it can be used as a predictive tool in the synthesis of nanodroplets, when the droplets are charged and the supersaturations are high, which is a common occurrence. The simulation makes it possible to calculate the size distributions as functions of elapsed time for wide ranges of time-scales and a large diversity of conditions. It is then straightforward to calculate the time-evolution of mean radius and the polydispersity according to the value of a control parameter, which is $\gamma\kappa R_1$. This parameter contains two quantities that can be tuned in a synthesis: the ionic strength, directly related to κ , and the surface charge density σ , directly related to γ . Also, the radius R_1 is the radius of a critical nucleus, e.g., in our case, the radius of a macromolecule in the bad solvent conditions.

First, one needs to control the mean droplet size. As displayed in Figure 11, the mean radius always increases logarithmically with elapsed time, $\langle R \rangle \propto \ln t$. This logarithmic growth is at the origin of the concept of colloidal stability, actually growth never stops, but it occurs over time-scales that increase exponentially. Besides, the proportionality factor in this relation decreases as $1/(\gamma\kappa R_1)$. This prefactor explains the otherwise qualitative observation that increasing the repulsive barriers will lead to smaller droplets, for a given growth time.

Second, one wishes to control the polydispersity of the droplet sizes. As displayed in Figure 11, the polydispersity is initially quite large since the population contains droplets that have been created at different times and have had different numbers of recombination events. However, at longer times above the millisecond, the polydispersity decreases according to a universal law that is independent from the initial conditions, as shown in Figure 9. After a few hours of synthesis, all the curves corresponding to various values of $\gamma\kappa R_1$ merge and the polydispersity no longer depends on this parameter. This has practical consequences since it suggests that the experimentalist has only limited control over the polydispersity of the nanodroplets dispersion. Under usual conditions and realistic

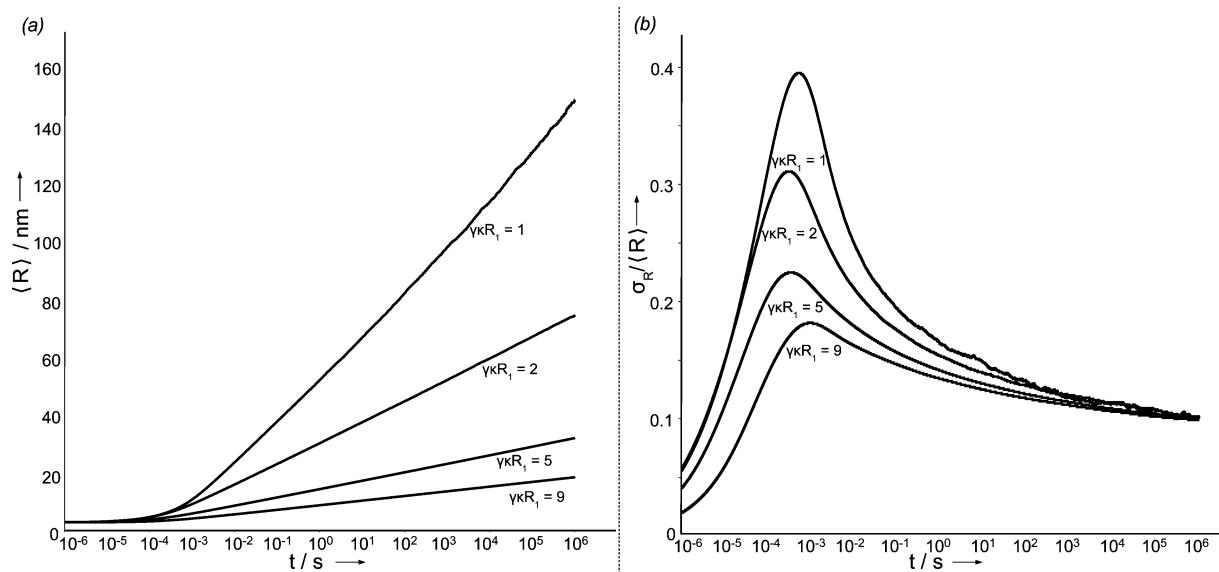


Figure 11. (a) Evolution of the mean radius for several values of the parameter $\gamma\kappa R_1$, which corresponds to the magnitude of the ionic repulsions. A logarithmic evolution is always observed and the slope of the variation decreases with an increase of the surface charge. (b) Evolution of the polydispersity for several values of the parameter $\gamma\kappa R_1$. The polydispersity only weakly depends on this parameter for times above a few seconds and is nearly independent from it for times above a few hours.

times, the polydispersity will be between 0.10 and 0.15, which corresponds to typical values for most nanodroplet dispersions, and also for nanoparticles made of silica,^{15,17,50,51} metals,^{11–13} and metal oxides⁵² (see Figure 11).

We have shown that the control parameter is the dimensionless number $\gamma\kappa R_1$. The behavior presented above corresponds to an evolution at constant value of $\gamma\kappa R_1$ but it can be extended to the cases of surface charge or ionic strength that vary during the synthesis. We have given above a method to evaluate the variation of $\gamma\kappa R_1$ with elapsed time from the experimental data. However the reverse operation can be performed instead, in order to obtain the simulated evolution at varying values of $\gamma\kappa R_1$. Experimentally, changes of the parameter $\gamma\kappa R_1$ can be performed by varying the amount of stabilizer or the ionic strength. With our considerations, it is possible to tune quantitatively the properties of the metastable colloidal dispersions obtained through synthesis. For example, if large droplets (~ 100 nm) of low polydispersity and good colloidal stability are desired in the time length of the hour, it may be better to start the coalescence at low values of $\gamma\kappa R_1$ and then increase the values of this parameter. To sum up, the model that we provide should lead to a more rational design of the synthesis schemes for nano-objects.

CONCLUSION

Coalescence and aggregation have been generally perceived as leading to populations of particles that become increasingly polydisperse. However, this may not always be the case. We have found that coalescence processes may lead to populations of decreasing polydispersity provided that the repulsions between two large particles are stronger than the repulsion between a small and a large particle. We investigated a population of droplets of a concentrated solution of macromolecules with ionic end groups, dispersed in water at moderate ionic strength. These droplets carry a number of electrical charges that is proportional to their surface area. Consequently they repel each other through ionic forces proportional to the surface area of each droplet. Through time-resolved SAXS, we found that the mean radius increases logarithmically with elapsed time while the relative width, or polydispersity, decreases as the inverse square root of the elapsed time. These experimental findings are in complete agreement with the results of numerical simulations of repelling droplet populations that evolve according to the kinetic Smoluchowski equations, whereas they contrast with what could be expected from the usual cluster aggregation processes (DLCA and RLCA). This hindered coalescence corresponds to a novel scaling of the solution of the Smoluchowski equations, known in the context of the critical phenomena as the "second-scaling law".

We predict that colloidal emulsions may evolve in this way, provided that the coalescence of droplets is determined by a nonlocal process, such as the crossing of a repulsive potential barrier during approach of droplets. Conversely, if coalescence is determined by a local event, such as the formation of a defect in the surfactant film that separates the droplets, larger droplets will coalesce together at a faster rate, and the population will evolve toward a larger polydispersity, as shown by Van den Tempel.⁵³ The same predictions can be made for the synthesis of colloidal particles at high particle concentrations: in this case as well, an evolution toward a narrow size distribution is predicted if the aggregation of particles is limited by a nonlocal event such as an overall repulsion between particles, as

postulated by Bogush and Zukoski.⁷ However, for colloidal dispersions, there is an additional condition, which is that solubility must be high enough so that the particles continuously return to a spherical shape. If this was not the case, the aggregates would take fractal structures, and the population would be expected to evolve as in RLCA processes.

Finally, the evolution of populations of colloidal objects that repel each other is closely linked to the concept of colloidal metastability. We find that, under the conditions stated above, colloidal systems will follow the second scaling law, which gives an explicit form (logarithmic) to the slow evolution of the metastable state.

ASSOCIATED CONTENT

Supporting Information

Electrophoretic mobility with pH variations and detailed calculation of the coalescence kernel in the Overbeek-Reerink approximation. This material is available free of charge via the Internet at <http://pubs.acs.org/>.

AUTHOR INFORMATION

Corresponding Author

*E-mail: kevin.roger@espci.fr.

Notes

The authors declare no competing financial interest.

ACKNOWLEDGMENTS

We gratefully acknowledge the ID2 beamline staff, in particular Dr. J. Gümmel for their assistance in the SAXS experiment and the ESRF for beamtime allocation. We thank Pr. J.-P. Cohen-Addad for his input in the phase behavior of ternary systems. This work was supported by ANR 2010 BLAN 942 03 "LimOuzIne".

REFERENCES

- (1) Bibette, J.; Leal-Calderon, F.; Schmitt, V. *Emulsion Science*; Springer, 2007.
- (2) Hasmy, A.; Paredes, R.; Sonnevile-Aubrun, O.; Cabane, B.; Botet, R. *Phys. Rev. Lett.* **1999**, *82*, 3368–3371.
- (3) Lin, M. Y.; Lindsay, H. M.; Weitz, D. A.; Ball, R. C.; Klein, R.; Meakin, P. *Phys. Rev. A* **1990**, *41*, 2005–2020.
- (4) Lin, M. Y.; Lindsay, H. M.; Weitz, D. A.; Klein, R.; Ball, R. C.; Meakin, P. *J. Phys.: Condens. Matter* **1990**, *2*, 3093–3113.
- (5) Sugimoto, T. *Adv. Colloid Interface Sci.* **1987**, *28*, 65–108.
- (6) LaMer, V. K.; Dinegar, R. H. *J. Am. Chem. Soc.* **1950**, *72*, 4847–4854.
- (7) Bogush, G. H.; Zukoski, C. F. *J. Colloid Interface Sci.* **1991**, *142*, 19–34.
- (8) Matijevic, E. *Chem. Mater.* **1993**, *5*, 412–426.
- (9) Privman, V.; Goia, D.; Park, J.; Matijevic, E. *J. Colloid Interface Sci.* **1999**, *213*, 36–45.
- (10) Matijevic, E. *Colloid J.* **2007**, *69*, 29–38.
- (11) Polte, J.; Erler, R.; Thünemann, A. F.; Sokolov, S.; Ahner, T. T.; Rademann, K.; Emmerling, F.; Kraehnert, R. *ACS Nano* **2010**, *4*, 1076–1082, PMID: 20088602.
- (12) Polte, J.; Tuae, X.; Wuithschick, M.; Fischer, A.; Thuenemann, A. F.; Rademann, K.; Kraehnert, R.; Emmerling, F. *ACS Nano* **2012**, *6*, 5791–5802.
- (13) Abécassis, B.; Testard, F.; Spalla, O.; Barboux, P. *Nano Lett.* **2007**, *7*, 1723–1727, PMID: 17530813.
- (14) Balmer, J. A.; Mykhaylyk, O. O.; Armes, S. P.; Fairclough, J. P. A.; Ryan, A. J.; Gummel, J.; Murray, M. W.; Murray, K. A.; Williams, N. S. *J. Am. Chem. Soc.* **2011**, *133*, 826–837.
- (15) Bertholdo, R.; dos Reis, F. V.; Pulcinelli, S. H.; Santilli, C. V. *J. Non-Cryst. Solids* **2010**, *356*, 2622–2625.

- (16) Boukari, H.; Long, G.; Harris, M. J. *Colloid Interface Sci.* **2000**, *229*, 129–139.
- (17) Fouilloux, S.; Désert, A.; Taché, O.; Spalla, O.; Daillant, J.; Thill, A. J. *Colloid Interface Sci.* **2010**, *346*, 79–86.
- (18) Pontoni, D.; Narayanan, T.; Rennie, A. R. *Langmuir* **2002**, *18*, 56–59.
- (19) Smoluchowski, M. *Phys. Z.* **1916**, *17*, 585–599.
- (20) Panine, P.; Finet, S.; Weiss, T.; Narayanan, T. *Adv. Colloid Interface Sci.* **2006**, *127*, 9–18.
- (21) Botet, R.; Cabane, B. J. *Appl. Crystallogr.* **2012**, *45*, 406–416.
- (22) Voter, A. F. In *Introduction to the Kinetic Monte Carlo Method in Radiation Effects in Solids*; Sickafus, K. E., Kotomin, E. A., Eds.; Springer: Dordrecht, 2005.
- (23) Henkelman, G.; Jonsson, H. J. *Chem. Phys.* **2001**, *115*.
- (24) Aubry, J.; Ganachaud, F.; Cohen Addad, J.-P.; Cabane, B. *Langmuir* **2009**, *25*, 1970–1979.
- (25) Addad, J. C. private correspondence.
- (26) Roger, K.; Cabane, B. *Angew. Chem., Int. Ed.* **2012**, DOI: 10.1002/anie.201207114.
- (27) Roger, K.; Cabane, B. *Angew. Chem., Int. Ed.* **2012**, *51*, 1521–3773.
- (28) Zhang, C.; Pansare, V. J.; Prud'homme, R. K.; Priestley, R. D. *Soft Matter* **2012**, *8*, 86–93.
- (29) Pusey, P. J. *Phys. (Paris)* **1987**, *48*, 709–712.
- (30) Drake, R. In *A general mathematical survey of the coagulation equation*; Hidy, G., Brock, J., Eds.; Pergamon Press: Oxford, 1972.
- (31) Fuchs, N. *The mechanics of aerosols*; Pergamon Press: New York, 1964.
- (32) Friedlander, S. *Smoke, Dust and Haze*; Oxford University Press: New York, 2000.
- (33) Verwey, E. J. W.; Overbeek, J. T. G. *Theory of the stability of lyophobic colloids*; Elsevier: Amsterdam, 1948.
- (34) Hidy, G.; Brock, J. J. *Colloid Sci.* **1965**, *20*, 477–491.
- (35) Melis, S.; Verduyn, M.; Stori, G.; Morbidelli, M.; Baldyga, J. *AIChE J.* **1999**, *45*, 1383.
- (36) Trulsson, M.; Forsman, J.; Åkesson, T.; Jönsson, B. *Langmuir* **2009**, *25*, 6106–6112.
- (37) van Dongen, P. G. J.; Ernst, M. H. *Phys. Rev. Lett.* **1985**, *54*, 1396–1399.
- (38) Friedlander, S. J. *Meteor.* **1961**, *29*, 537–547.
- (39) Drake, R. L. J. *Atmos. Sci.* **1972**, *29*, 537–547.
- (40) Lee, M. H. J. *Phys. A: Math. Gen.* **2001**, *34*, 10219–10241.
- (41) Menon, G.; Pego, R. *Commun. Pure Appl. Math.* **2004**, *1197*–1232.
- (42) Friedlander, S.; Wang, C. J. *Colloid Interface Sci.* **1966**, *22*, 126–132.
- (43) Harada, M.; Inada, Y. *Langmuir* **2009**, *25*, 6049–6061.
- (44) Botet, R.; Ploszajczak, M. *Universal Fluctuations: The Phenomenology of Hadronic Matter*; World Scientific Publishing Co. Pte. Ltd: New Jersey, 2002.
- (45) Lewin, L. *Polylogarithms and Associated Functions*; North-Holland, 1981.
- (46) Kahlweit, M. *Adv. Colloid Interface Sci.* **1975**, *5*, 1–35.
- (47) Reerink, H.; Overbeek, J. J. *Discuss. Faraday Soc.* **1954**, *18*, 74–84.
- (48) Dammer, S. M.; Wolf, D. E. *Phys. Rev. Lett.* **2004**, *93*, 150602.
- (49) Botet, R.; Ploszajczak, M.; Latora, V. *Phys. Rev. Lett.* **1997**, *78*, 4593–4596.
- (50) Chang, J.; Lesieur, P.; Delsanti, M.; Belloni, L.; Bonnet-Gonnet, C.; Cabane, B. J. *Phys. Chem.* **1995**, *99*, 15993–16001.
- (51) Stöber, W.; Fink, A.; Bohn, E. J. *Colloid Interface Sci.* **1968**, *26*, 62–69.
- (52) Wu, W.; He, Q.; Jiang, C. *Nanoscale Res. Lett.* **2008**, *3*, 397–415.
- (53) Tempel, M. V. D. *Stability of Oil-In-Water Emulsions*. Ph.D. thesis, Technische Hogeschool Delft, 1953.

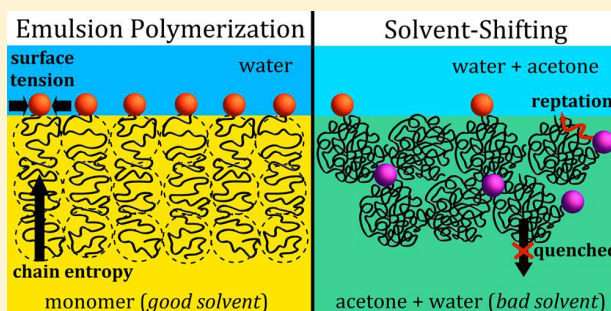
Surface Charge of Polymer Particles in Water: The Role of Ionic End-Groups

Kevin Roger,^{*,†} Mohammed Eissa,[‡] Abdelhamid Elaissari,[‡] and Bernard Cabane[†]

[†]PMMH, CNRS UMR 7636, ESPCI, 10 rue Vauquelin, F 75231 Paris Cedex 05, France

[‡]Université de Lyon, F-69622, Lyon, France, and Université Lyon-1, Villeurbanne, CNRS, UMR 5007, LAGEP, CPE-308G, 43 bd. 11 Nov. 1918, F-69622 Villeurbanne, France

ABSTRACT: Polymer particles, containing macromolecules made by the polymerization of nonionic monomers, can be ionized in water thanks to the end-groups of the macromolecules. We show that poly(methylmethacrylate) particles with ionic end-groups can acquire colloidal properties such as dispersion metastability and electrokinetic mobility. We demonstrate that the variation of these colloidal properties according to solution pH is uniquely determined by the chemical nature of the end-groups and therefore by the nature of the initiator used in the polymerization reaction. We compare polymer dispersions in which the polymer particles were made by different processes (e.g., surfactant-free emulsion polymerization or precipitation of the macromolecules induced by solvent shifting). For each colloidal dispersion, we determine the number of end-groups that are actually located at the surfaces of the particles, and we show that this number is a trace of the process by which the macromolecules were self-assembled into colloidal particles. We propose that it is possible to recover mechanistic details of this self-assembly process through measurements of the distribution of end-groups within the particles.



INTRODUCTION

Polymer particles are commonly made through the emulsion polymerization of mixtures of ionic and nonionic monomers in surfactant-free aqueous solutions.¹ These aqueous polymer latex dispersions are widely used in paints, paper coatings, and all sorts of water-based adhesives.¹ In these applications, the characteristics of the particle surfaces are of first importance in determining the behavior of the dispersions. Remarkably, the use of ionic monomers is not necessary for such surfactant-free processes. Indeed, it is well known that emulsion polymerization can proceed with nonionic monomers only, provided that the initiator yields ionic end-groups to the growing macromolecules.^{2–4} The resulting polymer particles have surfaces that are populated with ionic end-groups, and the variation of the surface charge with pH reflects that of the end-groups.^{5,6}

Polymer particles can also be made through the self-assembly of macromolecules that are initially dissolved in a good solvent and subsequently precipitated through the addition of a nonsolvent.^{7–10} In such solvent-shifting processes, the original solvent is usually a polar solvent that is miscible with water, and the nonsolvent is water. Here as well, it has been proposed that the colloidal stability of the resulting polymer particles is caused by the presence of ionic groups at the polymer/water interfaces and that these ionic groups could be end-groups of the macromolecules.^{10,11}

Our aim is to establish quantitative relationships among the process by which the particles were synthesized (e.g., emulsion polymerization or solvent shifting), the locations of the end-groups of the macromolecules within the particles, and the surface charges of the particles. For this purpose, we compare six aqueous dispersions of a hydrophobic polymer, poly(methylmethacrylate) (PMMA). Two of these dispersions were made through emulsion polymerization, two others were made through solvent-shifting, using the same macromolecules that were made through the emulsion polymerization process, and the last two were also made through solvent shifting, using macromolecules that were commercially available as molecular weight standards. We report measurements of electrophoretic mobility for each type of polymer particle and a determination of the limit of colloidal stability in solvent-shifting processes using mixtures of macromolecules with and without ionic end-groups. We present a quantitative analysis of these experimental results and use it to answer the following questions: (1) What is the relationship among the surface charge, the surface potential, the zeta potential, and the electrophoretic mobility of these particles? (2) Do these properties vary with pH in a way that can be quantitatively accounted for by the acidity (pK_a) of the end-groups? For particles with unknown end-groups, can we

Received: May 19, 2013

Revised: July 4, 2013

Published: July 11, 2013

invert these analytical procedures to determine the numbers of end-groups of various types (carboxylates, sulfates, etc.)? (3) Can we use these analytical results to determine mechanistic details of the processes by which the particles were synthesized (i.e., how the emulsion polymerization was conducted or how the different macromolecules were self-assembled during solvent-shifting)?

MATERIALS AND METHODS

Materials. Methylmethacrylate (MMA) and potassium persulfate (KPS) were purchased from Sigma-Aldrich and used as received (purity >99%). 4,4'-Azobis-(4-cyanovaleric) acid (ACPA) was purchased from Wako Chemicals (purity >98%) and purified through recrystallization. Two monodisperse calibration PMMA were purchased from Polymer Source Inc., PMMA-C₄H₉ ($M_w = 21\,000\text{ g}\cdot\text{mol}^{-1}$) and PMMA-COOH ($M_w = 9900\text{ g}\cdot\text{mol}^{-1}$).

Surfactant-Free Emulsion Polymerization. Dispersions of poly(methyl methacrylate) (PMMA) particles, at a final weight fraction of 0.2, were prepared by a surfactant-free emulsion polymerization method. Monomer methylmethacrylate (MMA) (100 g) was added to a three-necked flask reactor containing Milli-Q water purged with nitrogen gas. The dispersion was stirred at 300 rpm for 30 min at room temperature. An initiator (5g), either potassium persulfate (KPS) or 4,4'-azobis-(4-cyanovaleric) acid (ACPA), was used. Each initiator molecule is thermally unstable and will dissociate to yield two radicals. Prior to use, KPS was dissolved in Milli-Q water and ACPA was dissolved in a 0.1 mol·L⁻¹ NaOH solution. The temperature of the reactor was raised to 75 °C, and the initiator solution was added. The total amount of water was 395 g, and the ionic strength was evaluated to be 0.05 mol·L⁻¹ for the synthesis with KPS and 0.1 mol·L⁻¹ for the synthesis with ACPA. The whole reaction medium was maintained oxygen-free to avoid the hydrolysis reaction of sulfate functions to hydroxyl functions. The reaction was conducted for 18 h and was terminated by cooling to room temperature. Milky dispersions of PMMA particles were obtained in each case. The mean radius was 300 nm for the synthesis with KPS and 600 nm for the synthesis with ACPA. After sedimentation, the supernatant was removed and the polymer particles were used either for direct experiments or as a polymer source for a new preparation through solvent shifting.

Solvent Shifting. Dispersions of polymer particles were also prepared through an alternative route, the solvent-shifting of polymer solutions.^{7,8,10} This method proceeds through the addition of a nonsolvent (water) to a solution of the polymer in a good solvent (acetone). It leads to the formation of polymer particles that are slightly swollen by the mixed solvent.^{8,9} We prepared PMMA solutions in acetone for the purchased molecular weight standard and the synthesized polymers in a mass fraction of 10⁻³. Then, a NaCl solution, at 10⁻³ mol·L⁻¹, was added in a 1/1 ratio to the acetone solution. The resulting dispersions had colloidal metastability. According to the phase diagram of the PMMA/acetone/water system, the polymer particles were slightly swollen by the acetone + water mixture, which was a bad solvent. Subsequently, the polymer dispersions were diluted in aqueous NaCl solutions (ratio 1–19), and then the particles contained only PMMA.

Electrophoretic Mobility. Electrophoretic mobility measurements were performed with a Malvern Zetasizer. The ionic strength was set at 10⁻³ mol·L⁻¹ NaCl for all measurements, unless otherwise noted.

Scattering Techniques. Dynamic light scattering measurements were performed with a Cordouan Vasco on diluted polymer dispersions. The analysis was performed through a Padé-Laplace algorithm. A large number of measurements were performed to obtain statistical size distributions. Mean diameters were measured, which also yield the total surface area of the dispersed system. For dispersions prepared through solvent shifting, the typical distributions of particle radii were also determined through small angle X-ray scattering. We found that the width σ_R divided by the mean radius $\langle R \rangle$ was $\sigma_R/\langle R \rangle \approx$

0.1, indicating that solvent shifting produced dispersions that had narrow size distributions.⁹

Polymer Characterization. The weight-average molecular weight (M_w), number average molecular weight (M_n), and polydispersity index (M_w/M_n) of the prepared PMMA were determined using gel permeation chromatography (GPC). The measurements were carried out using tetrahydrofuran (THF) as the eluant at a flow rate of 1 mL/min at 40 °C. With KPS, we obtained $M_n = 34\,000\text{ g}\cdot\text{mol}^{-1}$ and $M_w/M_n = 4.1$, whereas with ACPA we obtained $M_n = 56\,000\text{ g}\cdot\text{mol}^{-1}$ and $M_w/M_n = 4.5$. The chemical structure of the repetition units was checked with infrared spectroscopy, and the spherical shape of the particles was checked with transmission electron microscopy (TEM). Particles prepared from solvent shifting were also spherical, as shown through previous TEM measurements.⁸

RESULTS

Electrophoretic Mobility. The electrophoretic mobility of charged colloids originates from their surface charge. The variations of their electrophoretic mobility with pH characterize the acid/base behavior of their interface, and the variations with ionic strength determine the attenuation factor between the surface potential and the zeta potential. Here we report such variations for particles prepared either through emulsion polymerization or solvent shifting and contain macromolecules with different end-groups.

At first we used PMMA dispersions synthesized through emulsion polymerization with the two initiators, KPS and ACPA. These dispersions were diluted with aqueous salt solutions (10⁻³ mol·L⁻¹ NaCl). The variations in electrophoretic mobility with pH are displayed in Figure 1. The particles produced through the synthesis with KPS as an initiator (average radius = 300 nm) had an electrophoretic mobility that was nearly constant with pH over the range of pH 3 to 11, as expected for sulfate end-groups. The particles produced through the synthesis with ACPA as an initiator (average radius = 600 nm) had an electrophoretic mobility that varied with pH in the range investigated, as expected for carboxylic acid end-groups.

We then used the same polymers to produce polymer particles through solvent shifting.

For this purpose, we took the dry polymers prepared through emulsion polymerization, dissolved them in acetone, and then added water. The rapid addition of this nonsolvent triggered a microphase separation of the polymer/acetone solution, and polymer particles ($d = 110\text{ nm}$) were generated through hindered coalescence events.⁹ Figure 2 presents the electrophoretic mobility variations with pH of these particles. For each polymer, these variations with pH were quite similar to those of emulsion polymerization particles, displayed in Figure 1, but the mobility was of a much smaller magnitude. Figure 3 presents the mobility of particles obtained through solvent shifting a molecular weight standard PMMA with carboxylic acid end-groups ($d = 100\text{ nm}$). Here as well the electrophoretic mobility variations were similar to those of the polymer synthesized with ACPA, displayed in Figure 1, but the mobility was smaller in magnitude.

Finally we measured the electrophoretic mobility variations of weight standard PMMA-COOH particles prepared through solvent shifting, as a function of the ionic strength, adjusted with sodium chloride. As expected, the magnitude of the mobility decreased with increasing ionic strength. For modeling purposes (detailed in the Discussion section), Figure 4 displays the variation of the zeta potential with ionic strength (or

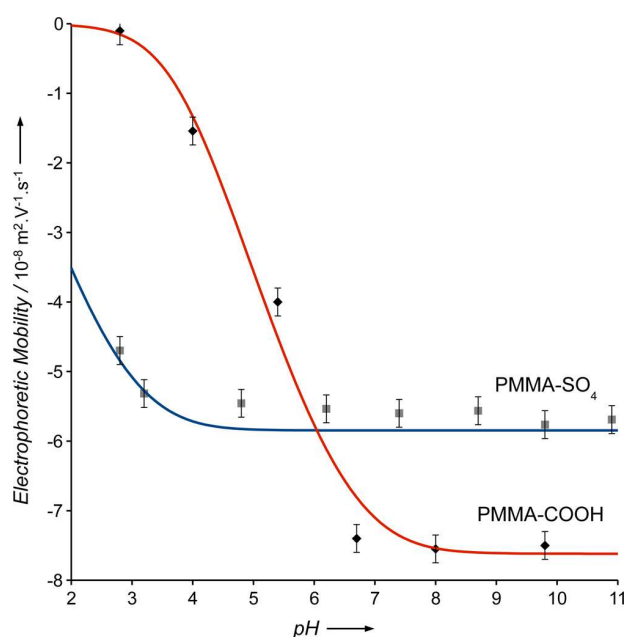


Figure 1. Electrophoretic mobility of PMMA particles synthesized through surfactant-free emulsion polymerization with either KPS (squares) or ACPA (diamonds) as the initiator. Each set of data points corresponds to one aqueous dispersion that was brought to the pH values indicated on the horizontal scale. The lines are fits to experimental data according to the modeling of an acid–base reaction at the interface (Discussion). The red line corresponds to the pK_a of carboxylic acid end-groups, $pK_a = 5$, and the blue line corresponds to the pK_a of sulfate end-groups, $pK_a = 1.8$. The fitting parameter is the surface charge density for which all end-groups at the interface are ionized (i.e., at the plateau value). The fit yields rather high surface charge densities, $\sigma_{\max} = 0.15e \text{ nm}^{-2}$ for carboxylic acid end-groups and $\sigma_{\max} = 0.12e \text{ nm}^{-2}$ for sulfate end-groups.

equivalently the reciprocal Debye length) rather than the raw mobility data.

Colloidal Stability. The numbers of charged end-groups at the interface can also be probed according to the colloidal stability of particles produced through solvent shifting. Indeed, in this process, the final particle sizes are directly related to their surface charge.⁹ Thus, replacing macromolecules that have charged end-groups with macromolecules that have uncharged end-groups should change their final sizes. If the macromolecules also differ through other features, such as their molar mass, then their final sizes may also yield some information regarding the mechanism of the solvent-shifting process.

We performed a set of solvent-shifting experiments in which macromolecules terminated by carboxylic acid groups (PMMA–COOH, $M = 9900 \text{ g}\cdot\text{mol}^{-1}$) were replaced with macromolecules terminated by a butyl group (PMMA–C₄H₉, $M = 21\,000 \text{ g}\cdot\text{mol}^{-1}$). Figure 5 displays the variation with pH of the average PMMA particle diameter upon gradually replacing PMMA–COOH with PMMA–C₄H₉ (i.e., decreasing the number of charged end-groups). The pH was set at 10, and the ionic strength constant was set at $10^{-3} \text{ mol}\cdot\text{L}^{-1}$. At first, the diameter increased slowly with the decrease in the number of charged end-groups and then much more steeply for small numbers of charged groups. When only PMMA–C₄H₉ was used, all particles were caught in macroscopic aggregates.¹¹

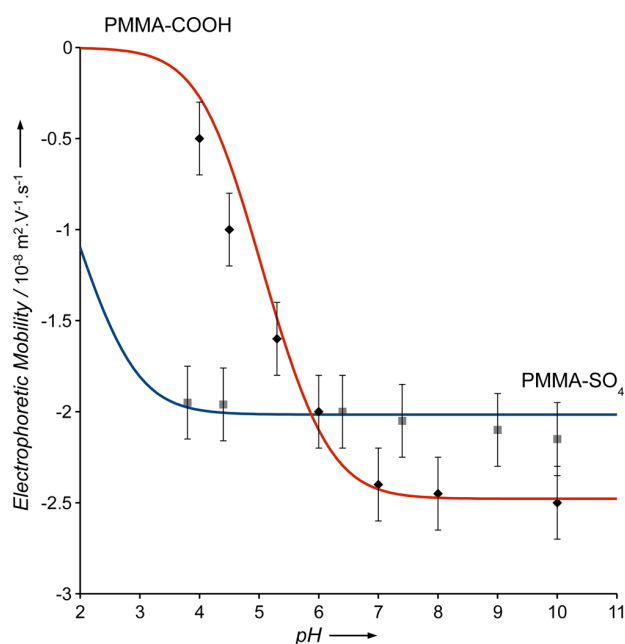


Figure 2. Electrophoretic mobility of PMMA particles produced through solvent shifting, using polymers prepared through surfactant-free emulsion polymerization, with either KPS initiator (squares) or ACPA initiator (diamonds). The lines are fits to the experimental data according to the modeling of an acid–base reaction at the interface (Discussion). The red line corresponds to the pK_a of carboxylic acid end-groups, $pK_a = 5$, and the blue line corresponds to the pK_a of sulfate end-groups, $pK_a = 1.8$. The fitting parameter is the surface charge density for which all end-groups at the interface are ionized (i.e., at the plateau value). The fit yields low surface charge densities, $\sigma_{\max} = 0.015e \text{ nm}^{-2}$ for carboxylic acid end-groups and $\sigma_{\max} = 0.011e \text{ nm}^{-2}$ for sulfate end-groups.

DISCUSSION

Surface Charge and pH. The variations of surface charge with pH are characteristic of the chemical nature of the functional groups that carry the electrical charge. The two aqueous PMMA dispersions prepared through surfactant-free emulsion polymerization had different end-groups because they were prepared using different initiators: one had carboxylic acid end-groups and the other had sulfate end-groups. These two functions have different pK_a values; consequently, their ionization does not occur over the same pH range. To model the variations with pH of the ionization of particle surfaces, we used the following relations: pH \rightarrow^A surface charge density \rightarrow^B surface potential \rightarrow^C zeta potential \rightarrow^D electrophoretic mobility.

First, to obtain relation A, we must describe the acid–base equilibrium between an acid (R–AH) and its conjugate base (R–A[−]) at the surface of the polymer particle. The chemical potential of an ion R–A[−] at the interface is expressed as

$$\begin{aligned}\mu_{R-A^-} &= \mu_{R-A^-}^0 + RT \ln(x_{R-A^-}) - eN_A\psi_s \\ &= \mu_{R-A^-}^0 + RT \ln(a_{R-A^-})\end{aligned}\quad (1)$$

where x_{R-A^-} is the fraction of R–A[−] and can be expressed as σ/σ_{\max} , where σ is the surface density of elementary charges (nm^{-2}), σ_{\max} is the maximal surface density of elementary charges, and ψ_s the surface potential. This yields the activity of the anions, a_{R-A^-} :

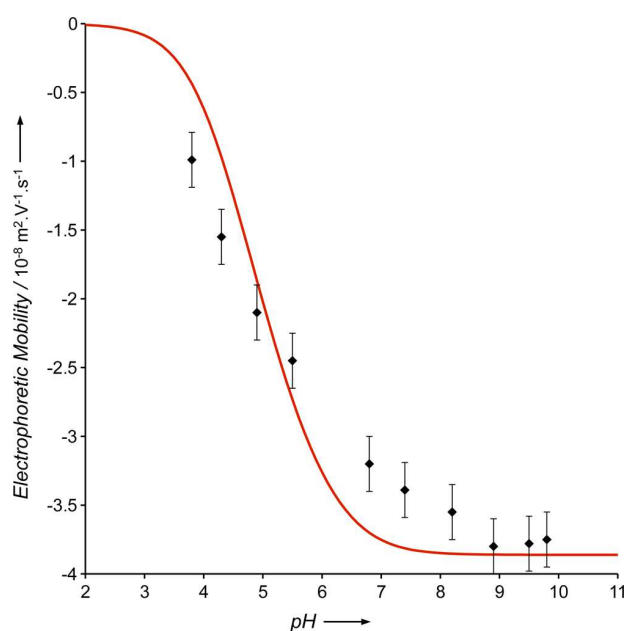


Figure 3. Electrophoretic mobility of PMMA particles produced through solvent shifting, using a molecular weight standard PMMA with COOH end-groups, as a function of pH. The line is a fit to the experimental data according to the modeling of an acid–base reaction at the interface, using the pK_a of a carboxylic acid end-group, $pK_a = 5$. The fitting parameter is the surface charge density for which all of the end-groups at the interface are ionized (i.e., at the plateau value). This yields a low surface charge density of $\sigma_{\max} = 0.04e \text{ nm}^{-2}$.

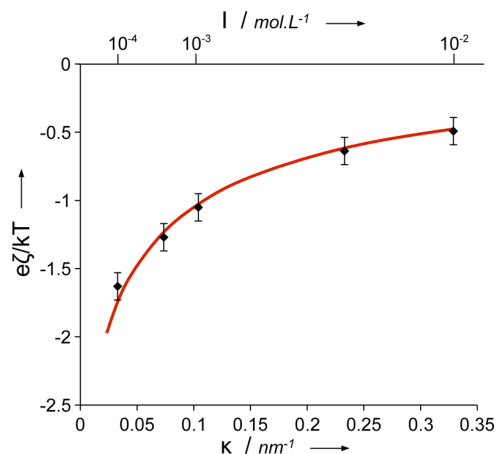


Figure 4. Variations of the zeta potential with the reciprocal Debye length of weight standard PMMA–COOH particles. The zeta potential is calculated from the electrophoretic mobility according to the O'Brien and Hunter expression detailed in the Discussion section. The red line is the variation of the surface potential with a maximal surface charge density of $\sigma_{\max} = 0.04e \text{ nm}^{-2}$ at $\text{pH} \sim 5.5$, according to the model developed in the Discussion section. The two variations are closely matched, and the zeta potential can thus be taken as a measurement of the surface potential for such low surface charge densities.

$$a_{R-A^-} = \frac{\sigma}{\sigma_{\max}} \exp\left(\frac{-e\psi_s}{kT}\right) \quad (2)$$

We introduce the acidity equilibrium constant, $K_a = (a_{R-A^-} \times a_{H_3O^+})/a_{R-AH}$ with $a_{H_3O^+} = 10^{-\text{pH}}$. The conservation of mass can

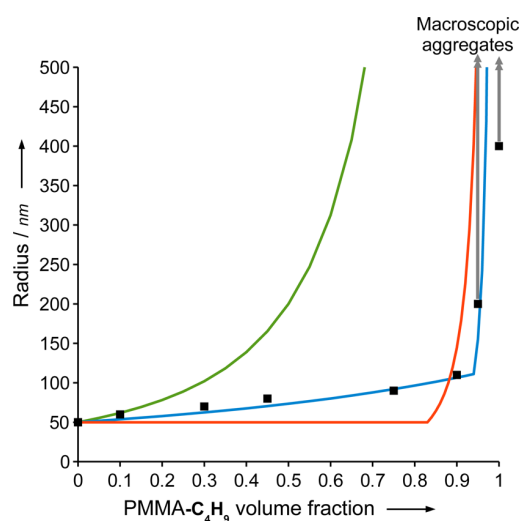


Figure 5. Mean diameter of mixed PMMA particles prepared through solvent-shifting, containing a mixture of PMMA with COOH end-groups ($M = 9900 \text{ g/mol}$) and PMMA with butyl end-groups ($M = 21\,000 \text{ g/mol}$). All COOH entities were ionized at $\text{pH} 10$, and the ionic strength was constant at $10^{-3} \text{ mol}\cdot\text{L}^{-1}$ NaCl. At high fractions of nonionizable PMMA– C_4H_9 , macroscopic aggregates are observed. Green line: homogeneous particle model; it is assumed that the interface was made of PMMA–COOH and PMMA– C_4H_9 at the same composition as the bulk composition. Red line: heterogeneous particle model; it is assumed that the interface preferentially contained PMMA–COOH. Blue line: intermediate model; it is assumed that the interface contained 65% PMMA–COOH and 35% PMMA– C_4H_9 , up to the point where there was not enough PMMA–COOH to maintain the composition.

be expressed through the mole fractions $x_{R-A^-} + x_{R-AH} = 1$. Because $a_{R-AH} = x_{R-AH}$ and $x_{R-A^-} = \sigma/\sigma_{\max}$, we have $a_{R-AH} = 1 - (\sigma/\sigma_{\max})$. This leads to an expression that contains two parameters only, the maximum surface charge density, σ_{\max} and the free energy, $-kT \ln(K_a)$:

$$\sigma = \frac{\sigma_{\max} K_a}{K_a + 10^{-\text{pH}} \exp\left(\frac{-e\psi_s}{kT}\right)} \quad (3)$$

To obtain relation B, we use the Poisson–Boltzmann theory in the form of the Grahame equation¹²

$$\frac{\sigma}{e} = \sqrt{8\epsilon\epsilon_0 kT I} \sinh\left(\frac{e\psi_s}{2kT}\right) \quad (4)$$

where $\epsilon\epsilon_0$ is the local dielectric constant and I is the ionic strength (number of ions per unit volume). This equation can be rewritten by introducing the reciprocal Debye screening length κ :

$$\sigma = 2\epsilon\epsilon_0 kT \kappa \sinh\left(\frac{e\psi_s}{2kT}\right) \quad (5)$$

There are no free parameters in these equations (i.e., the value of the surface charge uniquely determines the surface potential).

The surface potential may differ from the zeta potential by an attenuation factor. We have measured the electrophoretic mobility as a function of the ionic strength. This data can be plotted as the variations of the zeta potential, calculated from the mobility through relation D, with the reciprocal Debye length. To identify whether these variations, displayed in Figure

4, are due to an attenuation or the variation of the surface potential itself, we plotted the surface potential as a function of the ionic strength according to relation B. The calculation is displayed as a red line in Figure 4 and fits the variation of the zeta potential. We can thus deduce that the decrease in magnitude of the zeta potential with the ionic strength is solely due to the decrease in magnitude of the corresponding surface potential. This is due to the fact that the surface charge densities are quite low. We can then identify the zeta potential to the surface potential and use this as relation C for all of the calculations.

For relation D, we used the analytical expression developed by O'Brien and Hunter,¹³ which is more accurate than the simple linear Smoluchowski¹⁴ relation. It explicitly involves the product κR of the reciprocal Debye length κ with the radius R

$$\mu = \frac{\epsilon k T}{6 \pi \eta e} \left(\frac{3 \epsilon \zeta}{2 k T} - \frac{3 \epsilon \zeta}{k T} - \frac{6 \ln 2}{z} \left[1 - \exp\left(\frac{-z \epsilon \zeta}{k T}\right) \right] \right) \left(\frac{\kappa R \exp\left(\frac{-z \epsilon \zeta}{2 k T}\right)}{1 + \frac{3 m}{z^2}} \right) \quad (6)$$

with η being the solvent viscosity, $z = -1$ for negative charges, and m being a drag coefficient taken as 0.184. There are no free parameters, and the mobility is uniquely determined by the zeta potential. (Note that the reverse is not always true, and for this reason, we present our results as mobility values rather than zeta potential values, with the exception of Figure 4.)

At this point, it is possible to calculate the electrophoretic mobility as a function of pH using all four relations. The free parameters are K_a and σ_{\max} . We chose the acidity constants according to the type of end-groups on the macromolecules. For particles with carboxylic acid end-groups, we chose $K_a = 10^{-5}$, and for particles with sulfate end-groups, we chose $K_a = 10^{-1.8}$. The maximal surface densities of elementary charges were adjusted to fit the model to the experimental data. The results are displayed as solid lines in Figures 1–3. A quantitative fit is obtained for all dispersions of polymer particles, no matter how they were synthesized. This quantitative agreement demonstrates that the chemical structure of the end-groups determines the electrical properties of the polymer/water interfaces.

Number of End-Groups at the Interface. The model for the electrophoretic mobility variation with pH gives the values of the maximal surface charge density for each type of polymer particle, as shown in Figure 6. A striking observation is that particles of the same polymer prepared through two different methods have surface charge densities that differ by 1 order of magnitude. Therefore the number of end-groups that are located at the interface must depend on the mechanism by which the polymer particles were self-assembled. Conversely, the number of end-groups at an interface can be used to identify a geometric picture of the interface and then a self-assembly mechanism.

In the solvent-shifting method, the fast addition of nonsolvent causes the macromolecules to collapse individually and then to aggregate.¹⁵ In the collapsed state, they are unable to change conformations and to let buried end-groups reach the polymer/water interface. We assume that only macromolecules in the outermost layer of each aggregate can bring their end-groups to the interface. Their number is N_{layer} :

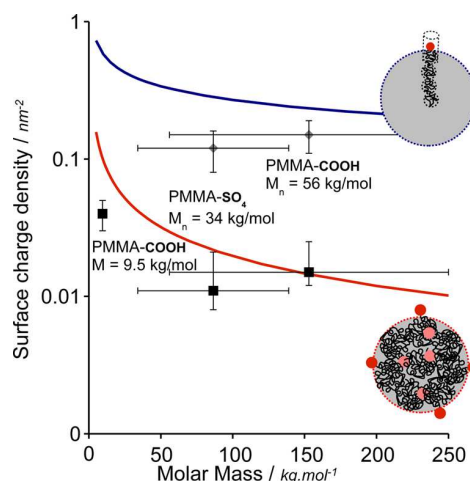


Figure 6. Maximal surface charge densities of polymer particles obtained from fitting the experimental variations with the pH of electrophoretic mobility, which are displayed on Figures 1–3. Gray diamonds correspond to particles prepared through emulsion polymerization, and black squares correspond to particles prepared through solvent shifting. The red line is a calculation that assumes that half the macromolecules in the surface layer expose their end-groups and are collapsed as a result of the rapid addition of a nonsolvent aqueous solution. The blue line is calculated by assuming that the macromolecules at the interface expose their end-groups and are at their conformational equilibrium.

$$N_{\text{layer}} = \frac{R_{\text{particle}}^3 - (R_{\text{particle}} - 2R_c)^3}{R_c^3} \approx 6 \frac{R_{\text{particle}}^2}{R_c^2} \quad (7)$$

Each one of the macromolecules has an end-group that can contribute to the surface charge. If we make the simple assumption that half of the end-groups are oriented toward water, then the surface charge density is

$$\sigma_{\text{random}} = \frac{N_{\text{layer}}}{2.4 \pi R_{\text{particle}}^2} \approx \frac{3}{4 \pi R_c^2} \quad (8)$$

This surface charge density is essentially a function of R_c and thus of the mass of the macromolecule. The result of this calculation is displayed as a red line in Figure 6. The fair agreement with the data supports the description of the mechanism of the solvent-shifting process where macromolecules first collapse and then aggregate to form dense polymer particles.

The results presented in Figure 6 show that, when prepared through emulsion polymerization, the particles have a much higher surface charge. Therefore, a larger number of end-groups are located at the polymer/water interface. This must be related to the mechanism of emulsion polymerization in which the particles are stabilized by a surface layer made of oligomers with ionized end-groups, and these oligomers grow through the capture of dissolved monomers. In this state, the ionized end-groups remain anchored at the interface whereas the reactive chain ends react with monomers in the liquid droplet core. Still assuming one ionized end-group per macromolecule, we calculate the surface charge according to the surface area occupied by each macromolecule at the interface. This equilibrium surface area is determined by the competition between the interfacial tension cost of contact between the macromolecular chain and water, the repulsions between

charged groups, and the stretching free energy of the chains. Under our synthesis conditions, the ionic repulsions are highly screened and are thus negligible compared to the stretching cost. We calculate the surface area by minimizing the total free energy variation from the unstretched state to a stretched state, modeled as a cylinder capped with hemispheres of radius R_s :

$$\Delta F = F_{\text{stretched}} - F_{\text{collapsed}} = \Delta F_{\text{interfacial}} + \Delta F_{\text{chain}} \quad (9)$$

If the surface of the hemisphere is taken as the interfacial area, then the interfacial tension free-energy variation is

$$\Delta F_{\text{interfacial}} = \gamma 2\pi(R_s^2 - R_c^2) \quad (10)$$

where γ is the polymer/water interfacial tension.

The chain stretching free-energy variation for an ideal chain may be written as¹⁶

$$\Delta F_{\text{chain}} = \frac{3kT}{2Nb^2}(R_{\text{stretch}}^2 - (2R_c)^2) \quad (11)$$

where N is the number of Kuhn segments and b is the length of a Kuhn segment.

R_{stretch} can be expressed by R_c and R_s using the cylindrical geometry with capped hemispheres and volume conservation:

$$R_{\text{stretch}} = \frac{4(R_c^3 - R_s^3)}{3R_s^2} + 2R_s \quad (12)$$

Both R_c and N depend on the molar mass of the macromolecules, and the resulting surface charge density is thus a function of the molar mass of the polymer. The result of this calculation is shown as a blue line in Figure 6. This simple model gives the correct order of magnitude for the surface charge densities. It thus validates the description made above for the mechanism of emulsion polymerization. Accordingly, these two examples of solvent shifting and emulsion polymerization show that the number of end-groups at the polymer/water interface is a trace of the mechanism by which the particles were synthesized.

Coprecipitation of Macromolecules with Charged and Uncharged End-Groups. Following the idea that end-groups can be used as markers of the particle-formation mechanism, we can study the effect of mixing macromolecules with different characteristics, such as their molar mass, if they have different end-groups. In the experiment reported in Figure 5, we measured the mean diameter of particles prepared through solvent shifting when mixing two monodisperse PMMAs of different molar masses and different end-groups, namely, PMMA-COOH ($M = 9900 \text{ g}\cdot\text{mol}^{-1}$, carboxylic acid groups) and PMMA-C₄H₉ ($M = 21\,000 \text{ g}\cdot\text{mol}^{-1}$, butyl groups). In our mechanistic study of the solvent-shifting method,⁹ we have established a relationship between the radius and the surface charge. If a spatial distribution of the end-groups is assumed, then the surface charge can be calculated and thus the radius of the particles may be determined. Because the two polymers have different molar masses, they will not start precipitating upon the same addition of nonsolvent (water). Two opposite models for the organization of the macromolecules within the particle can be envisioned: (1) The mixing is fast compared to the formation of the polymer particles. The supersaturations are then enormous, and both polymers precipitate simultaneously. The volume fraction of PMMA-C₄H₉ at the interface is then the same as in the core of the particle, and the surface charge thus decreases linearly with the volume fraction of PMMA-C₄H₉. The result of this calculation is displayed as a green line

in Figure 5. It does not reproduce the experimental variation, indicating that the model does not account for enough COOH end-groups at the interface. (2) The mixing is slow compared to the formation of the polymer particles. The polymer with the highest degree of polymerization, PMMA-C₄H₉, precipitates completely before PMMA-COOH starts to precipitate. The interface consists of PMMA-COOH, which yields a constant surface charge, until not enough PMMA-COOH is available to cover up the interface, at which point the surface charge decreases and the radius shoots up to very high values. The calculation is displayed as a red line in Figure 5 and reproduces the main feature of the experimental data, which is the sudden increase in the mean radius at low fractions of PMMA-COOH because there is no longer enough PMMA-COOH to cover the particle surfaces.

Our experimental data corresponds to an intermediate spatial distribution of the two types of macromolecules, in which the surface of a particle is enriched in the lighter PMMA-COOH compared to its core but still contains some PMMA-C₄H₉. We can use the fraction of PMMA-COOH at the interface as a fitting parameter, which yields a value of 65% for this fraction, as displayed by the blue line in Figure 5. This value is a measure of the mixing efficiency and quantifies the competition between the two steps of solvent-shifting, which makes it a valuable tool for the further characterization of the process. For example, the homogeneous, fast mixing situation (using a stopped-flow device), studied in our mechanistic study of solvent-shifting,⁹ should be described by the first model, whereas very bad mixing (slow nonsolvent addition) should be described by the second model. The experiments reported here (syringe addition to a stirred solution) are in an intermediate situation. Considering how frequently solvent-shifting is used for the synthesis of organic nanoparticles, we think that this information on the mechanism and on the resulting structures should be obtained systematically.

CONCLUSIONS

Macromolecules made of nonionic monomers and ionic end-groups can self-assemble in water to yield polymer particles in which a fraction of the end-groups are at the surfaces of the particles. Depending on the solution pH, these end-groups may ionize in water, and the polymer particles can thus acquire colloidal stability and electrophoretic mobility.

We have measured the variation of electrophoretic mobility with pH for particles made of poly(methyl methacrylate) (PMMA) with end-groups that are either carboxylic or sulfate. We found that this variation is characteristic of the chemical nature of the end-groups. From the variations of electrokinetic mobility with pH and with ionic strength, we have determined the surface charge density and the number of end-groups that are located at the particle surfaces. We have also derived these relations theoretically from Poisson-Boltzmann theory and Gouy-Chapman theory. Experimental and theoretical values of the variations of electrophoretic mobility with pH were found to be in good agreement, indicating that the end-groups were indeed the sole source of ionization at the particle surfaces.

Then we compared the surface charge values with the total number of end-groups per particle. We have shown that only a fraction of all of the end-groups have gained access to the particle surfaces. For particles that were made through emulsion polymerization, this fraction was predicted through a model in which the macromolecules that were located at the particle surfaces had enough time to change configuration

during polymerization and bring their ionic end-groups to the surface. For particles that were made through solvent shifting, the fraction of all end-groups that were located at the surface was found to be much lower; it was predicted from a model in which the macromolecules had no time during precipitation to reorganize their configurations, as if they were quenched into a glassy state. Therefore, we propose that measurements of the spatial distribution of end-groups within the particles can be used to find out how the macromolecules were self-assembled into particles.

In conclusion, we think that a study of the nature and locations of the macromolecules' end-groups makes it possible to perform "forensic" research on the processes that took place when the particles were synthesized.

AUTHOR INFORMATION

Corresponding Author

*E-mail: kevin.roger@espci.fr.

Notes

The authors declare no competing financial interest.

ACKNOWLEDGMENTS

We are grateful to François Ganachaud for supplying the PMMA molecular weight standards with known end-groups. We thank Christian Pichot for his careful reading of the manuscript. This work was supported by ANR 2010 BLAN 942 03 "LimOuzIne".

REFERENCES

- (1) Daniel, J.-C.; Pichot, C. *Les Latex Synthétiques: Élaboration, Propriétés, Applications*; Lavoisier: Cedex, France, 2006.
- (2) Dunn, A. S.; Chong, L. C.-H. Application of the Theory of Colloid Stability to the Problem of Particle Formation in Aqueous Solutions of Vinyl Acetate. *Br. Polym. J.* **1970**, *2*, 49–59.
- (3) Fitch, R. M. *Emulsion Polymers and Emulsion Polymerization*; Bassett, D. R., Hamielec, A. E., Eds.; ACS Symposium Series; American Chemical Society: Washington, DC; Chapter 2, pp 1–29.
- (4) Priest, W. J. Particle Growth in the Aqueous Polymerization of Vinyl Acetate. *J. Phys. Chem.* **1952**, *56*, 1077–1082.
- (5) Goodwin, J.; Hearn, J.; Ho, C. C.; Ottewill, R. Studies on the Preparation and Characterisation of Monodisperse Polystyrene Latices. *Colloid Polym. Sci.* **1974**, *252*, 464–471.
- (6) Goodwin, J.; Ottewill, R.; Pelton, R. Studies on the Preparation and Characterization of Monodisperse Polystyrene Latices V.: The Preparation of Cationic Latices. *Colloid Polym. Sci.* **1979**, *257*, 61–69.
- (7) Horn, D.; Rieger, J. Organic Nanoparticles in the Aqueous Phase—Theory, Experiment, and Use. *Angew. Chem., Int. Ed.* **2001**, *40*, 4330–4361.
- (8) Aubry, J.; Ganachaud, F.; Cohen Addad, J.-P.; Cabane, B. Nanoprecipitation of Polymethylmethacrylate by Solvent Shifting: 1. Boundaries. *Langmuir* **2009**, *25*, 1970–1979.
- (9) Roger, K.; Botet, R.; Cabane, B. Coalescence of Repelling Colloidal Droplets: A Route to Monodisperse Populations. *Langmuir* **2013**, *29*, 5689–5700.
- (10) Zhang, C.; Pansare, V. J.; Prud'homme, R. K.; Priestley, R. D. Flash Nanoprecipitation of Polystyrene Nanoparticles. *Soft Matter* **2012**, *8*, 86–93.
- (11) Roger, K.; Cabane, B. Uncontaminated Hydrophobic/Water Interfaces Are Uncharged: A Reply. *Angew. Chem., Int. Ed.* **2012**, *51*, 12943–12945.
- (12) Evans, F. D.; Wennerström, H. *The Colloidal Domain: Where Physics, Chemistry, Biology, and Technology Meet*; Advances in Interfacial Engineering Series; Wiley-VCH: New York, 1999.
- (13) O'Brien, R. W.; Hunter, R. J. The Electrophoretic Mobility of Large Colloidal Particles. *Can. J. Chem.* **1981**, *59*, 1878.

(14) Smoluchowski, M. V. Contribution à la Théorie de l'Endosmose Électrique et de Quelques Phénomènes Corrélatifs. *Bull. Int. Acad. Sci.* **1903**, *8*, 182–200.

(15) Grosberg, A.; Khokhlov, A. *Statistical Physics of Macromolecules*; AIP Press: New York, 1994.

(16) Rubinstein, M.; Colby, R. *Polymer Physics*; Oxford University Press: Oxford, U.K., 2003.

Destabilization of emulsions through molecular permeation : Contact Ripening

Kevin Roger^{1*}, Ulf Olsson², Ralph Schweins³, Bernard Cabane¹

Abstract

We demonstrate the existence of a destabilization process taking place of emulsions that is neither Ostwald ripening nor coalescence. This process occurs at contact of the droplets and molecular exchange takes place through permeation in the surfactant layer. This process takes place even for oils with extremely low water solubility. It is favored by dehydration of the surfactant layer and the absence of long range repulsion. It is unfavored by the use of long hydrophilic and hydrophobic surfactant chains.

¹ *PMMH, CNRS UMR 7636, ESPCI, 10 rue Vauquelin, F 75231 Paris cedex 05, France*

² *Physical Chemistry, Lund University, POB 124, Lund, S 22100, Sweden*

³ *Institut Laue-Langevin, 6 rue Jules Horowitz, F-38042 Grenoble cedex 09, France*

*Corresponding author: kevin.roger@espci.fr

Contents

| | |
|---|----------|
| Introduction | 1 |
| 1 Materials and Methods | 1 |
| 1.1 Materials | 1 |
| 1.2 Turbidity measurements | 2 |
| 1.3 Neutron scattering measurements | 2 |
| 1.4 Emulsion preparation | 2 |
| 2 Results | 2 |
| 2.1 Beyond Ostwald ripening and coalescence | 2 |
| 2.2 Hydration of the surfactant layer | 3 |
| 2.3 Exchange takes place at contact | 3 |
| 2.4 Concentration dependence or independence | 4 |
| 2.5 Oil exchange through the composition drive | 5 |
| 2.6 Oil exchange at equilibrium | 6 |
| 2.7 Influence of the surfactant structure | 6 |
| 3 Discussion | 7 |
| 3.1 A destabilization through exchange at contact | 7 |
| 3.2 Mean field approach | 7 |
| 3.3 Growth law | 7 |
| 3.4 Structure and Temperature variation | 8 |
| References | 8 |

Introduction

Inter-aggregate molecular exchange is a fundamental process in self-assembled systems, such as micelles, emulsions and microemulsions. It allows for size distribution fluctuations at thermal equilibrium and offers a relaxation mechanism in out of equilibrium systems. In emulsions and similar systems one often considers one of two cases for the exchange of molecules between droplets. The first one involves molecular

exchange via the finite solubility of the molecules in the continuous solvent. The rate of this exchange, and the average molecular lifetime in an aggregate depends on the solubility in the continuous solvent. Ostwald ripening is coarsening process that is a consequence of this exchange mechanism.[1] In this relaxation process there is a net flow of molecules from small droplets that shrink to larger drops that grow. Also the reverse process, solubilization, may occur by single molecule exchange[2]. The second case involves the simultaneous exchange or transfer of several molecules through droplet coalescence and break-up (fusion-fission) of aggregates[?]. Mechanisms, intermediate between the two have also been suggested previously by Taisne[3], Sonnevile[4] and Schmitt et al[5]. One example is so called contact ripening involving a relatively rapid transfer of molecules between two droplets in contact without rupture or fusion of the surfactant films.

In the present paper we report new results on the kinetics and mechanism of the destabilization of model emulsions, stabilized by non-ionic oligoethylene oxide based surfactants. The aim is to decide whether or not an alternate destabilization process to Ostwald ripening and coalescence existed. We have thus varied the range of physicochemical parameters of the model system to uncouple contributions.

1. Materials and Methods

1.1 Materials

The oxyethylenated surfactants, C₁₂E₅, C₁₂E₆, C₁₂E₇, C₁₄E₆ and C₁₆E₆ were obtained from Nikko Chemicals with a minimum purity of 99 %. Hexadecane, deuterated hexadecane, D₂O and Sodium Dodecyl Sulfate (SDS) were bought from Aldrich and the purity of all these products was at least 99 %.

1.2 Turbidity measurements

We have mainly followed the destabilization of the emulsion through measurements of the turbidity. The turbidity was recorded with a Varian spectrophotometer and the sample placed in a 1 cm thick quartz cuvette. The initial state of the sample was always a fine nanoemulsion that scatters light weakly. As the droplets increase in size, the scattering intensity increases and less light goes through the sample to the detector. This drop in transmittance corresponds to the turbidity τ :

$$\tau = \frac{1}{e} \log\left(\frac{I_0}{I}\right) \quad (1)$$

where e is the length of the cuvette, I_0 the reference detected intensity for the empty cell and I the detected intensity. The turbidity is dominated by the large droplets in a polydisperse population.

1.3 Neutron scattering measurements

We performed small angle neutron scattering experiments at the D11 instrument, ILL Grenoble. The sample was placed in a 1 mm thick quartz flat cuvette.

1.4 Emulsion preparation

All the emulsions were prepared by a rapid temperature quench from the equilibrium microemulsion region. Narrow populations of droplets are thus obtained, with a typical diameter of 15 nm for the oil/surfactant ratio chosen. The pathway and phase diagram are schemed in Figure 1.

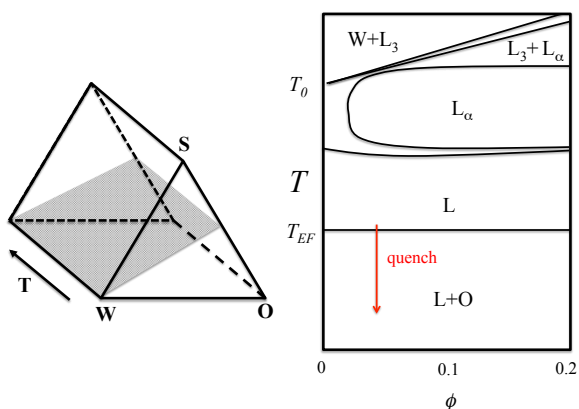


Figure 1. Ternary phase diagrams are conveniently represented within a Gibbs triangle. Adding temperature in the third dimension results in a phase prism. For C_iE_j -water-oil systems several cuts through such a phase diagram have been studied. For the study of spherical oil-in-water droplets, a convenient cut is that at a constant surfactant-to-oil ratio, ϕ_s/ϕ_o , where ϕ_s and ϕ_o are the volume fractions of surfactant and oil, respectively.

2. Results

We use monodisperse emulsions consisting of n-alkane oil droplets, covered by a monolayer of oxyethylenated surfactant, in water. These emulsions are prepared through the sub-PIT route[6], in which a microemulsion is rapidly cooled down to produce the final emulsion. The surfactant is then only at the interface of the oil droplets and the aqueous phase is thus free of micelles.

2.1 Beyond Ostwald ripening and coalescence

Once an emulsion is prepared it will destabilize to reach the equilibrium state of the system. However both time-scale and the mechanism controlling the destabilization highly depend on the system. We started by investigating the destabilization of emulsions of an even linear alkane oil, $C_{12}E_5$ and water. This choice stems from prior observations from Evilevitch[2] and Taisne[3]. The volume fraction of droplets in water was 2% and the diameter is set constant for all four oils (decane to hexadecane) by choosing the same oil/surfactant ratio (i.e. volume/area ratio). The destabilization of these emulsions must proceed by a simultaneous growth in size of some droplets and shrinkage in size of some others since the final equilibrium state is the phase separation of an oil layer from an aqueous micellar solution. Since large objects are the main contribution to light scattering[2], the growth can be monitored by measuring the scattered intensity or equivalently the turbidity of the sample with time. It can be shown that for small droplets the turbidity is proportional to the product of the droplets volume fraction by the mean volume.

A first experiment was to follow with time the turbidity of emulsions stored at about the same spontaneous curvature of the surfactant layer, i.e. the same temperature difference to their phase inversion temperature. Indeed, according to the Kabalnov-Wennerström model[?] for coalescence of uncharged emulsions, the probability of opening a hole between two droplets increases exponentially with lowering the spontaneous curvature. At a given spontaneous curvature, the coalescence probability should thus be the same. In addition, the temperature difference to the phase inversion temperature is around 15°C and the spontaneous curvature is thus fairly high, the free energy barrier to coalescence can be estimated to around 40 times the thermal energy kT , which results in a probability around 10^{-18} . Coalescence should thus be strongly unfavored.

As the volume fraction of droplets is constant when the temperature difference to the phase inversion temperature is constant. The turbidity is thus proportional to the mean volume. The variations of the turbidity with time of decane to hexadecane emulsions at the same spontaneous curvature of the $C_{12}E_5$ layer are displayed on the left part of Figure 2. A striking linear dependence of the turbidity, or the mean volume, with time is observed. This observation is general in this study and justifies the use of turbidity rates, which are the slopes of the turbidity variation with time, and are used in the rest of this work.

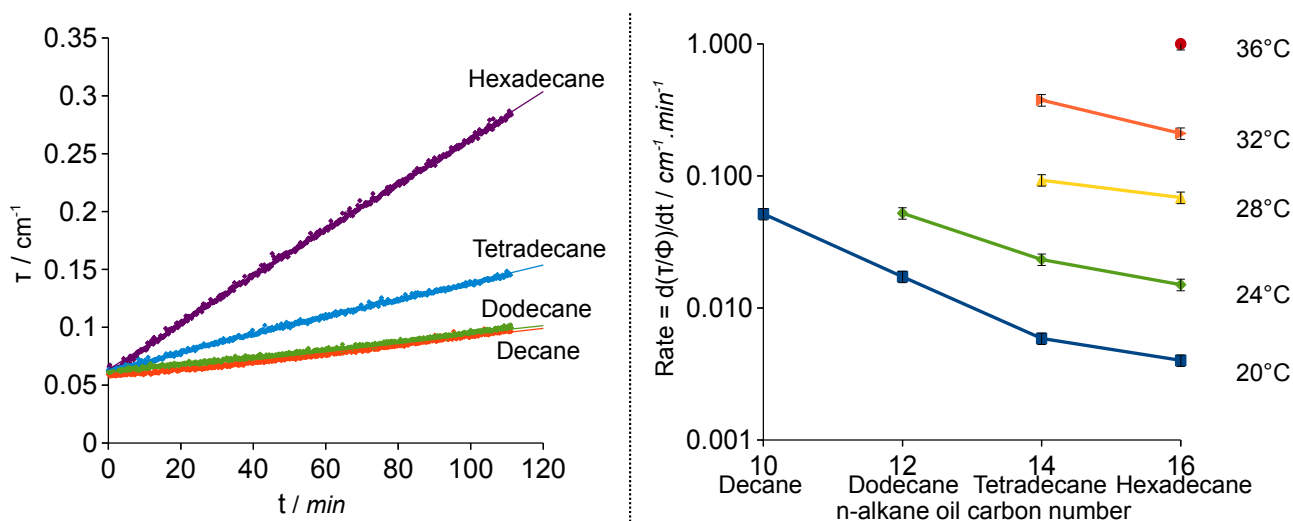


Figure 2. Left : Variation with time of the turbidity of emulsions at a constant temperature difference to the phase inversion temperature. The hexadecane emulsion is destabilized faster than the tetradecane and the dodecane and decane emulsion. Right : Variation with the oil for different temperatures of the normalized turbidity rates. The usual order of variation from decane to hexadecane is observed at low temperatures, while an inversion is observed at higher temperatures.

Another essential observation is the influence of the oil on the destabilization rate. At constant spontaneous curvature, emulsions destabilize faster with hexadecane than with tetradecane than with dodecane and decane. This can not be consistently explained by a coalescence model where the activation step is controlled by the spontaneous curvature. It is also inconsistent with a Ostwald ripening process that rely on solubilization of the oil in the continuous phase. Indeed the oil solubility decreases by one order of magnitude for each two carbon addition to the oil chain and should thus be 1000 lower for hexadecane than decane. Decane emulsions should thus evolve much faster than hexadecane emulsions.

Another complementary experiment to these observations is displayed on the right part of Figure 2 in which the rate of destabilization of the turbidity, normalized by the volume fraction of droplets which depends on the temperature, is displayed for the four oils at several temperatures. At 20°C, the order of variation is consistent with the order of solubilities since the decane emulsion is destabilized faster than the dodecane, than the tetradecane than the hexadecane, although the difference are smaller than what is expected. However this order breaks down quickly as the temperature is increased and conditions can be found in which the hexadecane emulsion is destabilized at least an order of magnitude faster than the very water soluble decane emulsion.

There must thus exist another path of oil exchange besides Ostwald ripening and coalescence that allows a destabilization of emulsions.

2.2 Hydration of the surfactant layer

The temperature, which controls the hydration of the hydrophilic head of the surfactant layer, is a key variable in

the destabilization of these emulsions, according to Figure 2. It allows the fast destabilization of emulsions made of very water-insoluble droplets, such as hexadecane droplets. We can focus on this unusual system C_{12}E_5 /hexadecane and measure the normalized rates of destabilization, i.e. the increase of the mean volume with time. A sharp increase of the destabilization rate with temperature is observed and the variations are displayed in Figure 3.

At 40°C, the equilibrium microemulsion region is reached and the turbidity thus remains constant since there is no drive anymore for the growth of the droplets. It should be emphasized that no metastability region, in which the droplets would be below the equilibrium boundary but still remain at constant size, is observed for this system. This contrasts to the C_{12}E_5 /decane system that was investigated by Morris et al[7], in which Ostwald ripening is the exchange mechanism, and that displays a 2°C large metastability region below the equilibrium microemulsion line.

2.3 Exchange takes place at contact

Since the destabilization process does not take place through solubilization of the oil in the aqueous phase and that no carriers are available, the oil exchange must take place at contact. Repulsions between droplets should thus hinder this destabilization process. We added small amounts of ionic surfactants in the non-ionic surfactant layer (up to 1.2%). Such low amounts do not influence significantly the phase diagram in our range of compositions[8]. We chose the surfactant C_{12}E_6 since the corresponding microemulsion regions are located at higher temperatures than with C_{12}E_5 , as the head is longer and thus more hydrophilic. Sodium docecyl sulfate was added at various fractions to emulsions of C_{12}E_6 /decane and

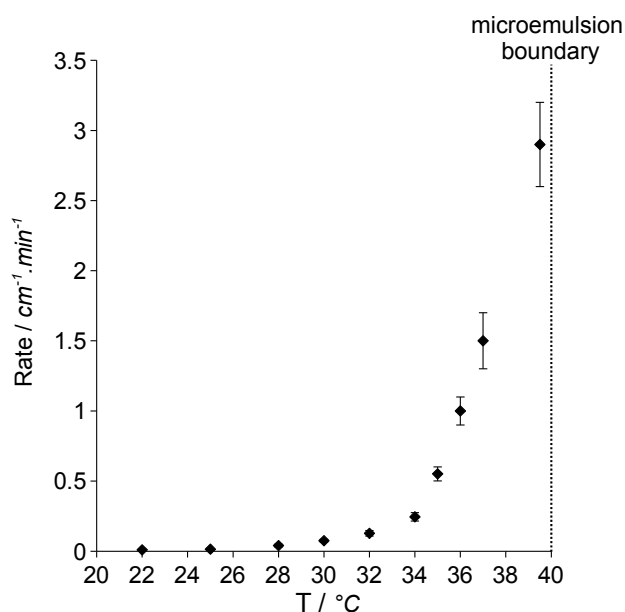


Figure 3. Variation with the temperature, i.e. dehydration, of normalized turbidity rates for the $C_{12}E_5$ /hexadecane system. The experimental data can be fitted by an exponential, typical of activated processes. At 40°C the microemulsion region is reached. No metastability region is observed below 40°C .

$C_{12}E_6$ /hexadecane and the variations of the normalized destabilization rates, at the same temperature 30°C , are displayed in Figure 4. For decane a moderate decrease by around 25% is observed when adding 1.2% of SDS, whereas for hexadecane the rate decreases by more than an order of magnitude. We can thus deduce that hexadecane is exchanged through a different pathway than decane. While decane is easily exchanged through solubilization in the continuous phase, which hardly depends on the repulsions between droplets, hexadecane is thus exchanged at contact of two droplets, which is highly dependent on the approach rate of two droplets, and thus their repulsions.

2.4 Concentration dependence or independence

If the destabilization process occurs through oil exchange at contact, it is interesting to study the influence of the droplets concentration on the exchange rate. Indeed, if the process is diffusion limited, an increase in the concentration will result in an increase of the destabilization rate, since the number of collisions will increase. To the contrary, if the process is reaction limited, the concentration will not influence the destabilization rate since the limiting step will then be the exchange at contact. We use the system $C_{12}E_5$ /hexadecane at a set temperature of 36°C , for which, according to Figure 2 corresponds, the destabilization occurs through contact ripening with negligible Ostwald ripening. The normalized destabilization rates, rates of turbidity increase divided by the volume

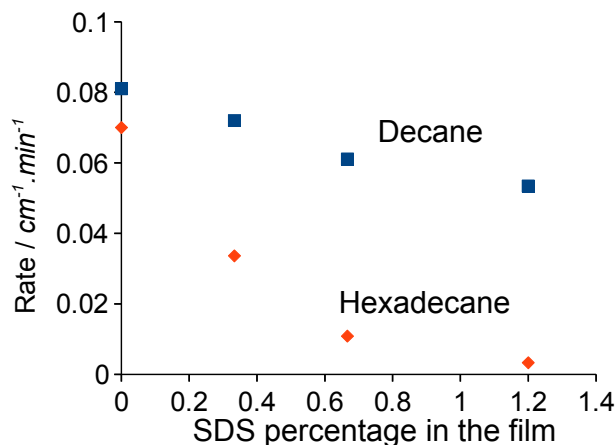


Figure 4. Variation of the normalized destabilization rates with the addition of an anionic surfactant, SDS, in the surfactant layer. The non-ionic surfactant is $C_{12}E_6$ and the oils are either decane, fairly water soluble, or hexadecane, water insoluble. The temperature is set at $T=30^\circ\text{C}$. A moderate decrease is observed for the decane emulsion, while the rate collapses for the hexadecane emulsion. Hexadecane is thus exchanged through a different mechanism than decane, which must operate at contact.

fraction of droplets, are displayed as a function of the volume fraction of droplets in Figure 5 using two different methods. In the first method (red diamonds), the emulsion prepared at the final concentration was placed in the spectrophotometer cuvette, under moderate stirring, and the turbidity was acquired continuously. This method is only appropriate in dilute enough conditions so that multiple scattering is negligible. In the second method (blue squares), the emulsion was kept in a vial without agitation (except for two samples displayed as yellow dots) and a small volume was regularly diluted in a larger volume of water prior to measurement. This discontinuous assay method has the advantage of being usable in the whole concentration range but suffers the drawback that less data points are obtained than in the previous method. The two methods have been used in the dilute regime and the rates are the same within the experimental error. It is interesting to notice that the agitation does not influence the rate in the dilute regime, and only mildly in the more concentrated regime.

We observe on Figure 2 that the rate is strikingly independent of the droplets concentration over two orders of magnitude in the dilute regime. Only upon reaching higher droplets fractions does the rate increase. This observation seems incompatible with a diffusion limited process and suggests that the limiting step is the exchange at contact. It suggests the use of a mean-field description of the destabilization process up to 5% droplets volume fractions.

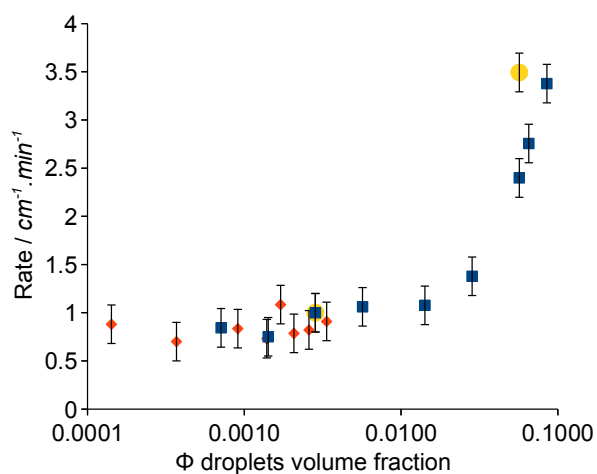


Figure 5. Variation of the normalized destabilization rates with the droplets volume fraction, at $T=36^{\circ}\text{C}$ with the system C_{12}E_5 /hexadecane. Red diamonds correspond to continuous assay in the spectrophotometer cuvette with stirring. Blue squares correspond to a discontinuous assay without stirring while yellow dots correspond to a discontinuous assay with stirring. The normalized rates are independent of the concentration over two order of magnitudes in dilute conditions and eventually increase upon concentrating the droplets above 5%.

2.5 Oil exchange through the composition drive

We have shown so far that the destabilization process we investigate operates at contact but is not diffusion-limited. A coalescence mechanism limited by the opening of a pore in the surfactant layer would meet such constraints. However, as mentioned previously, the Kabalnov-Wennerström theory predicts that coalescence should be infinitely slow in our set of conditions. Conversely, an alternate contact mechanism would be the diffusion of oil molecules from one droplet to the other by diffusion through the surfactant layer.

To monitor the oil exchange and decide between the two mechanisms, we used two oils with similar chemical and physical properties, hydrogenated and deuterated hexadecane, with the exception of their neutron scattering length density. Emulsions of hydrogenated and deuterated hexadecane will scatter differently a neutron beam due to the resulting contrast difference. If two types of droplets are mixed, an additional drive to the difference in radius arises. Indeed, mixing entropy will favor the homogenization in composition of all the droplets, which is a much stronger drive than the curvature.

We have chosen a mixed solvent $\text{H}_2\text{O}/\text{D}_2\text{O}$ at a precise ratio for which the scattering length density matched that of a droplet of 1-1 hydrogenated and deuterated hexadecane covered by the surfactant C_{12}E_5 , which then leads to zero contrast. Before oil exchange the scattered intensity will be the average of the scattered intensity of the deuterated and hydrogenated emulsion (incoherent addition). After total ex-

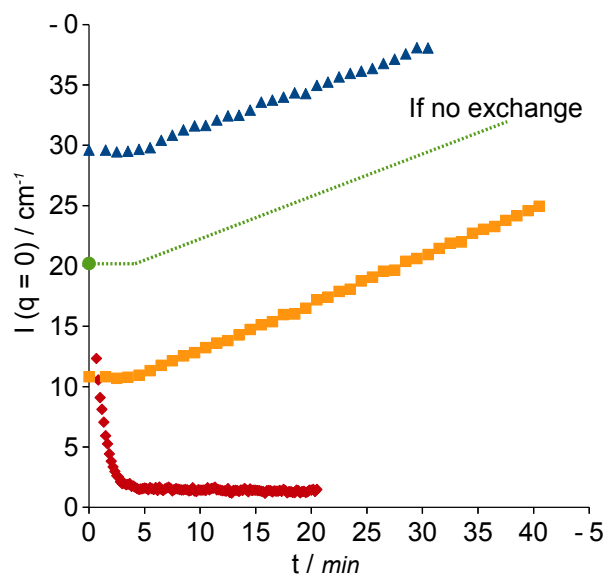


Figure 6. Variation of the neutron scattered intensity at low scattering vector normal values, q , for three emulsions, at $T = 25^{\circ}\text{C}$ and total oil+surfactant fraction of 2%. Blue triangles : emulsion of hydrogenated hexadecane. Orange squares : emulsion of deuterated hexadecane. Red diamonds : a 1-1 mixture of these two emulsions. The solvent $\text{H}_2\text{O}/\text{D}_2\text{O}$ contrast matches that of a droplet of a 1-1 mixture of the two hydrogenated and deuterated hexadecane covered by C_{12}E_5 . The collapse of the intensity upon mixing the two emulsions thus corresponds to a fast composition homogenization between the two populations of droplets. The total exchange takes place in 3 minutes, while during that time the two scattered intensity of the two reference emulsion remains constant, which means the droplets keep a constant size. This rules out coalescence as an exchange process.

change, the intensity should collapse to zero as the average scattering length density of the droplet is the same as that of the solvent (contrast match). We also followed the variation with time of the scattered intensity of the two reference emulsions of hydrogenated and deuterated hexadecane, so that we can monitor the size growth due to the curvature drive.

The experiment was performed at 25°C , where the destabilization is rather slow according to Figure 2 and Figure 3. Similar results but faster rates were observed at 30°C . The intensity at a low value of the scattering vector normal, q , is plotted as a function of time in Figure 6. Both references hydrogenated and deuterated emulsions display similar variations. Below 5 minutes the intensity is constant, which means that the mean size is also constant, whereas at longer times a slow linear increase of the intensity with time is observed. Since the scattered intensity, like the turbidity, is proportional to the mean droplet volume at constant fraction, this variation is thus identical to that of Figure 2. For the mixture of the

two hydrogenated and deuterated hexadecane emulsion the intensity collapses to a constant value in about 3 minutes. The first data point is taken around 30s since the mixing was not controlled and synchronized with the acquisition.

In the first minutes, the reference emulsions correspond to a constant intensity while the mixture of emulsions show that complete exchange of oil has taken place between the droplets. This means that the exchange proceeds at constant size and rules out a coalescence mechanism, that would necessarily involve a growth and thus an increase of the scattered intensity.

2.6 Oil exchange at equilibrium

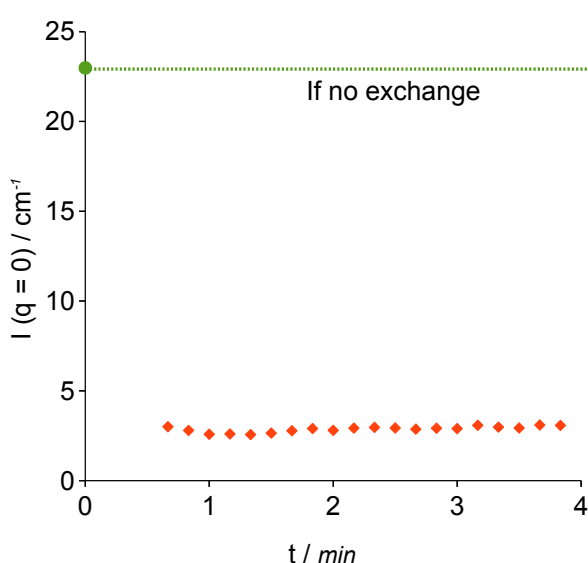


Figure 7. Variation of the neutron scattered intensity at low scattering vector norm values, q , for a 1-1 mixture of a microemulsion of hydrogenated hexadecane with a microemulsion of deuterated hexadecane. The temperature is set at $T = 40.8^\circ\text{C}$ and the total oil+surfactant fraction is 2%. The fast collapse of the intensity demonstrates that the droplets homogenize their composition to that of a 1-1 mixture of the two oils in less than minute.

We can extend this experiment to a situation in which the curvature drive is absent and only the mixing entropy drive is active. This can be done using an equilibrium microemulsion system, where the droplets (swollen micelles) keep a constant size. As we can observe on Figure 3, the rate of destabilization increases with the temperature until reaching the equilibrium microemulsion boundary, where it must be zero since the curvature drive vanishes. However we can wonder whether the exchange of oil vanishes. Similarly to the previous experiment with emulsions, we can mix a microemulsion of hydrogenated hexadecane with one of deuterated hexadecane, and monitor the change with time of the neutron scattered intensity. The corresponding variations are displayed in Figure 7. The initial

point could not be obtained for experimental reasons, since the mixing was not controlled and synchronized with the acquisition, but should correspond to the average of the two reference microemulsions, which is calculated from the experimental data as the dotted green line. From this intensity, we observe that the first data point around 30s corresponds to a much lower value that does not change with time. This means that complete exchange took place in less than a minute. The exchange thus takes place and even faster than in the previous experiment at 25°C , since the temperature is now higher.

2.7 Influence of the surfactant structure

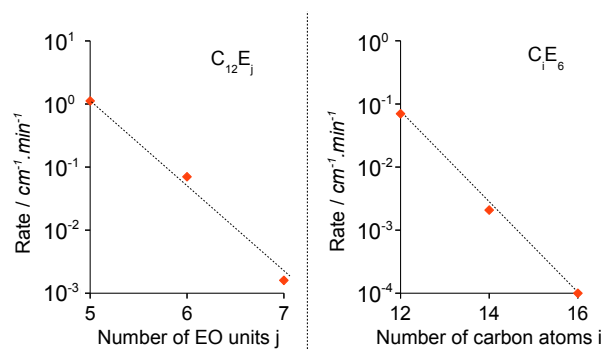


Figure 8. Variation of the normalized destabilization rates with the chain length of the hydrophilic group (left) and hydrophobic group (right). Increasing by one unit the hydrophobic or the hydrophilic chain results in a decrease of the destabilization rate by one order of magnitude, leading to the general conclusion that long surfactants hinder the exchange. The temperature is set at 36°C and dotted lines are plotted as a guide for the eyes.

Since the destabilization process operates at contact but is not a coalescence mechanism, it is interesting to evaluate the importance of the surfactant structure. As hydration is a key variable it must be set constant by choosing a constant temperature for proper comparison. We have used two series of oxyethylenated surfactants homologs of high purity to investigate the influence of both the hydrophobic and the hydrophilic chain. The sequence C_{12}E_5 , C_{12}E_6 , C_{12}E_7 was used to investigate the influence of the hydrophilic chain and the variations of the rate are displayed on the left part of Figure 8. The sequence C_{12}E_6 , C_{14}E_6 , C_{16}E_6 was used to investigate the influence of the hydrophobic chain and the variations of the rate are displayed on the right part of Figure 8. There is a striking similarity between the two variations and the destabilization rate decreases by around an order a magnitude per unit increase in either chain length. The use of long surfactants thus hinders the destabilization process studied in this work.

3. Discussion

3.1 A destabilization through exchange at contact

We start the discussion by considering a few experimental evidences given in the Results section that characterize the destabilization process investigated in this work :

- It can be observed for oils with very low water solubility as shown by Figure 2: this rules out a transfer through the continuous phase, such as Ostwald ripening.
- It can operate at constant droplets size if the drive is mixing entropy as shown by Figure 6: this rules out a destabilization through a coalescence process.
- It is much slower when adding long range repulsions between droplets as shown by Figure 4: this leads to a mechanism operating at contact
- It is favored by dehydrated surfactant layers as shown by Figure 3: this suggests an exchange through the surfactant layer

These four observations demonstrate that the existence of a destabilization mechanism, contact ripening, which operates through an oil exchange by molecular permeation through the surfactant layer when droplets come to contact.

3.2 Mean field approach

In Figure 5, we observe that the growth process through contact ripening is concentration independent in dilute conditions. This observation is puzzling because any process taking place through Brownian diffusion, with or without an activation barrier, is expected to be concentration dependent. At the simplest level the collision can be described as a second-order reaction and the rate should then vary as the square of the concentration and extrapolate to zero. However this is not observed experimentally although we argue in favor of an exchange mechanism that requires droplets contacts.

Two possible explanations can be considered. The first option is to draw a parallel with the concentration independence encountered in Ostwald ripening in the dilute regime, which stems from the existence of a concentration invariant. In Ostwald ripening this invariant is the oil concentration in the bulk, which depends only on the mean size of the population. In contact ripening this invariant could be the initial size distribution, that is independent of the concentration. This requires a careful modeling of the exchange process between several droplets. The second option is to argue that the limiting step of the process is the exchange rather than the approach. This requires the presence of attractive interactions to give the pair of droplet a lifetime much larger than the diffusion time. We leave the understanding of this dependence for later work but notice that this suggests the problem could be mean-field in the dilute regime, which we will test in the next sub-section.

3.3 Growth law

The experimental growth law of an emulsion undergoing contact ripening corresponds to a linear increase of the mean volume V_{mean} of the population of droplets with time t , $V_{mean} \sim t$, as displayed in Figure 2. This law is also experimentally observed and theoretically predicted for different processes such as Ostwald ripening and diffusion limited coalescence. We aim here to present a model of contact ripening that allows to capture this growth law. For this purpose we need to calculate the driving force and draw the exchange pathway.

For all the experiments that involve growth of the droplets, which excludes the neutron contrast match experiment, the drive is the reduction of the total interfacial area. This can be expressed as the difference of Laplace pressure between two droplets of radius r_1 and r_2 :

$$\Delta p_{Laplace} = 2\gamma\left(\frac{1}{r_2} - \frac{1}{r_1}\right) \quad (2)$$

where γ is the interfacial tension coefficient of the interface.

Due to this drive, exchange of oil molecules between droplets occurs, with some droplets growing and others shrinking. The difference with Ostwald ripening lies in the exchange pathway. While in Ostwald ripening the exchange takes place by molecular exchange through the continuous phase, in contact ripening the exchange should be modeled as taking place through the surfactant layer. This permeation can then be described as a steady-state process and we can use the Fick formalism.

Since we aim to capture the growth law rather than the pre factors, we can make further simplifications in the modeling. Indeed the concentration independence discussed above and shown in Figure 5 suggests that the problem can be described by a mean-field approach, which leads to focusing on the mean radius evolution rather than look at all the details of the size distribution evolution with time. Such an approach is also successful for Ostwald ripening, although the pre factor deviates from the LSW theory. We thus consider the exchange between one droplet, at the mean radius, and a reservoir of infinite radius.

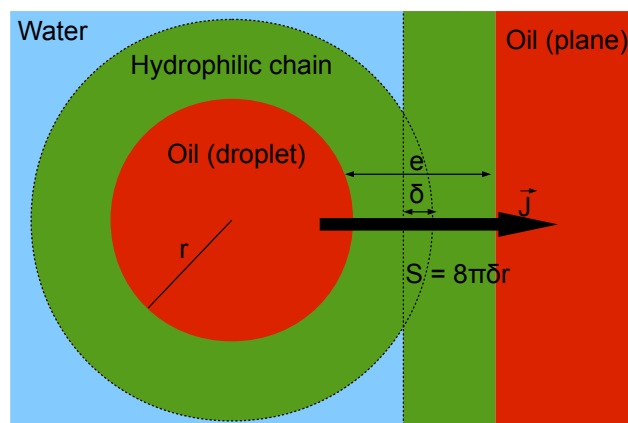


Figure 9

We can start by estimating the surface of contact S between the two objects. If we assume a length of penetration δ , small compared to the droplet radius r , the surface of contact writes as :

$$S_{contact}(r(t)) = 8\pi\delta r(t) \quad (3)$$

The flux density J can be estimated under steady state conditions with local thermodynamic equilibrium at each interface. This leads to a simple expression :

$$J(r(t)) \approx s_{oil/EO} \cdot \frac{D_{oil/EO}}{e_{EO}} \cdot \frac{p_{Laplace(t)} v_{oil}}{kT} \quad (4)$$

where $s_{oil/EO}$ is the solubility of the oil in the hydrophilic EO layer in molecules/unit volume, $D_{oil/EO}$ is the diffusion coefficient of the oil in the EO layer, e_{EO} is the length of the EO layer.

Using the expression of the Laplace pressure and the Stokes-Einstein expression of the diffusion coefficient :

$$J(r(t)) \approx s_{oil/EO} \cdot \frac{1}{e_{EO}} \cdot \frac{2\gamma v_{oil}}{r(t)} \cdot \frac{1}{6\pi\eta r_{oil}} \quad (5)$$

where η is the viscosity of the EO layer and r_{oil} is the equivalent radius of an oil molecule.

The flux between a droplet of radius r and a reservoir is thus

$$F = \frac{dV_{mean}}{dt} \approx \frac{8}{3} (s_{oil/EO} \frac{\gamma\delta}{e_{EO}}) (\frac{1}{\eta}) (\frac{v_{oil}^2}{r_{oil}}) \quad (6)$$

Then the increase of the mean volume with time is :

$$\frac{dV_{mean}}{dt} = \frac{8}{3} (s_{oil/EO} \frac{\gamma\delta}{e_{EO}}) (\frac{1}{\eta}) (\frac{v_{oil}^2}{r_{oil}}) \quad (7)$$

This expression does not depend on time and a simple integration can be performed :

$$V_{mean}(t) = [\frac{8}{3} (s_{oil/EO} \frac{\gamma\delta}{e_{EO}}) (\frac{1}{\eta}) (\frac{v_{oil}^2}{r_{oil}})] \cdot t \quad (8)$$

Regrouping the pre factor in a constant which is the rate R , we obtain the expression :

$$V_{mean}(t) = R \cdot t \quad (9)$$

This simple calculation thus captures the experimental growth law. However the pre factor contains many variables and we now turn to their examination in respect to the experimental evidence.

3.4 Structure and Temperature variation

We now turn to compare the predictions according to this pre factor and the experimental observations, especially the variations of the rate with temperature, displayed in Figure 3, and with the molecular structure of the surfactant, displayed in Figure 8.

From Figure 3, we observe that the rate R increases exponentially with the temperature. Several exponential based expressions can be used to model the set of data. One common option is to model permeation ripening as an activated process and reasonable agreement can be obtained. However an activation energy of 95kT is required, which is unreasonable. This discrepancy means that the activation energy depends on the temperature and makes it impossible to evaluate the absolute activation energy at a given temperature, since the pre factor can not then be obtained. Only the variations of activation energy can be obtained with temperature. Typically the activation energy then decreases by 6kT from 20 to 40°C using the set of data of Figure 3. Furthermore none of the variables of the previous expression of the rate seem to lead to such a rapid dependence with the hydration.

From Figure 8, we see a strong dependence of the destabilization rate on the molecular structure of the surfactant. The rate decreases by an order of magnitude when adding two carbons or one EO unit to the surfactant. Such an effect is not easily understood from previous pre factor expression. The symmetry between the effect of the hydrophobic chain and that of the hydrophilic chain breaks any explanation based on the surfactant layer preferred curvature and rather suggests that the event is linked to a symmetric deformation of the interface.

References

- [1] Alexey S. Kabalnov and Eugene D. Shchukin. Ostwald ripening theory: applications to fluorocarbon emulsion stability. *Advances in Colloid and Interface Science*, 38(0):69–97, 1992.
- [2] Alex Evilevitch. *Molecular Exchange in Colloidal Dispersions*. PhD thesis, Lund University, 2001.
- [3] Laurent Taisne. *Echanges d'huile entre gouttes d'émulsions*. PhD thesis, Paris 6, 1997.
- [4] Odille Sonnevile. *Mousses Biliquides*. PhD thesis, Paris 6, 1997.
- [5] V. Schmitt, C. Cattelet, and F. Leal-Calderon. Coarsening of alkane-in-water emulsions stabilized by nonionic poly(oxyethylene) surfactants: The role of molecular permeation and coalescence. *Langmuir*, 20(1):46–52, 2004. PMID: 15744998.
- [6] Kevin Roger, Bernard Cabane, and Ulf Olsson. Formation of 10-100 nm size-controlled emulsions through a sub-pit cycle. *Langmuir*, 26(6):3860–3867, 2010. PMID: 19899785.

- [7] Jane Morris, Ulf Olsson, and Håkan Wennerström. Homogeneous nucleation in a monodisperse oil-in-water emulsion. *Langmuir*, 13(4):606–608, 1997.
- [8] Keiichi Fukuda, Ulf Olsson, and Ulrich Wuerz. A surfactant-water-oil system with weakly charged films. *Langmuir*, 10(9):3222–3229, 1994.

The link between preferred curvature and nanoemulsion formation

Kevin Roger^{1*}, Bernard Cabane¹

Abstract

We show that nanoemulsions can be obtained by controlling the preferred curvature, similarly to the equilibrium microemulsions states. A large variety of triggers can be used and we present a few of them such as the temperature, the electrolyte concentration, the pH and the water fraction. The key is to take the system to an access state of a precise preferred curvature and then rapidly increase the preferred curvature. This quench leads to metastable nanoemulsions. The access state can be a spherical microemulsion (equilibrium or steady-state under shear) and then leads to size-controlled monodisperse emulsion with no surfactant excess in water. It can also be a bicontinuous sponge phase, which templates nucleating oil droplets, leading to a coarser nanoemulsion.

¹ *PMMH, CNRS UMR 7636, ESPCI, 10 rue Vauquelin, F 75231 Paris cedex 05, France*

*Corresponding author: kevin.roger@espci.fr

Contents

| | |
|---|----------|
| Introduction | 1 |
| 1 Results | 2 |
| 1.1 Curvature control by salt addition | 2 |
| 1.2 Curvature control by pH flip | 3 |
| 1.3 Curvature control by water flooding | 4 |
| OG/span system • C ₁₆ E ₈ /SDS system | |
| 2 Discussion | 6 |
| 2.1 Type of trigger and corresponding access state | 6 |
| 2.2 Special importance of access states in mixtures | 6 |
| References | 6 |

Introduction

The naming process of phases in oil/surfactant/water systems went astray half a century ago: swollen micelles and bicontinuous phases (sizes 3 to 30nm) were named microemulsions despite the fact that they are equilibrium systems, and extremely fine emulsions have been called nanoemulsions despite the fact that their sizes are in the 100 nm range, substantially larger than those of microemulsions[1]. That being said, nanoemulsions are extremely useful systems, with many applications in pharmacy (drug delivery systems) and in personal care (hydrating creams and lotions etc... [2]). Since their sizes are much larger than those of microemulsions, they may carry much larger volumes of drug molecules or other active ingredients; moreover, their Laplace pressure is moderate, and therefore the solubility of drug molecules in the oil phase of the nanoemulsion can be substantial[3]. Since they are not equilibrium states of the system, they may retain their structures over wider ranges of physical parameters, instead of changing structures continuously according to composition, temperature and external forces, as microemulsions do. Since

nanoemulsions are not equilibrium states of the system, they cannot be prepared through a simple mixing and equilibration route. It is usually necessary to prepare the system in a non-equilibrium state, and then let the system evolve until that state become metastable. The non-equilibrium state that will spontaneously evolve to the desired metastable state must be a homogeneous state of the system; we call it the “access state”. In order to reach it, we must place the system in a related initial equilibrium state, and then flip either a physical parameter (the temperature) or the composition (amount of water) so that the system finds itself “quenched” into the unstable “access state”, and then relaxes into the “metastable state”. Now the equilibrium structures of surfactant systems are determined by two parameters: area per molecule at the interface and spontaneous curvature of the interface. For droplet systems, the spontaneous curvature determines the droplet radii, e.g. a spontaneous curvature of 0.01 nm⁻¹ turned towards the oil will yield oil-in-water droplets of radius 100 nm. However, there are no equilibrium states of the water/surfactant/oil systems that have such low interfacial curvatures: the largest droplet sizes of microemulsions are about 30 nm, excepted for microemulsions that contain diblock copolymers[4]. For such very low curvatures, the equilibrium states of water/surfactant/oil systems may be bicontinuous structures, or else bicontinuous phases in coexistence with excess oil or excess water. Therefore we cannot start from that equilibrium state; instead, we must create a homogeneous non-equilibrium state of the water/surfactant/oil system where the structure is made of large droplets, starting from an equilibrium state that has the same curvature but in a non-droplet structure. From such access states, the systems will evolve spontaneously through different pathways. In the present work, we report the production of nanoemulsions through three pathways that we describe below.

Curvature control by salt addition. In this route, we start from an initial state that is a bicontinuous microemulsion co-existing with an oil phase and possibly an aqueous solution. This state has the right composition and the low spontaneous curvature that are adequate to solubilize a large amount of oil. However, it has but the wrong topology and it is not homogeneous. We create the homogeneous access state by imposing a turbulent flow to the structure[5]. This flow has two functions: it breaks the structure into droplets, and it mixes the 2 or 3 phases into a single phase that has a uniform composition throughout the system (access state). As a result, we obtain a non-equilibrium state, which is a superswollen microemulsion, consisting of a collection of oil droplets, stabilized by surfactant and dispersed in the aqueous phase, under permanent shear. In the present work, we report that we have discovered a convenient way to produce this access state at low temperature, by adding a monovalent salt that dehydrates the EG chains of the surfactant. Then, we quench this non-equilibrium state by changing abruptly a physical variable (temperature) or a composition variable (salt concentration). Through this change, the surfactant layers acquire a high spontaneous curvature whereas their actual curvature is low. In this situation, it is well known that the system has a high metastability against coalescence processes (metastable state). We also compare this method to the subPIT pathway in which the dehydration of the surfactant is achieved by changing temperature[6, 5]. From a conceptual point of view, both methods are identical, but from a practical point of view, the use of salt may be more convenient in two situations: (a) whenever one ingredient of the formula has a limited range of temperature stability;(b) when the formula must contain the very solutes that are used to dehydrate the surfactant.

Curvature control by pH flip. This is a more sophisticated variation of the subPIT pathway. It consists in creating the initial equilibrium state by supplementing a non-ionic surfactant with an unsaturated fatty acid. At acidic pH, the fatty acid is non-ionized. Consequently the mixed surfactant has a spontaneous curvature turned towards water, and the initial state has the structure of a bicontinuous microemulsion in equilibrium with an aqueous phase and an oil phase. Here as well, we use a moderate turbulent flow to produce a homogeneous access state, which consists of a superswollen bicontinuous microemulsion, Then we conveniently flip the pH by adding a small amount of base. The ionization creates a strong curvature of the surfactant, which quenches the structure into a metastable state made of oil droplets dispersed in water. This pathway requires a tighter control of transition temperatures, but it produces a nanoemulsion that has the same characteristics as that made by addition of salt or that made with the pure surfactant by raising temperature to the clearing boundary “CB” [6, 5].

Curvature control by water flooding. This method is related to what is now called the PIC pathway[7]. Here the initial state has almost no water or none of it. The initial state is a reverse, water-in-oil micellar phase. Then we add

water go through the access state, which is a sponge phase and jump over a set of unstable states, all the way to the highly hydrated states where the surfactant has a sufficient curvature to yield a good enough metastability. In the classical PIC pathway, the surfactant is a single component non-ionic molecule, with a polyethylene glycol chain. Here we extend the PIC method to the industrially more relevant surfactant + cosurfactant systems. In order to limit the complexity of the system, we chose two surfactants that can be obtained as sufficiently pure compounds, and that are both non-ionic and non ethylene-glycol surfactants (one with a glucose ring and the other with a sorbitan ring as a head-group. This choice introduces an additional composition variable, which makes the determination of phase diagrams more complex. On the other hand, it also facilitates the control of the two main structural parameters of the system, which are the area per head-group at the interface and the spontaneous curvature of that interface.

Choice of pathway. Each of these pathways introduces an additional composition variable, in comparison with model systems such as the classical C16E8/C16 oil/water system that has been used for the demonstration of the subPIT and of the PIC pathways[6, 7]. In the last section of this paper we examine what are the costs and benefits of the introduction of this additional variable, in terms of ease of complexity of the phase diagram (which is definitely a cost), but also ease of substitution of one component by another (benefit), better control of the ranges of physical (temperature) or chemical (pH) parameters, and better control of the emulsion stability and of its final properties.

1. Results

In this section we report the results of rapid changes in the surfactant layer properties in (surfactant + cosurfactant/oil/water systems). We either change the interactions of water with the hydrophilic head-groups, in excess water conditions, or add water to water-poor systems.

1.1 Curvature control by salt addition

The equilibrium structures in a surfactant/oil/water system are mainly controlled by the preferred curvature of the surfactant layer, which optimizes the intermolecular interactions at the interface. This curvature can thus be tuned through a modification of interactions, such as the interactions between water and the hydrophilic parts of the surfactant molecules. A large part of surfactant science and technology is based in the fact that oxyethylenated chains $(-OCH_2CH_2)_j$ have an enormous hydration, and that this hydration is temperature sensitive. Consequently we may tune the spontaneous curvature of the corresponding (C_iE_j) non-ionic surfactants by changing temperature. In previous articles we have shown that if a spherical microemulsion, either at equilibrium or in a steady-state under shear, was obtained along a temperature pathway, it could be trapped in a metastable state through a fast temperature quench. In the single surfactant case, any temperature higher than the one corresponding to this access

state could be used as starting point. Here we report data about alternate triggers that can be used and the possible extension to surfactant + cosurfactant systems. Our reference system is the $C_{16}E_8$ /hexadecane/water system[6].

A simple alternative to temperature is to change a solute concentration in the aqueous phase. The effect of temperature is limited mainly to the oxyethylene chain surfactants, but that of solutes, particularly electrolytes, is not. There are two possible effects depending on the concentration range. At low electrolyte concentrations, only ionic interactions will be changed through screening. This produces significant effects only for systems containing ionic surfactants. At high (molar) electrolyte concentration, however, the hydration of the surfactant is changed, with effects on both ionic and non-ionic surfactants. Consequently we may use the electrolyte concentration to tune the preferred curvature of surfactant layers. Using the $C_{16}E_8$ /hexadecane/water system, we may also tune the preferred curvature through temperature. Therefore, we can evaluate the variation of preferred curvature caused by changes of the electrolyte concentration, through the corresponding temperature changes. For example if we start from a superswollen microemulsion state (oil/surfactant ratio = 3.6 and $T=73^\circ\text{C}$), the preferred curvature equals the geometrical curvature $c_0 = c_{geo}$, with c_{geo} set by composition only. Since the addition of sodium chloride will decrease hydration, it will also decrease the preferred curvature and we then have $c_0 < c_{geo}$, which leads to a structural change. This can be compensated by rehydration through a drop in temperature, which brings the system back the superswollen microemulsion state. We have measured the variation of the temperature at which this superswollen microemulsion is obtained as a function of electrolyte concentration; the variations are displayed in Figure 1. Each dot thus corresponds to the same superswollen microemulsion, whose structure is determined by the set oil/surfactant ratio of 3.6, but different conditions (temperature and electrolyte concentration). We can then compare two types of quenches, whose aim is to rapidly increase the preferred curvature c_0 , which provided metastability against coalescence. One is through a temperature decrease, the other through a dilution by milli-Q water at constant temperature, which decreases the electrolyte concentration. The resulting emulsions are all brought to room temperature for characterization and the pathways are illustrated on Figure 1.

This figure also presents the mean diameter of the narrow size-distribution of the final emulsion. This mean diameter is absolutely independent of the pathway take, which demonstrates that the structure is indeed the same. It also demonstrates that variations of the electrolyte concentration can be used for rapid curvature quenches, which extends the validity of the results with temperature quenches on oxyethylenated surfactants to any type of surfactant system.

1.2 Curvature control by pH flip

Another trigger we investigated was the pH. This is only useful if the surfactant is an acid or a base and we have thus

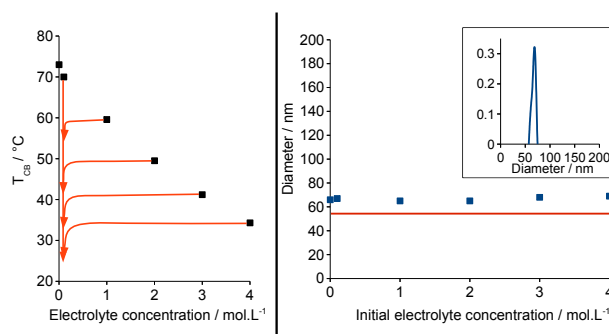


Figure 1. Clearing Boundary temperatures at which the superswollen microemulsion is obtained as a function of the electrolyte concentration. The quench pathways are indicated as red arrows from these temperatures and compositions. Right: Mean diameter of the emulsion resulting from a temperature quench or a dilution by water quench as a function of the initial composition. The red line corresponds to the theoretical size. The distributions are very narrow as displayed in the inset.

added oleic acid to the surfactant layer of $C_{16}E_8$ (10%). If we start from an acidic pH, much lower than the pKa of a fatty acids (around 5), which is ensured by using an aqueous phase of 10^{-2} mol.L⁻¹ HCl solution, the oleic acid is protonated and is a lipophilic surfactant. We observe a decrease of the temperature at which we form the superswollen microemulsion from 73°C to 55.2°C . If the oleic acid is deprotonated by the addition of a base, such as a sodium hydroxide aqueous solution (10^{-1} mol.L⁻¹ NaOH), the ionization must result in a strong increase of the temperature at which the superswollen microemulsion is obtained. This temperature could not be measured experimentally (we did not heat the water bath above 80°C). Starting from the superswollen microemulsion state at 55.2°C we added the sodium hydroxide solution and thus obtained a metastable nanoemulsion, whose mean diameter was the same as in previous quenches with temperature and salt. Indeed the oil/surfactant ratio is a constant. This method is interesting since many pH sensitive surfactants can be added to systems and simply requires the identification of the superswollen microemulsion line. Also it extends to a two surfactant system the mechanism developed on a single surfactant one.

However it also illustrates a major difference. While in the single surfactant case, any temperature above that of the superswelling microemulsion line leads to the same emulsion, this is not the case for this two-surfactant system. The final emulsion main diameters are given for several initial temperatures in Figure 2. As the temperature rises above 55.2°C and the initial state moves away from the superswollen microemulsion structure, the final emulsion mean diameter increases and so does the polydispersity. We are progressively losing the structural control of the emulsion. This shows that for a two-surfactant system, it is essential to start from the access state,

here the superswollen microemulsion.

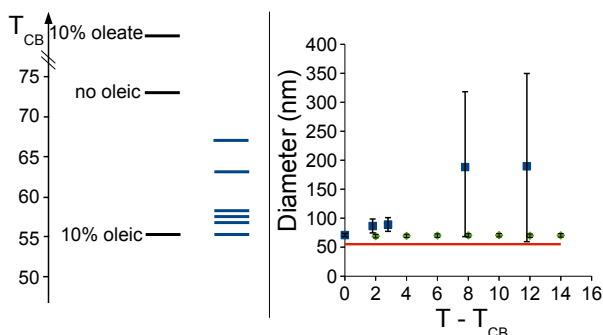


Figure 2. Left : Clearing boundary temperatures of the different surfactant mixtures and initial temperatures before the pH quench. Right : mean diameter of the emulsions resulting from pH quench as a function of the initial temperature. Blue dots correspond to pH quench for the surfactant mixture while green dots correspond to temperature quench for the pure non-ionic surfactant. The red line corresponds to the theoretical size.

1.3 Curvature control by water flooding

Starting from low water content the preferred curvature can also be tuned by addition of water. Indeed in water poor systems, hydrophilic heads will try to optimize their hydration by curving the surfactant layer towards the water. As the water content increases, the hydrophilic heads swell with water and the curvature decreases until it inverts at a given water fraction, the phase inversion composition. Further water addition turn the curvature towards the oil. The equilibrium phase behavior and the emulsification method upon rapid water addition have been described on a previous work on the $C_{16}E_8$ /hexadecane/water system. Contrarily to the previous method, the trigger is set, it is water addition. However like the previous method it is very important to know whether the emulsification can be performed for mixtures of surfactants. We have chosen two purified ($> 99\%$) systems to investigate this issue, which are good typical examples. One is the non-ionic mixture Octyl Glucoside/Span. Octyl Glucoside (OG) is a hydrophilic surfactant while sorbitan oleate (span) is a hydrophobic surfactant. Both are also mild biodegradable sources. The other is $C_{16}E_8$ /SDS, which is a modification of the reference system with addition of ionic surfactant. We kept hexadecane oil and milli-Q water.

1.3.1 OG/span system

We studied a cut of the phase diagram of the OG/span at constant oil/surfactant ratio of 3.52. The two parameters are the OG/Span ratio and the water fraction. The phase cut was investigated through slow addition of water and equilibration at constant OG/Span ratios, which corresponds to horizontal lines in Figure 3. The focus was to identify the one phase regions rather than a complete study. Visual inspection of the samples gives readily the number of phases and a crossed

polarizer/analyser setup is used to observe eventual birefringence. The sequence of states upon addition of water is well-known from previous phase diagrams and we can use the macroscopic properties of such tabulated states as references to those observed on this system. The phase cut is displayed in Figure 3. At zero water content, Span and hexadecane mix but OG remains as crystals. Small water addition solubilizes such crystals and at low OG/Span ratios an isotropic fluid phase is obtained. Since it occurs in dehydrated conditions and large fractions of the hydrophobic surfactant we can deduce that the structure is likely a water in oil microemulsion, i.e. water swollen mixed surfactant micelles. At high OG/Span ratio this phase coexists with OG crystals.

Adding more water results in three types of possible behaviors :

- At low OG/Span ratios, the water in oil microemulsion swell with water until phase separation of two isotropic phases at higher water content. The system then consists of a water in oil microemulsion coexisting with an oil in water microemulsion.
- At intermediate OG/Span ratios, the water in oil microemulsion transforms first into a birefringent fluid phase, that is likely a lamellar phase, and then into an isotropic fluid phase, that is likely a sponge phase. Further water addition leads globally to phase separation of some oil.
- At high OG/Span ratios, the OG crystals slowly dissolve in water and liquid crystals phase are observed in coexistence with an oil in water microemulsion that contains the Span.

The intermediate situation is itself divided in two categories. At the higher OG/Span ratios the lamellar/sponge sequence is observed for lower water contents than at the lower OG/Span ratios. Furthermore it separates into two isotropic phases before macroscopic oil phase separation. The full description of the equilibrium behavior of this system is outside the scope of the present work, with segregation of the surfactant as the cause of the additional complexity compared to the single surfactant systems. However the phase cut makes readily apparent a compatibility area of the two surfactants, in which the behavior closely mirrors that of the single surfactant system. This compatibility area is observed for intermediate OG/Span ratios.

Our aim is to link this equilibrium phase behavior to the emulsification outcome upon rapid addition of water. We chose a few initial compositions in these three regimes, which are displayed as lettered dots on Figure 4, and prepared the sample in its equilibrium state. Then we rapidly added a large volume of water and characterized the final state of the system. The behavior is described on Figure 4. At low and high OG/Span ratios, outside of the compatibility area, a very fast macroscopic separation within the minute is observed instead of a fine emulsion. At intermediate OG/Span ratios, in the

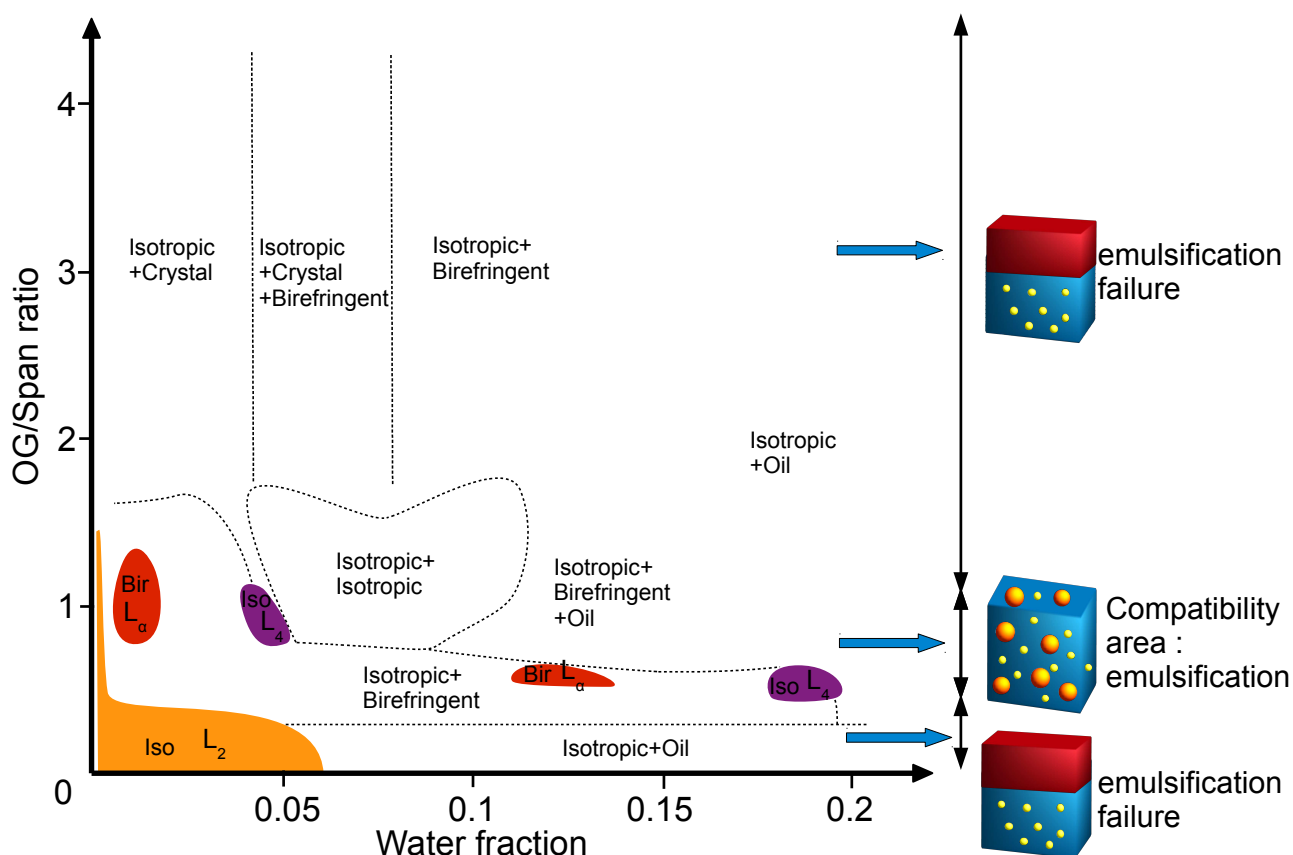


Figure 3. Phase cut of the OG/Span/Hexadecane/Water system at constant Surfactant/Oil ratio of 3.6. The colored areas correspond to monophasic region, isotropic or birefringent. Only a narrow range of OG/Span ratio yield a similar behavior to the single surfactant case. Starting from this compatibility area rapid water addition lead to a fine emulsion. Otherwise rapid water addition lead to a quick macroscopic phase separation.

compatibility area, emulsions are obtained, starting from low water fractions. However the properties and stabilities of the emulsions largely depend on the initial structure, determined by the initial water fraction. All the emulsions prepared from an initial state that is a single-phase structure are the same and have relatively narrow size distributions, similar to those obtained in our previous work using the surfactant $C_{16}E_8$. The mean diameter is always centered on 200 nm. However if the initial point was in a two-phase region the emulsion size distribution was broader and less stable. We noticed that the long-term stability of the emulsion was better at slightly lower than slightly higher OG/Span ratio, despite similar size distributions, which we will not discuss further here. Adding water after the last single phase region, that we identify as a sponge phase, always lead to very polydisperse emulsions that quickly separated.

We can conclude that similarly to the single surfactant systems, the presence of a sponge phase along the dilution pathway is essential to produce the final emulsion. For surfactants mixtures this requires to work in a compatibility area that can be obtained through a quick phase diagram mapping.

However, while for single surfactants the only condition was to start from water fractions below that of the sponge phase, mixtures of surfactants impose a stronger constraint since it is better to start only from single phases, i.e. avoid surfactant segregation between different phases.

1.3.2 $C_{16}E_8$ /SDS system

We investigated the system $C_{16}E_8$ /SDS as a perturbation by SDS addition of the $C_{16}E_8$ system. We found remarkably little changes in the equilibrium phase behavior, only the boundaries between the reverse micellar region and the lamellar region were slightly modified, with the lamellar phase obtained at lower SDS fractions. The position of the sponge phase was remarkably independent of the fraction of SDS replacing $C_{16}E_8$ up to 60% of SDS. From this point some SDS crystals do not solubilize at such low water fractions. Addition of water lead to the same emulsion, also centered around 200 nm, providing the fraction fraction is below or equal to that of the sponge phase. This system behaves much like a single surfactant system.

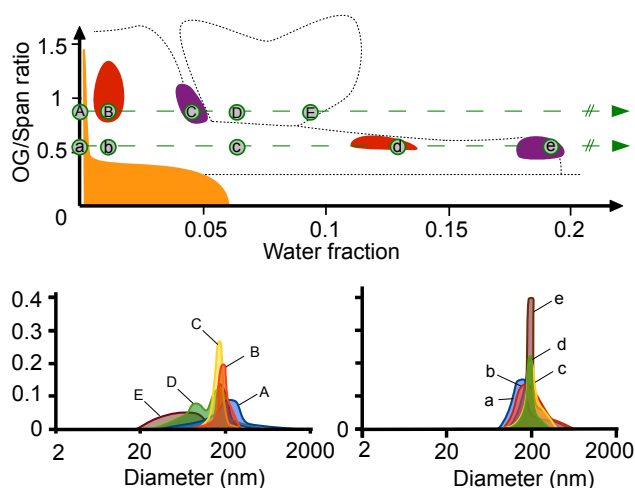


Figure 4. Zoom of the phase cut on the compatibility area. Several initial compositions are used before rapid addition of water and marked by letters. The corresponding size distributions of the resulting emulsion are displayed below. Starting from monophasic regions lead to narrower populations of droplets with better long term stability.

2. Discussion

2.1 Type of trigger and corresponding access state

Two types of emulsions are obtained depending on the type of trigger used. If the trigger consists in a modification of the hydrophilic head interaction with water we obtain a monodisperse emulsion with no excess surfactant. This is the case when modifying the temperature and using oxyethylenated surfactants, the electrolyte concentration, or the pH when using an acid or basic surfactant. If the trigger consists in the addition of water to a water poor mixture, the droplets are larger, the polydispersity higher and some surfactant is wasted. This general difference reflects a difference in the mechanism involved for each type of trigger.

When we modify the temperature, electrolyte concentration or pH, we work in water-rich conditions, i.e. the water/oil ratio is above unity. In this case we always identify an access state whose structure is the same as the final emulsion, that is a collection of droplets at the radius $R_{geo} = 3.l_s \frac{\phi_{oil}}{\phi_{surf}}$. This is shown in our previous work dedicated on the temperature trigger as well as the comparison between this theoretical radius (red line) and the experimental ones displayed in Figure 1 and Figure 2.

When we change the water fraction, we start from water-poor conditions, i.e. the water/oil ratio is far below unity. In this case we see from Figure 3 and Figure 4 that any successful emulsification pathway must cross the sponge phase. This bicontinuous phase has a curvature that we can calculate and matches the radius of the final droplet. Nucleation of the oil takes place in this sponge phase and leads to droplets templates at the curvature of the sponge phase and small

micelles. Some surfactant is thus wasted in solution and the droplets are larger than in the previous mechanism.

2.2 Special importance of access states in mixtures

Useful surfactant systems consists of several surfactant species. We aim to answer here what the changes are when moving from the single surfactant case to the mixture of surfactants case. We have performed two experiments with two different types of triggers, and thus mechanism to investigate this problem. The first case in the system oleic acid/C₁₆E₈/hexadecane/water. In this system the trigger is the increase of pH, which transforms the oleic acid in its conjugated base oleate. We can also tune the temperature to choose the initial structure from which we perform this pH quench. If we start from the access state, which is a super-swollen microemulsion, the quench is successful and gives exactly the same emulsion as with other types of quenches, such as temperature and salt. If we start from the access state, our previous work on pure surfactants would lead us to the conclusion that the same emulsion is also obtained. However for this mixture of surfactant, starting from above the access state leads first to larger diameter when moving slightly away from the binodal line and then much larger and polydisperse populations when crossing the phase inversion temperature. This means that the access state is not crossed during the rapid pH change and this prevents the good control of the size and polydispersity. It is thus essential to start directly from the access state and avoid phase inversion. It is worth noticing that no other monophasic state exist at higher temperatures.

The second experiment is in the system (OG + Span + Hexadecane + Water). In this case we can start from several monophasic states and they all give the same emulsion. Starting from regions of phase separations on the other hand leads to higher polydispersities.

We can conclude that for surfactant mixtures it is essential for good control to start from monophasic states located before the access state or from the access states. Any phase separation should be avoided since it has the effect of segregating the surfactant in different phases.

References

- [1] Conxita Solans and Isabel Solé. Nano-emulsions: Formation by low-energy methods. *Current Opinion in Colloid and Interface Science*, 17(5):246 – 254, 2012.
- [2] O. Sonneville-Aubrun, J.-T. Simonnet, and F. L'Alleret. Nanoemulsions: a new vehicle for skincare products. *Advances in Colloid and Interface Science*, 108–109(0):145 – 149, 2004.
- [3] Fennell D. Evans and Håkan Wennerström. *The Colloidal Domain: Where Physics, Chemistry, Biology, and Technology Meet (Advances in Interfacial Engineering)*. Wiley-VCH, February 1999.
- [4] H. Endo, M. Mihailescu, M. Monkenbusch, J. Allgaier, G. Gompper, D. Richter, B. Jakobs, T. Sottmann, R. Strey,

and I. Grillo. Effect of amphiphilic block copolymers on the structure and phase behavior of oil–water–surfactant mixtures. *The Journal of Chemical Physics*, 115(1):580–600, 2001.

- [5] Kevin Roger, Ulf Olsson, Malin Zackrisson-Oskolkova, Peter Lindner, and Bernard Cabane. Superswollen microemulsions stabilized by shear and trapped by a temperature quench. *Langmuir*, 27(17):10447–10454, 2011.
- [6] Kevin Roger, Bernard Cabane, and Ulf Olsson. Formation of 10–100 nm size-controlled emulsions through a sub-pit cycle. *Langmuir*, 26(6):3860–3867, 2010. PMID: 19899785.
- [7] Kevin Roger, Bernard Cabane, and Ulf Olsson. Emulsification through surfactant hydration: The pic process revisited. *Langmuir*, 27(2):604–611, 2011.

Solvent-Shifting : hydrodynamics vs. precipitation

Kevin Roger^{1*}, Christina Tang², Bernard Cabane¹, Robert Prud'homme²

Abstract

We investigate the coupling between the hydrodynamics of mixing and the precipitation in the solvent-shifting process. An acetonic solution of PMMA is mixed with an aqueous solution using confined impinging jets. At high flow rates we identify a regime where the diameter of the PMMA particles is independent of the polymer concentration and the particles are homogeneous if a mixture of PMMA is used. At low flow rates we identify a different regime where the diameter of the PMMA particles increase with the polymer concentration and the particles are core-shell if a mixture of PMMA is used.

¹ PMMH, CNRS UMR 7636, ESPCI, 10 rue Vauquelin, F 75231 Paris cedex 05, France

² Princeton university, chemical engineering department

*Corresponding author: kevin.roger@espci.fr

Contents

| | |
|--|----------|
| Introduction | 1 |
| 1 Materials and Methods | 1 |
| 1.1 Materials | 1 |
| 1.2 Methods | 1 |
| 2 Results | 1 |
| 2.1 Phase Diagram and solvent-shifting | 1 |
| 2.2 Concentration and mixing quality | 2 |
| 2.3 Repulsions depend on the composition | 3 |
| 2.4 Mixing of polymers | 3 |
| 3 Discussion | 4 |
| 3.1 Rapid mixing regime | 4 |
| 3.2 Slow mixing regime | 5 |
| References | 5 |

Introduction

Producing small droplets or particles of well defined sized in the nanometric scale could be thought of as a difficult task. However it is simply performed by mixing two homogeneous liquids. One liquid is a solute solution in a good solvent, while the other is a bad solvent. Providing the good and bad solvent are miscible in all proportions, the solute will precipitate upon addition of bad solvent. If a stabilizer is present, the resulting phase separation is restricted to the colloidal scale and uniform collections of droplets/particles are obtained.

This process involves two steps : the hydrodynamics of the mixing and the precipitation of the solute. In a previous work we have investigated the mechanism of precipitation in conditions where the mixing is rapid. We found that the swollen polymer droplets were obtained through a coalescence process hindered by ionic repulsions. This mechanism leads to uniform collections. The aim of this work is to investigate in details the importance of the hydrodynamic step by controlling the mixing process.

1. Materials and Methods

1.1 Materials

The PMMA were bought from polymer source are their distribution of masses are narrow, $M_w/M_n < 1.1$. One PMMA has a Butyl end-group and a molar mass of 25000 g/mol and will be noted in the rest of the text PMMA-Bu, another has a carboxylic acid end-group and a molar mass of 9900 g/mol and will be noted PMMA-COOH and a last one has a sec-butyldiphenylethene end-group and a molar mass of 9800 g/mol and will be noted PMMA-secBuDPE. Chromatographic grade acetone was purchased from sigma-Aldrich with an assessed purity above 99.9%. Milli-Q water was used for the preparation of aqueous solutions.

1.2 Methods

The mixing device is described in a previous work by Johnson and Prud'homme [1].

2. Results

2.1 Phase Diagram and solvent-shifting

A solute can be solubilized in a good solvent to form a solution or it can precipitate in a different phase from a bad solvent. From these two extreme cases we can mix the good and bad solvent together and the equilibrium state will then depend on the exact composition. At low fractions of the bad solvent a solution of the three species is obtained, whereas at high fractions of the bad solvent a solute rich solution separates from a solvent poor solution. The boundary between the two behaviors is named the binodal line, which corresponds to the precipitation line upon addition of bad solvent or the solubilization line upon addition of good solvent. We have determined experimentally these lines for the three polymers used and the phase diagram is plotted in 1. The binodal of the heaviest polymer (PMMA-Bu $M=25000$ g/mol) is located at higher fractions of acetone than the two lightest polymers (PMMA-COOH $M = 9900$ and PMMA-secBuDPE $M = 9800$).

The two PMMA have similar molar masses and their binodals are close but PMMA-COOH has a hydrophilic end-group while PMMA-secBuDPE has a very hydrophobic end-group, and this corresponds to a slightly higher binodal.

A solvent-shifting experiment consists in the rapid addition of a bad solvent, water, to a good solvent/solute solution, PMMA in acetone. This corresponds to vertical lines in Figure 1. Upon mixing there is a hydrodynamic fragmentation in domains. If the domains are small, diffusion takes place faster than the precipitation and precipitation occurs in a homogeneous solution of bad solvent and good solvent at the final concentration. If the domains are bigger, diffusion competes with the precipitation and the precipitation occurs in a solvent mixture that is not at the final concentration.

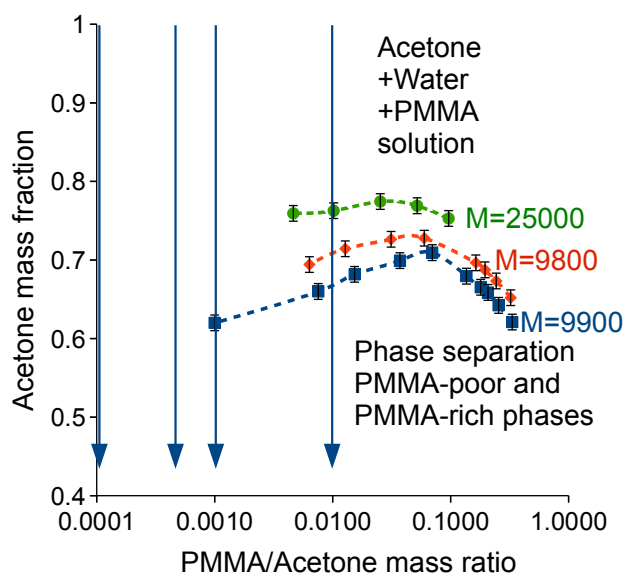


Figure 1. Phase diagrams of PMMA/Acetone/Water systems for the three PMMA used in this study PMMA-COOH ($M=9900$ g/mol), PMMA-Bu ($M=25000$ g/mol) and PMMA-secBuDPE ($M=9800$ g/mol). At high acetone fractions the equilibrium state is a PMMA/acetone/water solution whereas at low acetone fractions the equilibrium state is a phase separation of a PMMA rich solution with a PMMA poor solution. The domains are separated by the binodal line, located at higher acetone fraction for the heaviest PMMA than for the lightest. Addition of water to a PMMA/acetone solution corresponds to a vertical line in this diagram.

2.2 Concentration and mixing quality

In a previous work, we have investigated the mechanism through which narrow populations of droplets were obtained through the solvent-shifting method. This study was undertaken in good mixing conditions, using a stopped-flow apparatus. The only important parameter was then the ionic

repulsions between droplets that can arise from end-groups, surfactant or monomers. However we did not characterize the good mixing region, nor the concentration dependence and we aim to characterize the influence of these parameters in this work. Concentrations from 10^{-4} to 10^{-2} of PMMA-COOH in acetone were used, pH=10 and the ionic strength was set at 10^{-3} . The mixing quality is controlled by a mixed developed by the Prud'homme group and the flow rate of the syringes allow a control of the Reynolds number. Then the mean diameter was measured one hour after preparation through Dynamic Light Scattering. The results are displayed in Figure 2. For all concentrations and Reynolds numbers a narrow population of droplets were obtained. This contrasts with what is obtained with non-controlled mixing such as direct addition, where the mixing conditions are heterogeneous and large objects are usually obtained in addition to smaller ones at high polymer concentrations.

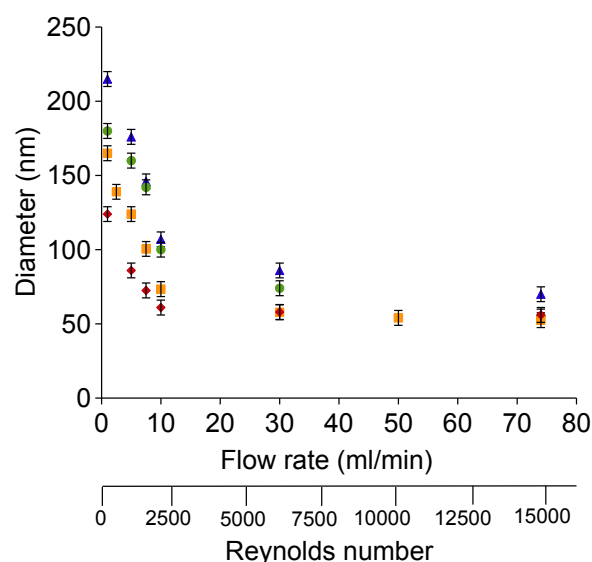


Figure 2. Variation of the mean diameter of PMMA droplets prepared by addition of water to a PMMA/acetone solution, as a function of the flow rate of the mixer, for four PMMA mass fractions (diamonds : 10^{-4} , squares : 10^{-3} , circles : $5 \cdot 10^{-3}$, triangles : 10^{-2}). The diameter always increases with decreasing the flow rate. At high flow rates the diameter does not depend on the concentration, whereas it does at lower flow rates. This separates a slow mixing regime from a rapid mixing regime.

Increasing the Reynolds number leads to a decrease of the mean diameter for all concentrations. Remarkably the data collapses at high Reynolds, which means that the diameter does not depend on the concentration in rapid mixing conditions. In slow mixing conditions, the higher the concentration the larger the particles. Two mixing regimes thus exist for the influence of the concentration.

2.3 Repulsions depend on the composition

To study differences between slow and rapid mixing regimes we perform a reverse experiment to probe the very slow regime. First we prepared a dispersion of PMMA droplets by rapid addition of water. The final acetone/water volume ratio was 1-1 and the measured diameter was measured after preparation. Then the dispersion was either left as, or diluted further with water or with acetone. After 22h the diameter was measured and the results are displayed in Figure 3. The dispersion in water rich conditions did not evolved in these 22 hours as the diameter is unchanged. For the other samples the diameter first increases slowly at intermediate acetone contents and then rapidly close to the binodal at higher acetone fractions. This means that the area below the binodal, rich in acetone, corresponds to poor metastability. This means that the ionic repulsions are not efficient in that acetone rich region. This will also be the case when crossing the binodal through water addition. Therefore in slow mixing the system stays longer in this dangerous region than in rapid mixing.

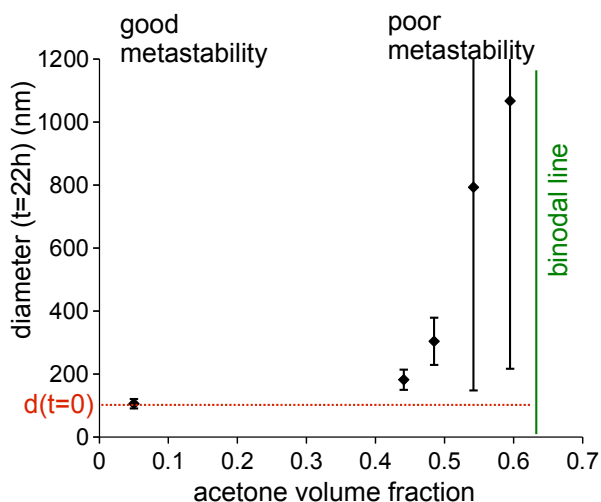


Figure 3. Variation of the mean diameter of a collection of PMMA droplets with the fraction of acetone. Initially the diameter is 100nm. After 22 hours it is unchanged if the medium is water rich but increases if the medium is acetone rich. In the vicinity of the binodal the colloidal metastability is poor, meaning that the ionic repulsions between the particles are weaker and thus do not slow as much the coalescence.

2.4 Mixing of polymers

To probe more locally the structure of the particles, depending on the mixing history of a sample, we can make use of the macromolecules end-groups. Although PMMA is composed of non-ionic monomers, each macromolecules possess an end-group of a different chemical structure than that of the monomer. This end-groups is the result of the initiation step of the polymerization reaction. The end-group can be charged, such as with carboxylate and sulfate based initiators,

or uncharged, such as in most anionic polymerization conditions where organometallic compounds are used. We have performed in a previous work the detailed study of the end-groups influence on polymer particles. The number of charged end-groups at the interface will regulate the surface charge and thus the size of the particles. If one type of macromolecule has a charged end-group and the other type an uncharged end-group, mixing the two types can results in many behaviors. They can mix, segregate within the droplet or even segregate as different droplets.

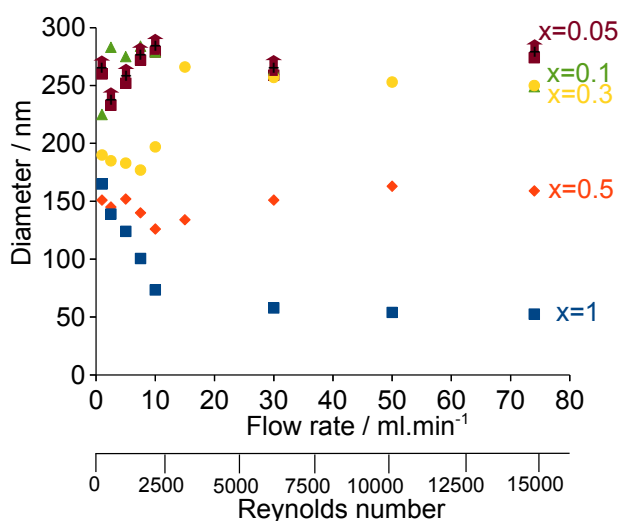


Figure 4. Variation of the diameter with the flow rate for several mixtures of PMMA-COOH ($M=9900$ g/mol) and PMMA-secBuDPE ($M=9800$ g/mol). The PMMA/acetone ratio is 10^{-3} . The arrows indicate a population of large visible aggregates in the solution in addition to the narrow population whose diameter is plotted. A narrow population of droplets is obtained for all conditions except at very low fractions of PMMA-COOH. At high flow rates the diameter increases rapidly upon replacing the charged PMMA-COOH by the uncharged PMMA-secBuDPE, while at low flow rates the diameter is nearly independent of the fraction of PMMA-COOH, except below 0.05. This leads to a reversal of the behavior observed in Figure 2, since the diameter is observed to decrease with decreasing the flow rates when the fraction of PMMA-COOH is below 0.5. This illustrates a competition between two effects.

We prepared solutions of PMMA at a mass fraction 10^{-3} in acetone. PMMA-COOH was mixed either with PMMA-Bu or with PMMA-secBuDPE at various mass ratio x . Water was mixed with the acetone solution to a 1-1 volume ratio at different flow rates, i.e. Reynolds numbers. The mean diameter was then measured and the variations are displayed in Figure 4 for the PMMA-COOH/PMMA-secBuDPE mixture and Figure 5 for the PMMA-COOH-PMMA-Bu.

Figure 4 corresponds to the mixing of two PMMA of sim-

ilar molar masses (9800 and 9900) and binodals but different end-groups, one charged the other uncharged. Replacing the charged PMMA with the uncharged one lead to important variations of the diameter variation with the Reynolds number. While for the pure PMMA-COOH the diameter increases when reducing the Reynolds number, as shown also in Figure 2, the replacement by PMMA-secBuDPE leads to a reversal of this behavior. Indeed replacing the PMMA-COOH by the uncharged PMMA-Bu leads to a much higher increase of the diameter at high Reynolds than at low Reynolds. Narrow populations are obtained in all cases except at very low fractions of PMMA-COOH ($x=0.5$) from which big aggregates are detected in addition to the smaller particles.

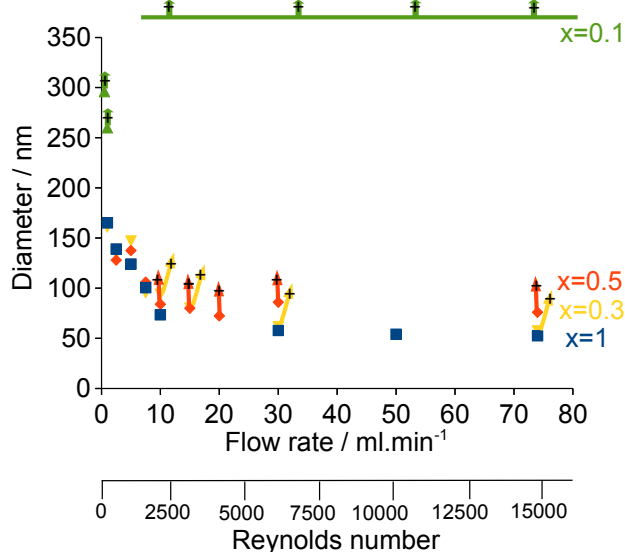


Figure 5. Variation of the diameter with the flow rate for several mixtures of PMMA-COOH ($M=9900$ g/mol) and PMMA-Bu ($M=25000$ g/mol). The PMMA/acetone ratio is 10^{-3} . The arrows indicate a population of large visible aggregates in the solution in addition to the narrow population whose diameter is plotted. Except for pure PMMA-COOH for which narrow populations are obtained, the addition of PMMA-Bu to the polymer mixtures leads to two populations. One is a narrow populations of small objects at the same size than for the pure PMMA-COOH, the other is a population of visible aggregates. This behavior contrasts with the mixtures of the two lighter polymers displayed in Figure 4

Figure 5 corresponds to the mixing of two PMMA of different masses (9900 and 25000), binodals and end-groups, one charged, one uncharged. The same type of experiment is performed as for the previous mixture. However the observations are very different. In this case we always observe two populations when using PMMA mixtures. One is narrow and the size is the same as for the pure PMMA-COOH for all mixing conditions. The other one corresponds to large aggregates that are visible by the eye. We thus produce two

types of objects.

3. Discussion

The set of data presented in the Results section makes apparent two different mixing regimes, rapid and slow. Each of these regime has its own specificities and we turn to examine the consequences for the design of a solvent-shifting process.

3.1 Rapid mixing regime

The rapid mixing regime is characterized by the concentration independence of the mean diameter. This is especially important for practical uses of solvent-shifting, when concentrations as high as possible are desired. To understand this observation we can use the model we designed to describe the mechanism of formation of the polymer droplets. Upon crossing the binodal line, phase separation occurs, it leads to a broad population of small swollen polymer droplets with charges provided by the macromolecules end-groups, which coalesce. If the mixing is rapid compared to this coalescence process, we can describe the coalescence process in a medium of constant composition, at the final acetone/water ratio. At a given instant the process depends only on the size distribution of the population of droplets. Since the rate of diffusion increases with the concentration, the process will occur faster at higher concentrations. However we found a law $R_{mean} \sim \ln(t)$, which means that the effect of the concentration will be small at experimental measurements times of an hour. This explains the concentration independence in the rapid mixing conditions.

This picture of rapid mixing supposes that there is an instantaneous mixing of the bad solvent with the good solvent so that the PMMA macromolecules coalesce in a homogeneous medium. This can be tested with another tool, the mixtures of PMMA. If we take a PMMA with a charged end-group and another with an uncharged end-group, we expect a mixture of the two in a particles, with no segregation in the particle. In this case the surface charge should be directly related to the number of charged and uncharged end-groups. Our model gives the relation between the surface charge and the diameter. The diameters at various mass ratios of the two polymers PMMA-COOH ($M=9900$ g/mol) and PMMA-secBuDPE ($M=9800$ g/mol) are displayed in Figure 4. Since the two polymer have the same mass, the mass ratio is also the mole ratio. As expected the diameter increases with decreasing the amount of charged end-groups.

The same situation could be expected to be similar for the mixture of PMMA-COOH ($M=9900$ g/mol) with PMMA-Bu ($M=25000$ g/mol) but as displayed in Figure 5, a very different behavior is observed. A narrow populations of droplets whose size does not depend on the fraction of uncharged polymer is obtained, and coexists with a population of visible aggregates. There is thus a segregation of two types of polymer based objects. Since the population of droplets is at the same size irrespective of the PMMA-Bu fraction, they must have the same number of charges at their interface and thus the same surface composition. Since the mixing is rapid there is no

strong reason for inhomogeneities in the particle. The amount of large aggregates increases with the amount of PMMA-Bu and this leads to the conclusion that these aggregates contain mainly the PMMA-Bu. The only difference with the previous case is the molar mass of the PMMA. Although the location of the binodal is irrelevant in rapid mixing conditions, the final swelling of the PMMA droplets changes with the molar mass. The heaviest PMMA is thus much less swelled than the lightest PMMA. This could lead to difficulties to coalesce the two types of droplets from the onset of the coalescence.

3.2 Slow mixing regime

The slow mixing regime is characterized by a concentration dependence of the final diameter as displayed in Figure 2. This requires another ingredient to be added to the mechanism through which the polymer particles are obtained. In slow mixing the composition changes during the coalescence process and the beginning of the coalescence thus takes place at higher acetone fractions than the end and that the final acetone fraction. This means that beginning of the process occurs at solvent conditions in the vicinity of the binodal line. In Figure 3 we have shown that the ionic repulsions are weakened in this vicinity, at high acetone fractions. Going to the extreme we could divide the addition of water as a two step process in the slow mixing regime. At first a regime without repulsions between droplets, which is then a diffusion-controlled mechanism, followed by a regime with repulsions between droplets, as what is used to describe the rapid mixing conditions. The first regime depends on the concentration, while the second is concentration independent. The size is bigger since most of the growth occurs at lower repulsions than the final composition.

Another argument in favor of this importance of this mechanism are the results obtained with the mixtures of PMMA. For both PMMA mixtures, a narrow population is obtained. As the binodals of the uncharged PMMA are higher than the charged PMMA they should precipitate at lower water fractions and thus lead to core-shell particles.

References

- [1] Brian K. Johnson and Robert K. Prud'homme. Chemical processing and micromixing in confined impinging jets. *AIChE Journal*, 49(9):2264–2282, 2003.

Bibliography

- [1] D. Anderson, H. Davis, J. Nitsche, and L. Scriven. Periodic surfaces of prescribed mean curvature. In J. Meunier, D. Langevin, and N. Boccara, editors, *Physics of Amphiphilic Layers*, volume 21 of *Springer Proceedings in Physics*, pages 130–130. Springer Berlin Heidelberg, 1987.
- [2] D. Anderson, H. Wennerström, and U. Olsson. Isotropic bicontinuous solutions in surfactant-solvent systems: the l3 phase. *The Journal of Physical Chemistry*, 93(10):4243–4253, 1989.
- [3] A. Bernheim-Groswasser, T. Tlustý, S. A. Safran, and Y. Talmon. Direct observation of phase separation in microemulsion networks. *Langmuir*, 15(17):5448–5453, 1999.
- [4] A. Bonfillon and D. Langevin. Viscoelasticity of monolayers at oil-water interfaces. *Langmuir*, 9(8):2172–2177, 1993.
- [5] B. Cabane and S. Hénon. *Liquides: Solutions, dispersions, émulsions, gels*. Collection Échelles. Belin, 2007.
- [6] P. Canham. The minimum energy of bending as a possible explanation of the biconcave shape of the human red blood cell. *Journal of Theoretical Biology*, 26(1):61 – 81, 1970.
- [7] J. Daicic, U. Olsson, H. Wennerström, G. Jerke, and P. Schurtenberger. Thermodynamics of the l3 (sponge) phase in the flexible surface model. *J. Physique*, 5:199–215, 1995.
- [8] Y. De Smet, L. Deriemaeker, and R. Finsy. A simple computer simulation of ostwald ripening. *Langmuir*, 13(26):6884–6888, 1997.
- [9] F. D. Evans and H. Wennerström. *The Colloidal Domain: Where Physics, Chemistry, Biology, and Technology Meet (Advances in Interfacial Engineering)*. Wiley-VCH, Feb. 1999.
- [10] D. Exerowa, D. Kashchiev, and D. Platikanov. Stability and permeability of amphiphile bilayers. *Advances in Colloid and Interface Science*, 40(0):201 – 256, 1992.

- [11] R. Finsy. On the critical radius in ostwald ripening. *Langmuir*, 20(7):2975–2976, 2004. PMID: 15835181.
- [12] F. C. Frank. I. liquid crystals. on the theory of liquid crystals. *Discuss. Faraday Soc.*, 25:19–28, 1958.
- [13] O. Glatter, G. Fritz, H. Lindner, J. Brunner-Popela, R. Mittelbach, R. Strey, and S. U. Egelhaaf. Nonionic micelles near the critical point : Micellar growth and attractive interaction. *Langmuir*, 16(23):8692–8701, 2000.
- [14] W. Helfrich. Elastic properties of lipid bilayers : Theory and possible experiments. *Z. Naturforsch.*, 28:693–703, 1973.
- [15] P. L. J. Jouffroy and P. de Gennes. Phase equilibria involving microemulsions (remarks on the talmon-prager model). *J. Physique*, 43:1241–1248, 1982.
- [16] A. Kabalnov, U. Olsson, and H. Wennerstrom. Polymer effects on the phase equilibrium of a balanced microemulsion. *Langmuir*, 10:2159–2169, 1994.
- [17] A. Kabalnov and J. Weers. Macroemulsion stability within the winsor iii region : Theory versus experiment. *Langmuir*, 12(8):1931–1935, 1996.
- [18] A. Kabalnov and H. Wennerström. Macroemulsion stability: the oriented wedge theory revisited. *Langmuir*, 12(2):276–292, 1996.
- [19] A. S. Kabalnov and E. D. Shchukin. Ostwald ripening theory: applications to fluorocarbon emulsion stability. *Advances in Colloid and Interface Science*, 38(0):69 – 97, 1992.
- [20] L. Landau and E. Lifshitz. *Statistical Physics I*. Pergamon Press, New York, 1980.
- [21] T. D. Le, U. Olsson, H. Wennerström, and P. Schurtenberger. Thermodynamics of a nonionic sponge phase. *Phys. Rev. E*, 60:4300–4309, Oct 1999.
- [22] I. Lifshitz and V. Slyozov. The kinetics of precipitation from supersaturated solid solutions. *Journal of Physics and Chemistry of Solids*, 19(1–2):35 – 50, 1961.
- [23] P. Lindner and T. Zemb. *Neutrons, X-rays and light : Scattering methods applied to soft condensed matter*. North-Holland, 2002.
- [24] A. Meroni, A. Pimpinelli, and L. Reatto. On the entropy of mixing of a binary mixture of hard spheres. *The Journal of Chemical Physics*, 87(6):3644–3646, 1987.
- [25] D. J. Mitchell, G. J. T. Tiddy, L. Waring, T. Bostock, and M. P. McDonald. Phase behaviour of polyoxyethylene surfactants with water. mesophase structures and partial miscibility (cloud points). *J. Chem. Soc., Faraday Trans. 1*, 79:975–1000, 1983.

- [26] U. Olsson and H. Wennerström. Globular and bicontinuous phases of non-ionic films. *Advances in Colloid and Interface Science*, pages 113–146, 1994.
- [27] C. W. Oseen. The theory of liquid crystals. *Trans. Faraday Soc.*, 29:883–899, 1933.
- [28] G. Porte, M. Delsanti, I. Billard, M. Skouri, J. Appell, J. Marignan, and F. Debeauvais. Scaling laws for some physical properties of the L3 (sponge) phase. *Journal of Physics II*, 1:1101–1120, 1991.
- [29] S. Safran, L. Turkevich, and P. Pincus. Cylindrical microemulsions : a polymer-like phase ? *J. Physique*, 45:69–74, 1984.
- [30] B. Seguin and E. Fried. Microphysical derivation of the canham–helfrich free-energy density. *Journal of Mathematical Biology*, pages 1–19, 2013.
- [31] O. Sonneville. *Mousses Biliquides*. PhD thesis, Paris 6, 1997.
- [32] O. Sonneville-Aubrun, V. Bergeron, T. Gulik-Krzywicki, B. Jönsson, H. Wennerström, P. Lindner, and B. Cabane. Surfactant films in biliquid foams. *Langmuir*, 16(4):1566–1579, 2000.
- [33] R. Strey. Microemulsion microstructure and interfacial curvature. *Colloid and Polymer Science*, 272(8):1005–1019, 1994.
- [34] L. Taisne. *Echanges d’huile entre gouttes d’émulsions*. PhD thesis, Paris 6, 1997.
- [35] Y. Talmon and S. Prager. Statistical thermodynamics of phase equilibria in microemulsions. *The Journal of Chemical Physics*, 69(7):2984–2991, 1978.
- [36] T. Tlustý and S. A. Safran. Microemulsion networks: the onset of bicontinuity. *Journal of Physics: Condensed Matter*, 12(8A):A253, 2000.
- [37] A. J. Webster and M. E. Cates. Stabilization of emulsions by trapped species. *Langmuir*, 14(8):2068–2079, 1998.
- [38] H. Wennerström and D. M. Anderson. Difference versus gaussian curvature energies; monolayer versus bilayer curvature energies; applications to vesicle stability. In H. Davis and J. Nitsche, editors, *Statistical Thermodynamics and Differential Geometry of Microstructured Materials*, volume 51 of *The IMA Volumes in Mathematics and its Applications*, pages 137–152. Springer New York, 1993.
- [39] H. Wennerström, J. Daicic, U. Olsson, G. Jerke, and P. Schurtenberger. Sponge phases and balanced microemulsions: What determines their stability? *Journal of Molecular Liquids*, 72(1-3), 1997.

- [40] H. Wennerström and U. Olsson. On the flexible surface model of sponge phases and microemulsions. *Langmuir*, 9(2):365–368, 1993.
- [41] P. Zakharov. Online mie scattering calculator for spheres, <http://zakharov.zzl.org/lstar.php>.

Chapter 6

Résumé

6.1 Introduction

Notre perception du monde repose sur une division en systèmes, comme des objets, des personnes ou des endroits différents. Chaque système peut adopter différents états, où chaque état correspond à un jeu de propriétés macroscopiques, qui sont la moyenne de propriétés microscopiques. Parmi tous les états possibles, certains sont plus favorables et correspondent à des vallées dans le paysage des états possibles, d'autres sont plus défavorables et peuvent être représentés par des montagnes. L'état le plus favorable du système est unique et est appelé état d'équilibre. Si le système peut explorer tous les états possibles, c'est à dire est ergodique, il atteindra son état d'équilibre, au bout d'un certain temps.

Lorsque qu'un système atteint son état d'équilibre tous les autres états possibles deviennent sans importance. Le système est alors contraint à demeurer au même endroit dans le paysage, la vallée la plus profonde. Cependant nous pouvons préférer exprimer d'autres propriétés du système que celle de son état d'équilibre pour atteindre un objectif donné. Un exemple caractéristique est donné par les états d'équilibre correspondant à une séparation de phase, macro et/ou microscopique, de deux phases qui ne se mélangent pas. Une phase étant une région de l'espace homogène en composition et en structure.

Ce travail se focalise sur deux exemples : les systèmes eau/huile et polymère/mauvais solvant, qui conduisent à l'équilibre vers une séparation macroscopique de phase, dans la majorité des conditions. Si une espèce supplémentaire est ajoutée, comme des molécules amphiphiles qui peuplent les interfaces, la séparation de phase peut être restreinte à l'échelle microscopique. Cela correspond à un auto-assemblage à l'équilibre, avec une grande diversité de structures formées seulement dans des gammes étroites de conditions et compositions. De tels états sont souvent à éviter parce qu'il n'est pas facile de maîtriser une séparation de phase macroscopique et délicat de garder les conditions particulières dans lesquelles on obtient une structure donnée de séparation de phase microscopique. Il est souvent préférable d'obtenir un type de structure correspondant à une plus grande

gamme de conditions et ce travail porte plus particulièrement sur la préparation de gouttes nanométriques de taille contrôlées.

Cependant se déplacer loin de l'état d'équilibre a également pour effet de diminuer le nombre de contraintes pesant sur le système. Puisque les contraintes sont nécessaires pour obtenir des structures contrôlées, il peut donc sembler paradoxal d'obtenir des gouttes de taille contrôlées loin de l'équilibre. Ce paradoxe peut être résolu en remarquant que toutes les contraintes ne sont pas équivalentes pour obtenir une structure donnée. Ainsi la sélection des contraintes, plus que leur nombre brut, détermine l'efficacité du contrôle structurel.

Les méthodes d'émulsification les plus répandues nécessitent une injection d'énergie mécanique dans le système pour franchir les barrières qui s'opposent à la fragmentation d'un grand domaine d'huile en deux plus petits. Plusieurs instruments existent, du fouet de cuisine à l'homogénéiseur haute pression, et chaque type correspond à un nombre de contraintes qui déterminent la gamme de taille et l'uniformité de la population de gouttes. Les méthodes mécaniques sont facilement applicables à une grande variété de systèmes eau/huile/tensioactif mais la fabrication de gouttes nanométriques de taille contrôlée nécessite d'importants coûts de fonctionnement et peuvent également endommager certains constituants fragiles. Le système est mené loin de l'équilibre à grands coûts d'énergie.

L'approche physico-chimique a été historiquement introduite comme une optimisation des méthodes mécaniques. En effet le coût des interfaces peut être réduit par un contrôle précis des interactions à l'interface et conduit à une diminution du coût de fragmentation. Ce coût est minimal lorsque la couche de tensioactif est équilibrée vers l'huile et vers l'eau. Cela correspond au voisinage de l'inversion de phase, qui est la transition d'un état eau dans huile vers un état huile dans eau. Les propriétés de la couche de tensioactif peuvent être ajustées par l'hydratation de la tête hydrophile. Pour les tensioactifs historiques oxyéthylénés, ce peut être réalisé par des variations en température, et on parle alors de Phase Inversion Temperature (PIT), ou par ajout d'eau et on parle alors de Phase Inversion Composition (PIC).

Bien que ce raisonnement soit correct, cette thèse démontre que la fragmentation à l'inversion de phase n'est en fait pas pertinente pour décrire le mécanisme d'émulsification. Pour les deux types d'hydratation un autre chemin franchit par un tunnel la barrière à la fragmentation. Le mécanisme consiste à la traversée d'un état d'accès qui détermine les propriétés et la structure de la nanoémulsion finale. Ces méthodes sont physico-chimiques parce que les contraintes sont liées aux interactions intermoléculaires, ici liées à la structure et la composition de l'interface, plutôt que déterminées par la géométrie du dispositif comme en émulsification mécanique.

Si l'hydratation est contrôlée par les interactions entre l'eau et les têtes hydrophiles, via par exemple la température, l'état d'accès est obtenu par cisaillement du système, ce qui modifie le coût relatif des structures bicontinues par rapport aux structures sphériques.

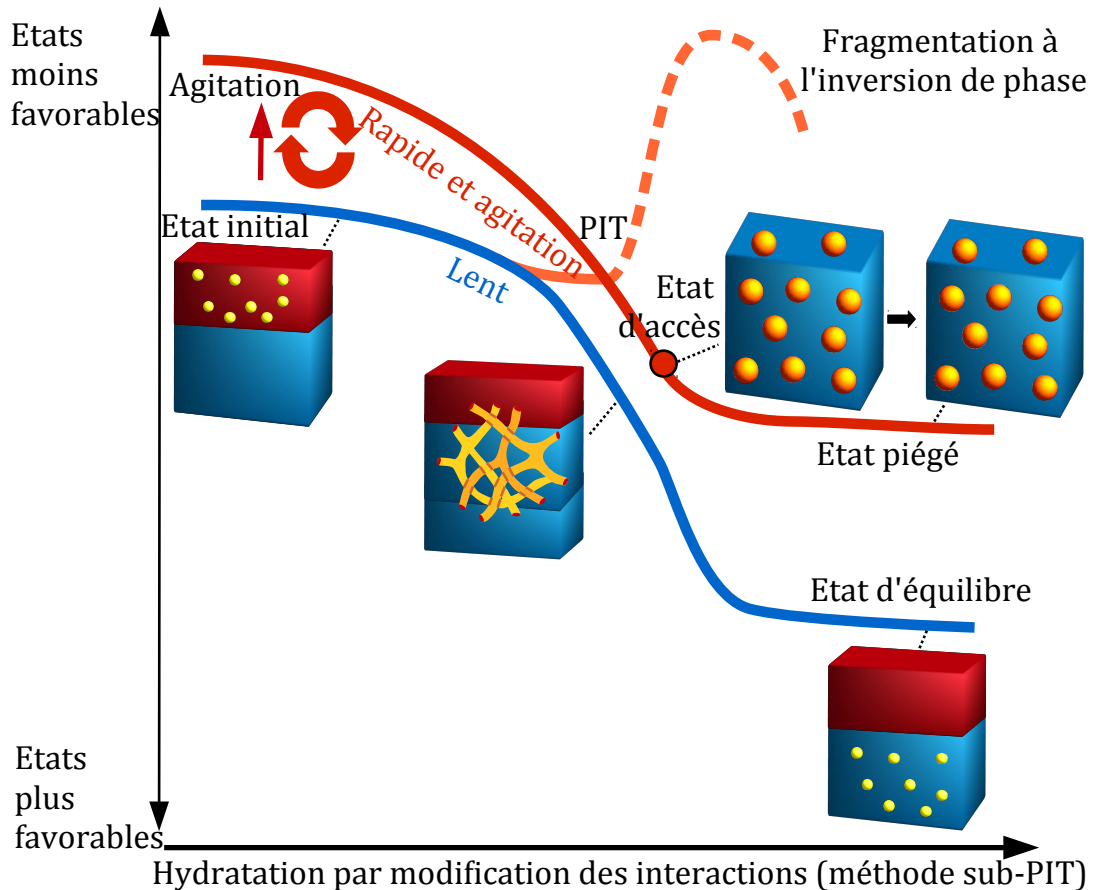


Figure 6.1: Une nanoémulsion peut être obtenue par hydratation d'un système eau/huile/tensioactif par modification des interactions, comme le changement de température pour les tensioactifs C_iEO_j . Une trempe en température sous cisaillement mène le système le long d'un chemin qui traverse un état d'accès contrôlant les propriétés et la structure de cette nanoémulsion.

La suite d'états sous cisaillement se décale de celle d'équilibre. Lorsque l'état d'accès est franchi, le système ne change pas sa structure et est piégé dans un état qui s'éloigne loin de l'équilibre. Ce déroulement est représenté dans la Figure 6.1. La structure de l'état d'accès est déterminée par les contraintes locales posées par les interactions dans la couche de tensioactif. En commençant depuis cet état d'accès, situé à des températures plus basses que la température d'inversion de phase, nous pouvons concevoir une méthode physico-chimique sub-PIT.

Si l'hydratation est régulée par l'addition d'eau, la suite d'états est dans un premier temps très proche de l'équilibre. A des concentrations en eau plus élevées que la composition d'inversion de phase, le chemin bifurque. Cela correspond à l'hydratation d'une phase éponge qui contrôle la séparation de l'huile plutôt que d'évoluer vers la nouvelle phase d'équilibre. Cette phase éponge est un autre type d'état d'accès qui est aussi contrôlé par les interactions dans la couche tensioactive et détermine les propriétés de la nanoémulsion finale. Cette méthode physico-chimique est une méthode sup-PIC représentée dans la Figure 6.2.

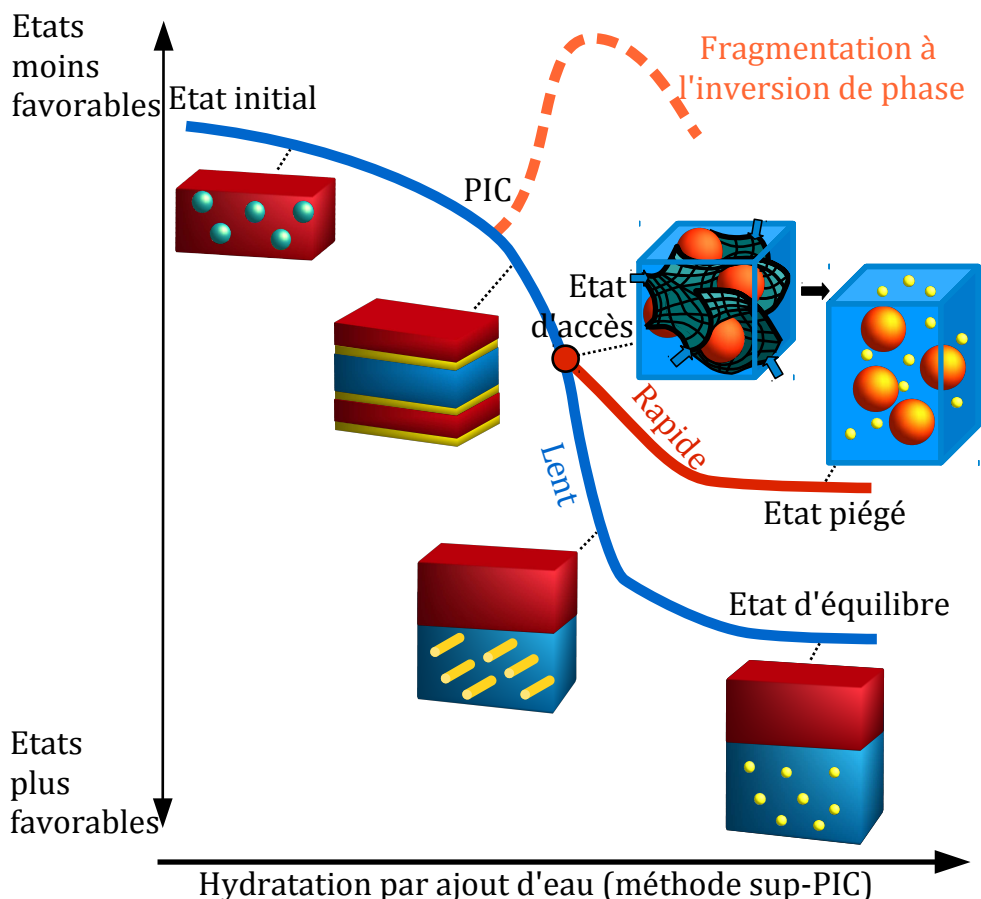


Figure 6.2: Une nanoémulsion peut être obtenue par hydratation d'un système eau/huile/tensioactif par ajout rapide d'eau. A basse fraction en eau la suite d'états est similaire à celle d'équilibre. L'addition supplémentaire d'eau conduit à une bifurcation correspondant à un état d'accès qui contrôle les propriétés et la structure de la nanoémulsion finale.

Ces deux variantes correspondent à un scénario commun dans lequel le système est amené vers un état d'équilibre bien contrôlé et duquel il ne peut s'échapper, alors que le paysage continue autour de lui d'évoluer.

Une toute autre possibilité est de pousser le système vers son état d'équilibre mais de jouer sur la succession de barrières qui l'y emmènent en freinant sa progression, ce qui permet de contrôler l'évolution des structures. Un bon exemple est celui du basculement de solvant qui est une méthode de nano-précipitation. La transformation est déclenchée par addition d'un mauvais solvant à une solution d'un soluté en bon solvant, ce qui provoque la précipitation du soluté. Sans contrôle du chemin le soluté va former des gouttes qui vont fusionner et en former de plus grosses jusqu'à atteindre la séparation macroscopique des phases. Cela peut-être décrit comme une descente avec des barrières de plus en plus petites au fur et à mesure que les gouttes grossissent. Au contraire si nous ajoutons maintenant des répulsions entre les gouttes, les barrières vont augmenter au fur et à mesure que les gouttes grossissent. Cette suite de barrières de hauteurs croissantes permettent d'obtenir une collection de gouttelettes de même taille, ce qui est illustré par la Figure 6.3.

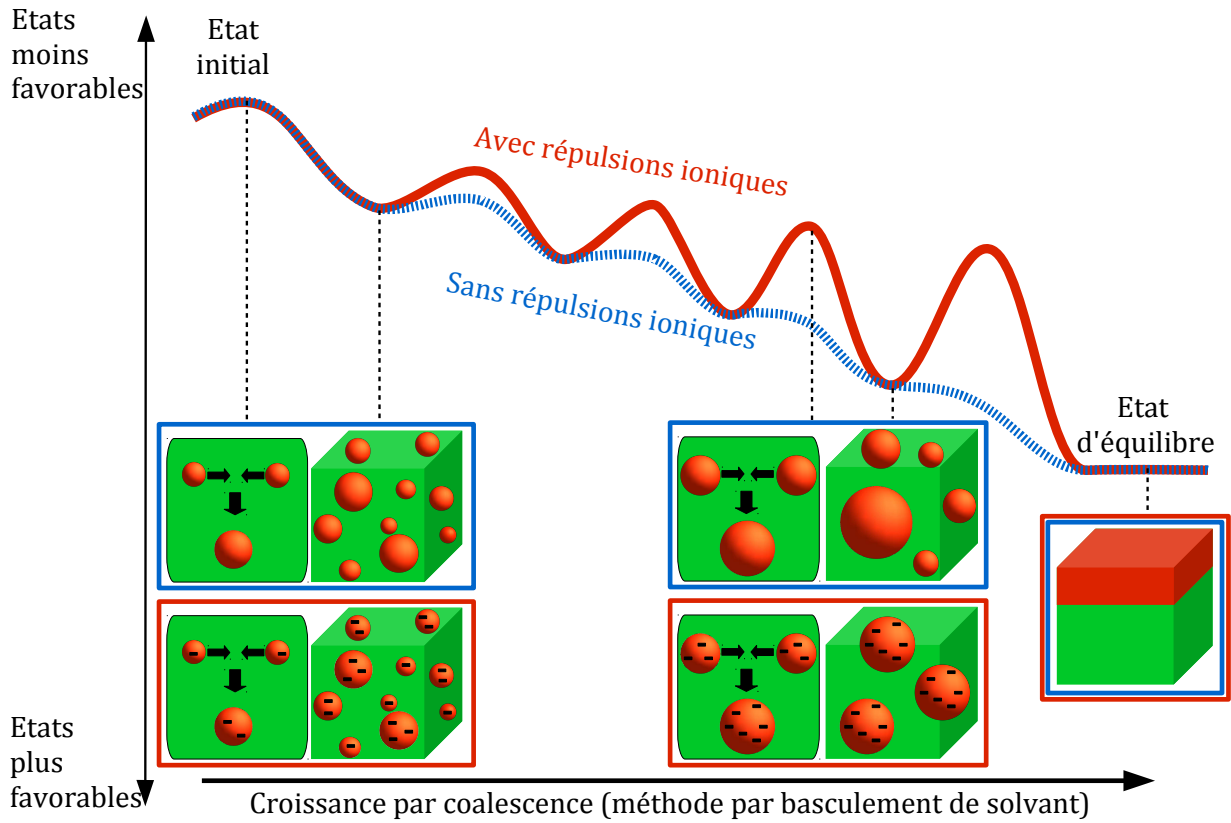
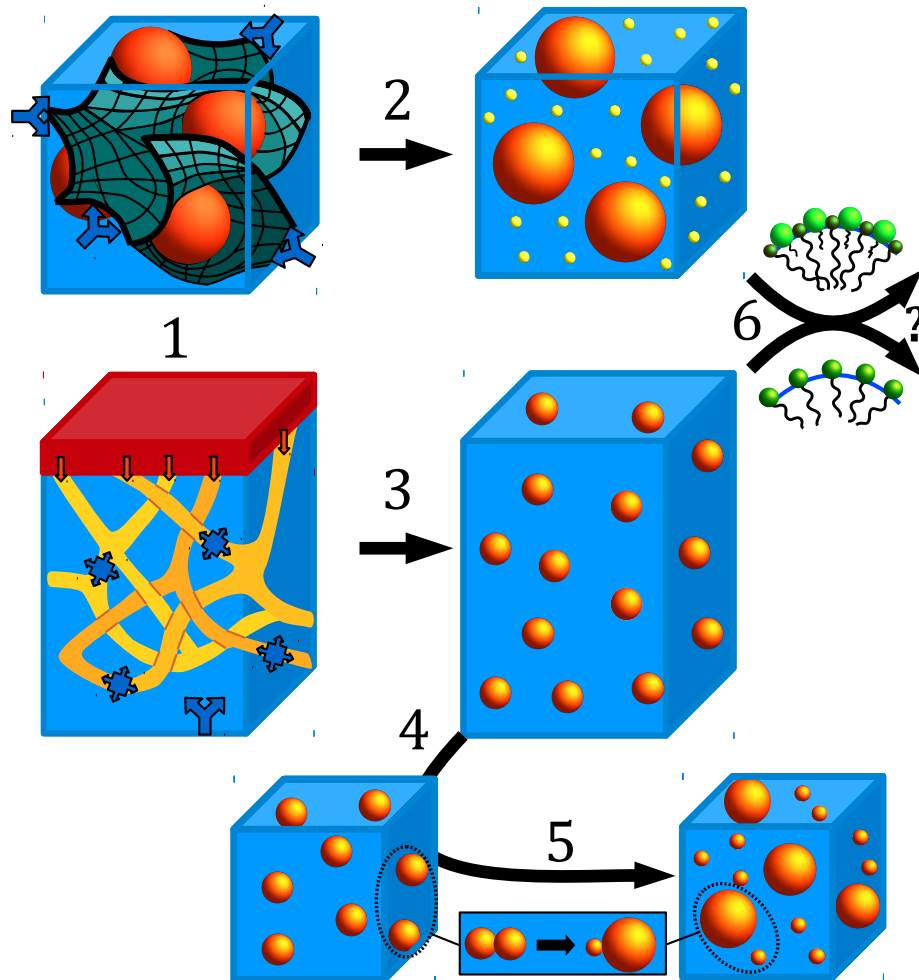


Figure 6.3: Une chute rapide de la qualité du solvant conduit à la précipitation du soluté sous la forme de gouttes. Si les gouttes ne se repoussent pas, la coalescence se déroule de plus en plus facilement lorsque la taille augmente et les barrières décroissent. Au contraire, si les gouttes se repoussent la coalescence est de plus en plus difficile au fur et à mesure que les gouttes croissent. Cette situation conduit à l'obtention de populations étroites de gouttes.

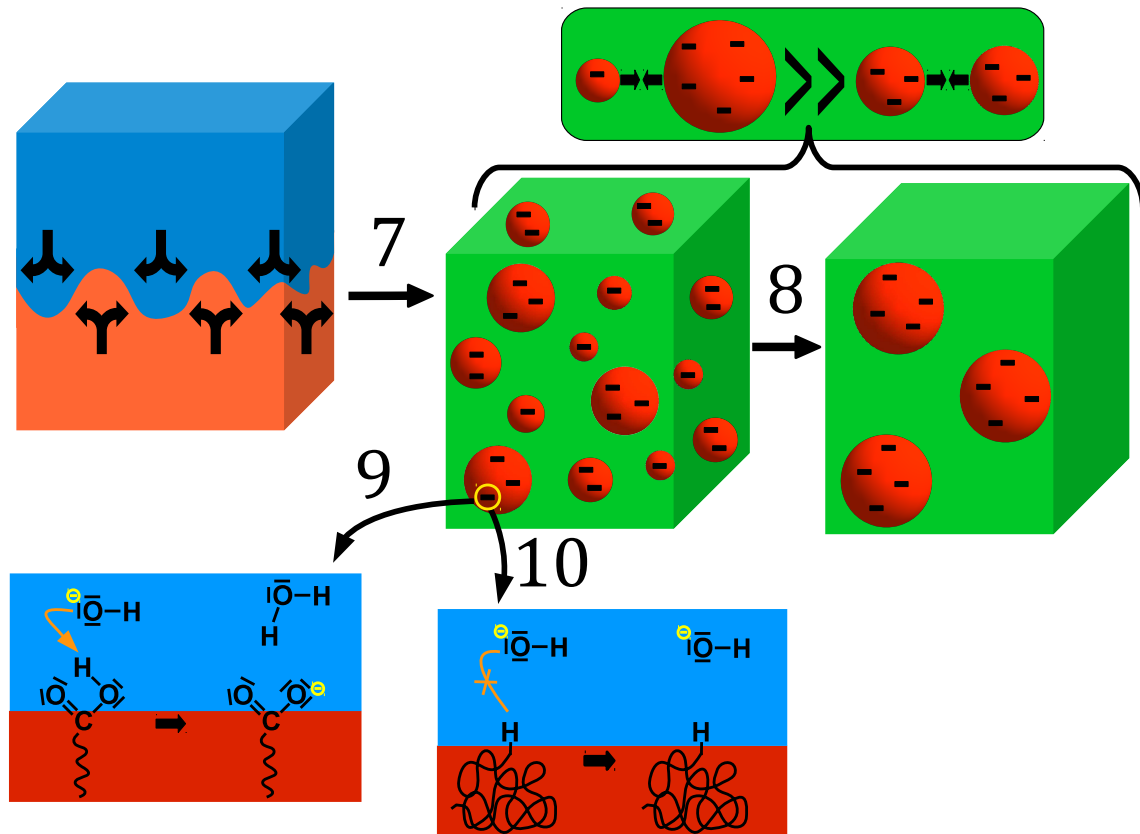
6.2 Méthodes d'auto-assemblage

| | Evolution 1 | Evolution 2 | Evolution 3 |
|--------------|--|---|---|
| Système | Eau+ Huile+ Tensioactif | Eau+ Huile+ Tensioactif | Polymère ou huile+ Bon solvant+ Mauvais solvant |
| Etat initial | Système pauvre en eau : déshydratation | Système riche en eau, déshydratation par interactions | Huile ou polymère en bon solvant |
| Déclencheur | Hydratation par ajout d'eau | Hydratation par modification des interactions (T, pH, force ionique) | Addition d'un mauvais solvant |
| Chemin | Nucléation d'huile dans une phase éponge | Formation d'une microémulsion surgonflée | Coalescence limitée par les répulsions |
| Piège | Couche tensioactive tournée vers l'huile | Couche tensioactive tournée vers l'huile | Répulsions ioniques entre surfaces chargées |
| Etat piégé | Nanoémulsion avec excès de tensioactif Taille typique : 100-300 nm | Nanoémulsion monodisperse sans excès de tensioactifs Taille typique : 10-100 nm | Nanoémulsion ou nanodispersion de particules polymères Taille typique : 50-200 nm |

6.3 Découvertes principales



1. La fragmentation d'un système lors d'une inversion de phase n'est pas liée à l'obtention de nanoémulsions (Articles 1 & 2).
2. Des nanoémulsions sont obtenues par dilution d'une solution huile/tensioactif par une séparation de phase contrôlée dans une phase éponge bicontinue (Article 2)
3. Une transition entre sphères et structures bicontinues est observée sous cisaillement permet l'obtention de microémulsions surgonflées (Article 3).
4. Des nanoémulsions monodisperses et de tailles contrôlées sont préparées sans excès de tensioactif par piégeage de microémulsions surgonflées (Article 1).
5. Un nouveau mécanisme de déstabilisation d'émulsion est identifié et caractérisé : le murissement de contact (Article 8).
6. Les méthodes de nanoémulsification sont étendues avec succès à des mélanges de tensioactifs et la gamme d'application est caractérisée (Article 9).



7. La nanoprécipitation par basculement de solvant a été caractérisée (mécanisme, effets de mélange, importance des répulsions (Articles 6 & 10)
8. Preuve théorique et expérimentale que la coalescence limitée par les répulsions conduit à des populations étroites de gouttes (Article 6)
9. La charge de surfaces hydrophobes purifiés en contact avec l'eau est expliquée par une contamination d'acides gras ce qui contredit une explication basée sur l'adsorption d'ions hydroxydes (Articles 4 & 5).
10. Les propriétés colloïdales de particules de polymères constituées d'unités neutres sont contrôlées par les bouts de chaîne des macromolécules (Article 7).

6.4 Auto-assemblage hors-équilibre : Hydratation du tensioactif

6.4.1 Trempe d'états d'accès plutôt qu'inversion de phase

Les systèmes eau/huile/tensioactif présentent une large variété de structures résultant d'auto-assemblages à l'équilibre dont le choix est principalement effectué par la courbure préférée de la monocouche de tensioactif. A basses courbures préférées, l'obtention de gouttes de taille contrôlée par gonflement de micelles est empêchée par la formation de réseaux bicontinus. Dans ces conditions la formation de gouttes par auto-assemblage à l'équilibre est impossible et nous devons alors emprunter des chemins hors-équilibre.

Néanmoins, pour obtenir des collections uniformes de gouttes de taille contrôlée, nous devons maintenir des contraintes fortes qui sont caractéristiques d'un processus d'auto-assemblage. Cela suppose d'entraîner le système hors de son état d'équilibre mais pas trop loin, ce qui correspond à garder intacte l'importance de la courbure préférée. Le système peut soit être mené le long de barrières le séparant d'états d'équilibre, ce qui correspond à des structures proches, ou plus loin, ce qui nécessite non seulement des barrières mais un changement de structure.

En pratique, la courbure préférée est contrôlée par l'hydratation de la tête hydrophile. Une tête hydrophile très hydratée fait pencher la balance des interactions à l'interface en faveur de l'hydrophilicité, ce qui se traduit par une courbure préférée tournée vers l'huile. Au contraire, une tête hydrophile très peu hydratée fait pencher la balance des interactions en faveur de l'hydrophobicité et la courbure préférée est vers l'eau. Des changements d'hydratation déclenchent donc des changements de courbure préférée et donc de structures. Si la courbure se tourne de l'eau vers l'huile, la transition est dénommée inversion de phase. Par ailleurs, de fortes valeurs de courbures préférées érigent de fortes barrières à la coalescence des gouttes.

Deux types de leviers ont été utilisés pour changer rapidement l'hydratation. L'un repose sur un changement soudain de l'interaction entre l'eau et la tête hydrophile, à travers un changement de paramètre physico-chimiques (température, force ionique, pH). L'autre est basé sur l'addition rapide d'eau à un système initialement pauvre en eau.

Dans les deux cas, un état déterminant les propriétés finales de la nanoémulsion a été identifié. Cet état d'accès a une structure bien définie, qui correspond à une courbure préférée précise, et contrôle le déroulement du processus hors-équilibre. Cet état d'accès correspond à un auto-assemblage hors-équilibre. Les états d'accès sont monophasiques et correspondent à une courbure préférée tournée vers l'huile, comme dans la nanoémulsion finale. La composition et le degré d'hydratation requis pour l'obtention de ces états sont contraints sur une ligne. Expérimentalement les états d'accès correspondent à un minimum de turbidité et la ligne de solubilisation a donc été nommée frontière d'éclaircissement

(Clearing Boundary).

Une brusque augmentation de courbure préférée par hydratation depuis ces états d'accès déclenche l'assemblage de la nanoémulsion finale. La séparation de phase macroscopique est contrée par de fortes barrières à la coalescence, qui empêchent le système d'atteindre son état d'équilibre.

Le mécanisme d'auto-assemblage hors-équilibre dans les systèmes eau/huile/tensioactif est contrôlé par les variations de courbure préférée, comme pour l'auto-assemblage à l'équilibre. Les états d'accès contiennent les contraintes structurales majeures et les transfèrent à la nanoémulsion finale. Le chemin hors-équilibre peut-être décrit en deux étapes, d'abord la formation de l'état d'accès, ensuite l'évolution rapide (trempe) vers la nanoémulsion finale, qui érige des barrières de métastabilité.

Ce nouveau mécanisme va à l'encontre d'une croyance répandue dans la littérature que l'émulsification se déroule par une fragmentation lors de l'inversion de phase. Un tel mécanisme par inversion de phase est basé sur les faibles valeurs de la tension interfaciale lorsque la courbure s'inverse de l'eau vers l'huile. Puisque nous montrons que le processus est contrôlé par la traversée d'états d'accès, dont les structures sont déjà situées après l'inversion de phase, cette dernière est sans rapport avec l'émulsification.

Malgré ces similitudes, des différences entre les états d'accès ont été identifiées selon que l'hydratation soit déclenchée par modification des interactions ou par addition d'eau. L'hydratation par modification des interactions est associée à des changements structuraux alors que l'hydratation par addition d'eau se déroule plus près de l'équilibre. Les différences de structures de ces états d'accès conduisent à des différences de propriétés dans nanoémulsions finales, dont les principales caractéristiques sont données dans les deux prochaines sous-sections. Les systèmes sont quant à eux précisés dans la dernière sous-section.

6.4.2 Hydratation par modification des interactions

Les changements d'hydratation peuvent être accomplis en excès d'eau, à travers un changement des interactions entre la phase aqueuse et les têtes hydrophiles du tensioactif. La courbure préférée, c_0 , peut être ajustée à la courbure géométrique, $1/R_{go}$, ce qui s'écrit : $R_{go} \cdot c_0 = 1$. Comme décrit dans le chapitre 1 portant sur l'auto-assemblage à l'équilibre, cette équation correspond à la frontière de formation des microémulsions sphériques, qui sont des collections uniformes de micelles gonflées de rayon $R_{go} = 1/c_0$. A basses concentrations en tensioactif, on observe expérimentalement que cette microémulsion sphérique est remplacée par un réseau bicontinu en équilibre avec un excès d'eau et d'huile. Nous avons réalisé la transformation inverse en cisillant le système. Le cisaillement détruit le réseau bicontinu et, si le système est sur la ligne $R_{go} \cdot c_0 = 1$, une collection uniforme de gouttes est obtenue. Ces états stationnaires sous cisaillement sont des microémulsions de taille caractéristique plus grande que les microémulsions à l'équilibre classiques et

ont donc été nommées microémulsions surgonflées. Leur rayon est le rayon géométrique $R_{go} = 3l_s(\phi_{huile}/\phi_{tensioactif})$, déterminé par un unique paramètre de composition, le ratio huile/tensioactif, qui est aussi le ratio volume/aire. Si l'agitation est stoppée, le système abandonne l'état surgonflé pour reformer son état d'équilibre bicontinu.

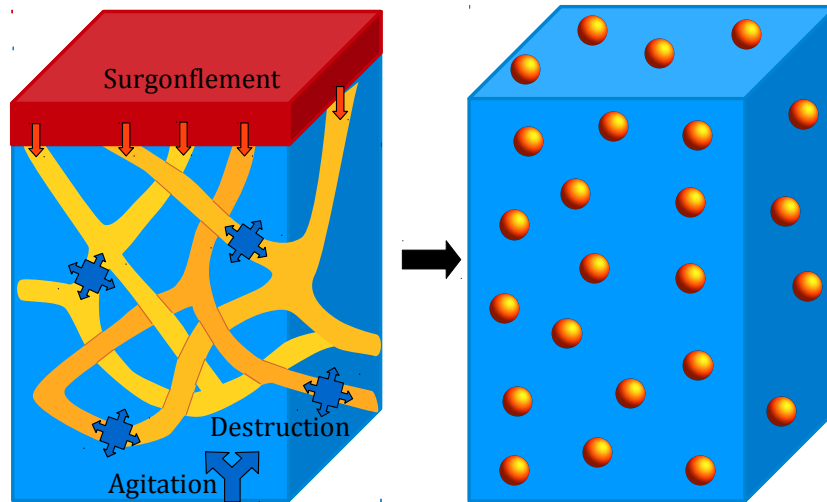


Figure 6.4: Les réseaux bicontinus en équilibre avec de l'eau et de l'huile sont détruits par le cisaillement. Si la courbure préférée correspond à la courbure de sphères monodisperses, la formation d'une microémulsion surgonflée est observée. Cet état stationnaire peut alors être piégé dans un état métastable, la nanoémulsion, par une brusque augmentation de courbure.

Néanmoins, une augmentation rapide de la courbure préférée depuis cette microémulsion surgonflée ne laisse pas au système de temps de modifier sa structure. Alors que la courbure préférée augmente, la coalescence des gouttes devient difficile. La trempe en courbure transforme alors la microémulsion surgonflée sous cisaillement en nanoémulsion métastable. Cette méthode d'émulsification est unique par la combinaison de trois propriétés :

- Tout le tensioactif est efficacement utilisé, c'est à dire que tout le tensioactif est aux interfaces eau/huile.
- Une population très étroite de gouttes est obtenue, c'est à dire une nanoémulsion monodisperse.
- La taille des gouttes est totalement contrôlée dans la gamme 10-100 nm par un unique paramètre de composition.

Néanmoins, son utilisation nécessite de traverser la ligne de surgonflement, $R_{geo}.c_0 = 1$. Il est dès lors nécessaire de connaître les variations de courbure préférée c_0 . La méthode la plus efficace est d'établir un diagramme de phase dont on peut extraire ces variations. La découverte de la microémulsion surgonflée comme état d'accès devrait simplifier l'utilisation de cette méthode de nanoémulsification. En effet elle rend inutile de procéder à l'inversion

de phase, qui est difficile à contrôler industriellement due à un changement rapide des propriétés macroscopiques dans sa proximité. A l'échelle du laboratoire cette méthode est très utile pour préparer des émulsions monodisperses de taille contrôlées, qui sont des systèmes modèles très utiles pour étudier des phénomènes colloïdaux. Ce potentiel a été partiellement exploré dans ce travail à travers l'étude d'un nouveau processus de déstabilisation dans les émulsions, le mûrissement de contact, dont nous reparlerons un peu plus loin.

6.4.3 Hydratation par ajout d'eau

Une autre manière de modifier l'hydratation du tensioactif est d'ajouter directement de l'eau. Si l'état initial est pauvre en eau, la monocouche de tensioactif est courbée vers l'eau pour maximiser l'hydratation insuffisante. L'addition d'eau va relâcher cette contrainte et la courbure préférée va se tourner progressivement vers l'huile au fur et à mesure que la tête hydrophile se gonfle d'eau. Un petit nombre d'états monophasiques, dans lesquels l'huile est solubilisée, sont obtenus à faible fraction d'eau. Le plus riche en eau de ces états correspond à une courbure déjà tournée vers l'huile, à une fraction en eau plus grande que celle correspondant à l'inversion de phase. La structure de cet état d'équilibre est une phase éponge bicontinue, qui est un réseau de bicouches gonflées d'eau, dont chaque monocouche est localement tournée vers l'huile.

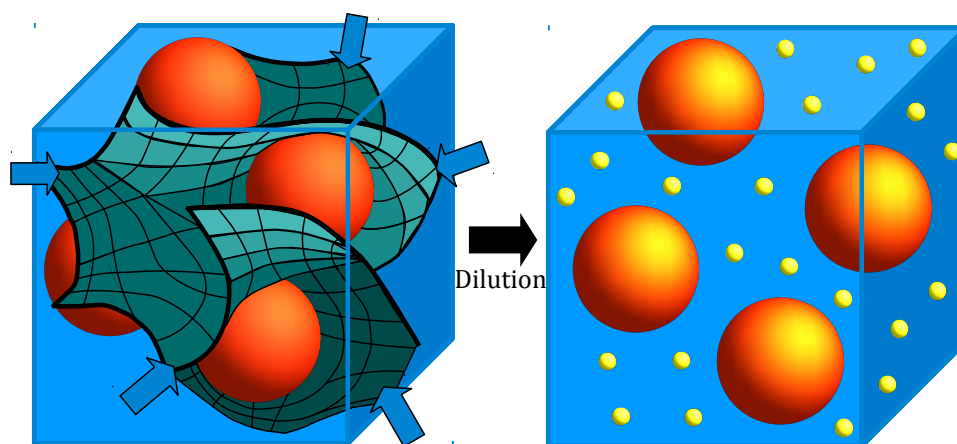


Figure 6.5: L'addition rapide d'eau à une phase éponge bicontinue provoque la nucléation d'huile dans cette matrice. La courbure moyenne des monocouches entourant ces gouttes détermine la taille finale des gouttes.

A l'équilibre cette structure est détruite lorsque plus d'eau est ajoutée, ce qui conduit à une séparation macroscopique de l'huile. Néanmoins, si l'addition d'eau est suffisamment rapide, la monocouche de tensioactif n'a pas le temps de changer sa courbure pour s'ajuster à la courbure préférée. La phase huile se sépare bien mais dans la matrice de la phase éponge. Les gouttes se forment par auto-assemblage jusqu'à un rayon qui correspond à la

courbure des monocouches de la phase éponge. Ces gouttes sont ensuite protégées de la coalescence par l'augmentation rapide de courbure préférée.

Puisque la courbure de la phase éponge est beaucoup plus faible que celle des microémulsions surgonflées, qui correspondent à la structure optimale, une partie du tensioactif est gachée et les gouttes sont plus grosses et polydisperses que dans la méthode précédente. Des gouttes de typiquement 100-300 nm coexistent avec des micelles du tensioactif en excès. Cependant, cette méthode est particulièrement facile à utiliser et porter à l'échelle industrielle. Une application industrielle importante est l'émulsification sur site pour produire des fluides lubrifiants.

6.4.4 Systèmes étudiés

Jusqu'à présent la présentation s'est focalisée sur les aspects mécanistiques avec l'introduction du concept d'état d'accès. Cependant, l'identification expérimentale de ces mécanismes est basée sur un choix attentif des systèmes. Les tensioactifs oxyéthylénés purifiés (> 99 %) ont par exemple été abondamment utilisés. Ces molécules sont constituées d'une chaîne alcane liée à une chaîne oxyde d'éthylène (EO or EG). L'eau est un bon solvant des chaînes EO à basse température mais la qualité de solvant diminue lorsque la température est augmentée. Cette propriété originale permet de contrôler finement l'hydratation de la tête du tensioactif, et donc la courbure préférée, par la température. C'est une des manières pour changer l'hydratation par modification des interactions entre l'eau et les têtes. La méthode d'émulsification associée était nommée la méthode Phase Inversion Temperature (PIT), puisque l'inversion de phase était censée décrire le mécanisme. Puisque nous avons identifié un état d'accès, la microémulsion surgonflée, à des températures plus basses, cette méthode est en fait une méthode sub-PIT (sans liens avec l'inversion de phase).

Le même système peut être utilisé pour l'hydratation par ajout d'eau. La gamme de température est alors toujours sub-PIT pour s'assurer que la courbure préférée soit tournée vers l'huile aux fortes fractions en eau. L'ajout d'eau fait gonfler la couche hydrophile, ce qui dirige la courbure vers l'huile. La composition correspondant à l'inversion de phase est nommée Phase Inversion Composition (PIC), ce qui a également conduit à la description incorrecte de la méthode d'émulsification comme une méthode PIC. Cependant elle n'est pas non plus liée à l'inversion de phase puisque la phase éponge est obtenue à des fractions en eau plus grandes que l'inversion de phase, cette émulsification est donc une méthode sup-PIC.

Les concepts d'auto-assemblages hors-équilibres ont été développés sur ces systèmes modèles et leur extension à des systèmes plus complexes peut être mise en cause. Une extension importante effectuée dans ce travail est d'utiliser deux tensioactifs. Cette étape est un bon intermédiaire entre le système à un tensioactif et les systèmes réels.

Un système à deux tensioactifs étudié consiste en un mélange d'un tensioactif oxyéthyléné

avec un acide gras. L'acide gras est un tensioactif lipophile à bas pH mais très hydrophile à haut pH. A bas pH la température peut-être ajustée pour atteindre la frontière d'éclaircissement. Sous agitation une microémulsion surgonflée est obtenue, comme pour le cas du tensioactif unique. La courbure préférée peut alors être augmentée rapidement à température constante par augmentation du pH. Le système est alors piégé dans un état métastable, une nanoémulsion monodisperse de taille contrôlée, comme dans le cas d'un tensioactif unique. Cependant une différence majeure est constatée : alors que n'importe quel état initial de plus basse hydratation que l'état d'accès menait au même état final dans le cas d'un tensioactif unique, dans le cas de mélanges il faut partir de l'état d'accès. Cela s'explique par la ségrégation possible du mélange de tensioactif entre différentes structures qui empêche la formation de l'état d'accès lors d'une trempe rapide. Il est donc essentiel de partir de l'état d'accès pour obtenir la nanoémulsion désirée. Cela souligne encore davantage l'importance du concept d'état d'accès développé dans ce travail.

La même conclusion a été atteinte avec des systèmes tensioactifs octylglucoside/span ou SDS/oxyethylenated. Dans ces cas la courbure préférée a été ajustée par addition d'eau à des états pauvres en eau. Comme pour le cas du tensioactif unique, l'état d'accès est une phase éponge bicontinue, qui contraint la séparation de l'huile et donne les gouttes finales.

La conclusion générale est que les mécanismes d'émulsification par hydratation de tensioactif sont générales et que leur utilisation requiert l'identification de l'état d'accès.

6.5 Auto-assemblage hors-équilibre : basculement de solvant

L'émulsification par hydratation est basée sur la modification de l'énergie libre des interfaces. Une alternative est d'utiliser des méthodes basées sur la modification de l'énergie libre des volumes. Plusieurs noms existent nous pouvons les dénommer nano-précipitations. En effet une bonne description est une précipitation restreinte à l'échelle colloïdale ("nano"). Prenons un soluté en solution dans un solvant. Le mélange est favorisé par l'entropie de mélange qui domine l'énergie d'interaction. Si cette énergie d'interaction est modifiée elle peut dominer l'entropie de mélange et conduire à une séparation de phase. Une telle modification peut se dérouler par la modification du soluté par réaction chimique ou par modification du solvant par addition d'un non-solvant, un changement de température, de force ionique ou autre. Des populations étroites de gouttes ou de particules sont souvent obtenues, ce qui signifie que le système est très contraint. Des dispersions de nanoparticules de métaux et d'oxydes sont généralement produites par réaction chimique sur le soluté afin de modifier les interactions solvant/soluté.

Dans ce travail, nous utilisons une autre route qui ne met pas en jeu de réaction chimiques. Elle conduit à des gouttes d'huile ou de solution de polymère gonflé et repose sur

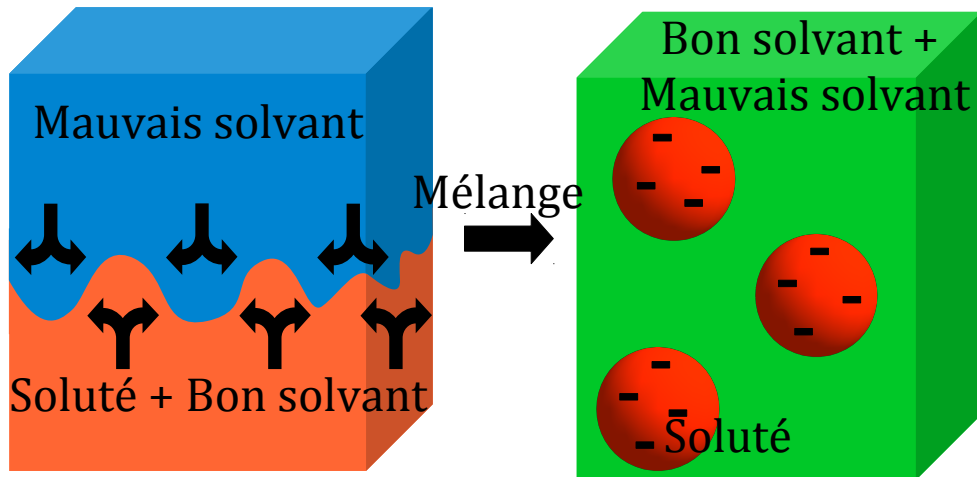


Figure 6.6: Le mélange d'une solution soluté/solvant avec un mauvais solvant peut conduire à la formation de gouttes du soluté ou de particules. Cette route par basculement de solvant couple l'hydrodynamique et la physico-chimie.

l'addition d'un mauvais solvant miscible avec un mélange soluté/solvant. L'eau a été utilisée comme non-solvant, l'acétone comme bon solvant et une huile ou un polymère comme soluté. Ce basculement de solvant conduit à une précipitation du soluté. La méthode se déroule en deux étapes : l'hydrodynamique du mélange et la précipitation du soluté.

La vitesse relative de chaque étape détermine leur degré de couplage. Nous avons utilisé un dispositif permettant de contrôler précisément le mélange. A grande vitesse de mélange, l'étape hydrodynamique est rapide devant celle de précipitation et elles sont donc découplées. Dans ce cas le diamètre des gouttes finales ne dépend pas de la concentration en soluté et est déterminé uniquement par les répulsions entre gouttes. Si des mélanges de macromolécules neutres et chargées sont utilisés, les particules sont homogènes. A faible vitesse de mélange, l'étape hydrodynamique est couplée à l'étape de précipitation. Le diamètre augmente alors avec la concentration en soluté, tout en dépendant des répulsions entre gouttes. Si des mélanges de macromolécules neutres et chargées sont utilisés, les particules tendent à avoir une structure coeur-écorce puisque les différentes macromolécules précipitent à des fractions en eau différentes. Cette connaissance permet un meilleur contrôle de la technique de basculement de solvant pour élaborer des systèmes modèles ou complexes.

6.6 Chemins hors-équilibre

6.6.1 Mûrissement de contact

La coalescence et le mûrissement d'Ostwald sont les deux mécanismes bien établis conduisant à la destruction des émulsions. Quelques études indiquent que cette description

des manuels ne semble pas couvrir toutes les observations expérimentales. Le murissement de contact a été postulé comme un mécanisme intermédiaire. Comme la coalescence les gouttes doivent venir au contact et comme le murissement d'Ostwald l'échange est moléculaire. Ce troisième mécanisme est difficile à isoler puisqu'il ressemble aux deux autres.

Nous démontrons dans ce travail l'existence du murissement de contact : nous visualisons l'échange rapide de deux isotopes d'une huile très peu soluble dans l'eau à taille de goutte constante. Cette étude tire profit des méthodes d'émulsification par hydratation qui permettent d'obtenir des émulsions monodisperse sans excès de tensioactif. Une variation systématique de la structure des huiles et tensioactifs a été menée, avec l'usage de composés purifiés.

Le murissement de contact est freiné par les répulsions entre gouttes et est ainsi plutôt favorisé dans les systèmes non-ioniques ou concentrés. Dans le régime dilué une approche champ moyen est efficace puisque le processus ne dépend pas de la concentration en gouttes. Comme pour le murissement d'Ostwald une loi de croissance $R_{moyen}(t) \sim t^{1/3}$ est observée, mais pour des raisons différentes. Cette similarité est à la base des difficultés expérimentales pour distinguer l'un au l'autre des processus et explique probablement de nombreux écarts dans les données de la littérature entre expériences et théorie. Nous montrons que le murissement de contact est activé par la déshydratation du tensioactif, ce qui permet à l'huile de perméer plus efficacement à travers la couche de tensioactif. Il est également favorisé par les courtes chaînes.

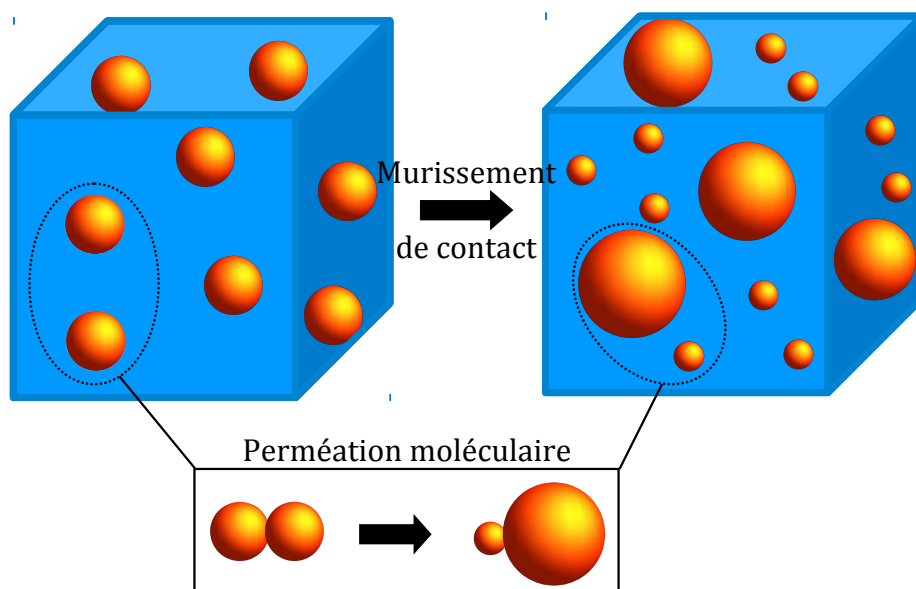


Figure 6.7: Le murissement de contact se déroule par perméation de molécule d'huile au contact de deux gouttes.

La mise en évidence et la caractérisation de ce nouveau processus de déstabilisation est essentielle pour améliorer la formulation d'émulsions. En effet même quand

l'expérimentateur prend soin de protéger l'émulsion contre la coalescence, avec de bonnes barrières tensioactives, ou du murissement d'Ostwald, en utilisant des huiles peu solubles dans l'eau, le murissement de contact peut tout de même avoir lieu et détruire l'émulsion.

6.6.2 Coalescence contrôlée par les répulsions

Le domaine de la synthèse de nanoparticules couvre un large champ de compositions et de conditions mais est centré sur un objectif : la préparation de populations étroites en tailles. En effet les propriétés originales à l'échelle nanométrique sont liées à la taille des objets. Pour sélectionner une propriété précise, il est donc nécessaire de sélectionner une taille précise. De faibles polydispersités sont également requises pour obtenir des cristaux colloïdaux. Malgré certaines critiques expérimentales, le schéma de synthèse dérive du schéma de nucléation/croissance. Dans cette approche le soluté précipite pour former des nuclei critiques qui croissent par capture de molécules de soluté.

Pour éviter les complications associées aux réactions chimiques, nous avons utilisé la méthode de basculement de solvant pour étudier la formation de nano-objets par précipitation. L'étape hydrodynamique a été écartée en utilisant un mélangeur rapide. Pour la première fois nous avons observé la recombinaison des gouttes. En utilisant une technique résolue en temps de diffusion de rayonnement nous avons observé que le nombre de gouttes diminuait avec le temps, au fur et à mesure de la croissance. Les gouttes croissent donc par coalescence. Une nouvelle loi de croissance a été identifiée dans laquelle le rayon croît logarithmiquement avec le temps $R_{moyen}(t) \sim \ln(t)$ alors que la polydispersité décroît ($\sigma R/R_{moyen} \sim R_{moyen}^{-1/2}$).

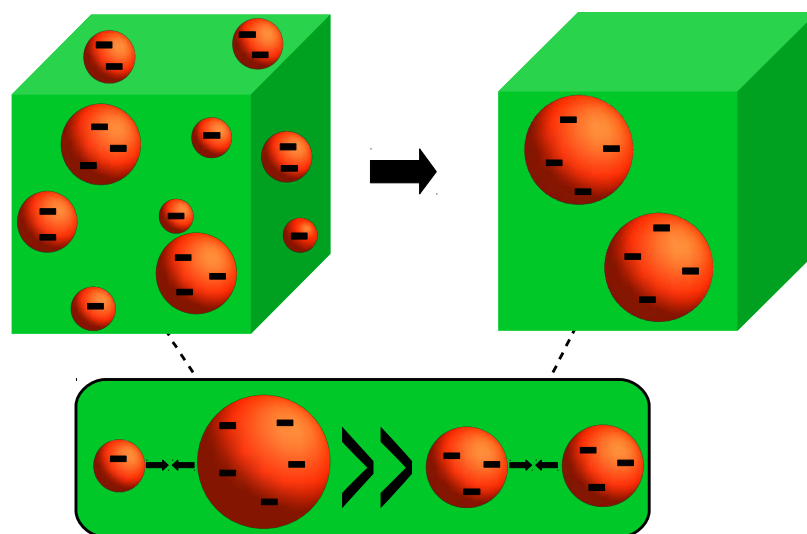


Figure 6.8: La coalescence contrôlée par l'approche des gouttes suit une loi de croissance originale. Le rayon croît logarithmiquement avec le temps avec une chute de la polydispersité. Cela s'explique par des évènements de coalescence moyen+moyen moins favorables que petit+gros.

Nous démontrons ainsi que la coalescence peut mener à des populations étroites, si l'étape limitante est l'approche des gouttes. C'est le cas de gouttes peu couvertes qui coalescent au contact. Peu courante dans le monde des émulsions, cette situation se rencontre aisément dans le domaine des dispersions de nanoparticules. Un modèle quantitatif est développé dans ce travail. L'idée centrale est que les répulsions augmentent avec la taille des gouttes. Les rencontres petites/grosses sont dès lors plus probables que moyenne/moyenne. Cela conduit à une fréquence de coalescence plus grande pour les petites gouttes et la queue de la distribution aux petites tailles se déplace vers les grandes tailles plus vite que la taille moyenne. Des populations étroites sont alors obtenues.

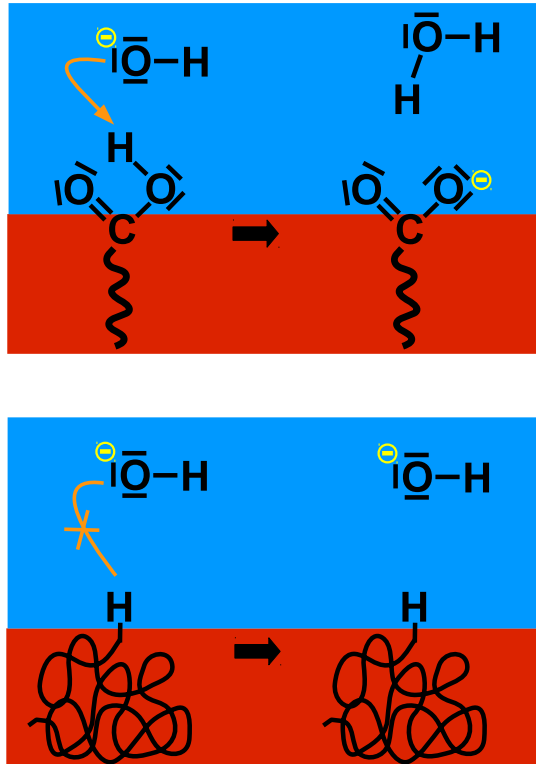
Dans le domaine colloïdal, les processus limités par la diffusion conduisent à un comportement auto-similaire (polydispersité constante durant la croissance), ce qui correspond dans la théorie des phénomènes critiques à la première loi d'échelle. Dans ce travail nous identifions pour la première fois dans le domaine colloïdale la deuxième loi d'échelle (polydispersité décroissante durant la croissance). Ce pont entre deux domaines différents de la physique est la clé pour concevoir des synthèses raisonnées de nano-objets par des méthodes de précipitation.

6.6.3 Origine des répulsions dans des conditions sans tensioactif

Dans le régime pauvre en tensioactif, les gouttes sont peu couvertes par le tensioactif. Au contact il n'y a donc pas de barrières à la coalescence. Cependant, lorsque les tensioactifs sont chargés, les répulsions ioniques entre gouttes freinent la coalescence. Dans la limite ultime, le régime sans tensioactif, la barrière répulsive devrait disparaître et la coalescence devrait être simplement limitée par le taux de collisions entre gouttes.

Pourtant, depuis plus d'un siècle, la présence d'une charge de surface négative sur des surfaces réputées pures a été observée. Les exemples typiques sont les bulles d'air dans l'eau, les gouttes d'huile purifiées dans l'eau et les particules de polymères dans l'eau. Deux communautés se sont affrontées sur une explication de ce phénomène. Les deux théories diffèrent par leur vocabulaire mais reposent toutes deux sur de subtiles modifications des propriétés de l'eau à une interface hydrophobe. Une expression usuelle est que les ions hydroxydes s'adsorbent à ces interfaces, une autre que le réseau de liaisons hydrogènes est perturbé.

Dans ce travail, nous sommes rentrés dans la controverse en montrant que toutes les observations pouvaient être expliquées par des traces d'acides gras dans les huiles. Cela correspond à l'impossibilité expérimentale de travailler en conditions sans tensioactif dans les émulsions. Cette conclusion a fait l'objet de deux commentaires dans la littérature, auxquels nous avons adressés une réponse. Nous y démontrons que des surfaces de polymère sans charges (ce qui est possible si les bouts de chaînes ne sont pas chargés) ne sont pas chargées et qu'aucune particule ne peut être stabilisée. Nous démontrons ainsi qu'aucune



altération de la structure de l'eau à proximité d'une interface hydrophobe ne peut donner des répulsions ioniques entre objets colloïdaux.

Des conditions sans tensioactifs peuvent être obtenues pour les dispersions de polymère dans l'eau. Dans ce cas, nous démontrons que la charge de surface est déterminée par les bouts de chaîne des macromolécules. Les bouts de chaîne sont créés lors de l'étape d'initiation, dans laquelle l'initiateur réagit avec le monomère. Les initiateurs comportent souvent des fonctions ionisables (sulfates ou carboxylates). Le contrôle des bouts de chaîne n'est d'habitude pas pris en compte dans les propriétés macroscopiques des matériaux polymères mais nous démontrons qu'il est essentiel pour celui des propriétés colloïdales, comme les rencontres entre particules. Nous montrons également que le nombre de bouts de chaîne est déterminé par les processus d'auto-assemblages et que la mesure de ce nombre peut donc donner des informations sur le processus de formation des particules.

Remerciements

Notre éducation souffre souvent d'une focalisation sur les concepts, idées, démonstrations donnant l'impression que la connaissance est générée dans un monde abstrait parallèle au nôtre. Il est alors facile d'oublier l'histoire du développement des idées, qui s'inscrit dans un contexte et repose sur des personnes. En science cet abandon est motivé par un souci d'objectivité, qui conduit à abandonner environnement, histoire et personnes pour se concentrer sur des concepts plus universels. Cette thèse ne déroge pas à la règle, néanmoins je tiens à faire de brefs remerciements aux acteurs de cette thèse, qui m'ont accompagné le long du chemin ou préparé à l'arpenter. Je n'échapperai pas à la répétition du mot merci.

Bernard Cabane a guidé ce travail de thèse. Je le remercie du fond du cœur pour m'avoir soutenu et accueilli au début de mes aventures au pays des émulsions, puis d'avoir accepté d'encadrer le projet de thèse qui se dégageait progressivement au fil des expériences. Son approche scientifique, sa curiosité, sa perspicacité, son exigence, son calme et son goût pour les échanges sont des modèles pour moi. Je le remercie pour son amitié au fil des années et j'espère que cette thèse reflète certaines de ces qualités.

Ulf Olsson a été mon guide culturel au pays des tensioactifs comme du Grand Nord. Je le remercie pour des collaborations fructueuses et un accueil toujours chaleureux à Lund. Je pense que cette thèse porte en elle un peu de l'approche scandinave.

Håkan Wennerström et Véronique Schmitt m'ont fait l'honneur d'accepter la charge de rapporteur de ce travail. Je les remercie pour des échanges particulièrement intéressants et enthousiastes au cours de mes années de thèse, à Lund ou à Bordeaux, qui ont été moteurs pour certains projets.

David Quéré a bien voulu co-encadrer cette thèse et je le remercie pour avoir donné un point de vue plus extérieur au déroulement de cette thèse, et finalement rassurant.

Jérôme Bibette m'a accueilli au sein de son laboratoire pendant ces trois années de thèse ce qui a été absolument essentiel à la conduite des projets expérimentaux, je le remercie d'avoir également accepté de participer au jury.

Martine Meireles-Mesbernat, Jean-François Berret et Jean-François Joanny complètent le cercle du jury et je les remercie de leur participation.

Je remercie Robert Botet, théoricien de tous les défis, Jean-Pierre Cohen-Addad, pour notre projet diagramme de phase, Hamid Elaissari, pour les synthèses de PMMA, Peter Lindner et Ralf Schweins, de l'instrument D11 de l'ILL, pour des collaborations fructueuses.

Je remercie également Robert Prud'homme pour son accueil dans son laboratoire, et Christina Tang pour sa collaboration sur place.

Je remercie mes amis pour leur soutien et leur compagnie.

J'ai eu la chance de fréquenter deux environnements très dynamiques. Je remercie le LCMD de m'avoir accueilli en ambassade PMMH dans leurs rangs. Bien sur tout d'abord Leslie, Hugo et Perrine puis le petit Léo qui ont partagés mes quelques présences dans notre salle de manip, mais aussi Denis, Damien, Fanny, Donatien, Julie ainsi que tous les autres membres du laboratoire (une mention particulière pour Florence pour son aide technique). I thank equally my friends and colleagues from the Physical Chemistry division, with special thoughts for Jonas (and Sussie), John (special mention for proofing one version of the thesis), Marianna, Marc, Lucia, Alexandra, Salomé, Luis, Azat, Luigi, Charlotte, Yukari, Wataru, Aleksandra, Celen and Marie. Je salue également mes collègues du PMMH, particulièrement David, Martin et Joaquim.

Some experiences in life are more difficult than others but often the opportunity to meet great people arise, I want to thank Tim for his friendship from the first day of this thesis. Following this line, I thank Celie for extremely interesting discussions as well as support and insight over the years.

Au cercle gourmand de mes amis parisiens, je remercie Gabriel, Mei, Justine, Alban, Benjamin et Baptiste. Merci également à Gonzague, Marine et Florent, Catherine pour leur amitié au fil des années. Une pensée également pour Alix, Faustine et Diane pour des rencontres rares mais précieuses. A Flavie pour sa compagnie des bancs du M2 au parquet de Jussieu.

A Tristan, binôme devant l'éternel, pour son amitié et son soutien au cours des années (merci aussi pour la relecture des premiers chapitres). Vanessa, Simon et Elisa complètent le cercle explosif des chimistes de Cachan et je les remercie pour leur amitié depuis notre rencontre.

A mes compagnons de théâtre de ces dernières années, mes adversaires aux lames effilées et Alexandra pour sa patience à m'apprendre l'art de la harpe. A toutes les personnes intéressantes rencontrées également au détour des conférences, avec une mention spéciale à Chantal qui le vaut bien.

J'adresse également une pensée à mes deux jeunes amis Sébastien et Léa, ainsi qu'au cercle de voisins de Locmiqel. Cette thèse a vu le jour au gré des marées et j'espère ainsi avoir capturé un peu de ma terre dans ces pages.

Je dédie cette thèse à ma famille.

A mon grand-père Jean et à Jacqueline. A ma grand-mère Henriette et sa sœur Anne-Marie pour toutes les mémoires heureuses qui ne sauraient être effacées par l'histoire. A mon grand-père Paul pour m'avoir tant appris, dont l'art subtil de naviguer dans différents univers de règles. Je pense que cette thèse bénéficie certainement de cette expérience.

A mon frère Yann, parti quelques jours avant le début de cette thèse, je dédie une vision des paysages et des chemins qu'il aurait sans doute pris plaisir à retrouver dans ces systèmes plus exotiques que ceux tracés sur notre terre. A mon frère Mikaël, je dédie le goût de m'avoir toujours poussé à progresser et à apprendre pour ne pas le laisser partir trop devant.

A mes parents pour m'avoir mis au monde, élevé et aimé. Leur soutien moral et matériel lors de l'écriture de cette thèse est à l'image du reste de leur contribution à ma vie, essentiel. A mon père Jean-Paul pour n'avoir jamais douté de moi et à ma mère Annie pour m'avoir appris tout ce qu'il y a d'important.

Résumé

Le but de ce travail est de détourner un système de son état d'équilibre, afin de le piéger dans d'autres états hors-équilibre. Les systèmes utilisés sont de type (eau+huile+amphiphile) ou (polymère+bon solvant+mauvais solvant). L'objectif est d'éviter la séparation macroscopique de phases en la restreignant à l'échelle microscopique, afin d'obtenir des collections uniformes de gouttes de taille contrôlées. Des méthodes physico-chimiques, pour lesquelles les contraintes sont les interactions entre molécules, sont employées. Un premier scénario consiste à mener le système le long d'états d'équilibre jusqu'à une bifurcation qui le conduit dans un piège ce qui l'éloigne alors de son état d'équilibre. Cela correspond expérimentalement à l'addition rapide d'eau à une solution (huile+amphiphile). Un deuxième scénario se déroule en menant le système un peu plus haut que ses états d'équilibres par perturbation, comme l'agitation, jusqu'à atteindre un état piégé dont il ne s'échappe pas alors que les états d'équilibre s'éloignent. Cette situation est observée lors de l'hydratation de la couche d'amphiphile par une variation des interactions entre l'eau et la tête hydrophile, à travers la température, la force ionique, le pH. Un troisième scénario consiste à pousser le système vers son état d'équilibre tout en érigeant sur son chemin des barrières de plus en plus hautes. Cela correspond au basculement de solvant où la coalescence, qui conduit à la séparation de phase, est freinée par les répulsions ioniques. Deux nouveaux types de chemins ont également été identifiés au travers de l'étude, le murissement de contact correspondant à un échange moléculaire entre gouttes au contact, et la coalescence limitée par l'approche de gouttes chargées. L'origine des barrières ioniques dans les systèmes purifiés a également été élucidée.

Abstract

The purpose of this work is to lure a system away from its equilibrium state and trap it into other non-equilibrium states. The systems investigated are (oil+water+amphiphile) or (polymer+good-solvent+bad-solvent). The aim is to avoid macroscopic phase separation and restrain it to the microscopic scale, in order to obtain uniform collections of size-controlled droplets. The approach is to use physicochemical methods, which use interaction constraints between the molecules to self-assemble the droplets. A first scenario is to take the system along equilibrium states until a bifurcation leading to a trapped state, while the equilibrium states move far away. It is observed when water is rapidly added to a (oil+amphiphile) solution. A second scenario is to take the system slightly above equilibrium states, through shear, to reach a trapped state, while the equilibrium states move far away. It is encountered when changing the surfactant layer hydration through physical parameters such as temperature, pH or ionic strength. A third scenario is to push the system towards equilibrium but raise increasingly high barriers as it evolves. This corresponds to the solvent-shifting technique where coalescence, which ultimately leads to macroscopic phase separation, is increasingly hindered by ionic repulsions. Two novel types of pathways have also been identified in this work, contact ripening, which corresponds to molecular exchange at droplets contact, and hindered coalescence, which corresponds to coalescence limited by the droplets approach. The origin of ionic barriers in purified systems has also been elucidated.